DOE/ER-0045/12

Alloy Development for Irradiation Performance

Semiannual Progress Report
For Period Ending March **31, 1984**

U.S. Department of Energy
Office of Fusion Energy

Printed in the United States of America. Available from
National Technical Information Service
U.S. Department of Commerce
5285 Port Royal Road, Springfield, Virginia 22161
NTIS price codes—Printed Copy: A10 Microfiche A01

This report was prepared as an account of work sponsored by an agency of the United States Government Neither the United States Government nor any agency thereof. nor any of their employees, makes any warranty. express or implied, or assumes any legal liability or responsibility for the accuracy, completeness. or usefulness of any information. apparatus. product. or process disclosed. or representsthat its use would not infringe privately owned rights. Reference herein to any specific Commercial product, process, or service by trade name. trademark. manufacturer. *or* otherwise. does not necessarily constitute *or* imply its endorsement. recommendation, or favoring by the United States Government or any agency thereof The views and opinions of authors expressed herein do not necessarily state or reflect those of the United States Government or any agency thereof.

DOE/ER-0045/12
Distribution
Category
uc-20. 20c

ALLOY DEVELOPMENT FOR IRRADIATION PERFORMANCE
SEMIANNUAL PROGRESS REPORT FOR PERIOD ENDING MARCH 31, 1984

ARGONNE NATIONAL LABORATORY

GA TECHNOLOGIES, INC.

McDONNELL DOUGLAS ASTRONAUTICS COMPANY

NAVAL RESEARCH LABORATORY

OAK RIDGE NATIONAL LABORATORY

SANDIA NATIONAL LABORATORIES

WESTINGHOUSE HANFORD COMPANY

Date Published: July 1984

Prepared by
OAK RIDGE NATIONAL LABORATORY
Oak Ridge, Tennessee 37831
operated by
MARTIN MARIETTA ENERGY SYSTEMS, INC.
for the
U. S. DEPARTMENT OF ENERGY
Under Contract No. DE-AC05-840R21400

Reports previously issued in this series are as follows:

DOE/ET-0058/1	Period Ending March 31. 1978
DOE/ET-0058/2	Period Ending June 30, 1978
DOE/ET-0058/3	Period Ending September 30, 1978
DOE/ET-0058/4	Period Ending Oecember 31. 1978
DOE/ET-0058/5	Period Ending March 31, 1979
DOE/ET-0058/6	Period Ending June 30, 1979
DOE/ET-0058/7	Period Ending September 30, 1979
DOE/ER-0045/1	Period Ending December 31, 1979
DOE/ER-0045/2	Period Ending March 31, 1980
DOE/ER-0045/3	Period Ending June 30, 1980
DOE/ER-0045/4	Period Ending September 30, 1980
DOE/ER-0045/5	Period Ending December 31, 1980
DOE/ER-0045/6	Period Ending March 31, 1981
DOE/ER-0045/7	Period Ending September 30, 1981
DOE/ER-0045/8	Period Ending March 31, 1982
DOE/ER-0045/9	Period Ending September 30, 1982
DOE/ER-0045/10	Period Ending March 31, 1983
DOE/ER-0045/11	Period Ending September 30, 1983

FOREWORD

This report is the nineteenth in a series of Technical Progress Reports on *"Alloy Development for Irradiation Performance"* (ADIP), which is one element of the Fusion Reactor Materials Program, conducted in support of the Magnetic Fusion Energy Program of the U.S. Department of Energy. Other elements of the Materials Program are

- *Damage Analysis and Fundamental Studies (DAFS)*
- *Plasm-Materials Interaction (PMI)*
- *Special-Purpose Materials (SPM)*
- *High Heat Flus* **Components**

The first seven reports in this series are numbered DOE/ET-0058/1 through 7. This report is the twelfth in a new numbering sequence that begins with DOE/ER-0045/1.

The ADIP program element is a national effort composed of contributions from a number of National Laboratories and other government laboratories, universities, and industrial laboratories. It was organized by the Materials and Radiation Effects Branch, Office of Fusion Energy, DOE, and a Task Group on *Alloy Development for Irradiation Performance,* which now operates under the auspices of the Reactor Technologies Branch. The purpose of this series of reports is to provide a working technical record of that effort for the use of the program participants, for the fusion energy program in general, and for the Department of Energy.

This report is organized along topical lines in parallel to a Program Plan of the same title so that activities and accomplishments may be followed readily relative to that Program Plan. Thus, the work of a given laboratory may appear throughout the report. Chapters 1, 2, 8, and 9 review activities on analysis and evaluation, test methods development, status of irradiation experiments, and corrosion testing and hydrogen permeation studies, respectively. These activities relate to each of the alloy development paths. Chapters 3, 4, 5, 6, and 7 present the ongoing work on each alloy development path. The Table of Contents is annotated for the convenience of the reader.

This report has been compiled and edited under the guidance of the Secretary of the Task Group on *Alloy Development for Irradiation Performance.* F. W. Wiffen, Oak Ridge National Laboratory, and his efforts and those of the supporting staff of ORNL and the many persons who made technical contributions are gratefully acknowledged. T. C. Reuther, Reactor Technologies Branch, is the Department of Energy Counterpart to the Task Group Chairman and has responsibility for the ADIP Program within DOE.

G. M. Haas, Chief
Reactor Technologies Branch
Office of Fusion Energy

CONTENTS

FOREWORD iii

1. ANALYSIS AND EVALUATION STUDIES 1

1.1 Materials Handbook for Fusion Energy Systems (McDonnell Douglas Astronautics Company and Westinghouse Hanford Company) 2

The handbook effort for this reporting period has been directed toward maintenance of a continuous flow of data sheets into the handbook. One hundred and thirty-five (135) new data sheets are being monitored through the various stages of preparation.

1.2 Lifetime Analysis: Thermally Driven Fatigue Crack Growth in an HT-9 First Wall (GA Technologies) 4

Fmcture mechanics calculations are used to predict crack growth behavior in an HT9 first wall.

2. TEST MATRICES, EXPERIMENT DESCRIPTIONS, AND METHODS DEVELOPMENT 12

2.1 Neutron Source Characterization for Materials Experiments (Argonne National Laboratory) . . . 13

Dosimetry measurements were conducted in the ORR during February 1984 to test the performance of a hafnium core piece for the MFE4 spectral-tailoring experiment. Flux gradients were measured in position C3, both with and without the hafnium liner. The results agree mther well with expectations. Results are also reported for the MFE4B experiment after 424 full power days. The maximum fluence was 1.9 × 10^{22} n/cm^2 producing about 64 appm helium and 5.1 dpa in 316 stainless steel.

2.2 Neutronics Calculations in Support of the ORR-MFE-4A and -48 Spectral Tailoring Experiments (Oak Ridge National Laboratory) 22

The calculated fluences from the ongoing three-dimensional neutronics calculations are being scaled to agree with experimental data. As of March 27, 1984, this treatment yields 158.5 at. ppm He (not including 2.0 at. ppm He from ^{10}B) and 10.36 dpa for type 316 stainless steel in ORR-MFE-4A and 99.4 at. ppm He and 7.10 dpa in ORR-MFE-4B.

2.3 Operation of the ORR Spectral Tailoring Experiments ORR-MFE-4A and ORR-MFE-48 (Oak Ridge National Laboratory) 24

The specimens contained in the ORR-MFE-4A experiment have operated for an equivalent of 833 d at 30 MW reactor power with temperatures of 330 and 400°C. The specimens contained in the ORR-MFE-4B experiment have opemted for an equivalent of 634 d at 30 MW reactor power with tempemtures of 500 and 600°C.

2.4 Summary of the EBR-II An-2 Ferritics Irradiation Experiment (Westinghouse Hanford Company) 26

Six uninstrumented B-7c capsules were removed from the EBR-11 after undergoing irradiation during Cycles 109-113 (August 1980 to June 1981). Several specimens were removed and distributed for interim examination, while the remaining specimens were re-encapsulated into four new B-7c capsules. In addition, some unirmdiated specimens were included in the new capsules. These capsules were removed after undergoing irradiation during Cycles 118-121 and 123 (February 1982 to April 19831.

2.5 High-Fluence Irradiation of Ferritic Steels in HFIR: HFIR-CTR-49 and -50 (Oak Ridge National Laboratory) 31

The HFIR-CTR-49 and -50 experiments contain tensile specimens and transmission electron microscopy (TEM) disks of various ferritic steels. Irradiation is planned at 400 and 600°C to damage levels of 50 and 100 dpa.

2.6 Irradiation of Miniature Charpy Impact 12 Cr-1 MoVW Specimens at 200 and 300°C: HFIR-CTR-53 (Oak Ridge National Laboratory) 33

The HFIR-CTR-53 experiment will contain 16 miniature Charpy specimens of the national fusion heat of 12 Cr-1 MoVW. Irradiation Will be at 200 and 300°C and will achieve a midplane damage level of 8 dpa.

2.1 Introduction to the U.S./Japan Collaborative Testing Program in HFIR and ORR (Oak Ridge National Laboratory and Japan Atomic Energy Research Institute) 35

An implementing arrangement between WE and Japan Atomic Energy Research Institute on U.S.-Japan collaborative testing of first wall and blanket structuml mterials with mixed-spectrum fission reactors initiated collaborative tests of eight HFIR capsules and two ORR spectral-tailoring capsules. The implementing arrangement also serves as a vehicle of future collaboration between DOE and JAERI on other areas of fusion technology. The HFIR and ORR spectral-tailoring capsules will be equally shared by the two programs.

2.8 Irradiation Experiments for the U.S./Japan Collaborative Testing Program in HFIR and ORR (Oak Ridge National Laboratory) 31

The design of all eight capsules HFIR-JP-I through -JP-8 is completed, and the parts for four capsules have been made. Two capsules have been assembled and are now being irmdiated. Design of the ORR capsule to operate at 60 and 200°C, designated ORR-MFE-6J, is complete, and parts procurement for a proof-ofdesign capsule is in progress.

2.9 The U.S./Japan Collaborative Testing Program in HFIR and ORR: Irradiation Matrices for HFIR Irradiation (Oak Ridge National Laboratory and Japan Atomic Energy Research Institute) 38

The first four capsules in the U.S./Japan collaborative program are currently being irmdiated in HFIR. The general objectives of the experiments are outlined and the detailed loading of each capsule described.

3. PATH A ALLOY DEVELOPMENT — AUSTENITIC STAINLESS STEELS 44

3.1 Effect of the Microstructure on Postirradiation Tensile Properties of Type 316 Stainless Steel (Oak Ridge National Laboratory) 45

Tensile specimens of type 316 stainless steel were given different solution-anneat heat treatments and irradiated in the ORR at 250, 290, 450, and 500°C to a fist neutron fluence of about 6.8 × 10^{25} neutrons/m^2 (~5 dpa and 40 at. ppm He). The tensile properties were determined at the irmdiation temperatures for steel solution annealed 1 h at 1050°C, I h at 1150°C, and 1 h at 1050°C fotlowed by 10 h at 800°C.

3.2 Irradiation Creep in Path A Alloys Irradiated to 5 dpa in the ORR-MFE-4B Spectral Tailoring Experiment at 500 and 600°C (Oak Ridge National Laboratory) 52

Pressurized tubes of 20%-cold-worked type 316 stainless steel and 25%-cold-worked Prime Candidate Alloy Were irmdiated at 500 and 600°C in the Oak Ridge Research Reactor spectral tailoring experiment to 5.1 dpa. Diametral measurements were mde to determine irmdiation creep mtes. Both alloys behaved mther similarly but exhibited lower creep mtes than. did the Fast Flux Test Facility first core type 316 stainless steel irmdiated in EBR-II.

3.3 Swelling Behavior of Manganese — Bearing Steel AISI 216 (Westinghouse Hanford Company) . . . 55

The inclusion of 8.5 wt% manganese in AISI 216 (Fe-6.7Ni-8.5Mn-20Cr-2.7Mo-0.32Si) does not appear to alter the swelling behavior from that found to be typical of austenitic alloys with comparable levles of austentite-stabilizing elements. The swelling in AISI 216 in EBR-II is quite insensitive to irmdiation temperature in the range 400 — 650°C. Microscopy reveals that this my arise from the low level of precipitation that occurs in the alloy.

3.4 The Development of Austenitic Steels for Fast Induced-Radioactivity Decay (Oak Ridge National Laboratory) 59

A program was started to develop austenitic steels for fusion reactors in which the induced mdioactiuity decays to low levels in a reasonable time. Ten smll button heats of Fe-Cr-Mn-C alloys were melted, cast, and rolled. These heats will be used to determine austenite-stable compositions that can serve as a base composition for further alloying.

3.5 The Tensile Properties and Bend Ductility of PCA After Irradiation in HFIR (Oak Ridge National Laboratory) 61

Three different microstructures of PCA were irmdiated in the High Flus Isotope Reactor at temperatures from 300 to 600°C to approximately 22 dpa and approzimtely 1750 at. ppm He. The E3 condition with coarse MC in the grain boundaries and cold-worked mtrix resisted helium embrittlement better than the PCA-AI (solution annealed) or PCA-A3 125% cold worked). Disk bend ductility data were useful for screening, but correlation with tensile ductility was poor.

4. PATH E ALLDY DEVELOPMENT -- HIGHER STRENGTH Fe-Ni-Cr ALLOYS 64

5. PATH C ALLOY DEVELDPMENT — REACTIVE AND REFRACTORY ALLOYS 65

5.1 Swelling of V-15Cr-5Ti Alloy on Single- and Dual-Ion Irradiation (Arqonne National Laboratory) 66

The effect of single ($^{58}Ni^{++}$)- and dual-ion ($^{58}Ni^{++}$ + 3 He^{+})-irradiation on the microstructure of the V-15Cr-5Ti alloy at 725°C was determined for irmdiation damage levels of 125 and 205 dpa and for either the pre-implanted helium 1780 appm) or simultaneously implanted helium (9.3 appm/dpa) condition. The swelling of the alloy that could be attributed to voids or cavities was negligible. The principle effect on the microstructure of the irradiation was to induce the formation of a high density of disc-like precipitates in the vicinity of grain boundaries and intrinsic precipitates and on the dislocation structure.

5.2 Helium Doping of a Vanadium Alloy by a Modified Tritium Trick (flak Ridge National Laboratory) 12

A tritium trick technique was used to implant ^{3}He in V-15Cr-5Ti. Modifications include wrapping specimens with tantalum foil and decay hold at 400°C. Removal of undecayed tritium at 700°C my have been excessive, because large helium bubbles in the grain boundaries severely embrittled the V-15Cr-5Ti alloy. More realistic helium distributions can probably be produced by reducing the removal temperature. The technique might facilitate the study of helium embrittlement arid provide a screening method for alloy development.

5.3 Environmental Effects on the Properties of Vanadium-Base Alloys (Argonne National Laboratory) 75

A pressurized-water refreshed autoclave system for experimentally investigating the aqueous corrosion behauior of selected vanadium-base alloys has been designed, constructed, and checked out. Test specimen material has been obtained from the ORNL Fusion Program Research Materials Inventory and sheared into corrosion coupons. A scanning Auger microprobe study of sulfur segregation in vanadium-base alloys has also been initiated.

6. INNOVATIVE MATERIAL CONCEPTS 80

6.1 The Tensile Properties and Rend Ductility of $(Fe,Ni)_3V$ Long-Range-Ordered Alloys After Irradiation in HFIR (flak Ridge National Laboratory) 81

Seveml $(Fe,Ni)_3V$ LRO alloys were irradiated in HFIR-CTR-42 and -43 at 400 to 600°C, to approximately ID dpa and approximately 1000 at. ppm He. Additions of cerium or carbon and the use of cold-worked microstructures did not improve the embrittlement resistance of the LRO alloys. The LRO-37-SRS alloy, with a microstructure produced by rapid solidification, eshibited the highest ductilities, and further study of the RS microstructure is warmnted. The correlation between bend ductility and tensile ductility was poor.

7. PATH E ALLOY DEVELOPMENT — FERRITIC STEELS 85

7.1 Postirradiation Fracture Toughness Tests of ESK Alloy HT-9 and Modified 9Cr-1Mo Alloy from URR Reactor Experiments (Naval Research Laboratory) 86

PCC_v specimens of Alloy HT-9 and Modified 9Cr-1Mo alloy were irradiated at 300°C and 149°C, respectively, to ~0.8 × 10^{20} n/cm^2, E >0.1 MeV. During this period, postirradiation tests for fracture toughness uere completed and results compared to notch ductility determinations from standard Ckarpy-V (C_v) specimens irradiated in the same reactor experiments. Fracture surface examinations by SEM are also reported.

1.2 Elevated-Temperature Tensile Properties of 9 Cr-1 MoVNb Steel Irradiated in the EBR-II AD-2 Experiment (Oak Ridge National Laboratory) 100

Tensile specimens of normalized-and-tempered 9 Cr-1 MoVNb steel Were irmdiated in EBR-II to 10 to 12 dpa at 390 to 550°C. Tests uere conducted at room temperature and at the irradiation tempemture on irradiated and unirradiated specimens. Irradiation at 390°C increased the yield stress and ultimate tensile strength. No change in strength was observed for irradiation at 450, 500, and 550°C.

7.3 Fracture Toughness of Irradiated Hi-9 (Westinghouse Hanford Company) 104

Compact tension specimens of HT-9 from the AD-2 recon experiment were tested at 205°C. Specimens of base metal have two different grain sizes: ASTM 8-9 and ASIM 3-4. One specimen of weld metal was also tested at 205°C. Test results showed that the fracture toughness of HT-9 with a larger grain size was lower and the toughness degradation due to high flue ices was more severe for the YT-9 weld metal than for the base metal.

7.4 Variation of Postirradiation Strength Properties of Ferritic Steels with Irradiation Temperatures (Oak Ridge National Laboratory) 110

Data on postirradiation strength properties have been plotted as a function of irradiation temperature, arid a consistent trend has been observed for the three ferritic steels under investigation.

7.5 Evaluation of Ferritic Alloy Fe-2-1/4Cr-1Mo After Neutron Irradiation - Microstructural Microstructural nevelopment (Westinghouse Hanford Company) 113

Microstructural examinations are reported for nine specimen conditions of 2-1/4Cr-1Mo steel which had been irradiated by fast neutrons over the temperatiire range 390 to 510°C. Void swelling is found following irradiation at 400 to 480°C. Concurrently dislocation structure arid precipitation formed. Peak void swelling, void density, dislocation density and precipitate number density developed at the lowest temperature, approximately 400°C, whereas mean void size, am? mean precipitate size increased with increasing irradiation temperature. The examination results are used to provide interpretation of in-reactor creep, density change arid post irradiation tensile behavior.

7.6 Microstructural Examination of Several Commercial Alloys Irradiated to Very High Neutron Fluence (Hanford Engineering Developnent Laboratory) 138

No contribution.

7.7 Alloy Development for Improved Swelling Resistance in Ferritic Steels (flak Ridge National Laboratory) 139

Eleven buttn melt heats of ferritic steel have been produced and are being processed to sheet form. Transmission electron microscopy disks of these heats will he irradiated in High Flux Isotope Reactor, and their postirradiation evaluation is expected to provide insight toward improving the swelling resistance of ferritic steels.

7.8 The Influence of Step Austenitizing Treatment on the Toughness and Tensile Ductility of Hydrogen Charged HT-9 (Sandia National Laboratories, Livermore) 141

Prior research on the tensile behavior of the quenched and tempered steel HT-9 has shown that the steel exhibits marked susceptibility to hydrogen embrittlement and hydrogen induced intergranular fracture. The severity of the embrittlement can he significantly reduce? and the intergranular fracture mode entirely eliminated by swaging and retempering the steel. These improvements are attributed to a reorientation of the prior austenite grain boundaries with respect to the tensile axis and to reduced carbide and impurity coverages of grain boundary interfaces. The swaging results suggest that the hydrogen compatibility of HT-9 could be increased by reducing the grain size. To assess the role of grain size, two different austenitizing treatments were employed. The first employed reductions in austenitizing tempemture to refine the prior austenite grain size. To asses8 the roles of microstructural features other than grain sine, a two step austenitizing treatment was used. In these treatments specimens were quenched from a fixed initial austenitizing temperature which determines the austenite grain size to a second, lower, austenitizing temperature. The second austenitizing temperature will redistribute the carbides and grain boundary segregants. As the same temperatures Were used in varying the austemitizing temperature and the second austenitizinq temperature in the step treatments, comparison of the two treatments should provide some insight as to the rote of grain size in the hydrogen embrittlement of this steal. The major effects of lowering the austenitizing temperature from 1050°C are to increase the hydrogen charged tensile ductility and to reduce the yield strength. Decreasing the austenitizing temperature from 1050° to 900°C increases the hydrogen charged tensile ductility from 13% to 47% and decreases the yield strength from 110 ksi to 72 ksi. Decreasing the second austenitizing temperature in the step treatment does not lower the yield strength as much as lowering the austenitizing temperature. Therefore, at the same austenitizing and second austenitizinq temperatures, the carbide morphologies are not the same and comparison of the two heat treatments cannot he used to define the role of grain size.

7.9 Hydrogen-Induced Ductility Losses in the Heat-Affected Lone of HT-9 Weldments (Sandia National Laboratories, Livermore) 146

The effect of internal hydrogen introduced by cathodic charging on the tensile hehavior of simulated HAZ microstructures has been evaluated. The loss in ductility of the HAZ after a postweld heat treatment at 750°C is equivalent to that observed in the quench-and-tempered base material. A postweld heat treatment at 600°C results in tensile ductilities which are inferior to those of the base metal at comparable charging levels.

7.10 The Development of Ferritic Steels for Fast Induced-Radioactivity Decay (Oak Ridge National Lahoratory) 156

In the 2 1/4 Cr-I Mo, 9 Cr-I MoVNb, and 12 Cr-1 MoVW steels currently of interest as structural materials for fusion reactors, the molybdenum will form long-lived isotopes that will make such alloys difficult to dispose of after reactor operation. As an alloying element, tungsten is often similar to molybdenum. To determine if tungsten can replace molybdenum in the ferritic steels of interest, eight 18-kg heats of chromium-tungsten steels have been prepared and are being investigated.

8. STATUS OF IRRADIATION EXPERIMENTS AND MATERIALS INVENTORY 158

8.1 Irradiation Experiment Status and Schedule (Oak Ridge National Lahoratory) 159

Principal features of many ADIP irradiation experiments are tabulated, with schedules for recent, current, and planned experiments. Experiments in ORR, HFIR, EBR-II, and FFTF are included.

8.2 Fusion Program Research Materials Inventory (Oak Ridge National Lahoratory, Mcnonnell Douglas Company, and GA Technologies) 166

A central inventory of research materials is maintained for use in the Fusion Reactor Materials research and development programs. A condensed, qualitative listing of the content of the inventory in given, along with a record of materials transfers in the reporting period.

9. MATERIALS COMPATIBILITY ANI) HYDROGEN PERMEATION STUDIES 169

9.1 Corrosion of Type 316 Stainless Steel, Path A PCA, and 12 Cr-1 MoVW Steel in Thermally Convective Lithium (Oak Ridge National Lahoratory) 170

Results from lithium thermal convection loops are (1) microstructural variations of prime candidate alloy did not strongly influence weight loss behavior, (2) kinetic analysis of data from six runs with type 316 stainless steel showed phase boundary reaction control for dissolution, and (3) the mass transfer of a 12 Cr-1 MoVW steel in lithium changed significantly when the loop temperatures were raised.

9.2 Environmental Effects on Properties of Structural Alloys in Flowing Lithium (Argonne National Laboratory) 176

Corrosion data on weight loss and internal penetration are presented for austenitic and ferritic steels exposed for up to 5500 h in flowing lithium at temperatures of 700 and 755 K. A flowing lithium environment has no effect on the tensile properties of the HT-9 alloy at temperatures between 505 and 755 K.

9.3 Corrosion of Structural Alloys in Flowing Ph-17Li Environment (Argonne National Laboratory) 183

Corrosion data on weight toss and internal penetration are presented for austenitic PCA and Type 316 stainless steel and ferritic HT-8 and Fe-9Cr-1Mo steel exposed in flowing Pb-17Li up to 3700 h at tempemtures of 700 and 727 K. The ferrite scales on austenitic steels show significant depletion of chromium and complete depletion of nickel from the steel.

9.4 Corrrosion of Type 316 Stainless Steel in Flowing Pb-17 at. % Li (Oak Ridge National Lahoratory) 190

Results from the exposure of type 316 stainless steel to thermally convective Pb-17 at. % Li at a maximum temperature of 500°C are reported. Weight losses Were large, hut the effects of the postexposure lithium rinse to remove the lead-lithium needed to be taken into account in the data analysis.

1. ANALYSIS AND EVALUATION STUDIES

1.1 MATERIALS HANDBOOK FOR FUSION ENERGY SYSTEMS - J. W. Davis (McDonnell Douglas Astronautics Company - St. Louis Division)

1.1.1 ADIP Task

Task Number 1.A.1 - Define material property requirements and make structural life predictions

1.1.2 Objective

To provide a consistent and authoritative source of material property data for use by the fusion community in concept evaluation, design, safety analysis, and performance/verification studies of various fusion energy systems. A secondary objective is the early identification of areas in the materials data base where insufficient information or voids exist.

1.1.3 Summary

During the past six months the handbook effort has been towards developing data sheets. For this period the effort has been to maintain a continuous flow of data sheets into the handbook. Substantial progress has been made towards the achievement of this goal by the careful monitoring of the processing of new data sheets in various stages of preparation.

1.1.4 Progress and Status

The Materials Handbook for Fusion Energy Systems (MHFES) continues to develop as a useful tool for those working in the design of fusion reactors. Publication package No. 9 continued the expansion of data in five of the eight major chapters. The latest addition to the handbook consists of data pages on a ferritic steel designated HT-9 prepared by D. S. Gelles of Westinghouse Hanford Company. The HT-9 data consists of specific heat as a function of temperature.

In addition to the data sheet that has been incorporated into the handbook during this reporting period there are 135 data sheets in various stages of review prior to incorporation into the handbook.

Twenty-two (22) data sheets on HT-9 and 316 steels rnd fiberglass epoxy have been approved and are awaiting publication at Westinghouse Hanford Company. The HT-9 data sheets, prepared by D. S. Gelles of Westinghouse Hanford Company, provide information on the effect of temperature on Poisson's Ratio, Young's Modulus and Shear Modulus, as well as physical property information on specific heat, thermal diffusivity, thermal emissivity (in vacuum and stably oxidized) and thermal conductivity. The 316 stainless steel data sheets, prepared by N. J. Simon of National Bureau of Standards, provide information on impact energy, fatigue life, fatigue crack growth and fracture toughness at cryogenic temperatures. The fiberglass epoxy data sheets, prepared by C. E. Klabunde of Oak Ridge National Laboratory, are revisions to data sheets currently in the handbook on the effect of irradiation on resistivity and weight loss.

In addition, fifty-four (54) data sheets on lithium, HT-9, 316 stainless steel, fiberglass epoxies, and polyimides have been through the review cycle and were returned to the authors to have the reviewers' comments incorporated. The lithium data sheets, prepared by W. F. Brehm of Westinghouse Hanford Company, provide thermal, mechanical, and electrical property intormation as a function of temperature. The HT-9 data sheets prepared by D. S. Gelles of Uestinghouse Hanford Company provide information on irradiation induced stress-tree swelling. The 316 stainless steel data sheets, prepared by N. J. Simon of NBS, provide mechanical property information on fracture toughness, ultimate tensile strength, tensile yield, tensile elongation, tensile reduction of area and engineering stress-strain, and thermal property information on specific heat, thermal conductivity and thermal expansion, as well as irradiation induced void swelling (stress-free and stress-affected) and precipitate-related densification. The fiberglass epoxy and polyimide data sheets, prepared by C. E. Klabunde of Oak Ridge National Laboratory, provide mechanical property information on the effect of irradiation on flexure and compressive strength for several epoxies and polyimides.

Four (4) data sheets on 21Cr-6Ni-9Mn stainless steel are being reviewed by the MHFES advisory group. These pages, prepared by El. J. Simon of NBS, provide general and mechanical property information on composition and tensile strength.

Fifty-five (55) data sheets on lithium compounds (Li_2O and Li_8ZrO_6), 21Cr-6Ni-9Mn, HT-9, 316 and stainless steel have been submitted for inclusion into the handbook. The lithium oxide data sheet, prepared at McDonnell Douglas, provides thermal conductivity information. The lithium octarirconate data sheet, prepared by G. W. Hollenberg of Westinghouse Hanford Company, providesinformation on theoretical density vs ^6Li enrichment. The 21Cr-6Ni-9Mn data sheets, prepared by N. J. Simon of NBS, provide mechanical, thermal and electrical property information at cryogenic temperatures. The 316 stainless steel data sheets, prepared by Bob Simons, M. L. Hamilton, J. S. Pintler, and D. K. Gutierrez of Westinghouse Hanford Company, prcvide mechanical and thermal property information at elevated temperatures.

Data sheets currently in preparation or planned will cover structural materials (vanadium alloys and copper alloys), supercanducting magnet case materials, ceramic electrical insulators (MACOR, alumina) and

neutron multipliers/breeders (beryllium and lithium lead). In addition, effort is underway to develop data sheets on specific design related issues such as irradiation creep and its treatment in structural design, swelling, and magnetic effects when magnetic materials are used (e.g. ferritic steels).

In our continuing effort to make the handbook more useful to the fusion energy community, we are directing our efforts towards inclusion of materials that are candidates for machines such as TFCX. These efforts include requests for submittals of data sheets for copper and magnesium oxide.

1.1.5 Conclusions

Substantial progress has been made with regard to putting information in the handbook during this period. Additional work is needed on the part of everyone, especially reviewers and page preparers. There are still a number of data pages in the review cycle awaiting approval, however, once these data pages are included in the handbook, additional new pages will be needed if the current momentum is to be sustained. Researchers in ADIP and other task groups can help by turning their experimental results into data sheets.

1.2 LIFETIME ANALYSIS: THERMALLY DRIVEN FATIGUE CRACK GROWTH IN AN HT-9 FIRST WALL - C. F. Dahms and T. A Lechtenberg (GA Technologies)

1.2.1 ADIP Task

The Department of Energy, Office of Fuslon Energy, has cited the need to Investlgate ferritic alloys under the ADIP Program Task, Ferritic Steel Development (Path El.

1.2.2 Objective

To develop a fracture management method wlth which lifetlme calculations can be performed to assess the englneerlng feasibility of using HT-9 as a first-wall and breedlng blanket structural material.

1.2.3 Summary

1.2.4 Progress and Status

1.2.4.1 Introduction

Body-centered cubic alloys such as ferritic steels and vanadium base alloys exhibit ductile to brittle transition characterlstlcs. In deslgning with such materlals. It is necessary to develop criteria and deslgn procedures to assure that canponents made from these alloys will not suffer fast or brlttle fracture. In order to develop an effective fracture management, methodology for fusion first wall/breed-lng blankets (FW/B), a definition of the critical materials parameters is requlred In conjunction with a suitable stress analysis of specific configuratlons. Then, the acceptable beginning-of-1lfe (BOL) flaw sizes and shapes can be calculated for various lifetimes. The results fran these studies can guide the manufacturing, quality assurance, inspection, and allowable operating conditions of the canponent. This contrlbution reports data on a lifetlme code uslng HT-9 as a structural material and relying on design guidelines and conflguratlons frm the Blanket Comparlson Selection Study (BCSS).[1]

An important Issue involved in uslng BCC materlals In a high energy neutron environment Is the increase In the ductile-brlttle transition temperature (DBTT) that results frm Irradlatlon. In order to fully demonstrate the potential of BCC materials such as HT-9, a computer analysls technlque based on the University of Wlsconsln WISECRACK[2] code has been developed In which crack growth is studied in a FW/B design generated by the BCSS. Mechanical property data, modifled for neutron affects (such as changes in strength, DBTT temperature, upper and lower shelf fracture toughness, and fatlgue crack grath rates) are incorporated Into the code which permits calculations of llfetimes for varlous load cycle types.

1.2.4.2 Analytical

Design Loadings

Design guidelines are specified In the BCSS for both tokamak and mlrror configurations. The main difference between the two configurations Is that the tokamak surface wall loadlng is approximately 20 times greater than that for the mlrror. The loadings used for this analysls are for the tokamak design only. Table 1.2.1 describes the loadings whlch were used to perform the thermal, stress, and fracture analyses of a tokamak flrst-wall deslgn[1].

Table 1.2.1 Oeslgn load guidelines

Neutron Wal I Loadlng = 5 MW/m^2
Surface Wall Loading = 1 MW/m^2
Irradiation Rate = 100 dpa/2 yr llfe
Wall Erosion Rate = 2 mm/2 yr llfe
Tokamak Burn Cycle = 1 x 104 sec ON. 30 sec OFF

A typical BCSS lobe type configuration was used for this analysls. Other configurations are also being studied In the BCSS and slmllar results would be anticipated for these configuratlons.

The plasma side of the wall is smooth and the coolant-breeder slde Is a flnned or ribbed configuration. This Is seen In Fig. 1.2.1. The coolant is helium and the breeding material is Li_2O. On the plasma side the wall is allowed to erode 0.1 cm per year. At the end of llfe (EOL), the thickness of the first wall at the minimum section is 0.15 cm The deslgn guideline specifies a minimum two-year iifetime which corresponds to approximately 100 dpa. A psuedo steady-state tokamak burn cycle of 10^4 sec with a 30 sec off time for resetting of the OH coll, removal of the ash and recharging of the fuel was assumed from the BCSS.

Stress Analysls

Because of the loss of material (erosion) due to the Interaction between the plasma and first wall, a sacrificial layer of 0.2 cm Is allowed for the two year minimum lifetime used In the BCSS guidelines. A thermal analysis was performed for both the BOL 0.35 cm first wall thickness and an EOL geanetry with 0.15

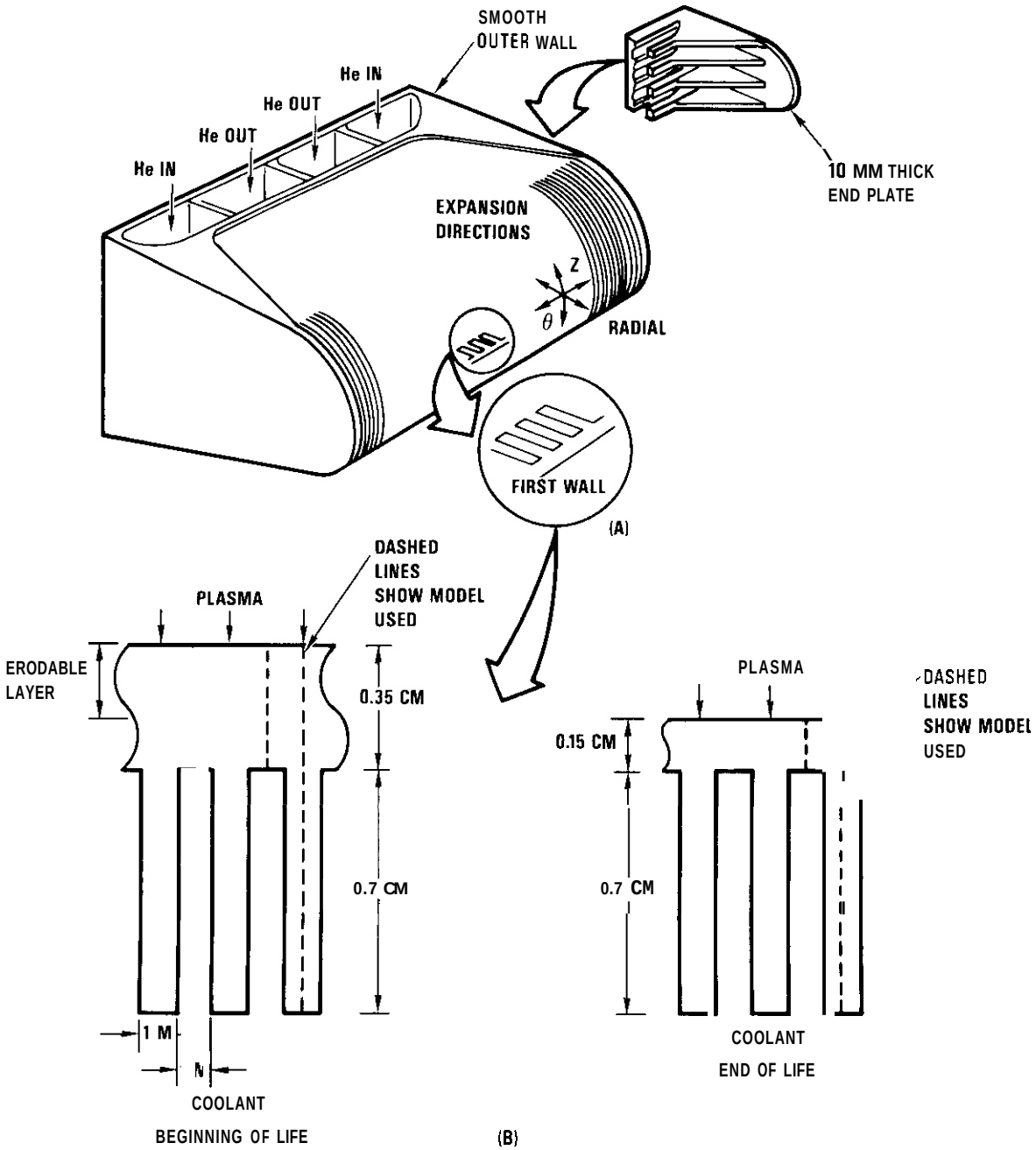

Fig. 1.2.1. Helium cooled blanket module with details.

cm thickness. Figure 1.2.2 shows the calculated surface temperatures at three locations on the first-wall at BOL and EOL. A linear distribution was assumed between these temperatures.

Figures 1.2.1 (b) shows cross-sections of the lobe wall at beginning and end of life. The dashed lines show the configuration of the models used in the computer analyses. Figure 1.2.2 shows the boundary conditions assumed for the stress analysis models. The first wall is allowed to expand freely in the z-direction by expansion joints between the module end plates and the first wall. in the cross sectional plane (r,θ), normal to the reactor toroidal direction, the lobe is attached to the distribution ducting and is not a true circular cylinder. However, the use3of an axisymmetric model has been shown to be conservative in calculating detailed first wall stresses .

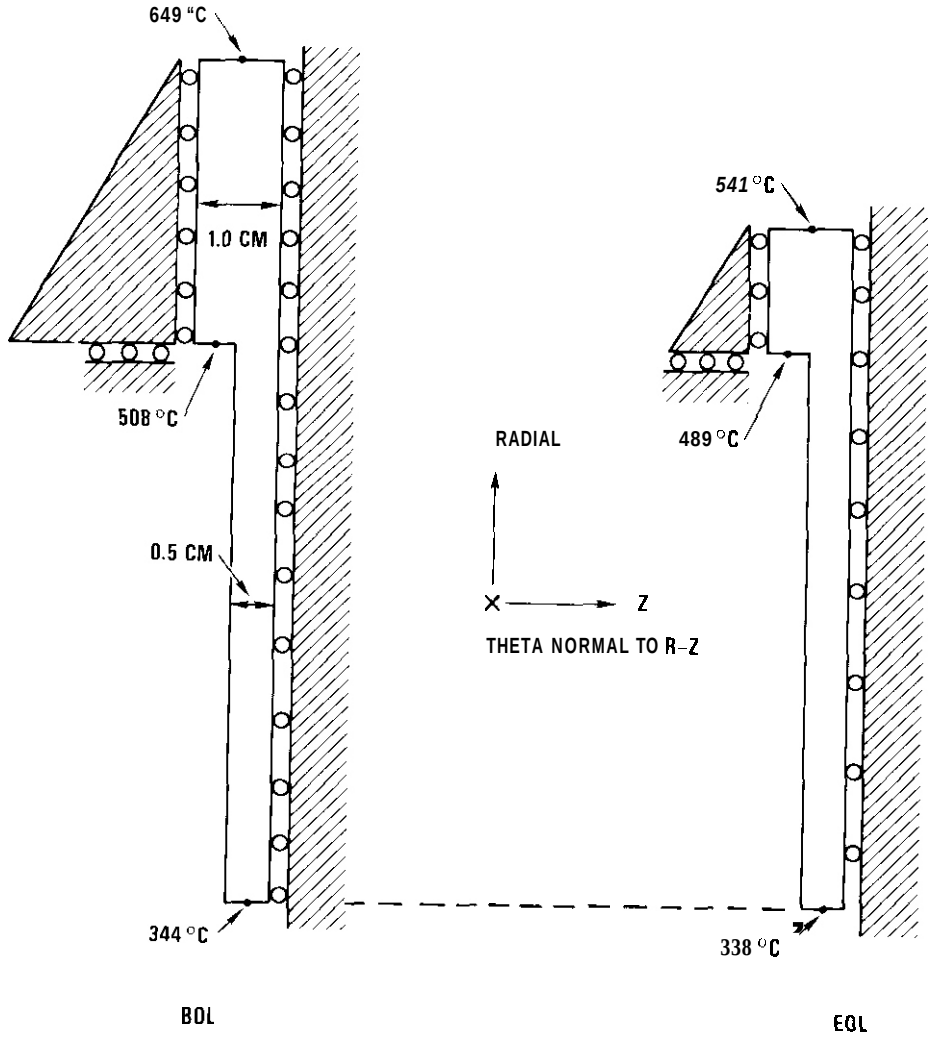

Fig. 1.2.2. Axisymmetric stress model - free body diagram for the Beginning-of-life and End-of-life condition.

The thermal stresses calculated by TEPC[4] are shown for BOL (Fig. 1.2.3) and EOL (Fig. 1.2.4). The most critical area of the first wall is the thin wall section between the cooling fins. The primary pressure stress caused by the 50 atm coolant pressure Is superimposed on the secondary thermal stresses resulting in the total stress distributions shown in Fig. 1.2.5. The thermal strains are induced only during a burn cycle ('On' cycle) as shown, but the coolant pressure stays constant during all load conditions. The end plate structure (Fig. 1.2.1) is assumed to support the pressure loads in the 2-direction and therefore no pressure stresses are experienced by the first-wall in this direction.

Two different stress cycles were utilized for the crack propagation analysis. These are intended to bracket (or bound) the possible stress states which will develop during operation and are summarized below.

Assuming an initially stress free state, the application of the first burn cycle will induce a stress distribution which is essentially linear through the wall--as long as no plasticity occurs (i.e., linear elastic material). During the 'on' part of the burn cycle, temperatures, and therefore thermal

strains, are held constant and, if no creep occurs, stresses will remain constant. For the burn 'off' cycle, the temperature gradients are removed and only the pressure stress remains. This cycle Is termed the elastic stress state cycle.

If, on the other hand, creep occurs during the burn 'on' part of the cycle, stress relaxation will occur. The bounding case for this will be If all thermally induced (secondary) stresses relax to zero. In this case, after a period of time the stresses In the "burn on" part of the cycle will simply change to those caused by the pressure (primary). This Is called the relaxed state of stress. Then, during the "burn off" part of the cycle when the temperature distributions are removed, a thermal stress distribution equal and opposite to that initially induced will be superimposed on the pressure stress. This is called the reversed state of stress. Subsequently during "burn on" and "burn off" periods, the stress distributions will cycle between the relaxed state and reversed state respectively. This cycle is termed the relaxed state stress cycle.

The elastic state stress cycle and the relaxed state stress cycle were used for the crack propagation analyses. In service operation., these states will be modified bv time independent plastic deformation and by the fact that 100% creep relaxation may not occur. However, the assumptions are adequate for the preliminary bounding analyses performed here.

It must be noted that this smooth wall design meets all the design allowable criteria except that the BOL model has a peak temperature of 649°C which exceeds the structural material temperature limit[1] of 550% by 100°C. More recent designs for the BCSS utilize a "grooved" concept for the first wall In which the material at temperatures above 550°C do not experience thermal stress. The material is grooved to a depth corresponding to the amount of wall that may be eroded during the module life. This technique is used as necessary for all candidate materials. For simplicity, the groove was not included in this analysis.

Fracture Analysis

The ccmputer code "WISECRACK"[2] was used to perform the fracture analysis of the thin wal I section using the stress distributions summarized above. The code utilizes a modified Forman equation, originally proposed by Speidel[5],

$$\frac{da}{dN} = \frac{B\lambda^m[\Delta K - K_o]^n}{K_{Ic} - \lambda f \Delta K}$$

where $\lambda = 1/(1-R)$
$R = K_{min}/K_{MAX}$
$f = E(T_o)/E,T \quad (\geq 1)$
$\Delta K = K_{max} - K_{min}$
K_o = threshhold stress Intensity
K_{Ic} = plane-strain fracture toughness
and where $B = 1.3 \times 10^{-5}$
$m = 1.0$
$n = 1.65$

are constants calculated fran test data for HT-9 at 25°C and 600°C[6]. The resulting da/dN mode Is p r e sented in Fig. 1.2.6.

The values of 100 and 9MPa $\sqrt{m}$ respectively were used for the fracture toughness, K_{Ic}, and the threshold stress Intensity factor, K_o. A K_{Ic} of 100 MPa $\sqrt{m}$ Is valid for unirradiated material only. It is estimated that irradiation will cause the fracture toughness to decrease to a "lower shelf" value of approximetely 60 MPa $\sqrt{m}$[7]. The time required for the toughness to decrease depends on the neutron fluence and damage but is probably short (<1yr)[7]. Because the fluence is not well characterized it conservatively was assumed that K_{Ic} remained constant at a value of 60 MPa $\sqrt{m}$ fran the beginning of life. Later, a changing K_{Ic} will be Incorporated Into the model. The effect of a lower K_{Ic} value can be Incorporated Into the fatigue-crack growth equation either by shifting the whole curve to the left or simply defining a cutoff point for the unirradiated curve as shown schematically In Figure 1.2.7. The conservative assumption of shifting the whole curve was assumed In this analysis.

The fracture analysis utilized both the elastic stress distribution and the relaxed distribution. It was assumed that these two extreme cases would bound the problem, and sane interpolation to a more realistic state might be performed using the results of these two conditions. Initial flaw depths of 0.5, 0.25. 0.10. and 0.05 of the total thickness were assumed. The flaw's aspect ratio (crack depth ÷ 1/2 surface crack length) was taken to be between 1.0 (semi-circular) and 0.2 since these represent extremes. The canputer code WISECRACK calculates the varying K-value ahead of the crack front as the crack growth rate.

1.2.4.3 Results

The fracture analyses for both the BOL and EOL showed very little crack growth for a circumferential crack. The stress distribution In the Z-direction (Fig. 1.2.5) was not severe enough In either the elastic or relaxed state to cause significant K-values for flaws on either the plasma or coolant side. This is due to the way In which the end plates are connected to the first wall - both pressure loads and overall axial thermal constraint loads are minimized.

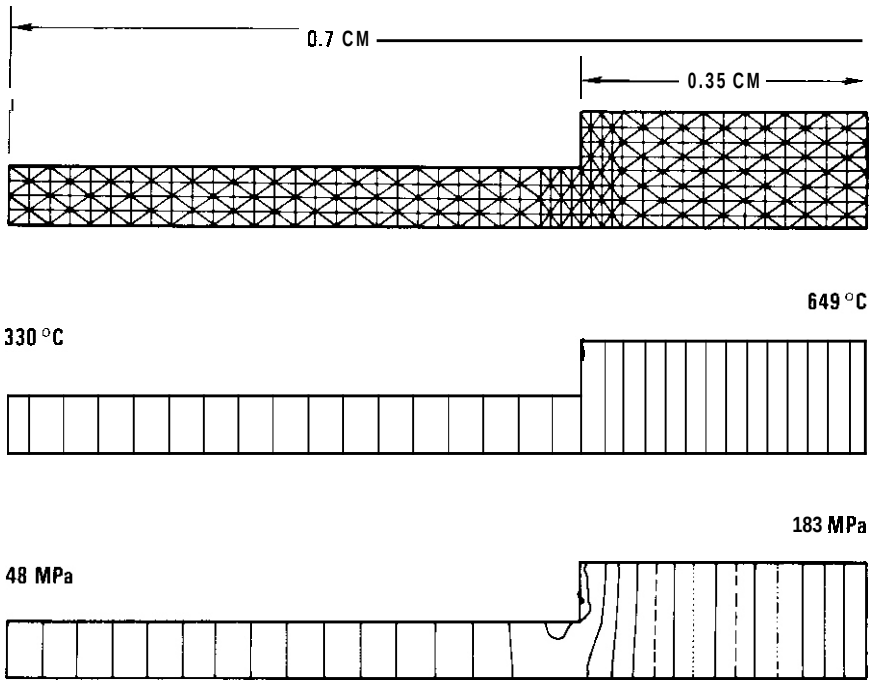

Fig. 1.2.3. The finite element model (a) used for Beginning-of-life calculations including the (b) temperature distribution and (c) resulting theta direction stresses due to cyclic thermal loading and primary coolant pressure stress.

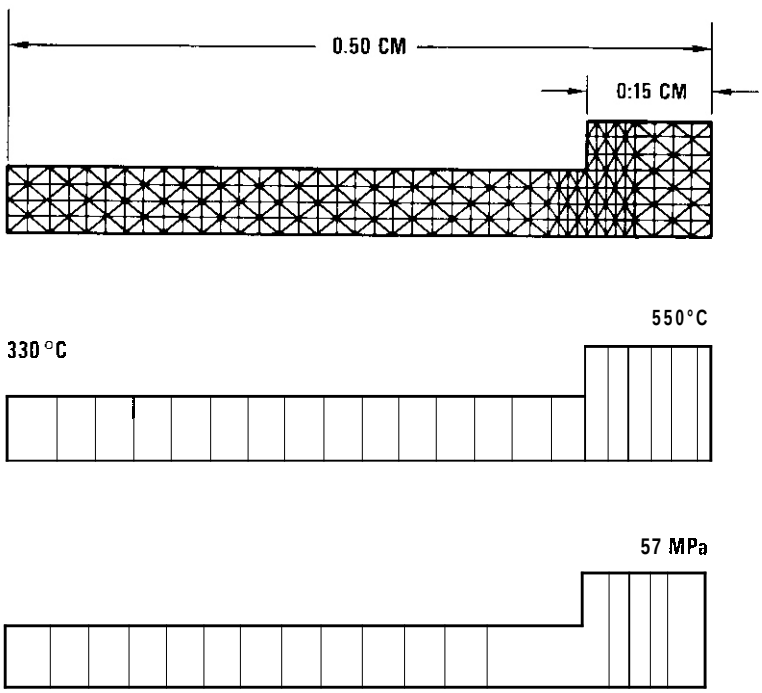

Fig. 1.2.4. The finite element model (a) used for End-of-life (EOL) calculations including the (b) temperature dlstrlbution, and (c) EOL elastic theta stresses.

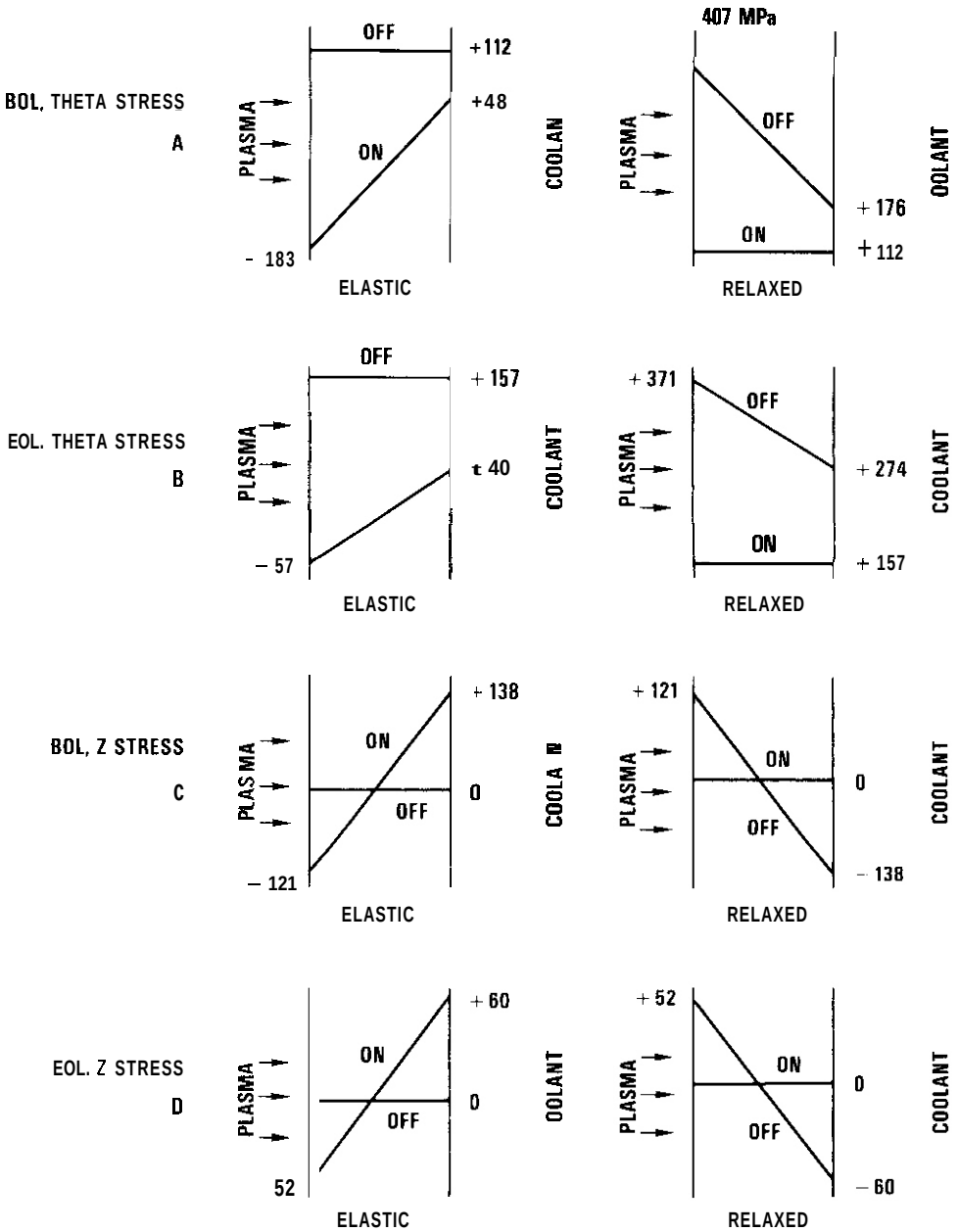

Fig. 1.2.5. The stress distributions for the Beginning and End-of-life for theta and Z-direction stresses In HT-9 first wall material for the elastic and relaxed stress conditions.

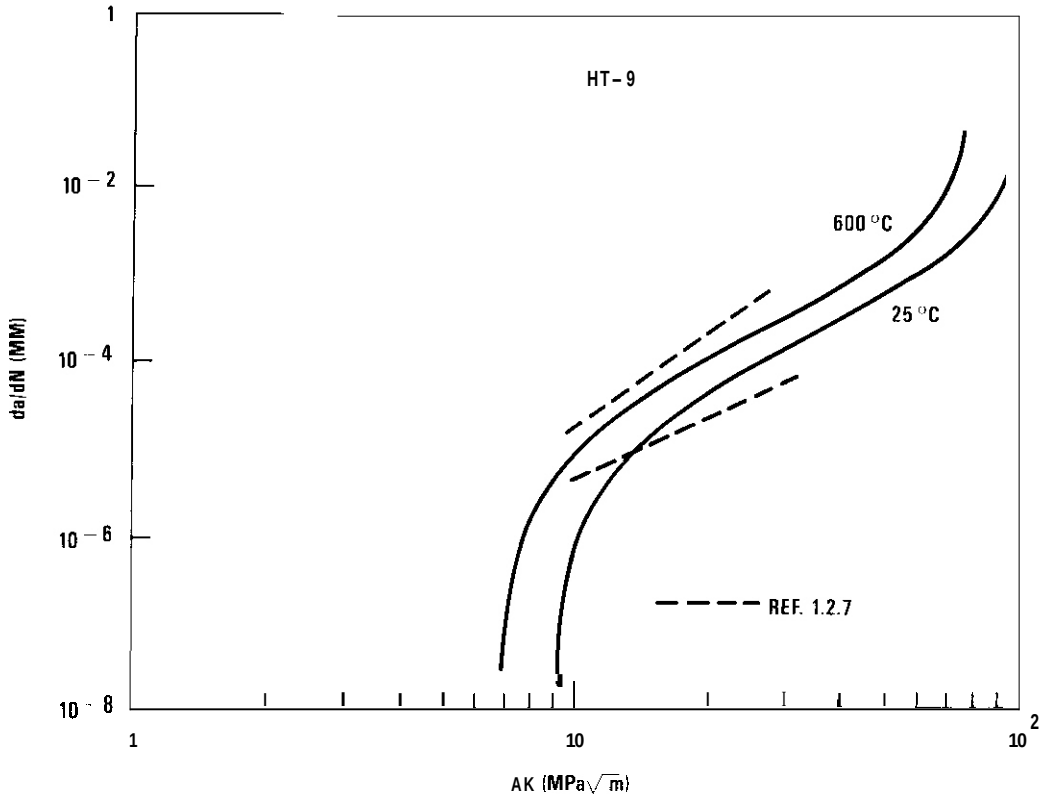

Flg. 1.2.6. The fatlgue crack growth curve for HT-9 plotted from a modlfled Forman equation using data at 25°C and 600°C (dashed llnes) to calculate constants.

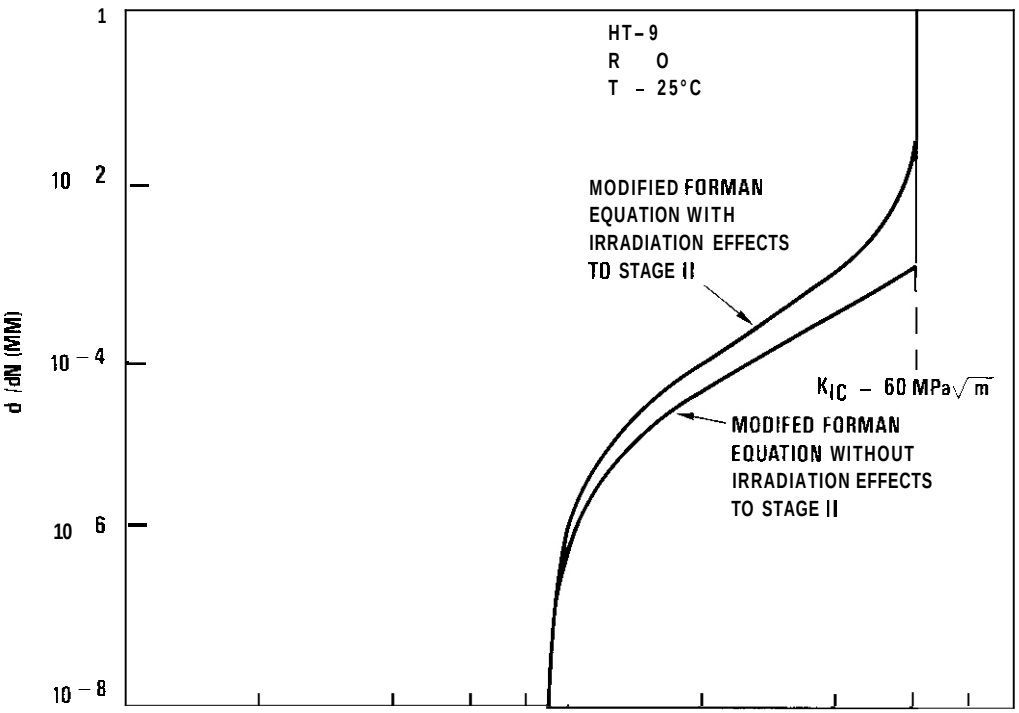

In the theta-stress direction, however, the analysis predicts that axial cracks can grow through the wall from either the plasma side or the coolant side depending on aspect ratio and initial flaw depth. The results of the lifetime calculations are given in Table 1.2.2 for the beginning of life and end of life conditions, for flaw depths ranging between .5 and .1 times the thickness of the wall, and for aspect ratios (a/c) between .2 and 1.0. Results are given for both the elastic stress and the relaxed stress cycles.

Table 1.2.2. Lifetimes calculated for various aspect ratios for plasma and coolant sides of ferritic steel first wall for Beginning-of-Life (BOL) and End-of-Life (EOL)

	a/t	a/c	Lifetime (yrs) Elastic Stress		Relaxed Stress	
			Plasma	Coolant	Plasma	Coolant
BOL	0.50	0.2	7.2	10.4	0.35	1.37
		0.4	18.7	30.0	1.3	3.4
		0.6	30.0	30.4	2.1	6.8
		0.8	30.0	30.4	2.8	12.5
		1.0	30.2	---	3.4	22.3
	0.25	0.2	30.1	---	2.1	22.4
		0.4	30.2	---	4.2	30.4
		0.6	30.3	---	5.7	---
		0.8	30.4	---	6.9	---
		1.0	---	---	8.0	---
	0.10	0.2	30.1	---	7.07	27.0
		0.4	30.4	---	11.1	30.4
		0.6	30.4	---	14.4	---
		0.8	---	---	17.4	---
		1.0	---	---	20.4	---
EOL	0.50	0.2	6.1	7.9	1.0	1.5
		0.4	28.1	30.4	2.9	4.3
		0.6	30.4	---	5.2	9.1
		0.8	---	---	7.4	16.9
		1.0	---	---	9.6	29.0
	0.25	0.2	30.4	---	5.4	14.8
		0.4	---	---	12.2	30.2
		0.6	---	---	19.6	---
		0.8	---	---	28.1	---
		1.0	---	---	30.0	---

a = length of crack
c = depth of crack
t = wall thickness

1.2.4.4 Conclusions

Specific conclusions from the results are:

(1) If significant creep occurs crack propagation rates will be higher than if no creep occurs.

(2) A crack initiating on the plasma side will propagate through the wall at a higher rate than a crack initiating on the coolant side.

(3) Crack growth rates are higher if a thicker wall (BOL) is used.

(4) If the initial flaw size is less than 1/4 the wall thickness, the wall erosion will remove the crack during the design life.

(5) At no time during the service cycling did the flaw size exceed the critical flaw size which would cause a brittle fracture.

These conclusions may give some important guidance to manufacturing and quality assurance requirements which must be incorporated into a fracture management scheme.

Future work will include an analysis of the capabilities of current NDE techniques with the calculated quality assurance needs.

1.2.4.5 Future Work

Calculations will continue to determine what the lower bound fracture toughness (K_{Ic}) must be to prevent brittle failure in this design configuration. Data will be generated and incorporated into the fracture analysis to reduce the uncertainty of the da/dn, crack growth rates, and fracture toughness all of which have important influence on the lifetime.

1.2.4.6 References

1. M. Abdou, et al, "Blanket Comparison Selection Study", Argonne National Laboratory report ANL/FPP-83-1, Oct. 1983.
2. R. D. Watson and W. G. Wolfer, "WISECRACK - A Fracture Mechanics Code for Lifetime Analysis of High Heat Components In Fusion Reactors", University of Wisconsin Report UWFDM-440 (1981).
3. C. Charman and F. Tzung, "TEPC-2D - A Two-Dimensional Finite Element Computer Program for Thermal-Elastic-Plastic-Creep Analysis", GA Technologies, GA-A12753 (1973).
4. Private Discussions with R. H. Ryder, GA Technologies, June 1984.
5. M. O. Speidel, "Fatigue Crack Growth at High Temperatures", Proceedings of the Symposium on High-Temperature Materials In Gas Turbines, ed. P.R. Sahm and M. O. Speidel. Baden, Switzerland (1973).
6. F. H. Huang, D. A. Mervyn and D. T. Peterson, "Microstructural and Fatigue Crack Growth Characterization of HT-9", Hanford Engineering Development Laboratory, ADIP Semiannual Progress Report DOE-ER0045 17, Dec. 1981.
7. Lechtenberg, T. A., GA Technologies, private communications.

2. TEST MATRICES, EXPERIMENT DESCRIPTIONS, AND METHODS DEVELOPMENT

2.1 NEUTRON SOURCE CHARACTERIZATION FOR MATERIALS EXPERIMENTS -

L. R. Greenwood and R. K. Smither (Argonne National Laboratory)

2.1.1 ADIP/DAFS Tasks

ADIP - Task I.A.2 - Define Test Matrices and Procedures
DAFS - Task II.A.1 - Fission Reactor Dosimetry

2.1.2 Objective

To characterize neutron irradiation facilities in terms of neutron flux, spectra, and damage parameters (DPA, gas production, transmutation) and to measure these exposure parameters during fusion materials irradiations.

2.1.3 Summary

Dosimetry measurements were conducted in the ORR during February 1984 to test the performance of a hafnium core piece for the MFE4 spectral-tailoring experiment. Flux gradients were measured in position C3, both with and without the hafnium liner. The results agree rather well with expectations. Results are also reported for the MFE4B experiment after 424 full power days. The maximum fluence was 1.9 x 10^{22} n/cm^2 producing about 64 appm helium and 5.1 dpa in 316 stainless steel.

2.1.4 Progress and Status

The status of all other experiments is sumnarized in Table 2.1.1.

Table 2.1.1. Status of Dosimetry Experiments

	Facility/Experiment	Status/Comments
ORR	- MFE 1	Completed 12/79
	- MFE 2	Completed 06/81
	- MFE 4A1	Completed 12/81
	- MFE 4A2	Completed 11/82
	- MFE 48	Comoleted 04/84
	- MFE 4C	Irradiation in Progress
	- TBC 07	Completed 07/80
	- TRIO-lest	Completed 07/82
	- TRIO-1	Completed 12/83
	- Hf Test	Completed 03/84
HFIR	- CTR 32	Completed 04/82
	- CTR 31, 34, 35	Completed 04/83
	- CTR 30	Irradiation in Progress
	- T2, RE1	Completed 09/83
	- TI, CTR 39	Completed 01/84
	- RB2, RB3, T3	Irradiations in Progress
	- CTR 40-52	Irradiations in Progress
	- JP 1-8	Irradiations in Progress
Omega West	- Spectral Analysis	Completed 10/80
	- HEDL1	Completed 05/81
	- HEDL2	Samples Sent 05/83
EBR II	- X287	Completed 09/81
IPNS	- Spectral Analysis	Completed 01/82
	- LANL1 (Hurley)	Completed 06/82
	- Hurley	Completed 02/83
	- Coltman	Samples Received 08/83

2.1.4.1 Hafnium Core Piece Test in ORR

Dosimetry measurements have been completed for a test of the hafnium core piece designed for the WE4 spectral-tailoring experiment in the Oak Ridge Research Reactor (ORR). The purpose of the Hf liner is to reduce the thermal flux, thereby reducing helium production from the two-step thermal capture on ^{58}Ni. A recent description of the experiment has been published by R. A. Lillie (Neutronics Calculations in Support of the ORR-MFE-4A and 4B Spectral-Tailoring Experiments. Alloy Oevelopment for Irradiation Performance, Semiannual Progress Report, pp. 38-39, DOE/ER/-0045/11, September 19831. The present tests were conducted in core position C3 of the ORR on February 25-26, 1984, both with and without the Hf liner. Roth irradiations lasted four hours at a reduced power level of 330 kW.

Dosimetry tubes were placed at four locations inside the core piece, labeled North, South, East, and West. Each aluminum dosimetry tube measured 18" in length and contained Fe. Ni, Ti, and Co-A1 dosimetry wires. Following the irradiations, the tubes were shipped to Argonne for analysis. Each wire was cut into 17 pieces, 16 one-inch pieces, and one 1/2" piece. The wires were then weighed and mounted for Ge(Li) gama spectroscopy. The Co and Ni wires were completely analyzed on the North side. In all other cases only every third section of each wire was analyzed.

The measured radioactivities are listed in Tables 2.1.2-2.1.6 and plotted in Figures 2.1.1-2.1.2. The values have an estimated accuracy of ±1.5% in all cases. As can be seen, the bare wires indicate that the flux peak occurs at about 5" below midplane. The uncovered thermal flux also rises at about 4" above midplane corresponding to the top of the inner aluminum core piece which also clearly attenuates the thermal flux by about 40-50%.

The hafnium covered wires clearly show a large reduction in the thermal flux. Near the bottom the flux falls as we go up the core piece, then flattens out, and finally rises near the top. The seemingly strange behavior on the ends is clearly due to "end effects", since our dosimetry wires are longer than the hafnium shield. The Hf piece measured 12-1/4" in lenqth and the position relative to our wires is indicated on Figures 2.1.1 and 2.1.2.

The radial gradients between the four different tubes at a given height are certainly rather small, <10% in all cases. The North and East positions are typically 5-10% higher than the South and West positions, presumably due to the fact that the center of the ORR core lies Northeast of the C3 position.

The shielding effect of the hafnium liner is about 50% for the ^{58}Fe and $^{59}Co(n,\gamma)$ reactions. The fast reactions also show an effect of about 10%, probably due to the unusually large scattering cross Section of Hf of about 7b in the 1-3 MeV energy range.

Table 2.1.2. $^{59}Co(n,\gamma)^{60}Co$ Activities Measured in ORR-Hf Test
(Average power = 330 kW: core position C3)
Activation Rate, x 10^{-11} atom/atom-s

	Rare				Hf Shield			
Average Height, in.	N	E	S	W	N	E	S	W
-9.84	7.22	6.71	6.71	6.85	4.53	4.55	4.36	4.46
-8.84	7.48				3.91			
-7.84	7.87				3.90			
-6.84	8.23	7.99	7.73	7.69	3.94	3.82	3.67	3.60
-5.84	8.28				3.87			
-4.84	8.33				3.91			
-3.84	8.34	7.95	7.74	7.93	3.83	3.83	3.62	3.60
-2.84	7.90				3.69			
-1.84	7.51				3.50			
-0.R4	6.78	6.56	6.66	6.54	3.33	3.28	3.23	3.13
0.16	6.06				3.09			
1.16	5.58				2.99			
2.16	5.26	5.18	5.14	5.07	3.41	3.47	3.65	3.44
3.16	4.84				4.11			
4.16	5.34	5.79	5.81	5.62	5.25	5.13	5.71	5.51
5.16	7.12				6.73			
5.41							6.93	6.83
5.91	7.09	7.31	7.35	6.93	6.87	7.16		

Table 2.1.3. $^{58}Ni(n,p)^{58}Co$ Activities Measured in ORR-Hf Test
Activation Rate, x 10^{-13} atom/atom-s

	Bare				Hf Shield			
Average Height, in.	N	E	S	W	N	E	S	W
-9.84	1.78	1.72	1.64	1.65	1.59	1.55	1.45	1.50
-8.84	1.90				1.71			
-7.84	1.97				1.78			
-6.84	2.04	2.02	1.94	1.99	1.83	1.85	1.70	1.73
-5.84	2.03				1.83			
-4.84	2.01				1.82			
-3.84	1.92	1.98	1.93	1.91	1.80	1.79	1.71	1.72
-2.84	1.81				1.69			
-1.84	1.70				1.65			
-0.84	1.55	1.73	1.68	1.62	1.48	1.53	1.52	1.51
0.16	1.47				1.40			
1.16	1.34				1.28			
2.16	1.25	1.37	1.38	1.31	1.22	1.27	1.25	1.23
3.16	1.17				1.12			
4.16	1.04	1.12	1.17	1.06	1.01	1.10	1.09	1.08
5.16	0.945				0.927			
5.41				0.955			0.777	0.930
5.91	0.883	0.934	0.982		0.871	0.959		

Table 2.1.4. $^{54}Fe(n,p)^{54}Mn$ Activities Measured in ORR-Hf Test
Activation Rate, x 10^{-13} atom/atom-s

	Bare				Hf Shield			
Average Height, in.	N	E	S	W	N	E	S	W
-9.84	1.23	1.25	1.18	1.22	1.22	1.12	1.05	1.10
-6.84	1.48	1.47	1.41	1.42	1.39	1.30	1.23	1.30
-3.84	1.43	1.45	1.45	1.40	1.33	1.28	1.22	1.25
-0.84	1.18	1.26	1.24	1.20	1.09	1.15	1.08	1.06
2.16	0.936	0.996	0.985	0.954	0.893	0.928	0.909	0.852
4.16	0.809	0.834	0.862	0.813	0.740	0.814	0.816	0.762
5.41			0.759	0.702			0.751	0.709
5.91	0.650	0.680			0.645	0.693		

Table 2.1.5. $^{58}Fe(n,\gamma)^{59}Fe$ Activities Measured in ORR-Hf Test
Activation Rate, x 10^{-12} atom/atom-s

	Bare				Hf Shield			
Average Height, in.	N	E	S	W	N	E	S	W
-9.84	2.20	2.12	2.07	2.06	1.32	1.29	1.27	1.31
-6.84	2.47	2.38	2.31	2.36	1.04	1.01	0.957	0.947
-3.84	2.46	2.45	2.31	2.36	1.03	1.01	0.956	1.00
-0.84	2.02	2.03	1.96	1.95	0.862	0.901	0.842	0.834
2.16	1.49	1.58	1.54	1.50	0.976	1.01	1.05	1.04
4.16	1.73	1.63	2.02	1.74	1.70	1.59	1.85	1.79
5.41			2.42	2.11			2.13	2.21
5.91	2.28	2.39			2.09	2.19		

Table 2.1.6. $^{46}Ti(n,p)^{46}Sc$ Activities Measured in ORR-Hf Test
Activation Rate, x 10^{-14} atom/atom-s

	Bare				Hf Shield			
Average Height, in.	N	E	S	W	N	E	S	W
-9.84	*1.60*	1.62	1.62	1.57	1.53	1.50	1.42	1.47
-6.84	1.96	1.92	1.83	1.89	1.75	1.71	1.63	1.64
-3.84	1.87	1.93	1.88	1.82	1.73	1.69	1.64	1.64
-0.84	1.56	1.59	1.63	1.58	1.46	1.50	1.42	1.42
2.16	*1.28*	1.43	1.34	1.25	1.16	1.23	1.21	1.16
4.16	1.06	1.11	1.15	1.07	1.00	1.14	1.08	1.02
5.41			1.01	0.964			0.969	0.926
5.91	0.920	0.961			0.885	0.956		

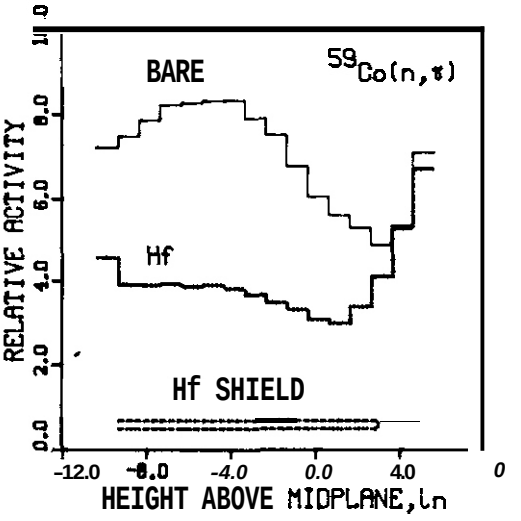

Fig. 2.1.1. Measured $^{59}Co(n,\gamma)^{60}Co$ activities for the Hf test in ORR. The position of the Hf shield is indicated.

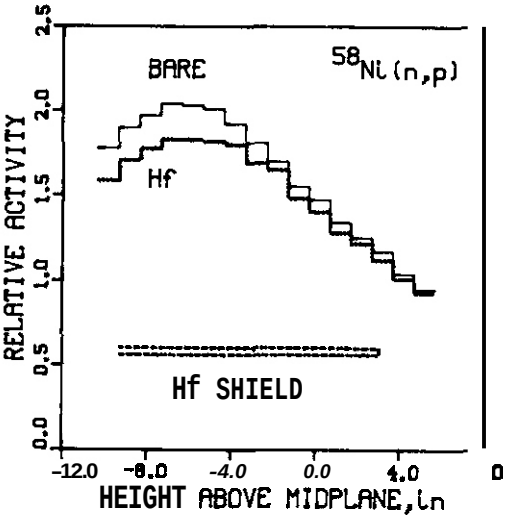

Fig. 2.1.2. Measured $^{58}Ni(n,p)^{58}Co$ activities for the Hf test in ORR. The position of the Hf shield is indicated.

The maximum bare and shielded activities were used to adjust the neutron flux spectrum used previously in the ORR-MFE4 experiments.[1] Table 2.1.7 lists our adjusted fluxes for each case. A simple analytical approximation[2] was used to calculate the Hf shielding due to the 40 mil thick liner. This treatment should be a good approximation in the present case due to the small thickness of the liner. However, scattering effects are not treated properly. The shielded spectrum is compared to the bare spectrum in Figure 2.1.3. As can be seen, the epithermal shielding is greater than the thermal since the resonance integral is 1900b compared to a thermal cross section of 104b.

Table 2.1.7. Adjusted Flux Values-ORR-Hf Test
Average Power 330 kW; Core C3

Energy Range	Neutron Flux, x 10^{12} n/cm^2-s		Ratio
	Bare	Hf Shield	Shield/Bare
Total	7.22	4.75	0.66
Thermal*	2.36	1.41	0.60
0.5eV-0.11MeV	2.40	1.05	0.44
>0.11MeV	2.46	2.29	0.93

*Total flux <0.5eV assuming an average temperature of 95°C.

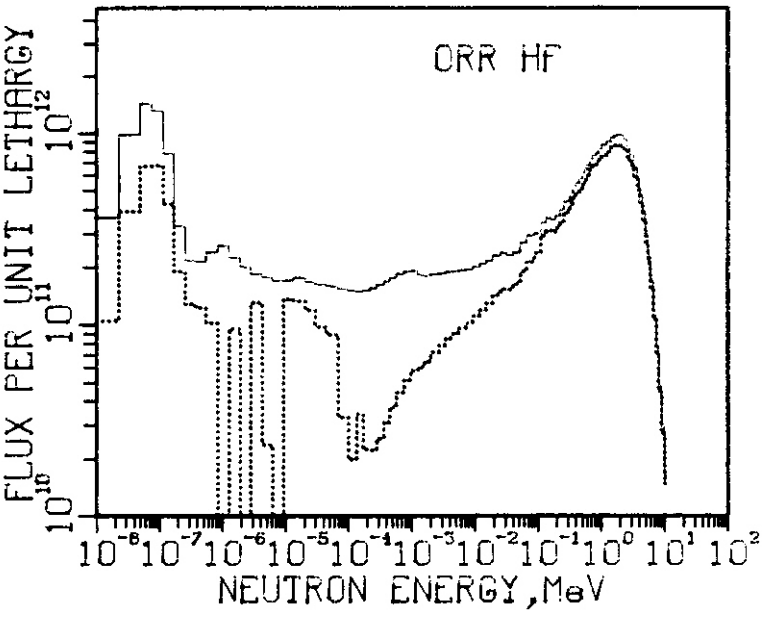

Fig. 2.1.3. Comparison of the unshielded and Hf shielded neutron spectra derived by spectral adjustment with the STAYSL computer code.

The net effect of the Hf liner is to reduce the thermal flux by 40%. the eipthermal flux by 56%, and the fast flux by about 7%. These results will be compared to a more exact neutronics calculation by R. A. Lillie (ORNL).

2.1.4.2 Dosimetry Measurements and Damage Calculations for the ORR-MFE4B Experiment

The MFE4B experiment in the Oak Ridge Research Reactor (ORR) is a spectral-tailoring irradiation designed to achieve fusion-like helium-to-dpa ratios in stainless steel.[3] The experiment is nearly identical to the MFE4A irradiation reported earlier.[1] The irradiation took place in core position E7 from April 22, 1981 to October 20, 1982 for a total exposure of 424 full power days. The present analysis is based on four dosimetry tubes removed from the assembly when it was repackaged. New replacement dosimetry tubes were inserted at that time and the experiment is now undergoing further exposure in ORR. The present interim measurements are thus designed to check on the progress of the experiment, especially regarding the critical helium-to-dpa ratio and the subsequent insertion of the hafnium core piece to reduce the helium accumulation. 3

The four stainless steel dosimetry tubes measured 1/16" O.D. x 2-3/4" long and contained small specimens of Fe, Ni, Co, Ti, Nb, Cu, 80% Mn-Cu, and helium accumulation monitors supplied by Rockwell International. All of the samples were gama counted by Ge(Li) spectroscopy and the measured activation rates are listed in Table 2.1.8. One dosimetry tube apparently burst during the irradiation and some of the dosimeters could not be removed from the tube for gama analysis. Two of the tubes were located on the upper level and two on the lower level of the MFE4B assembly. In each case, one tube was outside and one inside of a stainless steel annulus surrounding the NaK and experimental samples. The top tubes were at 600°C while the lower tubes were in the 500°C temperature region.

Table 2.1.8. Activation Rates Measured for ORR-MFE4B Dosimeters removed 10/82 at 424 FPO; normalized to 30 MW Burnup corrections included: accuracy ±2% unless noted

Reaction	Height, in.	Activity (atom/atom-s) Inside		Outside	
$^{58}Fe(n,\gamma)^{59}Fe$	-0.84	1.60	E-10	1.69	E-10
(±4%)	-2.41	1.68	E-10	1.78	E-10
	-3.91			1.70	E-10
	-4.03	1.73	E-10		
	-5.72	1.49	E-10	1.54	E-10
$^{59}Co(n,\gamma)^{60}Co$	-1.02			5.52	E-9
	-4.08			5.46	E-9
	-4.20	5.10	E-9		
$^{93}Nb(n,\gamma)^{94}Nb$	-1.56	2.72	E-10	2.89	E-10
	-4.88	2.72	E-10	2.77	E-10
$^{54}Fe(n,p)^{54}Mn$	-0.84	9.80	E-12	9.89	E-12
	-2.41	10.48	E-12	10.22	E-12
	-3.91			10.47	E-12
	-4.03	10.76	E-12		
	-5.72	10.22	E-12	10.03	E-12
$^{46}Ti(n,p)^{46}Sc$	-1.31			1.40	E-12
	-4.37	1.37	E-12	1.45	E-12
	-4.62	1.42	E-12	1.43	E-12
$^{55}Mn(n,2n)^{54}Mn$	-1.81	3.71	E-14	3.96	E-14
	-5.12	3.71	E-14	3.33	E-14
$^{63}Cu(n,\alpha)^{60}Co$	-2.06			6.94	E-14
	-5.37	7.19	E-14	6.83	E-14
$^{58}Ni(n,p)^{58}Co$*	-2.25	3.96	E-12	4.29	E-12
	-4.17			4.46	E-12
	-5.56	4.76	E-12	5.00	E-12
$^{60}Ni(n,p)^{60}Co$*	-2.25	1.29	E-12	1.58	E-12
	-4.37			1.57	E-12
	-5.56	1.26	E-12	1.30	E-12

*Burnup corrections not included but estimated to be 50% of more for both nickel reactions.

The activities listed in Table 2.1.8 can all be fit to a simple polynomial of form:

$$f(h) = fmax\ [1 + c\ (x-x_0)^2] \qquad (1)$$

where fmax = highest value and x_0 = center of flux gradient. The thermal and fast reactions were fit separately and the resultant parameters are listed in Table 2.1.9. As can be seen, the vertical gradient is only about 15% over the sample region while the inner-to-outer gradient is quite small, with a thermal difference of about 5% and no apparent fast gradient.

The maximum activity values were used as input to the STAYSL computer code to adjust the neutron spectrum calculated by R. A. Lillie.3 The adjusted flux and fluence values are listed in Table 2.1.10 and the spectrum is shown in Fig. 2.1.4. These values are quite similar to those reported previously for the MFE4A experiment after a similar exposure.[1] The thermal flux was calculated assuming a temperature distribution centered at 95°C, the temperature of the surrounding moderator. The derived 2200 m/s flux is also listed for comparison.

Table 2.1.9. Maximum Activities for ORR-MFE4B
(Values Determined from Polynomial Fit)

Reaction	Activation Rate (atom/atom-s) Inside		Outside		Ratio $(\frac{out}{in})$
$^{58}Fe(n,\gamma)^{59}Fe$	1.72	E-10	1.77	E-10	1.03
$^{59}Co(n,\gamma)^{60}Co$	5.75	E-9	5.70	E-9	1.08
$^{93}Nb(n,\gamma)^{94}Nb$	2.85	E-10	2.96	E-10	1.04
$^{54}Fe(n,p)^{54}Mn$	1.07	E-11	1.06	E-11	0.99
$^{46}Ti(n,p)^{46}Sc$	1.42	E-12	1.43	E-12	1.01
$^{55}Mn(n,2n)^{54}Mn$	3.85	E-14	3.85	E-14	1.00
$^{63}Cu(n,\alpha)^{60}Co$	7.20	E-14	7.20	E-14	1.00

Gradient Polynomial Function

$F(x) = Fmax\,[1 + c\,(x-x_0)^2]$
where Fmax = maximum value
x_0 = center of activity (inches)

	c		x_0
Fast	-1.269	E-7	-3.35"
Thermal	-1.521	E-2	-2.81"
Global	-1.395	E-2	-3.06

Table 2.1.10. Maximum Flux and Fluence Values for ORR-MFE4B
(Values at 30 MW after 424 FPD at -3" below midplane)

Energy	Error, %	Flux, x 10^{14} n/cm^2-s Inside	Outside	Fluence, x 10^{21} n/cm^2 Inside	Outside
Total	6	5.19	5.36	19.0	19.6
Thermal (<.5 eV) (2200 m/s)	6	1.70	1.83	6.24	6.72
Fast, >.11 MeV	10	1.76	1.70	6.43	6.43
0.5 eV - 0.11 MeV	12	1.73	1.77	6.33	6.48

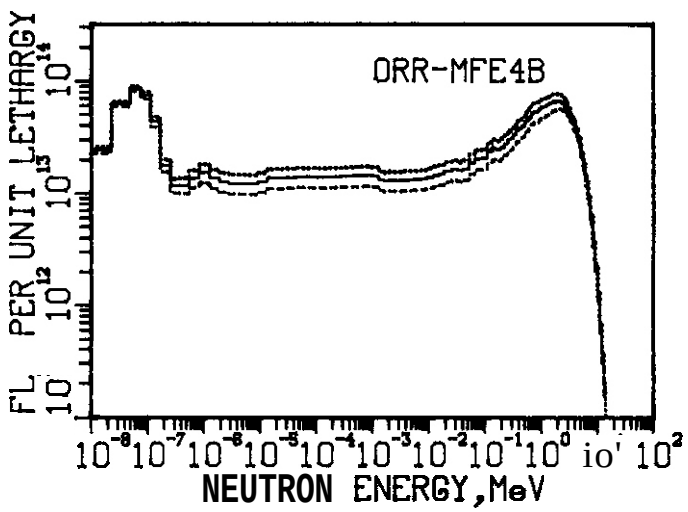

Fig. 2.1.4. Adjusted flux spectrum for the ORR-MFE4B experiment normalized to 30 MW after 474 full power days. The dotted and dashed lines indicate one standard deviation: however, the flux groups are highly correlated.

Displacement damage and helium calculations were performed using the SPECTER computer code. Values are listed for a number of elements at the maximum flux position in Table 2.1.11. The He and dpa values at other heights in the assembly can be determined using Eq. (1) and the maximum values in Table 2.1.11.

Table 2.1.11. Damage Parameters for ORR-MFE4B (424 FPD)

Element		He (appm)		DPA	
		Inside	Outside	Inside	Outside
Al		3.91	3.92	8.65	8.65
Ti		2.96	2.96	5.51	5.51
V		0.14	0.14	6.12	6.12
Cr		0.97	0.97	5.48	5.48
Mn[a]		0.81	0.81	5.86	5.87
Fe		1.68	1.68	4.57	4.87
Co[a]		0.81	0.81	5.61	5.66
	Thermal	457.0	517.8	0.81	0.91
Nib	Fast	23.9	23.8	5.13	5.14
	Total	480.9	541.6	5.94	6.05
cu		1.45	1.46	4.70	4.70
Zr		0.15	0.15	5.08	5.08
Nb		0.31	0.31	4.68	4.68
Mo		--	--	3.44	3.44
Ta		--	--	2.36	2.36
316 ss[c]		63.8	71.7	5.10	5.12

[a]Self-shielding corrections may be needed for the (n,γ) damage in Mn (5%) and Co (17%).

[b]See references 3 and 4 for nickel calculations.

[c]316 ss: Cr (.18), Mn (.019), Fe (.645), Ni (.13), Mo (0.026)

Helium and damage rates for nickel and 316 ss were computed separately and are listed in Table 2.1.12 and shown in Fig. 2.1.5. The procedure used in these calculations was described in detail in a recent publication.4 The extra dpa from the ^{56}Fe recoils is also included using the formula of one displacement for every 567 appm helium.[5] As shown in reference 4, we expect the helium calculations to be quite accurate (±5-10%). Of course, samples from this experiment will also be analyzed by Rockwell International and measurements will then become available for a number of elements. These data will be used to refine our helium production cross sections and to improve our dosimetry technique.

Table 2.1.12. Helium and DPA Gradients for ORR-MFE4B (424 FPD)
(Values are listed for the inner position)

Height, in.	Fluence ($\times 10^{22}$ n/cm^2)	Helium, appm		DPA	
		Ni	316 ss	Ni	316 ss
0	1.67	381.	50.7	5.18	4.48
-1	1.81	441.	58.5	5.61	4.85
-2	1.88	472.	62.6	5.87	5.04
-3	1.90	481.	63.8	5.94	5.10
-4	1.86	463.	61.4	5.80	4.99
-5	1.76	419.	55.7	5.46	4.72
-6	1.61	357.	47.5	4.93	4.30

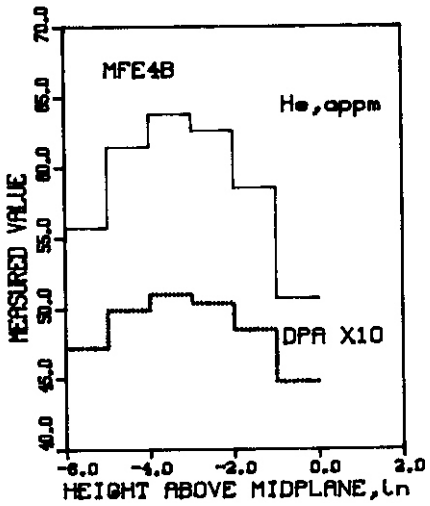

Fig. 2.1.5. Helium (appm) and dpa (x 10) values are shown for 316 stainless steel as a function of the height above midplane.

2.1.5 Conclusions

We will continue to monitor the progress of the MFE4 spectral-tailoring experiment in ORR. Samples were also prepared for further experiments in HFIR.

2.1.6 References

1. L. R. Greenwood, Dosimetry and Damage Analysis for the MFE4A Spectral Tailoring Experiment in ORR, Damage Analysis and Fundamental Studies Quarterly Progress Report, DOE/ER-0046/12, pp. 14-23, 1983.

2. Neutron Fluence Measurements, IAEA Technical Reports Series 107, IAEA, Vienna, 1970

3. R. A. Lillie, Neutronics Calculations in Support of the ORR-MFE4A and 48 Spectral-Tailoring Experiments, Alloy Development for Irradiation Performance, Semiannual Progress Report, pp. 38-39, DOE/ER/0045/11, September 1983.

4. L. R. Greenwood, D. W. Kneff, R. P. Skowronski, and F. M. Mann, A Comparison of Measured and Calculated Helium Production in Nickel Using Newly Evaluated Neutron Cross Sections for ^{59}Ni, to be published in the Journal of Nucl. Mater., 1984.

5. L. R. Greenwood, A New Calculation of Thermal Neutron Damage and Helium Production in Nickel, Journal of Nucl. Mater. 115, 137-142 (1983).

2.1.7 Publications

Two papers have been submitted for publication in the Proceedings of the 12th International Symposium on the Effects of Radiation on Materials, Williamsburg, VA, 18-20 June 1984.

1. Measured Radiation Environment at the LAMPF Irradiation Facility, D. R. Davidson, R. C. Reedy, W. F. Sommer, and L. R. Greenwood.

2. The Calculation of Radiation Damage Parameters for the LAMPF Irradiation Facility, D. R. Davidson, W. F. Sommer, M. S. Wechsler, and L. R. Greenwood.

2.2 NEUTRONICS CALCULATIONS IN SUPPORT OF THE ORR-MFE-4A AND -4B SPECTRAL TAILORING EXPERIMENTS

R. A. Lillie (Oak Ridge National Laboratory)

2.2.1 ADIP Task

ADIP Task 1.A.2, Define Test Matrices and Test Procedures.

2.2.2 Objective

The objective of this work is to provide the neutronic design for materials irradiation experiments in the Oak Ridge Research Reactor (ORR). Spectral tailoring to control the fast and thermal fluxes is required to provide the desired displacement and helium production rates in alloys containing nickel.

2.2.3 Summary

The calculated fluences from the ongoing three-dimensional neutronics calculations are being scaled to agree with experimental data. As of March 27, 1984, this treatment yields 158.5 at. ppm He (not including 2.0 at. ppm He from ^{10}B) and 10.36 dpa for type 316 stainless steel in ORR-MFE-4A and 99.4 at. ppm He and 7.10 dpa in ORR-MFE-40.

2.2.4 Progress and Status

The operating and current calculated data based on the fluence scaling factors' are summarized in Table 2.2.1 for the ORR-MFE-4A and -4B experiments.

The real-time projections of the helium-to-displacement ratios based on current calculated data as of March 27, 1984 are presented in Fig. 2.2.1(*a*) and (*b*) for the ORR-MFE-4A and -48 experiments, respectively. The projected dates were obtained by assuming an ORR duty factor of 0.86. As noted, the solid aluminum corepieces were inserted in the ORR-MFE-4A experiment on December 7, 1982 and in the ORR-MFE-40 experiment on August 5, 1983. The 1.0-mm-thick hafnium corepiece should be inserted in the ORR-MFE-4A experiment within the next month. The target date for insertion in the ORR-MFE-4B experiment is currently projected for December 20, 1984.

The effect of delaying the insertion of the first hafnium corepiece until the 15-dpa level is obtained in the ORR-MFE-4A experiment has been estimated. This investigation indicates that at 50 dpa a helium level approximately 19% above the first wall level would result. However, if the hafnium thickness were increased to 1.25 mm, a helium level comparable to the level projected with the insertion of the 1.0-mm-thick hafnium corepiece at the 10-dpa level would be obtained. Current plans call for insertion of the 1.0-mm-thick hafnium corepiece as soon as possible since the calculated date of obtaining the 10-dpa level in the ORR-MFE-4A experiment was February 20, 1984.

Table 2.2.1. Operating and calculated data for experiments ORR-MFE-4A and -4B as of March 27, 1984

	ORR-MFE-4A	ORR-MFE-40
ORR cycles	71	49
Power (MWh)	597,022	453,614
Equivalent full-power days[a]	829.2	630.0
Thermal fluence (neutrons/m^2)	1.27×10^{26}	9.69×10^{25}
Total fluence (neutrons/m^2)	4.27×10^{26}	3.01×10^{26}
He (at. ppm)[b]	158.5	99.4
dpa[b]	10.36	7.10

[a]Full power for ORR is 30 MW.

[b]Helium and dpa values are for type 31h stainless steel.

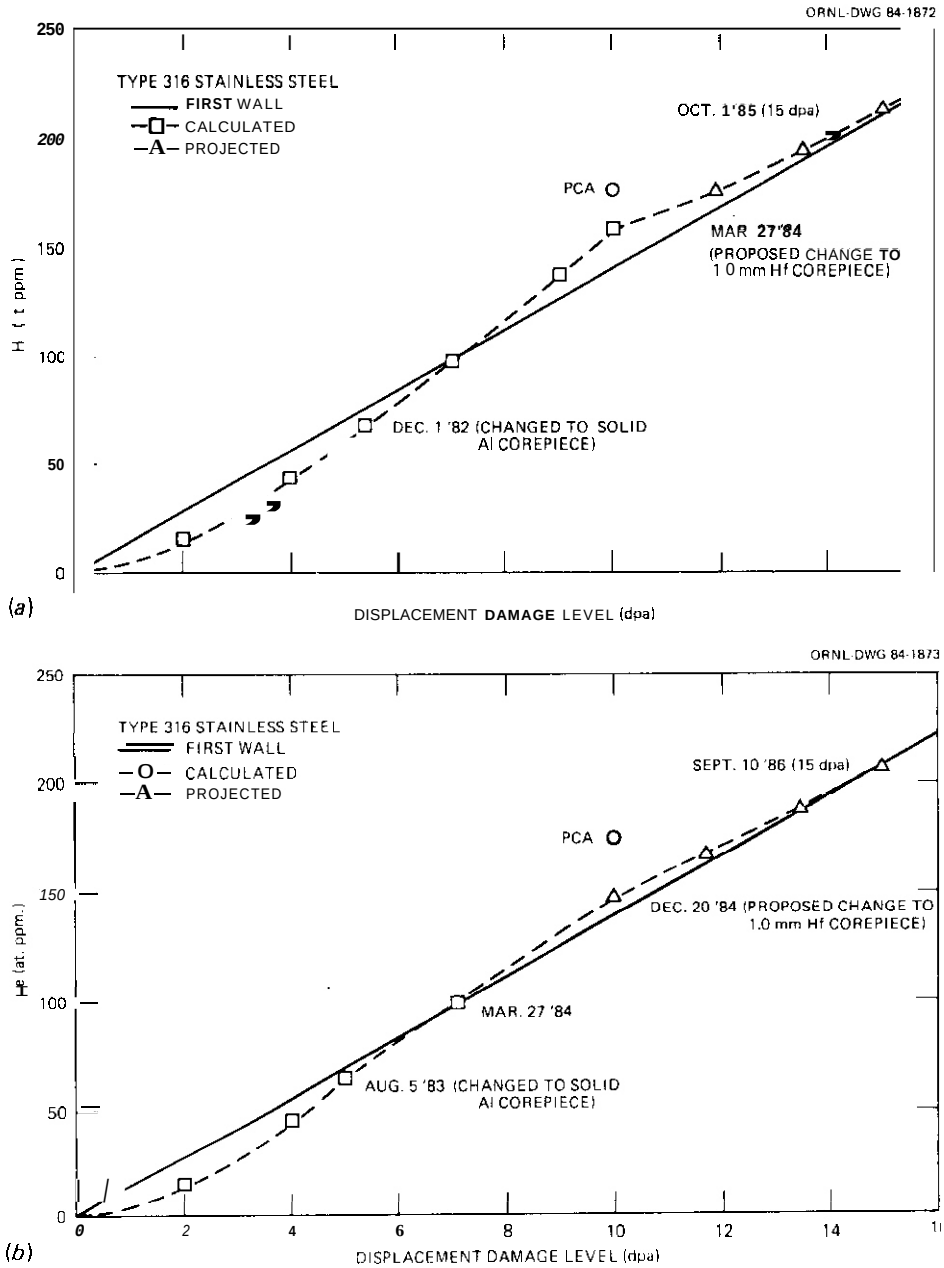

Fig. 2.2.1. Current and projected helium and displacement damage levels in the (a) ORR-MFE-4A and (h) ORR-MFE-4B experiments.

2.2.5 Future Work

The three-dimensional neutronics calculations that monitor the radiation environment in the ORR-MFE-4A and -4B experiments will continue with each ORR cycle. The scale factors used to scale the fluences ohtained from these calculations will be updated as new experimental data become available.

2.2.h Reference

1. R. A. Lillie and T. A. Gabriel, "Neutronics Calculations in Support of the ORR-MFE-4A and -4B Spectral Tailoring Experiments," pp. 19-20 in *ADIP Semiannu. Prog. Rep. Mar. 31, 1983*, DOE/ER-0045/10, 11.5. DOE Office of Fusion Energy.

7.3 OPERATION OF THE ORR SPECTRAL TAILORING EXPERIMENTS ORR-MFE-4A and ORR-MFE-4B — J. A. Conlin, I. T. Dudley, and E. M. Lees (Oak Ridge National Laboratory)

2.3.1 AOIP Task

ADIP Task I.A.2, Define Test Matrices and Test Procedures.

2.3.2 Objectives

Experiments ORR-MFE-4A and -4B, which irradiate austenitic stainless steel, use neutron spectral tailoring to achieve the same helium-to-displacement-per-atom (He/dpa) ratio as predicted for fusion reactor first-wall service. Experiment ORR-MFE-4A contains mainly type 316 stainless steel and Path A Prime Candidate Alloy (PCA) at irradiation temperatures of 330 and 400°C. Experiment ORR-MFE-4B contains similar materials at irradiation temperatures of 500 and 600°C.

2.3.3 Summary

The specimens contained in the ORR-MFE-4A experiment have operated for an equivalent of 833 d at 30 MW reactor power with temperatures of 330 and 400°C. The specimens contained in the ORR-MFE-4B experiment have operated for an equivalent of 634 d at 30 MW reactor power with temperatures of 500 and 600°C.

2.3.4 Progress and Status

The details of the flak Ridge Research Reactor (ORR) spectral tailoring experiments have been described previously.'-'

A hafnium sleeve for neutron spectral tailoring of the ORR-MFE-4A experiment has been designed, fabricated, and tested. The sleeve was made from a sheet of hafnium 1.04 mm (0.041 in.) thick rolled into a cylindrical shape 50.R mm (2.0 in.) in diameter by 311.2 mm (17.25 in.) long and then seam welded. The sleeve was fitted into an aluminum cylinder, which in turn was fitted into an aluminum core piece having the external shape of a fuel element. The midplane of the hafnium sleeve, which is located 76.2 mm (3 in.) below the ORR core midplane, coincides with the midplane of the ORR-MFE-4A capsule.

A test was conducted in the ORR to study the effects of the addition of the hafnium sleeve on neutron flux, qamma heating rate, and reactivity. The effect on the gamma heating rate is of particular importance to the ORR-MFE-4A experiment because it is critical to the capsule temperature control. The test, which was conducted in ORR C-3 core position during the week beginning February 26, 1984, consisted of the following six steps:

1. qamma heat measurements at zero power and N_L (330 kW) without hafnium sleeve,
2. 4 h irradiation of dosimeters at N_L (330 kW) without hafnium sleeve,
3. gamma heat measurements at zero power and N_L (330 kW) with hafnium sleeve,
4. 4 h irradiation of dosimeters at N_L (330 kW) with hafnium sleeve,
5. heat balance run at 12 MW with hafnium sleeve, and
6. heat halance run at 12 MW without hafnium sleeve.

The dosimeters, which were supplied by Argonne National Lahoratory, were returned there for postirradiation analysis.

Results of the gamma heating measurements shown in Table 2.3.1 indicate a reduction of less than 10% in the gamma heating rate due to the hafnium sleeve installation. A test was then made on the ORR-MFE-4A experiment, operating in the ORR core position E-3, to determine whether or not the specified capsule temperatures can he maintained with a 10% reduction of qamma heating: the gamma heating reduction was accomplished by simply reducing the ORR power hy 10% durinq the test. We found that the capsule temperatures can be maintained even at the reduced qamma heatinq rate.

Tahle 7.3.1. Gamma heatinq measurements for ORR core position C-3

Distance from ORR midplane		Gamma heating (W/g)	
(mm)	(in.)	Without hafnium sleeve	With hafnium sleeve
+229	+9	2.4	2.7
+76	+3	4.7	3.9
0	n	4.9	4.5
–76	–3	5.4	4.9
–152	–6	5.4	5.1
–229	--9	4.7	4.3

A core flux map of the ORR was made following the refueling shutdown on February 27, 1984, with the hafnium sleeve installed around the ORR-MFE-4A experiment located in core position E-3. The mapping was accomplished by irradiating dosimeter wires at a reactor power of N_L (−330 kW). The core was also mapped without the hafnium sleeve in place. The results of these tests will be available in April 19114.

Subject to approval by the Reactor Experiment Review Committee (RERC), we plan to install the core piece containing the hafnium sleeve in the E-3 core position for use with the ORR-MFE-4A experiment during the refueling shutdown scheduled for April 22, 1984. Reactivity measurements with the hafnium sleeve in place will be made at that time. The ORR-MFE-4A experiment will then be operated with the hafnium sleeve in place for the remainder of this irradiation period, which will last until about October 1985.

The specimens contained *in* this experiment have operated for an equivalent of 833 d at 30 MW reactor power with temperatures of 330 and 400°C.

The ORR-MFE-4B capsule experiment continues to operate satisfactorily, although the temperatures indicated by thermocouples 4 and 5 continue to fluctuate. The fluctuations are believed to be caused by the movements of bubbles of argon cover gas in the NaK. This result is tentatively attributed to the absorption of argon cover gas in the upper region NaK; convection currents (due in part to the radial temperature gradient) carry this NaK into the lower region where, if the temperature is lower, the absorbed gas forms bubbles. A three-day test was made to determine the effects of lowering the temperature of the upper capsule region on gas bubble formation. Reduction of the upper region temperature from 600°C to about 440°C during the test did, as expected, reduce the fluctuation of temperatures indicated by thermocouples 4 and 5 to negligible levels. There was also a reduction in the capsule lower region vertical temperature differential. It was lowered from the normal differential of 127°C to only 36°C. After the upper region temperature was returned to 600°C the fluctuations of temperatures indicated by thermocouples 4 and 5 resumed and the vertical temperature differential of the lower capsule region returned to the normal value of 127°C.

The specimens contained in this experiment have operated for an equivalent of 634 d at 30 MW reactor power with temperatures of 500 and 600°C.

2.3.5 References

1. K. R. Thoms and M. L. Grossbeck, "Operation of the ORR Spectral Tailoring Experiment ORR-MFE-4A,' pp. 20–24 in *ADIP Quart. Prog. Rep. Sept. 30, 1980,* DOE/ER-0045/4, U.S. DOE, Office of Fusion Energy.

2. K. R. Thoms, "Ooeration of the ORR Spectral Tailorina Experiment ORR-MFE-4A." pp. 18–21 in *ADIP Quart. Prog. Rep. Mar. 31, 1982,* DOE/ER-0045/6, U.S. DOE, Office of Fusion Energy.

3. I. T. Dudley, "Operation of the ORR Spectral Tailoring Experiments ORR-MFE-4A and ORR-MFE-48," pp. 24-29 in *ADIP Semiannu. Prog. Rep. Sept. 30, 1981,* DOE/ER-0045/7, U.S. DOE, Office of Fusion Energy.

4. I. T. nudley and J. A. Conlin, "Operation of the ORR Spectral Tailoring Experiments ORR-MFE-4A and ORR-MFE-4B," pp. 10–12 in *ADIP Semiannu. Prog. Rep. Mar. 31, 1982,* DOE/ER-0045/8, U.S. DOE, Office of Fusion Energy.

5. J. A. Conlin, I. T. Dudley, and E. M. Lees, "Operation of the ORR Spectral Tailoring Experiments ORR-MFE-4A and ORR-MFE-4B," pp. 17–20 in *ADIP Semiannu. Prog. Rep. Sept. 30, 1.982,* DOE/ER-0045/9, U.S. DOE, Office of Fusion Energy.

6. J. A. Conlin, I. T. Dudley, and E. M. Lees, "Operation of the ORR Spectral Tailoring Experiments ORR-MFE-4A and ORR-MFE-4B," pp. 21–22 in *ADIP Semiannu.* Prog. *Rep. Mar. 31, 1983,* DOE/ER-0045/10, U.S. DOE, Office of Fusion Energy.

1. J. A. Conlin, I. T. Dudley, and E. M. Lees, "Operation of the ORR Spectral Tailoring Experiments ORR-MFE-4A and ORR-MFE-4B," DD. 40–41 in *ADIP Semiannu. Prog. Rep. Sept. 30, 1883,* DOE/ER-0045/1I, U.S. DOE, Office of Fusion Energy.

2.4 SUMMARY OF THE EBR-II AD-2 FERRITICS IRRADIATION EXPERIMENT - A. M. Ermi (Westinghouse Hanford Company)

2.4.1 ADIP Task

ADIP Program Task: Ferritic Steels Development [Path E).

2.4.2 Objectives

The objective of the AD-2 experiment is to provide baseline, high fluence data at several temperatures for the ferritic alloys HT-9 and 9Cr-1Mo. Developmental 2-1/4Cr-1Mo is also being scoped in this experiment. The AD-2 experiment is designed to yield data concerning the irradiation effects on the mechanical properties of these alloys with emphasis on their tensile fatigue, fracture toughness and weld properties. Characterization of the irradiation effects on the microstructure of these alloys will also be performed.

2.4.3 *Summary*

Six uninstrumented B-7c capsules were removed from the EBR-II after undergoing irradiation during Cycles 109-113 (August 1980 to June 1981). Several specimens were removed and distributed for interim examination, while the remaining specimens were re-encapsulated into four new B-7c capsules. In addition, some unirradiated specimens were included in the new capsules. These capsules were removed after undergoing irradiation during Cycles 118-121 and 123 (February 1982 to April 1983).

2.4.4 Progress and Status

2.4.4.1 Introduction

The AD-2 experiment has been designed to provide mechanical properties data on selected ferritic alloys for application in fusion reactor first walls and blankets. Of particular concern are the irradiation effects on the fracture and weld properties of the materials. Alloy selection and irradiation temoeratures have been soecified by the Allov Development for Near Term Applications Working Group. This is the final report on the AD-2 experiment, which summarizes the experimental parameters for both'the initial and reconstitution test matrices.

2.4.4.2 Test Matrices

Details regarding specimen preparation, heat treatments, test matrices and capsule loadings have been reported in previous ADIP Progress Reports. The initidl specimen preparation and loading were reported in June 1980,[1] while the reconstitution test matrix was reported in March 1982.[2,3] The complete AD-2 test matrix encompassing both irradiations is detailed in Table 2.4.1.

2.4.4.3 Irradiation Parameters

The initial irradiation utilized six uninstrumented B-7C capsules, two at both 390°C and 500°C, and one at each 450°C and 550°C. These capsules were inserted into the EBR-II in August 1980 for Cycle 109 and were removed in June 1981 after Cycle 113. Specimens in the peak flux position accumulated a fluence of 13.5 dpa (based on 4.R dpa/10^{22} n/cm^2 for Hi-9).

The second irradiation, including reconstituted specimens plus new. unirradiated soecimens., utilized four B-7c capsules, one at each of the four temperatures. These cdpsules were inserted' in February 1982 for Cycle 118 and were removed in April 1983 after Cycle 123. [The capsules were removed during the transient cycle, 122). Specimens in the peak flux position during the second irradiation accumulated a fluence of 16.2 dpa. Reconstituted specimens in the peak positions for both irradiations accumulated 29.7 dpa.

A summary of the experimental parameters for the entire AD-2 experiment is given in Table 2.4.2. Included are the fluences for each irradiation as a function of the seven levels along the B-7c capsules. Details of fluences for particular specimens are available from the author on request.

Specimens from the AD-2 experiment were distributed as follows: ORNL received all tensile, Grodzinski fatigue and fatigue initiation specimens; WHC received all fracture toughness and fatigue crack growth specimens; the Charpy specimens were distributed to both ORNL and WHC; and the TEM disk Specimens were distributed to various participants in the ADIP and DAFS programs.

2.4.5 Future Work

This concludes the irradiation phase of the AD-2 experiment

2.4.6 References

1. R. J. Puigh and N. F. Panayotou, "Specimen Preparation and Loading for the AD-2 Ferritics Experiment", pp. 260-293 in *ADIP Semiannu. Prog. Rep. June 1980*, DOE/ER-0045-3, U.S. DOE, Office of Fusion Energy.

2. D. T. Peterson, "TEM Specimen Matrix for the AD-2 Reconstitution", pp. 13-16 *ADIP Semiannu. Proa. Rep. March 1982*, DOE/ER-0045/8, U.S. DOE, Office of Fusion Energy.

3. A. M. Ermi, "Reconstitution of the AD-2 Ferritics Experiment", pp. 431-441 in *ADIP Semiannu. Prog. Rep. March 1982*, DOE/ER-0045/8, U.S. DOE, Office of Fusion Energy.

Table 2 1. AD 2 Test Matrix

Material [Code]	Initial Test Matrix				Interim Examination				Recon of Irradiated Spec.				Recon of Unirradiated Spec.				Total Recon Test Matrix			
	390C	450C	500C	550C	390C	450C	500C	550C	390C	450C	500C	550C	390C	450C	500C	550C	390C	450C	500C	550C
TENSILE [T]																				
HT-9(#1)[UH]	20	10	20	10	10	5	10	5	10	5	10	5	--	--	--	--	10	5	10	5
HT-9(#2)[TW]	10	5	10	5	10	2	10	2	--	3	--	3	--	--	--	--	--	3	--	3
HT-9(XAA-3587)[SB]	--	--	--	--	--	--	--	--	--	--	--	--	4	4	1	4	4	4	1	4
HT-9,1Ni[SC]	--	--	--	--	--	--	--	--	--	--	--	--	4	4	--	2	4	4	--	2
HT-9,2Ni[SD]	--	--	--	--	--	--	--	--	--	--	--	--	4	4	1	4	4	4	1	4
HT-9,2Ni Adj [SE]	--	--	--	--	--	--	--	--	--	--	--	--	4	--	--	--	4	--	--	--
9Cr-1Mo(30182)[XT]	9	3	9	6	4	1	4	3	5	2	5	3	--	--	--	--	5	2	5	3
9Cr-1Mo(XA-3590)[TA]	--	--	--	--	--	--	--	--	--	--	--	--	4	4	--	4	4	4	--	4
9Cr-1Mo-2Ni[TB]	--	--	--	--	--	--	--	--	--	--	--	--	4	4	1	4	4	4	1	4
9Cr-1Mo-2Ni Adj[TC]	--	--	--	--	--	--	--	--	--	--	--	--	--	4	--	--	--	4	--	--
2-1/4Cr-1Mo[ZT]	6	3	6	3	3	1	3	1	3	2	3	2	--	--	--	--	3	2	3	2
LRO-16D [6]	--	--	--	--	--	--	--	--	--	--	--	--	--	--	--	2	--	--	--	2
LRO-42 [VH]	--	--	--	--	--	--	--	--	--	--	--	--	2	2	--	2	2	2	--	2
CRACK GROWTH [CG]																				
HT-9(#1)[HT]	22	11	22	11	10	4	13	4	12	7	9	7	--	--	--	--	12	7	9	7
HT-9(#2)[MR]	10	5	10	5	10	2	10	2	--	3	--	3	--	--	--	--	--	3	--	3
9Cr-1Mo(30182)[AS]	10	5	10	5	4	2	4	2	6	3	6	3	--	--	--	--	6	3	6	3
2-1/4Cr-1Mo[ZC]	10	5	10	5	4	2	10	2	6	3	--	3	--	--	--	--	6	3	--	3
HT-9(W)[RW]	10	--	10	10	4	--	5	4	6	--	5	6	--	--	--	--	6	--	5	6
HT-9(HAZ)[WR]	5	--	5	5	2	--	2	2	3	--	3	3	--	--	--	--	3	--	3	3
HT-9(W/HAZ)[RW]	2	--	2	2	2	--	2	2	--	--	--	-	--	--	--	--	--	--	--	--
9Cr-1Mo(W)[WM]	6	--	6	6	2	--	2	2	4	--	4	4	--	--	--	--	4	--	4	4
FATIGUE INITIATION [FI]																				
HT-9(#4)[SF]	6	3	6	3	4	3	4	3	2	--	2	--	--	--	--	--	2	--	2	--
9Cr-1Mo(30182)[SI]	6	3	6	3	4	3	4	3	2	--	2	--	--	--	--	--	2	--	2	--
GRODZINSKI FATIGUE [GF]																				
HT-9(#1)[SG]	10	5	10	5	10	3	10	3	--	2	--	2	--	--	--	--	--	2	--	2
9Cr-1Mo(30182)[SH]	2	--	2	2	2	-	2	2	--	--	--	--	--	--	--	--	--	--	--	--

Table 2.4.1 AD Z Test Matrix (cont'd)

Material [Code]	Initial Test Matrix				Interim Examination				Recon of Irradiated Spec.				Recon of Unirradiated Spec.				Total Recon Test Matrix			
	390C	450C	500C	550C	390C	450C	500C	550C	390C	450C	500C	550C	390C	450C	500C	550C	390C	450C	500C	550C
FRACTURE TOUGHNESS [FT]																				
HT-9(#3)[T4]	10	6	10	6	6	6	6	6	4	--	4	--	--	--	--	--				
HT-9(#4)[T5]	6	--	6	--	4	--	4	--	2	--	2	--	--	--	--	--				
9Cr-1Mo(30182)[T6]	6	6	6	--	6	6	6	--	--	--	--	--	--	--	--	--				
HT-9(W)[T7]	7	6	7	3	6	6	6	3	1	--	1	--	--	--	--	--				
HT-9(W/HAZ)[HT],[TA]	7	6	7	3	6	6	6	3	1	--	1	--	5	7	5	5				
CHARPY [C]																				
HT-9(#1)[KT]	--	--	--	--	--	--	--	--	--	--	--	--	8	8	--	8	8	8	--	8
HT-9(#3)[TT]	10	8	10	8	6	4	6	4	4	4	4	4	--	--	--	--	4	4	4	4
HT-9(XAA-3587)[SB]	--	--	--	--	--	--	--	--	--	--	--	--	5	--	--	--	5	--	--	--
HT-9,1Ni[SC]	--	--	--	--	--	--	--	--	--	--	--	--	--	--	3	--	--	--	3	--
HT-9,2Ni[SD]	--	--	--	--	--	--	--	--	--	--	--	--	3	--	3	--	3	--	3	--
9Cr-1Mo(30176)[AF]	--	--	--	--	--	--	--	--	--	--	--	--	8	8	6	8	8	8	6	8
9Cr-1Mo(30182)[TV]	8	4	8	4	4	4	4	4	4	--	4	--	--	--	--	--	4	--	4	--
9Cr-1Mo(XA-3590)[TA]	--	--	--	--	--	--	--	--	--	--	--	--	--	5	--	5	--	5	--	5
9Cr-1Mo-2Ni[TB]	--	--	--	--	--	--	--	--	--	--	--	--	--	3	--	3	--	3	--	3
HT-9(W)[T1]	7	4	7	4	7	4	7	4	--	--	--	--	--	--	--	--	--	--	--	--
HT-9(W/HAZ)[TX]	7	--	7	--	7	--	7	--	--	--	--	--	--	--	--	--	--	--	--	--
9Cr-1Mo(W)[NL]	--	--	--	--	--	--	--	--	--	--	--	--	8	8	8	8	8	8	8	8
DISK PACKETS [D]																				
Various Alloys	8	4	8	4	4	2		2		2	4	2	2	2	2	2	6	4	6	4

Table 2.4.2. Summary of the EBR-II AD-2 Experiment

	AD-2	AD-2 RECON
Date In Reactor:	August 1980 - June 1981	February 1982 - April 1983
Cycle Numbers:	109 - 113	118 - 121 & 123
Reactor Power:	57.25 MW	57.25 MW
Accumulated Exposure:	10,680 MWD	12,780 MWD
Capsules/ Temperature:	B-317/390°C B-318/500°C B-319/550°C B-320/390°C B-321/450°C B-322/500°C	B-317a/390°C B-318a/450°C B-319a/500°C B-321a/550°C

Subassembly:	X-3440		X-3440	
Core Position:	4C2		4B2	
Peak Fluence[a]:	2.82 x 10^{22} n/cm^2 (13.5 dpa)		3.37 x 10^{22} n/cm^2 (16 2 dpa)	
Reactor Level Number Within Each Capsule	Distance From Core Mid-Plane	Fluence[b] 10^{22} n/cm^2 (dpa)	Distance From Core Mid-Plane	Fluence[b] 10^{22} n/cm^2 (dpa)
1	153 mm	1.88 (9.0)	159 mm	2.24 (10.8)
2	108 mm	2.35 (11.3)	109 mm	2.80 (13.5)
3	56 mm	2.67 (12.8)	56 mm	3.20 (15.4)
4	0 mm	2.82 (13.5)	0 mm	3.37 (16.2)
5	-54 mm	2.76 (13.3)	-53 mm	3.31 (15.9)
6	-102 mm	2.53 (12.1)	-102 mm	3.02 (14.5)
7	-152 mm	2.10 (10.1)	-155 mm	2.48 (11.9)

[a]Based on a nominal value of peak flux for Row 4 of 1.75 x 10^{15} n/cm^2-s, E > 0.1 MeV (from dosimetry); dpa values based on 4.8 dpa/10^{22} n/cm^2 for HT-9 (HEDL TC-160-1, 1974).

[b]Based on the Row 4 flux profile from HEDL TME 78-84, 1979

2.5 HIGH-FLUENCE IRRADIATION OF FERRITIC STEELS IN HFIR: HFIR-CTR-49 AND -50 — J. M. Vitek (flak Ridge National Laboratory)

2.5.1 ADIP Task

ADIP Task I.A.2, Define Test Matrices and Test Procedures.

2.5.2 Objective

These experiments are intended to evaluate the tensile properties and microstructure of ferritic steels after high-fluence elevated-temperature irradiation in High Flux Isotope Reactor (HFIR) (to nominal damage levels of 50 and 100 dpa). In conjunction with similar but lower neutron exposure experiments (HFIR-CTR-39, -40, and -41), the fluence dependence of tensile properties of ferritic steels will be determined. This experiment will also be a followup to experiments HFIR-CTR-30, -31, and -32, which evaluated the microstructural response of several ferritic steels to damaqe levels of up to 40 dpa. Irradiation of three alloy types is planned: 2 1/4 Cr-1 Mo, 9 Cr-1 MoVNb, and 12 Cr-1 MoVW. A few samples of nickel-doped alloys will be included to assess the effect of helium on microstructure and properties: the helium levels will vary with nickel levels because of a helium-producing transmutation reaction of nickel during HFIK irradiation.

2.5.3 Summary

The HFIR-CTR-49 and -50 experiments contain tensile specimens and transmission electron microscopy (TEM) disks of various ferritic steels. Irradiation is planned at 400 and 600°C to damage levels of 50 and 100 dpa.

2.5.4 Progress and Status

2.5.4.1 Introduction

Previous irradiation experiments in HFIR were conducted to evaluate the postirradiation tensile properties of ferritic steels.' These experiments involved irradiations to a damage level of 10 dpa or less. Several nickel-doped alloys were irradiated in order to evaluate the effect of helium on the tensile properties. As a result of a two-step transmutation reaction that produces helium from nickel, the helium level is directly proportional to the nickel content of the alloys. The HFIR-CTR-49 and -50 experiments are intended to supplement these earlier irradiations by providing postirradiation tensile data on the same alloys subjected to considerably higher damage levels and helium concentrations.

Another set of earlier experiments was carried out to evaluate the microstructural response of ferritic steels after irradiation in HFIR to damage levels of up to 40 dpa (ref. 2). Transmission electron microscopy disk packets consisting of approximately 100 disks each are also to be irradiated in HFIR-CTR-49 and -50 to evaluate the microstructural response of ferritic steels following higher fluence irradiation. A variety of alloys will be included as TEM disks, including nickel-doped ferritic steels, austenitic steels, and experimental ferritic alloys.

2.5.4.2 Experiment Design

Each experiment will contain a combination of 10 rod tensile specimens and 1 packet of TEM disks. The design for the tensile specimen arrangement will be identical to that used successfully in the past in experiments HFIR-CTR-39, -40, and -41. The rod tensile samples will be held in place by spurs at each end. A gas gap around the sample gage section and shoulder will provide for the elevated temperatures required. The gas gaps are adjusted for each specimen to account ?or the different nuclear heating rates and desired temperatures. The design for the one TEM disk packet position will be basically the same as that used before.[2] A low-swelling 9 Cr-1 MoVNb ferritic alloy will be used for the TEM disk tube enclosure to minimize swelling and ensure that the designed gas gaps are maintained throughout the irradiation.

2.5.4.3 Test Matrix and Irradiation Conditions

The test matrices of both experiments are identical with regard to tensile specimens. Five alloys will be included as tensile specimens: two 12 Cr-1 MoVW alloys, two 9 Cr-1 MoVNb alloys, and one 2 1/4 Cr-1 Mo alloy. Each of the 12 Cr-1 MoVW and 9 Cr-1 MoVNb alloys contains two different nickel levels in order to produce two different helium concentrations during irradiation. Five tensile specimens are to irradiated at 400°C, while the other five specimens are to he irradiated at the relatively high irradiation temperature of 600°C; this high temperature is being used to exaggerate the effects of helium. The test matrix, alloy heat numbers, and heat treatments are detailed in Table 2.5.1. Alloy chemistries for the 9 Cr-1 MoVNb and 12 Cr-1 MoVW alloys have been reported elsewhere.[3] The 2 1/4 Cr-1 Mo alloy (heat 38649) contains 2.16 Cr, 0.97 Mo, 0.40 Ni, 0.52 Mn, 0.087 C, 0.18 Si, 0.011 P, and 0.014 S (wt %).

The TEM disk packet will contain various alloys and heat treatments too numerous to detail here. Basically, though, the 50-dpa capsule (HFIR-CTR-49) will contain disks of experimental alloys described in Sect. 7.1 of this report. The 100-dpa capsule (HFIR-CTR-50) will contain disks of the same alloys already irradiated in HFIR to 40 dpa and known to be low-swelling alloys. These will include various ferritic steels and also 19 austenitic prime candidate alloy (PCA) samples. Irradiation will be at 400°C, the peak swelling temperature for ferritics.[4]

Tahle 2.5.1. Specimen matrix for HFIR-CTK-43 and -50

Position	Temperature (°C)	Specimen type	Alloy	Heat	Heat treatment
1	400	Tensile	2 1/4 Cr-1 Mo	38649	900°C/0.5 h/AC + 700°C/1 h/AC
2	400	Tensile	9 Cr-1 MoVNb-2 Ni	XA 3591	1040°C/0.5 h/AC t 700°C/8 h/AC
3	400	Tensile	9 Cr-1 MoVNb	XA 3590	1040°C/0.5 h/AC + 760°C/1 h/AC
4	400	Tensile	12 Cr-1 MoVW-2 Ni	XAA 3589	1050°C/0.5 h/AC + 700°C/8 h/AC
5	400	Tensile	12 Cr-1 MoVW	XAA 3587	1050°C/0.5 h/AC + 780°C/2.5 h/AC
6	400	TEM[a]	Various		
7	600	Tensile	12 Cr-1 MoVW	XAA 3587	1050°C/0.5 h/AC + 780°C/2.5 h/AC
8	600	Tensile	12 Cr-1 MoVW-2 Ni	XAA 3589	1050°C/0.5 h/AC + 700°C/8 h/AC
9	600	Tensile	9 Cr-1 MoVNb	XA 3590	1040°C/0.5 h/AC + 760°C/1 h/AC
10	600	Tensile	9 Cr-1 MoVNb-2 Ni	XA 3591	1040°C/0.5 h/AC + 700°C/8 h/AC
11	600	Tensile	2 1/4 Cr-1 Mo	38649	900°C/0.5 h/AC + 700°C/1 h/AC

[a]Transmission electron microscopy.

The HFIR peripheral target positions will be used. Irradiation is planned to achieve midplane exposures of 55,000 and 110,000 MWd, corresponding to displacement damage levels of 50 and 100 dpa and helium concentrations in the nickel-doped alloys of 500 and 1000 at. ppm He, respectively. Irradiation of HFIR-CTR-50 began in April 1984, and irradiation of HFIR-CTK-49 will likely begin in May 1984.

2.5.5 References

1. J. M. Vitek. "Elevated-Temperature Irradiation of Ferritic Steel Tensile Specimens: Experiments HFIR-CTR-39, -40, and -41," pp. 91–95 in *ADIP Semiannu. Prog. Rep. Mar. 31, 1982*, DOE/ER-0045/8, U.S. DOE, Office of Fusion Energy.
2. M. L. Grossbeck, J. W. Woods, and G. A. Potter, "Experiments HFIR-CTR-30, -31, and -32 for Irradiation of Transmission Electron Microscopy Disk Specimens," pp. 36–44 in *ADIP Quart. Prog. Rep. Sept. 30, 1980*, DOE/ER-0045/4, U.S. DOE, nffice of Fusion Energy.
3. R. L. Klueh and J. M. Vitek, "Characterization of Ferritic Steels for HFIR Irradiation,'' pp. 294–308 in *ADIP* Quart. *Prog. Qep. June 30, 1980*, DOE/ER-0045/3, U.S. DOE, nffice of Fusion Energy.
4. J. M. Vitek and R. L. Klueh, "Microstructure of 9 Cr-1 MoVNb and 12 Cr-1 MoVW Ferritic Steels After Irradiation at Elevated Temperatures in HFIR," pp. 108–14 in *ADIP Semiannu. Prog. Rep. Sept. 30, 1983*, DOE/ER-0045/11, U.S. DOE, Office of Fusion Energy.

2.6 IRRADIATION OF MINIATURE CHARPY IMPACT 12 Cr-1 MoVW SPECIMENS AT 200 AND 300°C: HFIR-CTR-53 — J. M. Vitek (Oak Ridge National Laboratory)

2.6.1 ADIP Task

ADIP Task I.A.2, Define Test Matrices and Test Procedures.

2.6.2 Objective

The objective of this experiment is to determine the postirradiation impact properties of the fusion heat of 12 Cr-1 MoVW at 200 and 300°C. Previous experiments to damage levels greater than 1 dpa have been at 55 and 300°C, and higher. This experiment will provide information in the critical temperature range 100 to 300°C.

2.6.3 Summary

The HFIR-CTR-53 experiment will contain 16 miniature Charpy specimens of the national fusion heat of 12 Cr-1 MoVW. Irradiation will he at 200 and 300°C and will achieve a midplane damage level of 8 dpa.

2.6.4 Progress and Status

2.6.4.1 Introduction

The postirradiation impact properties of ferritic steels are one of the primary concerns in the ADIP ferritics program. It has become clear that low-temperature irradiations may he critical in assessing the potential of these steels. Previous irradiations[1,2] to damage levels of greater than 1 dpa have been at 55°C and above 300°C. With the introduction of one-third size Charpy impact specimens, it has been determined that irradiation temperatures between 55 and 300°C are now achievable in the High Flux Isotope Reactor (HFIR). This experiment is intended to provide the first impact data at high damage levels (>1 dpa) at 200°C.

The fusion heat of 12 Cr-1 MoVW will he used in order to correlate the information on one-third size specimens with previous experiments on one-half size specimens.[2] This will then result in an extensive data base of impact properties on the same alloy with the same heat treatment as a function of irradiation temperature from 200 to 400°C.

2.6.4.2 Experimental Design

The experimental design is basically the same as that used in previous HFIR experiments,[2] with many of the parts scaled down to accommodate the smaller one-third size specimens. The samples are contained in type 316 stainless steel holders, which are inserted in aluminum sleeves. The gamma heating of the specimen and holder accounts for the specimen heating. The specimen subassemblies are stacked in a water-cooled aluminum containment tube.

Two irradiation temperatures are being used. The 300°C temperature is being included in order to correlate the properties with those obtained from a previous experiment on the same heat of material at 300°C but with one-half size specimens.[2]

2.6.4.3 Specimen Preparation, Test Matrix, and Irradiation Conditions

The miniature Charpy V-notch impact specimens are to be made from the national fusion heat of 12 Cr-1 MoVW, heat 9607-R2. The alloy chemistry is available elsewhere.[2] The samples will be machined from normalized-and-tempered plate stock (1050°C/0.5 h/AC + 780°C/2.5 h/AC), the same condition used for specimen preparation in HFIR-CTR-46.

The HFIR-CTR-53 capsule will contain 16 miniature Charpy V-notch specimens, 3.3 × 3.3 mm (0.13 × 0.13 in.) in cross section and 25.4 mm (1.0 in.) in length. Of the 16 samples, eight are to be irradiated at 200°C and eight at 300°C. A specimen matrix is given in Table 2.6.1.

The HFIR peripheral target position will be used. In order to have comparable irradiation doses for the 300°C irradiated samples in this experiment with those in the HFIR-CTR-46 experiment, the midplane damage level will be about 8 dpa. Irradiation of HFIR-CTR-53 is scheduled to begin in 1984.

Table 2.6.1 Miniature Charpy V-notch specimen matrix for HFIK-CTR-53

Position	Nominal temperature (°C)	Position	Nominal temperature (°C)
1	200	9	3nn

2.6.5 References

1. J. M. Vitek and J. W. Woods, "Experiments HFIR-MFE-RB1, -RB2, and -RB3 for Low Temperature Irradiation of Path E Ferritic Steels," pp. 30–35 in *ADIP Semiannu. Prog. Rep. Sept. 30, 1981*, DOE/ER-0045/7, U.S. DOE, Office of Fusion Enrrgy.
2. J. M. Vitek, "Irradiation of Miniature Charpy Specimens of 12 Cr-1 MoVW: Experiment HFIR-CTR-46," pp. 23–24 in *ADIP Semiannu. Prog. Rep. March 31, 1983*, DOE/ER-0045/10, U.S. DOE, Office of Fusion Energy.

2.7 INTRODUCTION TO THE U.S./JAPAN COLLABORATIVE TESTING PROGRAM IN HFIR AND ORR — J. L. Scott (flak Ridge National Laboratory) and T. Kondo (Japan Atomic Energy Research Institute)

2.7.1 ADIP Task

ADIP Task I.A.2, Define Test Matrices and Test Procedures.

2.7.2 Objective

The objective of this collaborative program is to design, conduct, and evaluate joint irradiation experiments in the High Flux Isotope Reactor (HFIR) and the Oak Ridge Research Reactor (ORR). The experiments will investigate the irradiation response of Japanese and U.S. structural alloys to high levels of atomic displacement and helium content in order to evaluate their use for first wall and blanket structural applications in future fusion reactors.

2.7.3 *Summary*

An implementing arrangement between DOE and Japan Atomic Energy Research Institute (JAERI) on U.S.-Japan collaborative testing of first wall and blanket structural materials with mixed-spectrum fission reactors initiated collaborative tests of eight HFIR capsules and two ORR spectral-tailoring capsules. The implementing arrangement also serves as a vehicle of future collaboration between DOE and JAERI on other areas of fusion technology. The HFIR and ORR spectral-tailoring capsules will be equally shared by the two programs.

2.7.4 Background

There exists an international consensus that the fusion materials test matrix of candidate materials, microstructural condition, temperature, stress state, and response is too large for any one country to accomplish alone, especially in the alloy scoping stage. For this reason, international collaboration is viewed generally to be highly desirable. There are, however, many barriers to be overcome, including language, distance, institutions, and financing. These barriers can he discouraging at times, and perservance is required to overcome them.

The Japanese have recognized the value of irradiations ion HFIR and ORR for a long time. They consider helium effects to he important and testing in mixed-spectrum fission reators to be one of the best available simulation techniques, especially for austenitic steels and ferritic steels containing nickel. Unfortunately for them, there is no mixed-spectrum fission reactor in Japan with the flux of HFIR (peak 5×10^{19} neutrons/$m^2 \cdot s$), and use of other thermal reactors is such that the spectral tailoring as we do in ORR is also not possible. In August 1978, Dr. J. Shimokawa, Head, Division of Nuclear Fuel Research at JAERI, wrote to E. E. Bloom, ORNL, indicating that JAERI wished to irradiate capsules in HFIR and requesting information about costs and schedules. This letter initiated a long series of letters, discussions, meetings, and agreements leading to the present collaboration.

It is unnecessary to give a blow-by-blow account of the history of the negotiations, hut it might be helpful to list the series of agreements that have been signed. In this listing it should not be inferred that all the agreements came about as a result of HFIR-ORR discussions, but each agreement is an essential step.

May 2, 1979 — Agreement between the government of Japan and the government of the United States of America on cooperation in research and development in energy and related fields.

August 24, 1979 — Exchange of notes between the two governments that established a coordinating committee on fusion energy and provided cooperative activites in (a) exchange programs, (b) a joint research project using Doublett III, (c) joint research for plasma physics, and (d) promotion of joint planning.

January 23, 1983 — Exchanqe of notes between the two governments on the cooperation in fusion research and development between U.S. DOE and Monbusho, the Japanese Ministry of International Trade and Industry, and the Japanese Science and Technology Agency. The cooperation may take the following forms:

1. exchange of scientific and technical inforination:
2. holding of seminars and other meetings;
3. short-term visits of scientists, engineers, and other experts to the facilities of the implementing agencies or of their designees:
4. exchange and loan of equipment, instruments, and materials for testing;
5. exchange of scientists, engineers, and other experts for participation in research, development, analysis, design, planning, and experimental activities conducted at the facilities of the implementing agencies or of the designees; and
6. other forms of cooperative activities as may be mutually agreed.

November 8, 1983 — Implementing arrangement between the JAERI and DOE on cooperation in fusion research and development.

November 8, 1983 — Annex I to implementing arrangement between JAERI and DOE on cooperation in fusion research and development — U.5.-Japan collaborative testing of first wall and blanket structural materials with mixed-spectrum fission reactors.

March 15, 1984 — Funds from Japan arrived at ORNL.

March 16, 1984 — Personnel assignment agreement between JAERI and ORNL on collaborative testing of first wall and blanket structural materials with mixed spectrum fission reactors.

March 19, 1984 — Shiro Jitsukawa arrived at ORNL.

Now that all elements of the collaboration are in place the work has commenced.

2.7.5 Scope

This experimental program consists of eight HFIR capsules and two ORR spectral-tailoring capsules with sample numbers equally shared between the U.S. and Japanese programs. Four HFIR capsules will be irradiated to peak exposures of 30 dpa, and four capsules will he irradiated to 50 dpa. In one capsule the specimens will be exposed to HFIR cooling water at about 60°C. The other seven capsules are designed so that specimen temperatures will he in the range 300 to 600°C. Tensile, fatigue, and transmission electron nicroscopy specimens are included.

The two spectral-tailoring capsules will be irradiated in ORR to exposures of 50 dpa with interin examinations at 10, 20, and 30 dpa. Each capsule will have two temperatures, so that specinens will be irradiated at 60, 200, 300, and 400°C. There are about 650 specinens at each temperature. Data will be obtained on swelling, creep, tensile propertier, fatigue, fracture toughness, and microstructural evolution.

The schedule and costs for the collaboration are shown in Fig. 2.7.1.

ORNL-DWG 84-9053

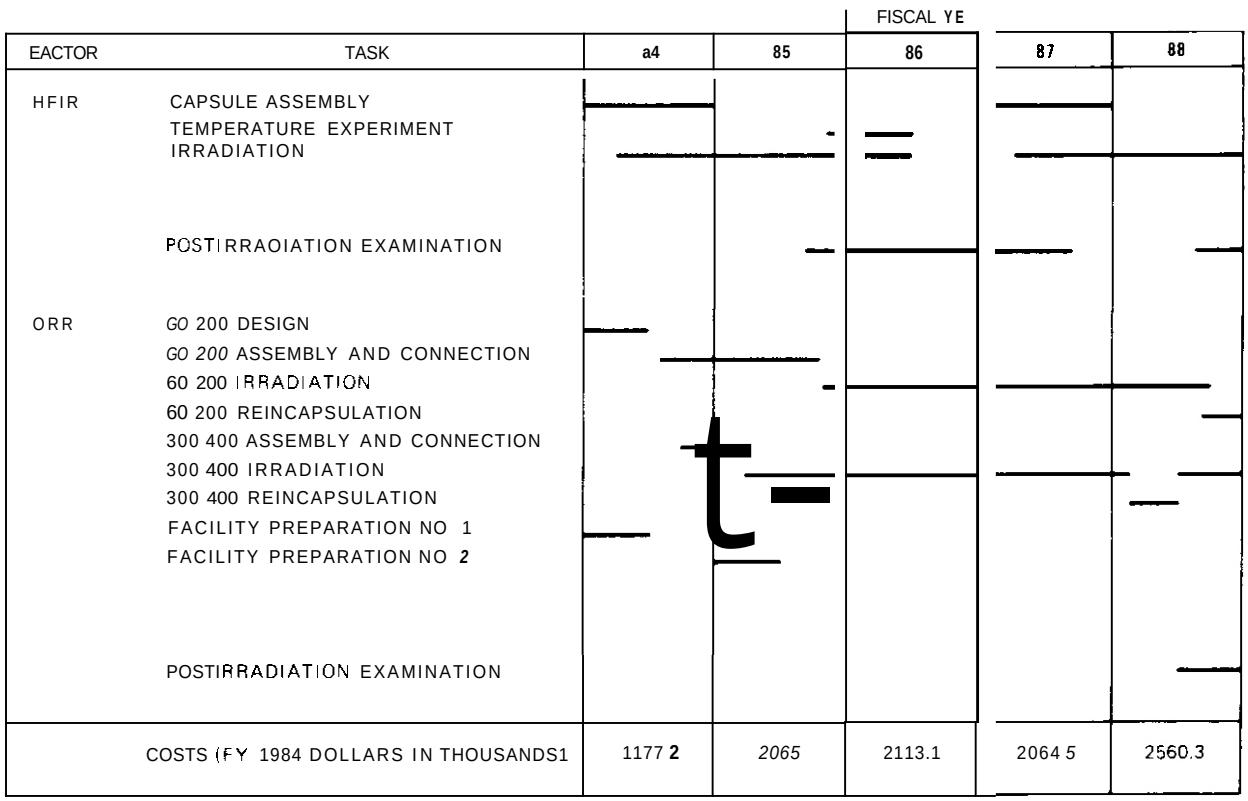

Fig. 2.7.1. Schedule and costs for U.S./Japan collaboration in the High Flux Isotope Peactor and the Oak Ridge Research Reactor.

2.R IRRADIATION EXPERIMENTS FOR THE U.S./JAPAN COLLABORATIVE TESTING PROGRAM IN HFIR AND ORR —

J. A. Conlin and J. W. Woods (Oak Ridge National Laboratory)

2.8.1 ADIP Tasks

ADIP Task I.A.2, Define Test Matrices and Test Procedures.

2.8.2 Objectives

The experiments in the U.S./Japan collaborative testing program for HIIR and ORR irradiate austenitic stainless steel candidate alloys for use as first wall and blanket structural materials in fusion reactors. They will be irradiated with mixed-spectrum neutrons and with spectral tailoring to achieve helium-to-displacement-per-atom (He/dpa) ratios predicted for fusion reactor service.

2.8.3 Summary

The design of all eight capsules HFIR-JP-1 through -JP-8 is completed, and the parts for four capsules have been made. Two capsules have been assembled and are now being irradiated. nesign of the ORR capsule to operate at 60 and 200°C, designated ORR-MFE-6J, is complete, and parts procurement for a proof-of-design capsule is in progress.

2.8.4 Progress and Status

2.R.4.1 Irradiation Experiments for the HFIR

The HFIR-JP experiments consist of eight irradiation capsules designed to evaluate the tensile, fatigue, and microstructural properties of austenitic stainless steels. These capsules are to be irradiated in the HFIR target region in positions adjacent to the PTP positions.

Thermal design and associated engineering drawings of all capsules were completed. Parts were fabricated for the first four experiments. Two capsules have been assembled and are presently being irradiated. Assembly of two additional capsules is in progress. Irradiation of these capsules is expected to begin in May 1984.

2.8.4.2 Irradiation Experiments for the ORR

The U.S./Japan collaborative irradiation program in the ORR consists of two spectral tailored capsules to irradiate materials specimens at 60, 200, 300, and 400°C. The 300 and 400°C irradiations will be carried out in an irradiation capsule (ORR-MFE-7J) similar in design to that of the ORR-MFE-4A irradiation capsule. The only significant difference is in the length of the specimen test region, which is to be increased to 24 cm (9.5 in.) from 15.2 cm (6 in.) to accommodate the larger specimen complement. The design inodification is to be done in the last quarter of FY 1984. However, a number of parts that are identical to those of ORR-MFE-4A have already been fabricated for the capsule. Irradiation is scheduled to begin in March 1985.

The 60 to 200°C capsule, designated ORR-MFE-6J, has been designed, and parts procurement is in progress for a proof-of-design "dummy" capsule to be irradiated early in the fourth quarter of FY 1983. The irradiation of the real ORR-MFE-6J capsule is scheduled to begin in July 1985.

The ORR-MFE-6J capsule is, in effect, two independent capsules in a concentric geometry, with the outer uninstrumented capsule at 60°C and the inner instrumented capsule at 200°C. The outer 60°C assembly consists of a stainless steel cylinder with a reactor water coolant annulus over both the inner and outer surfaces. The test specimens occupy a 24-cm-long region of the cylinder centered around the peak flux (7.6 cm below the ORR midplane). The specimen region of the cylinder has vertical grooves in which the test specimens are positioned. The speciinens are held in place by a thin stainless steel sheath, which slips over the specimen region to cover the grooves. The grooves extend beyond the sheath at both ends to provide access for reactor coolant water in direct contact with, and at the same temperatures as, the reactor coolant water.

The inner (200°C) capsule consists of a singly contained vessel in which the specimens are supported in an aluminum cylinder, which provides for both specimen support and heat removal. The aluminum cylinder has close fitting cavities machined into it, in which the specimens and thermocouples will be positioned.

The aluminum cylinder is contained within a water-cooled thin-wall stainless steel vessel on the outer surface and by a reentrant coolant tube that penetrates the inner wall of the assembly for heat removal. Gas gaps containing helium-argon gas mixtures for temperature control are provided between both the inner and outer water-cooled surfaces.

2.9 THE U.S./JAPAN COLLABORATIVE TESTING PROGRAM IN HFIR AND ORR: IRRADIATION MATRICES FOR HFIR IRRADIATION — A. F. Rowcliffe, M. L. Grossbeck (Oak Ridge National Laboratory), and S. Jitsukawa (Japan Atomic Energy Research Institute)

2.9.1 ADIP Task

ADIP Task I.A.2, Define Test Matrices and Test Procedures.

2.9.2 Objective

The objective of this program is to investigate the behavior and properties of Japanese and U.S. structural alloys after irradiation in the mixed-spectrum fission reactors, the High Flux Isotope Reactor (HFIR) and the Oak Ridge Research Reactor (ORR).

2.9.3 Summary

The first four capsules in the U.S./Japan collaborative program are currently being irradiated in HFIR. The general objectives of the experiments are outlined and the detailed loading of each capsule described.

2.9.4 Progress and Status

The U.S./Japan collaborative agreement' calls for eight HFIR capsules to be built in FY 84 with space equally shared between the two participants. This contribution describes the objectives of the experiments, the overall test matrix, and the detailed loading of the four capsules that have been inserted into HFIK.

2.9.4.1 General Description of HFIR Experiments

The primary objective of the experiments for both the United States and Japan is to determine the tensile. fatigue, and swelling properties of titanium-modified austenitic stainless steels under conditions of moderate levels of displacement damage and high rates of helium generation. Major emphasis is placed on the behavior of the Path A prime candidate alloys [PCA and Japanese PCA (JPCA)]. In addition, the swelling and microstructural behavior of a range of PCA variants will be studied. When space is available, disk specimens of other alloys types (e.g., ferritic alloys) will also he included.

The tensile properties of the U.S. PCA were determined recently following irradiation in HFIR to 22 dpa (Sect. 6.1 of this report). The U.S./Japan series of irradiations will enable this data base to be extended to 30 and to 50 dpa. Information on helium effects will be obtained hy comparison with identical tensile specimens recently inserted into the Fast Flux Test Facility (FFTF) Materials Open Test Assembly (MOTA) above-core basket.

The U.S. fatigue specimens are divided between PCA and the reference heat of type 31h stainless steel (X15893). The latter are included to allow completion of a matrix of fatigue tests at 30 dpa, which was initiated with the earlier HFIR-CTR-36 experiment. By combining the HFIR-CTR-36 specimens with the specimens in the HFIR-JP capsules, we will obtain a total of five specimens at 430°C and four specimens at 550°C irradiated to 30 dpa. The HFIR-JP capsules will provide a further three specimens at 430°C irradiated to 50 dpa. The combined PCA fatigue specimen matrix is also of limited scope and consists of four Specimens at 430°C and five specimens at 500°C irradiated to 30 dpa. There will be only three specimens irradiated to 50 dpa at 430°C. In the Japanese program, the tensile and fatigue specimens in capsules HFIR-JP-1, -JP-2, and -JP-3 are devoted entirely to the JPCA, and these experiments will provide the first neutron irradiation data on this material. The distributions of speciinens at each temperature and damage level are shown in Table 2.9.1.

Each capsule contains one disk packet containing 60 to 70 transmission electron microscopy (TEM) disks divided equally between the two programs. In the U.S. program, the TEM disk packets are being used to explore the precipitation and swelling behavior and bend ductility of a range of PCA compositional variants. These compositions (Table 2.9.2) have been selected to explore recently developed ideas on extending the low-swelling transient regime. Following HFIR irradiation to 30 dpa to build up helium levels, it is planned to continue irradiating the most promising compositions in FFTF to achieve total doses in excess of 100 dpa. Capsules HFIK-JP-I and -JP-2 also contain disks of alloys provided by the DAFS program (H. R. Brager, HEDL). Details of these alloys will be provided in the next progress report. For Japan, 5ix different alloys are being irradiated in the form of TEM disks. Two different heats of JPCA are being evaluated together with two low-carbon austenitic alloys. Also included is a ferritic alloy of the duplex 9 Cr-2 Mo type doped with approximately 1.4% Ni. The compositions of these alloys are shown in Table 2.9.3.

Capsule HFIR-JP-4 is being irradiated at 55°C and contains sheet tensile specimens (SS-1) and a set of rectanqular strip specimens. The United States program has included tensile specimens of the manganese steel EP-838 (USSR) and specimens of the 12 Cr-1 MoVW (HT9) and 9 Cr-1 MoVNb (T9) ferritic alloys. To study the effects of increasing the heliun qeneration rate, heats of the ferritic steels doped with 2% Ni are also being investigated (Table 2.9.4). In the Japanese program, this capsule is being used to evaluate the irradiation behavior of welds. The SS-1 speciinens have been machined from welded plates of both type 316 stainless steel and JPCA so that the weld zone is in the middle of the qage section.

Table 2.9.1. Distribution of HFIR specimens

Irradiation temperature (°C)	30 dpa			50 dpa		
	Tensile[a]	Fatigue[a]	Disk packet	Tensile[a]	Fatigue[a]	Disk packet
			Specimens for United States			
55	0	0	0	20[b]	0	6[c]
300	2	0	0.5	2	0	0.5
400	3	0	0.5	2	0	0.5
430	0	6	0	0	6	0
500	4	0	0.5	3	0	0.5
550	0	2	0	0	0	0
600	3	0	0.5	2	0	0
TOTALS	12	8	2.0	9	6	1.5
			Specimens for Japan			
55	0	0	0	20[b]	0	8[c]
300	4	0	0.5	3	0	0.5
400	4	0	0.5	3	0	0.5
430	0	6	0	1	4	0
500	4	0	0.5	3	0	0.5
550	0	0	0	0	0	0
600	2	0	0.5	1	0	0
TOTALS	14	6	2.0	11	4	1.5

[a]Rod specimens, identical to those used in previous HFIR experiments, except as noted.

[b]Sheet tensile specimens (SS-1).

[c]Rectangular strips, 42 × 1.5 × 0.25 mm.

Table 2.9.2. Alloy chemistries for U.S. disk specimens in capsules HFIR Jp 1 through Jp 4

Alloy	Content (wt %)[a]														
	Cr	Ni	Mo	Mn	Si	Ti	Nb	V	C	N	P	Co	Cu	B	S
PCA	14.0	16.2	2.3	1.8	0.4	0.24			0.05	0.01	0.01			0.001	0.003
PCA-1	14.0	16.0	2.5	2.1	<0.01	0.13	0.12	<0.01	0.04	0.003	<0.001	<0.01	0.02	<0.001	0.008
PCA-3	14.3	15.8	2.5	2.0	0.4	0.13	0.11	<0.01	0.056	0.005	<0.001	<0.01	0.02	<0.001	0.007
PCA-6	14.0	16.0	2.4	1.9	0.4	0.23	0.01	<0.01	0.083	0.004	<0.001	<0.01	0.02	<0.001	0.007
PCA-8	13.9	16.0	2.7	2.1	<0.01	0.17	0.14	<0.01	0.081	0.007	<0.001	<0.01	0.02	<0.001	0.008
PCA-9	13.8	16.0	2.5	2.0	0.4	0.25	<0.01	<0.01	0.073	0.005	0.03	<0.01	0.02	<0.001	0.007
PCA-10	13.8	15.9	2.5	1.9	0.4	0.3	0.1	0.02	0.04	0.002	0.002	<0.01	0.02	<0.001	0.009
PCA-11	13.8	16.0	2.5	1.9	0.4	0.3	0.1	0.5	0.04	0.002	0.002	<0.01	0.03	<0.001	0.008
PCA-12	13.8	15.9	2.4	1.9	0.4	<0.01	0.47	0.01	0.044	0.004	0.002	0.01	0.02	<0.001	0.008
PCA-13	13.8	15.9	2.5	1.9	0.4	0.3	0.1	0.5	0.063	0.002	0.002	<0.01	0.02	<0.001	0.009
PCA-16	15.9	14.1	2.5	1.9	0.4	0.27	<0.01	0.02	0.051	0.002	0.002	<0.01	0.02	<0.001	0.009
PCA-17	15.8	16.0	2.5	1.9	0.4	0.3	<0.01	0.03	0.047	0.002	0.002	<0.01	0.02	<0.001	0.009
PCA-18	17.6	16.1	2.5	1.9	0.4	0.27	<0.01	0.02	0.044	0.002	0.002	<0.01	0.02	<0.001	0.009
PCA-00	14.0	16.0	2.46	2.0	0.4	0.24	<0.01	0.02	0.056	0.001	0.002	0.01	0.02	<0.001	0.008
PCA-19	13.8	19.9	2.44	2.1	0.44	0.28	0.1	0.5	0.076	0.002	0.030	0.01	0.01	<0.001	0.006
PCA-20	13.8	16.1	2.5	2.1	0.42	0.28	0.1	0.5	0.083	0.006	0.07	0.01	0.01	0.001	0.007
PCA-21	15.8	15.8	2.44	3.4	0.4	0.27	0.1	0.5	0.077	0.006	0.06	<0.01	0.05	0.001	0.007
PCA-22	13.8	15.9	2.4	2.5	0.4	0.28	0.1	0.5	0.078	0.004	0.03	<0.01	0.05	0.003	0.007
EP-838[b]	11–13	4.4–4.8	0.3–0.6	12–14	0.6				0.02	0.05–0.09	0.4			0.0005	0.4
N-lot 316	16.5	13.5	2.5	1.6	0.5				0.05	0.006	0.013			0.0008	0.006
Ref. 316	17.3	12.4	2.1	1.7	0.7		0.08		0.05		0.04	0.35		0.0004	0.015
D0-316	18.0	13.0	2.6	1.9	0.8	0.05			0.05	0.05	0.01	0.004		0.0005	0.016
D9-699	14.2	15.2	1.95	2.1	0.5	0.23	0.01	0.02	0.033	0.004	0.005	0.02	0.02	<0.001	0.001
D9-697	14.4	16.2	1.5	1.9	0.5	0.25	<0.01	0.02	0.035	0.009	0.003	0.03	0.02	0.0001	0.002
D9-A7	13.7	16.3	2.5	2.0	1.42	0.18	0.01	0.023	0.045	0.011	0.075	0.06	0.00	0.0005	0.017

[a]Balance iron.

[b]This alloy also contains approximately 1% Al.

Table 2.9.3. Alloy chemistries for Japanese disk specimens in capsules HFIR-JP-1 through -JP-4

Alloy	Content (wt %)												
	C	Si	Mn	P	S	Ni	Cr	Mo	Ti	Nb	B	N	Co
JPCA	0.06	0.50	1.77	0.027	0.005	15.60	14.22	2.28	0.24		0.0031	0.0039	0.002
JPCA(QS)	0.06	0.53	1.79	0.027	0.009	16.22	14.51	2.37	0.20		0.0035	0.009	0.025
C	0.02	0.51	1.56	0.017	0.007	15.6	15.4	2.4	0.25	0.08		0.0018	
K	0.02	0.48	1.46	0.015	0.005	17.56	17.99	2.6	0.29			0.004	
Type 316	0.058	0.61	1.80	0.028	0.003	13.52	16.75	2.46	0.005	<0.1			<0.1
Ferritic steel[a]	0.056	0.74	0.70	0.008	0.0059	1.37	8.86	2.46		0.06		0.0069	

[a]Also Al, 0.04; V, 0.11; Cu, 0.02; W, 0.01.

Table 2.9.4. Alloy chemistries for tensile and fatigue specimens in capsules HFIR-JP-1 through -JP-4

Alloy	Heat	Content (wt %)[a]															
		Cr	Ni	Mo	Mn	Si	Ti	Nb	V	C	N	P	Co	Cu	B	S	W
U.S. PCA	K-280	14.0	16.2	2.3	1.8	0.4	0.24			0.05	0.01	0.01			0.0001	0.003	
JPCA		14.22	15.60	2.28	1.77	0.50	0.24			0.06	0.004	0.027	0.002		0.0003	0.005	
Ref. 316	X15893	17.3	12.4	2.1	1.7	0.70		0.08		0.05		0.04	0.35		0.0004	0.015	
J316		16.75	13.52	2.46	1.80	0.61	0.005			0.058		0.028	<0.1			0.003	
EP-838 (USSR)		12.0	4.6	0.4	13.0	0.6				0.02	0.08	0.4			0.0005	0.4	
HT9	XAA3587	11.99	0.43	0.93	0.50	0.18	0.003	0.008	0.27	0.21	0.020	0.011	0.017	0.05	<0.001	0.004	0.54
HT9–2 Ni	XAA3589	11.71	2.27	1.02	0.49	0.14	0.003	0.007	0.31	0.20	0.017	0.011	0.021	0.05	<0.001	0.004	0.54
T9 Mod	XA3590	8.62	0.11	0.98	0.36	0.08	0.002	0.063	0.21	0.10	0.050	0.008	0.013	0.03	<0.001	0.004	0.01
T9 Mod–2 Ni	XA3591	8.57	2.17	0.98	0.36	0.08	0.002	0.066	0.22	0.09	0.053	0.008	0.015	0.04	<0.001	0.004	0.01

[a]Balance iron

Detailed loading lists for capsules HFIR-JP-1 through -JP-4 are presented in Tables 2.9.5 and 2.9.6. The compositions of both the U.S. and Japanese alloys used for the fatigue and tensile specimens are shown in Table 2.9.4. The codes used to designate thermal mechanical conditions are explained in Table 2.9.7.

Table 2.9.5. Loading list for capsules HFIR-JP-1, -JP-2, and -JP-3[a]

Level	Specimen type	Temperature (°C)	Alloy	Condition	Identification		
					HFIR-JP-1	HFIR-JP-2	HFIR-JP-3
1	Tensile	300	PCA	83	EL15	EL36	EL30
2	Tensile	400	PCA	83	EL21	EL37	EL34
3	Tensile	500	PCA	83	EL28	EL39	EC29
4	Fatigue	430	PCA[b]	A3[b]	AA1	EC157	EC152
5	Fatigue	430	Ref. 316	20% cold worked	AA2	AA3	AAR
6	TEM	c	c	c	c	c	c
7	Fatigue	430	JPCA	PC2	FE1	FE3	FE5
8	Fatigue	430	JPCA	PC2	FE2	FE4	FE6
9	Tensile	500	JPCA	PS2	TB1	TB4	TB7
10	Tensile	400	JPCA	PS2	TB2	TB5	TB8
11	Tensile	300	JPCA	PS2	TE1	TB6	TB9

[a]Capsules HFIK-JP-I and -JP-3 irradiated to 30 dpa; HFIR-JP-2 irradiated to 50 dpa.

[b]Reference heat type 316 20% cold worked in HFIR-JP-1.

[c]Capsules HFIR-JP-1 and -JP-2 at 300°C; HFIR-JP-3 at 400°C. See also Tables 2.9.2 and 2.9.3.

Table 2.9.6. Loading list for capsule HFIR-JP-4 (50 dpa)

Level	Specimen	Temperature (°C)	Alloy	Condition	Identification
1	SS-1 Tensile	55	Ref. 31h	20% CW	AB-41, -42. -45
			EP-83R	20% CW	EP05
2	SS-1 Tensile	55	EP-838	20% CW	EP06, EP10
			PCA	83	ELD, EL2
3	SS-1 Tensile	55	PCA	A3	EC284
			PCA20	25% CW	HV01
			PCA13	25% CW	HA1
			PCA19	25% CW	HT01
4	SS-1 Tensile	55	T9 Mod—2 Ni	NT4	TB01
			T9 Mod-2 Ni	NT4	TB02
			HT9	NT1	SB2
			HT9	NT1	SB3
5	SS-1 Tensile	55	HT9—2 Ni	NT2	SD01
			HT9—2 Ni	NT2	SD02
			T9 Mod	NT3	TA01
			T9 Mod	NT3	TA04
6	a	55	(Various)		
7	SS-1 Tensile	55	J316	15% CW weld	D-46, -47, -4R
			J316	SA weld	D-16
R	SS-1 Tensile	55	J316	SA weld	D-17, -18
			JPCP	SA weld	CLW-1, -2
9	SS-1 Tensile	55	JPCA	SA weld	CLW-3
			JPCA	CW weld	DLW-1, -2, -3
10	SS-1 Tensile	55	J316	SA	D-1, -2
			J316	CW	D-31, -32
11	SS-1 Tensile	55	JPCA	SA	CL-1, -2
			JPCA	CW	DL-1, -2

[a]Fourteen strip specimens 42 × 1.5 × 0.25 mm.

Table 2.9.7. Thermal-mechanical treatment codes

Code	Alloy	Final alloy condition
PS-1	JPCA	Solution annealed 1175°C
PS-2	JPCA	Solution annealed 1100°C
PS-3	JPCA	Solution annealed 1050°C
PC-1	JPCA	Solution annealed 1100°C + 10% cold worked
PC-2	JPCA	Solution annealed 1100°C + 15% cold worked
PC-3	JPCA	Solution annealed 1100°C + 20% cold worked
A0	U.S. PCA	Solution annealed 1050°C/1 h
A1	U.S. PCA	Solution annealed 1100°C/0.5 h
A3	U.S. PCA	A1 treatment + 25% cold worked
B3	U.S. PCA	A1 treatment + 800°C/8 h + 25% cold worked
NT-1	U.S. ferritic alloys	Normalized 1050°C/0.5 h, tempered 780°C/2.5 h
NT-2	U.S. ferritic alloys	Normalized 1050°C/0.5 h, tempered 700°C/5 h
NT-3	U.S. ferritic alloys	Normalized 1040°C/0.5 h, tempered 760°C/1 h
NT-4	U.S. ferritic alloys	Normalized 1040°C/0.5 h tempered 700°C/5 h

2.9.4.2 Current Status

The first four capsules HFIR-JP-1 through -JP-4 were all inserted into HFIR on schedule and are operating satisfactorily. Specimens are being readied for capsules HFIR-JP-5 and -JP-6, which are due for insertion in August 1984, and for HFIR-JP-7 and -JP-8, which will commence irradiation in January 1985. Details of these capsules will be presented in the next report.

2.9.4.3 Reference

1. Annex I to the Implementing Arrangement between the Japan Atomic Energy Research Institute and the United States Department of Energy on Cooperation in Fusion Research and Development (November 1983).

3. PATH A ALLOY DEVELOPMENT — AUSTENITIC STAINLESS STEELS

3.1 EFFECT OF THE MICROSTRUCTURE ON POSTIRRADIATION TENSILE PROPERTIES OF TYPE 316 STAINLESS STEEL – R. L. Klueh (Oak Ridge National Laboratory)

3.1.1 AOIP Task

AOIP Task I.B.13, Tensile Properties of Austenitic Alloys.

3.1.2 Objective

The objective of this study is the determination of the effect of microstructure on the tensile properties of irradiated type 316 stainless steel. The test material was given different levels of cold work and different heat treatments before irradiation in the Oak Ridge Research Reactor (ORR).

3.1.3 Summary

Tensile specimens of type 316 stainless steel were given different solution-anneal heat treatments and irradiated in the ORR at 250, 290, 450, and 500°C to a fast neutron fluence of about 6.8 × 10^{25} neutrons/m^2 (–5 dpa and 40 at. ppm He). The tensile properties were determined at the irradiation temperatures for steel solution annealed 1 h at 1050°C, 1 h at 1150°C, and 1 h at 1050°C followed by 10 h at 800°C.

3.1.4 Progress and Status

3.1.4.1 Introduction

The present study is part of an investigation to determine the effect of the preirradiation microstructure of type 316 stainless steel on tensile properties. Specimens with three cold-work levels and three different solution-annealed conditions were irradiated in the ORR. The effect of cold work was previously reported.' In this report, the type 316 stainless steel given the different solution-anneal treatments will be discussed.

3.1.4.2 Experimental Procedure

The type 316 stainless steel used in this study was taken from the Magnetic Fusion Energy (MFE) reference heat (X-15893). The chemical composition (wt %) of this heat is Cr, 17.3; Mn, 1.7; P, 0.03; Ni, 12.4; Si, 0.7: S, 0.015; Mo, 2.2: C, 0.05; B, 0.0004; Co, 0.35; and Fe, bal.

Tensile specimens were machined from 0.76-mm-thick sheet. Three solution-annealed conditions were irradiated and tested: 1 h at 1050°C, 1 h at 1150°C, and 1 h at 1050°C followed by 10 h at 800°C.

Sheet tensile specimens in this experiment were of the SS-1 type with a reduced gage section 20.3 mm long by 1.52 mm wide by 0.76 mm thick (Fig. 3.1.1). Specimens were irradiated in the E-7 position of the ORR in experiment ORR-MFE-2. These specimens were irradiated in holders that contained 22 sheet samples. The cylindrical holders were contained in a water-cooled aluminum block: each holder contained a central hole that contained an electric heater. Temperature was measured and controlled by two thermocouples located at the position of the center of the gage section in two unused sample positions located 180° apart.

ORNL-DWG 78-7701R1

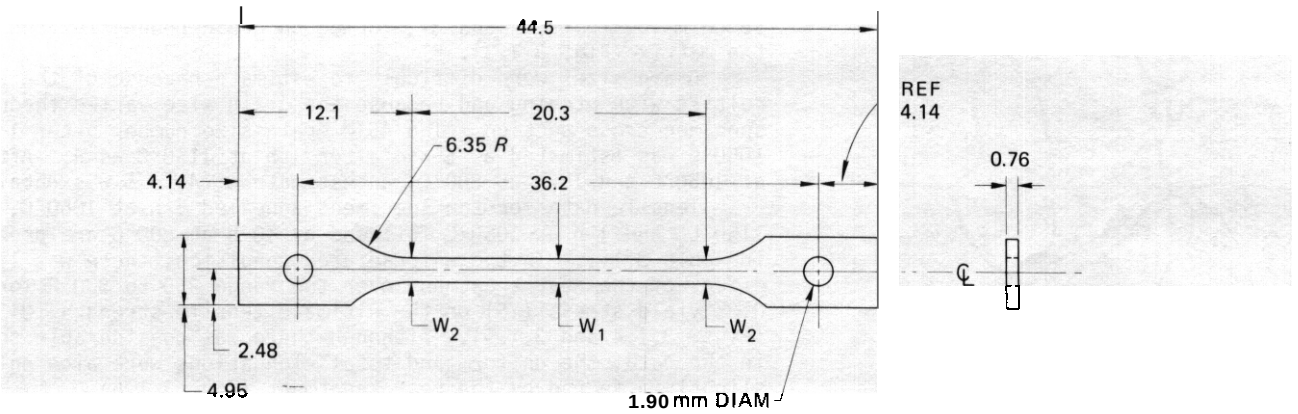

W_1 = 1.52 mm
W_2 = 0.025 TO 0.038 mm
GREATER THAN W_1

DIMENSIONS IN MILLIMETERS

Fig. 3.1.1. The SS-1 type tensile specimen,

Irradiation temperatures obtained in this experiment were approximately 250, 290, 450, and 500°C. The neutron fluence of approximately 6.8 × 10^{25} neutrons/m^2 (>0.1 MeV) produced approximately 5 dpa and approximately 40 at. ppm He.

Tensile tests were made on unirradiated and irradiated specimens at the irradiation temperatures. Tests were conducted in a vacuum chamber on a 44-kN capacity Instron universal test machine at a strain rate of 4.2 × 10^{-5}/s.

3.1.4.3 Results and Discussion

The microstructures after the different solution-anneal heat treatments are shown in Figs. 3.1.2 and 3.1.3. The steels given only the elevated-temperature solution treatment were difficult to etch, and differential-interference microscopy was used to make the grain structure more easily visible (Fig. 3.1.2).

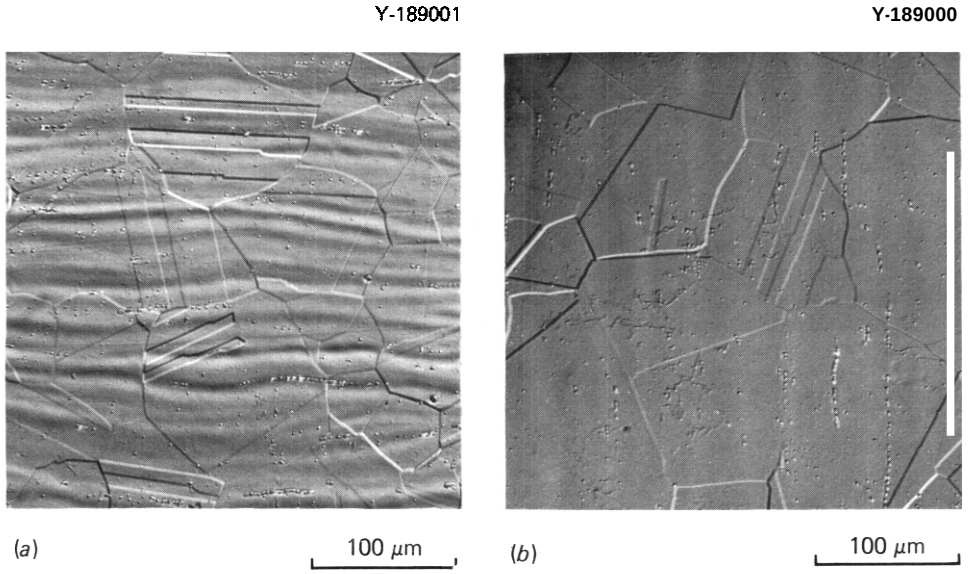

Fig. 3.1.2. Microstructure of type 316 stainless steel solution annealed 1 h at (*a*) 1050°C and (*b*) 1150°C. Differential-interfence microscopy was used to show the grain size.

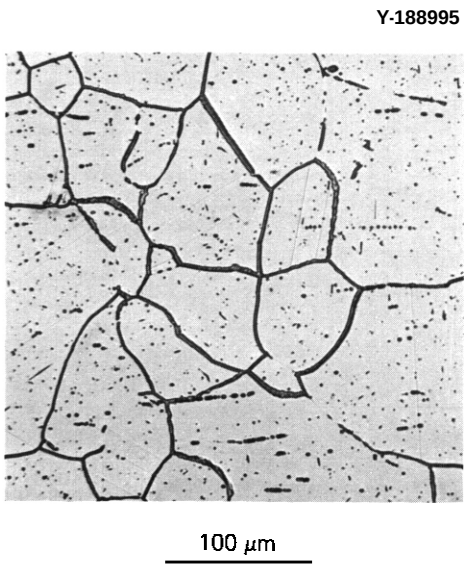

Fig. 3.1.3. Microstructure of type 316 stainless steel solution annealed 1 h at 1050°C and then further annealed 10 h at 800°C.

After a solution anneal of 1 h at 1050 or 1150°C, the microstructures have relatively clean grain boundaries, and only a few large precipitates are scattered through the matrix (Fig. 3.1.2). When the solution anneal for 1 h at 1050°C was followed by the anneal for 10 h at 800°C, considerable precipitate, which is taken to he $M_{23}C_6$ (refs. 2 and 3), formed on arain boundaries and within the matrix (Fig. 3.1.3).

Grain sizes were difficult to estimate because of the difficulties with etching and because the grain size varied through the specimen cross section. The ASTM grain size number after 1 h at 1050°C was estimated as 5 and after 1 h at 1150°C as 4. After 1 h at 1050°C and 10 h at 800°C, an estimate of 4 to 5 was obtained.

Tensile data for the specimens annealed 1 h at 1050°C, 1 h at 1150°C, and 1 h at 1050°C followed hy 10 h at 800°C are presented in Table 3.1.1. In the unirradiated condition, there was little effect of the heat treatment over the range 250 to 500°C for the 0.2% yield stress (YS) or the ultimate tensile strength (UTS) (Figs. 3.1.4 and 3.1.5). Although there was considerable scatter in the data, the uniform and total elongations were also only slightly affected by the heat treatment (Fig. 3.1.6).

After irradiation, the YS values of all three materials were above the unirradiated values at all test temperatures (Fig. 3.1.4). The most hardening occurred at 250 and 290°C, followed by a large decrease in the irradiated strength at the higher irradiation and test temperatures.

For the UTS after irradiation (Fig. 3.1.5), a large increase over the unirradiated strength was again observed at 250 and 290°C; the strength decreased rapidly with increasing irradiation

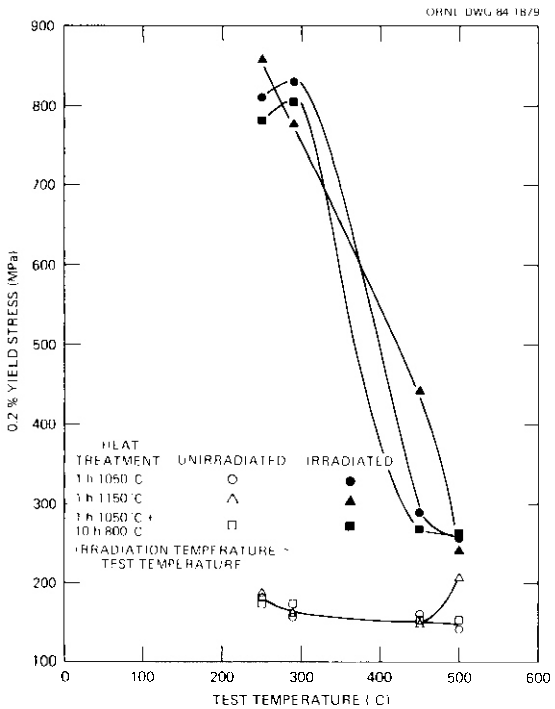

Fig. 3.1.4. The 0.2% yield stress of unirradiated and irradiated solution-annealed type 316 stainless steel. Irradiations were at test temperatures to approximately 5 dpa and 40 at. ppm He.

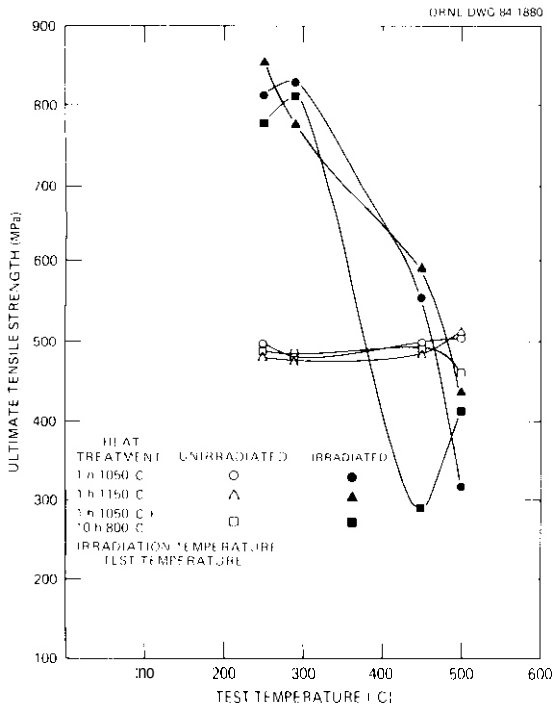

Fig. 3.1.5. The ultimate tensile strength of unirradiated and irradiated solution-annealed type 316 stainless steel. Irradiations were at test temperatures to approximately 5 dpa and 40 at. ppm He.

Table 3.1.1. Tensile properties of unirradiated and irradiated solution-annealed type 316 stainless steel (heat X-15893)

Temperature (°C)		Strength (MPa)		Elongation (%)	
Test	Irradiation	Yield	Ultimate	Uniform	Total
Solution anneal 1 h at 1050°C					
250	250	812	812	0.2	9.8
250		181	496	35.0	31.8
290	291)	830	830	0.2	1.5
290		157	479	36.5	38.8
450	450	288	556	22.5	24.3
450		161	499	40.4	47.6
500	500	255	315	2.8	4.4
500		143	503	39.4	43.1
Solution anneal 1 k at 1150°C					
250	250	851	857	0.1	5.3
250		183	481	36.7	39.9
290	290	717	717	3.9	6.1
290		160	475	33.1	35.3
450	450	441	591	11.1	13.5
450		148	486	39.0	42.8
500	500	241	436	19.5	21.9
500		206	514	26.3	29.5
.Solution anneal 1 h at 1050°C + 10 h at 800°C					
250	250	778	778	0.2	6.4
250		115	487	36.6	38.1
290	290	806	812	0.1	5.1
290		177	419	29.8	30.1
450	450	268	287	0.5	I.R
450		151	494	38.6	40.1
500	500	264	413	13.5	13.8
500		153	460	32.0	35.0

temperature above 290°C. As opposed to the YS behavior, the UTS for the irradiated materials fell below the UTS of the unirradiated material at the highest test temperature (500°C). The UTS of the steel given the 10 h at 1100°C was less than that of the unirradiated steel at both 450 and 500°C. In addition, the strength at 500°C for this heat treatment exceeded that at 450°C. The behavior of this steel at 450°C is the only indication of a strength difference for the three different heat treatments. Because only one specimen was available for each test condition, it is difficult to document the meaning of this observation. Without the test at 450°C, the UTS behavior of the steel given the 10 h at 800°C anneal would be similar to that for the steel given the other two heat treatments.

The observations on uniform and total elongation after irradiation indicated slight differences for the three steels (Fig. 3.1.6). The total elongations of all three materials were similar at 250 and 290°C. The steels with solution-anneal treatments of 1 h at 1050°C and 1 h at 1150°C both had higher ductility at 450°C than at the lower temperatures. Between 450 and 500°C, the trend in the ductility for these two steels diverged. The total elongation of the steel given the 1 h at 1050°C decreased to less than 5% at 500°C, while that for the specimen with 1 h at 1150°C increased further to greater than 21%. The trend for the ductility for the specimens with the 800°C anneal showed

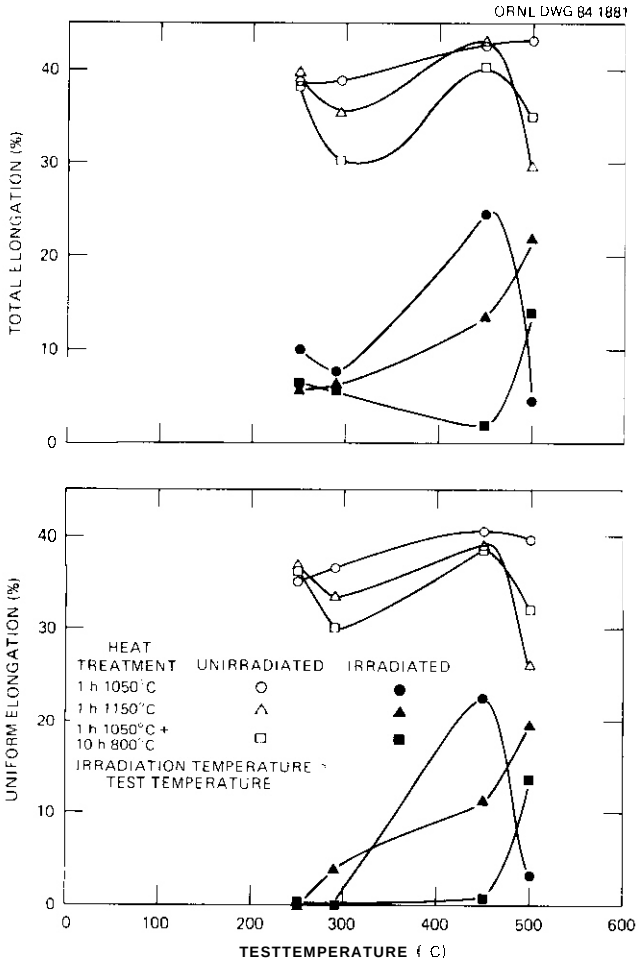

Fig. 3.1.6. The uniform and total elongations of unirradiated and irradiated solution-annealed type 316 stainless steel. Irradiations were at test temperatures to approximately 5 dpa and 40 at. ppn He.

a small decrease between 250 and 450°C and then an increase between 450 and 500°C. Because of the large scatter that is often observed in ductility data, such trends must be treated with considerable caution.

Scanning electron microscopy (SEM) observations, showed that the specimen annealed 1 h at 1050°C and irradiated and tested at 500°C fractured intergranularly [Fig. 3.1.7(*a*)]. This contrasted with a completely transgranular failure for the control specimen tested at 500°C [Fig. 3.1.7(*b*)] and the control and irradiated specimens at the other temperatures. Figure 3.1.7(*c*) shows the irradiated specimen tested at 250°C; this specimen displayed a large amount of hardening and a fairly low ductility (Table 3.1.1), hut, nevertheless, a ductile fracture.

The specimens annealed 1 h at 1150°C also developed ductile fractures. At 500°C, there was a slight amount of intergranular separation on the fracture surface, hut over 90% of the fracture surface was transgranular (Fig. 3.1.8). The ductility behavior of the steel solution annealed at 1050°C and then annealed 10 h at 800°C was similar to the behavior of the steel solution annealed at 1150°C.

Most of the previous tensile studies on irradiated type 316 stainless steel have been on 20%-cold-worked material. Of the studies on solution-annealed steel,[4-6] the most detailed appears to he that of Fish and Holmes,' who studied the postirradiation tensile properties after EBR-II irraiation up to a maximum fluence of 7×10^{26} neutrons/m^2 (>0.1 MeV) at 430 to 820°C. This irradiation resulted in a maximum of 35 to 40 dpa and 15 to 20 at. ppm He. The solution anneal was 1 h at 1065°C, which resulted in an ASTM grain size number of 5 through 6. Specimens irradiated and tested at 430, 480, and 540°C (temperatures similar to those used in the present study) were irradiated to maximum fluences of only up to ahout one-half of the maximum fluence, thus considerably decreasing the displacement damage and the amount of helium produced.[4]

The results from the present tests are in excellent Qualitative aoreement with the Fish and Holmes results.[4] For temperatures up to 700°C, irradiation caused an increase in YS (ref. 4). The UTS was increased by irradiation only at 430 and 480°C, and not at 540°C and higher.[4] In the present tests. the YS also increased at all temperatures, whereas the UTS increased at the three lower temperatures, hut decreased at 500°C (the only exception was the UTS for the test at 450°C of the steel given the 800°C anneal).

Fish and Holmes found that the total elongation became a function of the helium concentration at 540°C and that failure was initiated by grain boundary fracture.' In those ERR-I1 studies, there was probahly less than 20 at. ppm He present, compared with about 40 at. ppm in the present experiment. Fish and Holmes concluded that at 540°C or higher the helium is able to start collecting at grain boundaries by diffusion, and this helium can then assist grain boundary separation during deformation.' The loss of ductility accompanied by a change in fracture mode at 500°C in the present study for the steel solution-annealed at 1050°C appears similar to the Fish and Holmes observations and is attributed to helium embrittlement.

The major difficulty with the ahove hypothesis is that helium embrittlement is generally not felt to be a problem below $0.6T_m$ (650–700°C for type 316 stainless steel),[5] althouqh for high helium contents, nmbrittlement at temperatures as low as 550°C is thought possible.[6] It is generally not helieved to occur as low as 500°C. However, most helium-embrittlement studies have heen conducted above approximatedly 600°C. Furthermore, most studies on type 316 stainless steel have heen on 20%-cold-worked material.

No explanation is readily available for why a specimen solution annealed at 1050°C would exhibit helium enbrittlement at 500°C and one solution annealed at 1150°C would not. The small difference in grain size would not appear to offer an explanation. One possibility night he a difference in precipitate structure that could occur because of different supersaturation conditions produced for material cooled from 1050 and 1150°C (e.g., if complete carbide dissolution did not occur at 1050°C). Transmission electron microscopy studies are planned to examine this possibility. The reason that the specimen annealed 10 h at 800°C after 1 h at 1050°C does not embrittle may De the result of the large amount of grain boundary precipitate observed in this material (Fig. 3.1.3). It has been shown that grain boundary precipitation can inhibit elevated-temperature helium embrittlement.[7]

M-15324

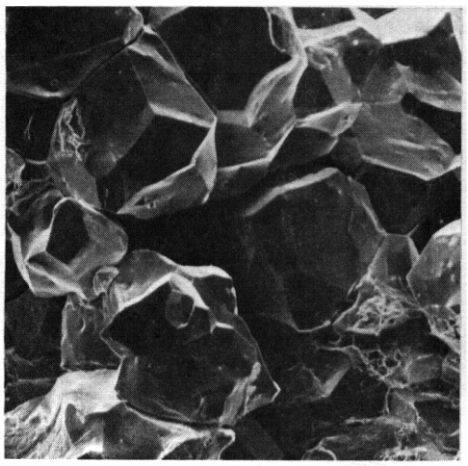

(a) 50 μm

M-15313

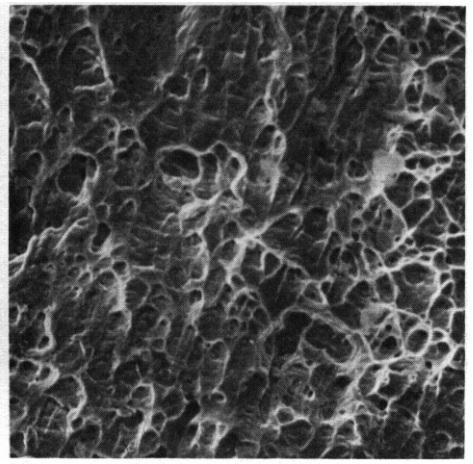

(b) 20 μm

M-15307

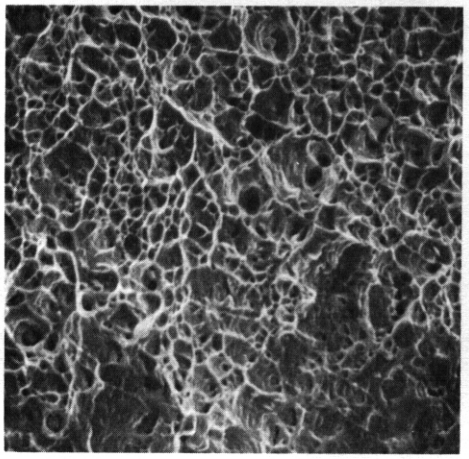

(c) 20 μm

Fig. 3.1.7. Scanning electron micrographs of fracture surface of tensile specimens of type 316 stainless steel annealed 1 h at 1050°C. (a) Irradiated and tested at 500°C, (b) unirradiated and tested at 500°C, and (c) irradiated and tested at 250°C.

M-15293

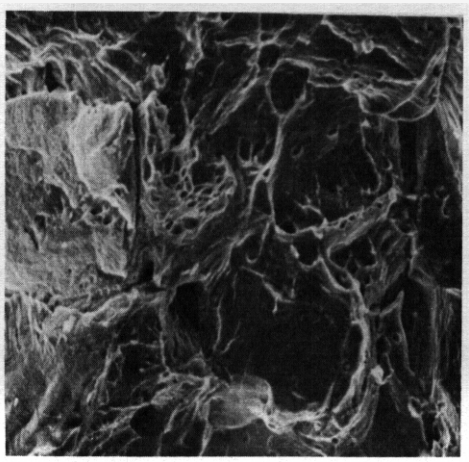

20 μm

Fig. 3.1.8. Scanning electron micrograph of fracture surface of tensile specimen of type 316 stainless steel annealed 1 h at 1150°C and irradiated and tested at 500°C.

The change in uniform elongation with temperature (Fig. 3.1.6) is also similar to that observed by Fish and Holmes.[4] Although they found transgranular fractures below 540°C, low uniform and total elongations were observed — often lower than for specimens in which helium embrittlement occurred. This was explained by stating that, at the lower temperatures, "ductility loss occurs as a result of reduced work hardening which leads to premature plastic instability."[4] Depending on the fluence, Fish and Holmes found that the uniform and total elongations decreased from values near 10% at 540°C to values as low as 0.9% at 430°C (ref. 4). With decreasing temperature, the authors expected the uniform elongation to decrease to a low but constant value, similar to the observations in the present work.

In addition to the agreement with the Fish and Holmes study,[4] there is also qualitative agreement with the work of Fahr, Bloom, and Stiegler' and Bloom and Wiffen.6 However, for those studies there was much less overlap in test conditions, and thus a detailed discussion of those results will not be presented.

Because of the greater resistance of 20%-cold-worked type 316 stainless steel to swelling, the steel in that condition is of most interest for nuclear applications, and that condition has been investigated most extensively after irradiation. The ORR-MFE-2 experiment also contained tensile specimens of type 316 stainless steel with 20, 30, and 50% cold work.' In Figs. 3.1.9 through 3.1.11, the tensile data for the 20%-cold-worked material are compared with the steel solution annealed 1 h at 1050°C.

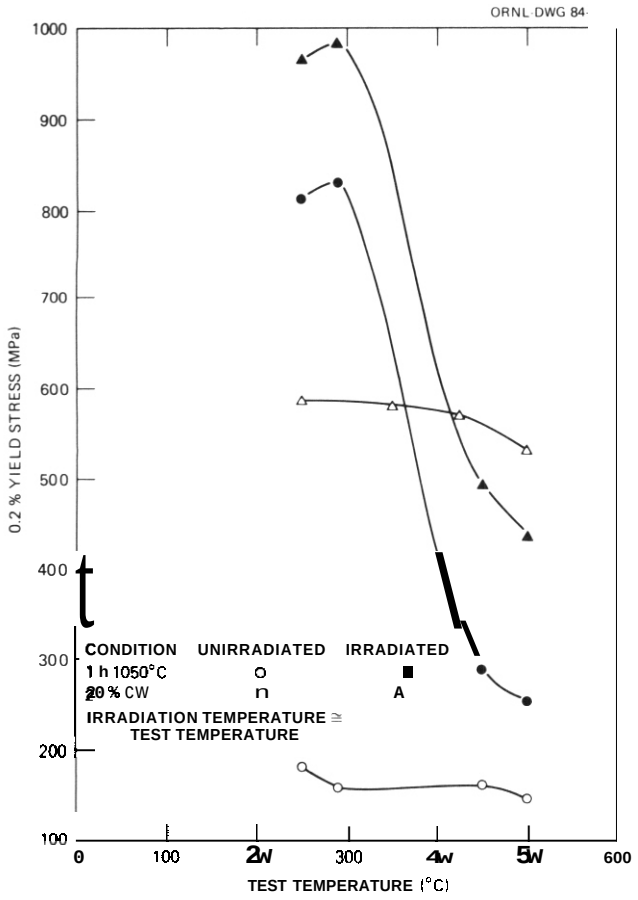

Fig. 3.1.9. The 0.2% yield stress of unirradiated and irradiated solution-annealed (1 h at 1050°C) and 20%-cold-worked type 316 stainless steel. Irradiations were at test temperatures to approximately 5 dpa and 40 at. ppn He.

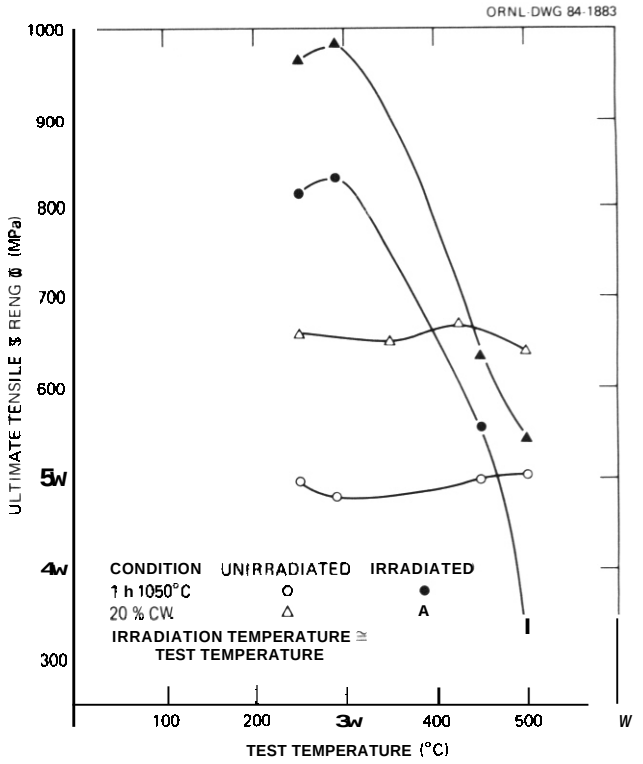

Fig. 3.1.10. The ultimate tensile strength of unirradiated and irradiated solution-annealed (1 h at 1050°C) and 20%-cold-worked type 316 stainless steel. Irradiations were at test temperatures to approximately 5 dpa and 40 at. ppm He.

After irradiation at 250 and 290°C, the YS and UTS of the solution-annealed material showed a greater increase relative to the unirradiated condition than did the YS and UTS for the cold-worked condition. Between 290 and 450°C, the strength of both the cold-worked and the solution-annealed steel in the irradiated condition decreased rapidly with temperature. The YS of the irradiated cold-worked steel became less than that of the unirradiated material, while that of the irradiated solution-annealed steel always remained above that of the unirradiated steel (Fig. 3.1.9). The UTS after irradiation for both conditions became less than the unirradiated values for the 500°C tests. Since at some temperature the cold-worked material will recrystallize, the strengths of the two steels will eventually become equal. However, as seen in Figs. 3.1.9 and 3.1.10, at 500°C there is still a substantial difference in the strength of the Solution-annealed and cold-worked steels before and after irradiation.

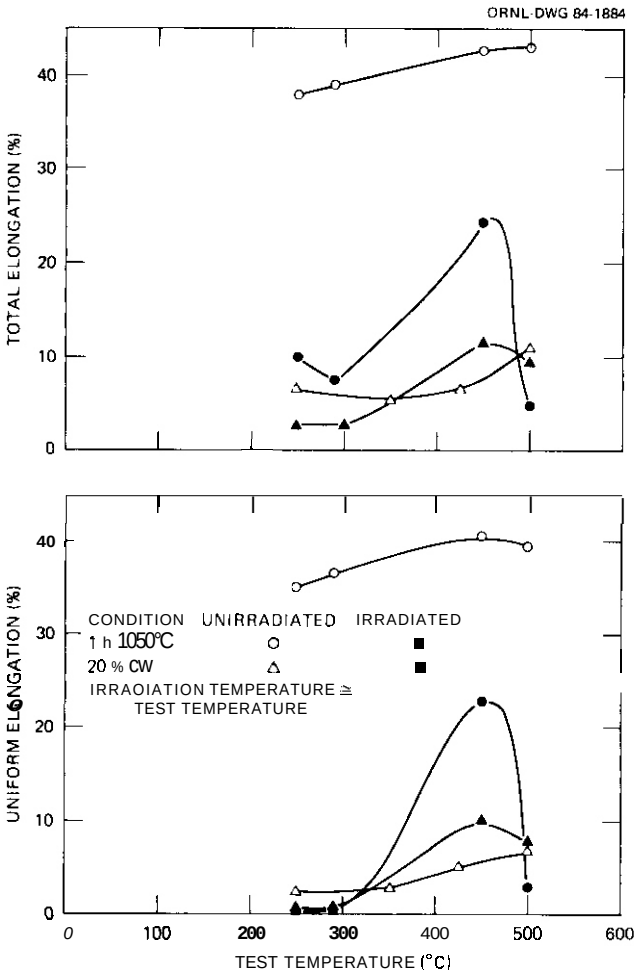

Fig. 3.1.11. The uniform and total elongations of unirradiated and irradiated solution-annealed (1 h at 1050°C) and 20%-cold-worked type 316 stainless steel. Irradiations were at test temperatures to approximately 5 dpa and 40 at. ppm He.

If the loss of ductility for the steel solution-annealed at 1050°C is attributed to helium embrittlement, as postulated above, Fig. 3.1.11 is an indication of the difference in the propensity of solution-annealed and cold-worked type 316 stainless steel toward helium embrittlement at 500°C. The cold-worked specimen irradiated at 500°C shows little change in ductility over the unirradiated specimen, and it failed in a ductile. transgranular mode.

Summary and Conclusions

A series of solution-annealed type 316 stainless steel tensile specimens was irradiated in ORR at 250, 290, 450, and 500°C to a neutron fluence of approximately 6.8×10^{25} neutrons/m^2 (>0.1 MeV). This produced a displacement damage of approximately 5 dpa and 40 at. ppm He. Specimens with three different heat treatments were irradiated and tested 1 h at 1050°C, 1 h at 1150°C, and 1 h at 1050°C followed by 10 h at 800°C. Unirradiated and irradiated tensile properties were determined. The following is a summary of the observations and conclusions.

1. The microstructures of the steels annealed at 1050 and 1150°C were relatively precipitate-free, with the major difference in the two steels being a slight difference in the grain size. The steel with the extra 10 h at 800°C had considerable precipitate on the grain boundaries.

2. At all irradiation temperatures, irradiation increased the YS for each heat treatment over the YS of the unirradiated condition. The relative increase became smaller with increasing irradiation temperature. The UTS was increased by irradiation for all but the specimens tested at 500°C for the steels annealed 1 h at 1050 and 1150°C, and all but 450 and 500°C for the steel given the extra 10 h at 800°C.

3. The uniform and total elongations of the irradiation-hardened steels were lowest at the lowest irradiation temperatures, where hardening was the greatest. With the exception of the steel given the 1 h at 1050°C anneal, the ductility increased with increasing temperature (decreasing strength). The ductility of the steel annealed 1 h at 1050°C went through a maximum, with the ductility smaller at 500°C than at 450°C. The loss of ductility, which was attributed to the helium enbrittlement, was accompanied by a change from transgranular to intergranular fracture.

3.1.6 References

1. R. L. Klueh, "Effect of the Microstructure on Tensile Properties of Type 316 Stainless Steel," pp. 55-59 in *ADIP Semiannu. Prog. Rep. Mar. 31, 1883,* DOE/ER-0045/10, U.S. DOE, Office of Fusion Energy.

2. B. Weiss and R. Stickler, "Phase Instabilities During High Temperature Exposure of 316 Austenitic Stainless Steel," *Metall. Trans.* 3, 851–66 (1972).

3. P. J. Maziasz, "Precipitation Response of Austenitic Stainless Steel to Simulated Fusion Irradiation," pp. 160–80 in *The Metal Science of Stainless Steels,* AIME, New York, 1978.

4. R. L. Fish and J. J. Holmes, "Tensile Properties of Annealed Type 316 Stainless Steel After EBR-II Irradiation," *J. Nucl. Mater.* **46**, 113–20 (1973).

5. O. Fahr, E. E. Bloom, and J. O. Stiegler, "Post-Irradiation Tensile Properties of Annealed and Cold Worked Type 316 Stainless Steel," pp. 167–77 in *Irradiation Embrittlement and Creep in Fuel Cladding and Core Components,* British Nuclear Energy Society, London, 1973.

6. E. E. Rloom and F. W. Wiffen, "The Effects of Large Concentrations of Helium on the Mechanical Properties of Neutron-Irradiated Stainless Steel," *J. Nucl. Mater. 58,* 171–84 (1975).

7. P. J. Maziasz and T. K. Roche, "Preirradiation Microstructural Development Designed to Minimize Properties Degradation During Irradiation of Austenitic Alloys," *J. Nucl. Mater.* 104, 797–802 (1982).

3.2 IRRADIATION CREEP IN PATH A ALLOYS IRRADIATED TO 5 dpa IN THE ORR-MFE-4B SPECTRAL TAILORING EXPERIMENT AT 500 AND 600°C — M. L. Grossbeck and J. A. Horak (Oak Ridge National Laboratory)

3.2.1 ADIP Task

ADIP Task I.C.6, Irradiation Creep in Austenitic Alloys.

3.2.2 Objective

The experiment will determine irradiation creep in an environment that produces helium with the He:dpa ratio characteristic of a fusion reactor.

3.2.3 Summary

Pressurized tubes of 20%-cold-worked type 316 stainless steel and 25%-cold-worked Prime Candidate Alloy (PCA) were irradiated at 500 and 600°C in the Oak Ridge Research Reactor (ORR) spectral tailoring experiment to 5.1 dpa. Diametral measurements were made to determine irradiation creep rates. Both allovs behaved rather similarly but exhibited lower creep rates than did the Fast Flux Test Facility (FFTF) first core type 316 stainless steel irradiated in EBR-II.

3.2.4 Progress and Status

3.2.4.1 Introduction

The ORR-MFE-4 spectral tailoring experiment has been designed to irradiate path A alloys under conditions producing an He:dpa ratio characteristic of a fusion reactor first wall. This is achieved by tailoring the neutron spectrum by changing the immediate environment of the irradiation capsule as irradiation proceeds. The surrounding region is changed from water to aluminum to hafnium in order to progressively decrease the thermal component of the flux as ^{59}Ni is produced from ^{58}Ni. The nickel produces helium through the reaction sequence

$$^{58}Ni(n,\gamma)^{59}Ni$$

and

$$^{59}Ni(n,\alpha)^{56}Fe \ .$$

At intervals of approximately 10 dpa the capsule is removed from the reactor, the specimens are recovered and either destructively examined or examined and returned to the reconstituted irradiation vehicle. The irradiation creep experiment employs specimens that are measured at each removal interval and then returned for continued fluence accumulation. It will provide data on neutron irradiation creep with internal helium qeneration and displacement damaqe Droduction in the proportion characteristic of the fusion environment. No-previous data of this nature existed prior to this experiment, the first phase of which (330 and 400°C) was previously reported.'

3.2.4.2 Experimental Procedure

Commercially drawn tubing of 4.57-mm (0.180-in.) outside diameter, with 0.25-mm (0.010-in.) wall thickness, was prepared from the fusion program reference type 316 stainless steel, heat X15893, and Path A PCA, heat K-280, in the 20- and 25%-cold-worked conditions, respectively. Specimens of the type shown in Fig. 3.2.1 were prepared and pressurized to the stress levels indicated in Table 3.2.1.

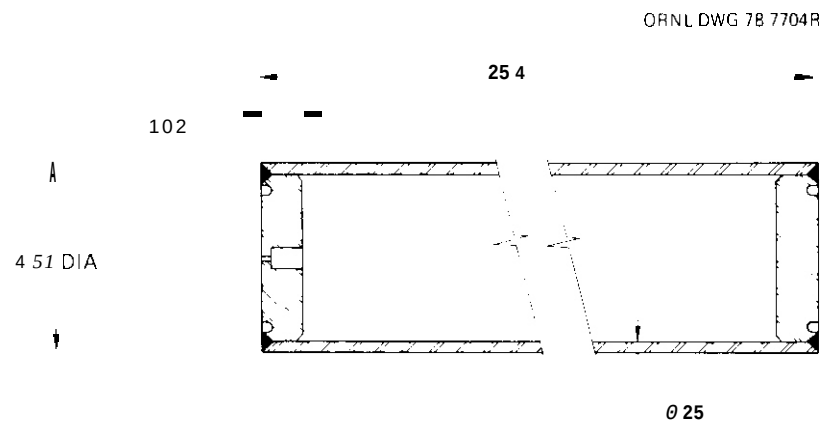

Fig. 3.2.1. Pressurized tube specimen used in irradiation creep experiments in the Oak Ridge Research Reactor spectral tailoring experiment. Dimensions in millimeters.

Table 3.2.1. Irradiation creep measurements for two path A alloys irradiated in ORR-MFE-4B to 4.9 dpa

Specimen	Stress (MPa)		Irradiation temperature (°C)	Strain (%)	
	Hoop	Effective		Diametral $\Delta D/D$	Effective
20%-Cold-worked type 316 stainless steel (heat X15893)					
AC01	80	69	500	0.033	0.044
AC34	100	86.6	500	0.048	0.064
AC44	140	121	500	0.064	0.085
AC05	170	147	500	0.067	0.089
AC15	200	173	500	0.082	0.110
AC45	240	208	500	0.091	0.120
AC36	270	234	500	−0.021	−0.028
AC43	20	17	600	−0.020	−0.027
AC13	35	30	600	−0.037	−0.049
AC32	50	43	600	0.048	0.064
AC61	65	56	600	0.076	0.057
AC21	80	69	600	0.036	0.048
AC50	90	78	600	0.044	0.059
AC10	100	86.6	600	−0.008	−0.011
25%-Cold-worked prime Candidate Alloy (heat K-280)					
EB66	80	69	500	−0.011	−0.015
ER36	100	86.6	500	0.030	0.040
EB59	140	121	500	0.030	0.040
EB58	170	147	500	0.054	0.072
E854	200	173	500	0.064	0.085
EB46	240	208	500	0.035	0.047
AE	270	234	500	0.049	0.065
ER71	20	17	600	0.021	0.028
EB70	35	30	600	0.040	0.053
EB69	50	43	600	0.129	0.172
EB68	65	56	600	0.085	0.113
EB67	80	69	600	0.086	0.114
EB65	90	78	600	0.049	0.065
EB64	100	86.6	600	0.216	0.287

The specimens were irradiated in the ORR in the ORNL-MFE-4B experiment. The tubes were contained in NaK at controlled temperatures of 500 and 600°C. The specimens were removed for examination at a fluence level of 0.64×10^{26} neutrons/m^2 (>0.1 MeV), which had produced 5.1 dpa in both alloys and helium levels of 67 at. ppm in type 316 stainless steel and 87 at. ppm in Path A PCA.

Profilometry measurements were made by a computer-controlled stylus-type laser interferometer. A total of 800 diametral measurements on each tube was used to calculate an average diameter for the central three-fifths of the tube. The instrument is capable of a precision of ±250 nm ($\pm 1 \times 10^{-5}$ in.).

3.2.4.3 Results

Results of the diametral measurements appear in Table 3.2.1 and are plotted in Fig. 3.2.2(*a*) and (*b*). The strain values have not been corrected for swelling because density measurements indicate no measurable swelling at this low fluence.

Effective strain ($1.33\ \Delta D/D_0$) is plotted as a function of effective stress ($0.866\sigma_{hoop}$) in Fig. 3.2.2(*a*) for both alloys irradiated at 500°C. Both sets of data show a linear relation between effective strain and effective stress, with stress coefficients of creep strain of 5.31 and 8.34×10^{-6}/MPa for 20%-cold-worked type 316 stainless steel and 2%;-cold-worked PCA, respectively. The data for the two highest stress levels (for PCA) have been neglected in the analysis since the tubes appear to have ruptured, as evidenced by their positions significantly below the curve. These failures are likely weld failures since they occur well below the expected rupture life.

The results for 600°C have been plotted for both alloys in Fig. 3.2.2(*b*), but a curve appears only for PCA. The excessive scatter in the type 316 stainless steel data precludes drawing a curve at this low fluence. For PCA at 600°C, the stress coefficient is 2.17×10^{-5}/MPa.

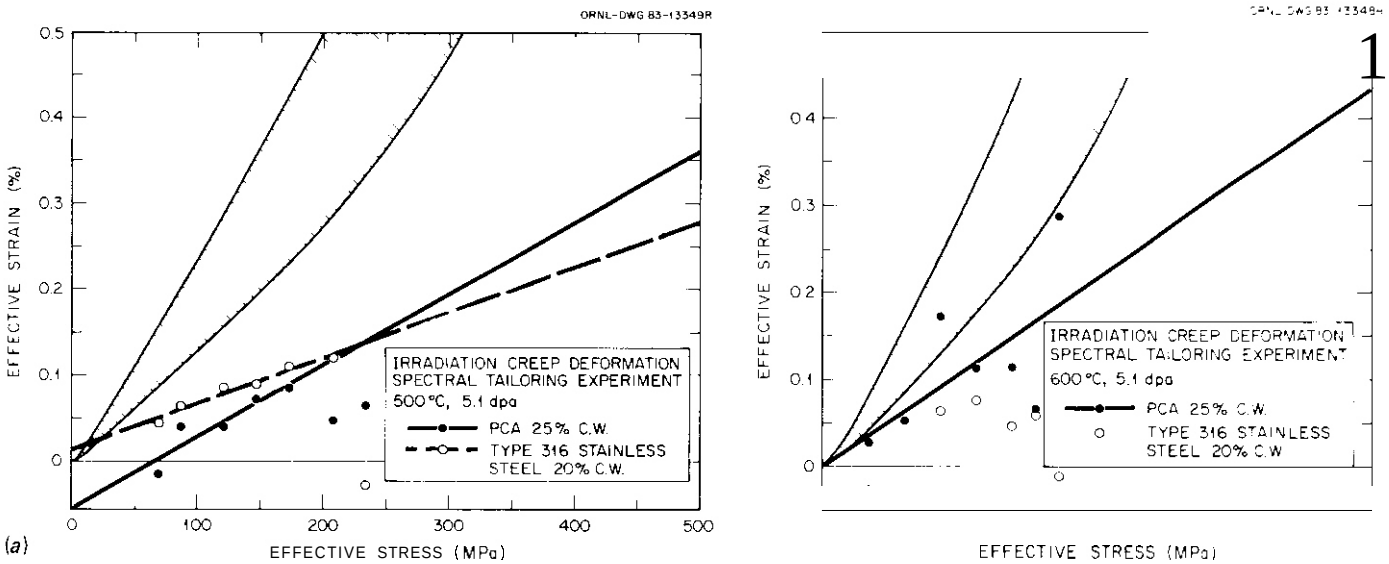

Fig. 3.2.2. Effective strain as a function of effective stress for type 316 stainless steel and Path A PCA irradiated in the Oak Ridge Research Reactor spectral tailoring experiment at (*a*) 500°C and (*b*) 600°C. The cross-hatched region is for the Fast Flux Test Facility first core type 316 stainless steel irradiated in EBR-II.

3.2.4.4 Discussion

As shown in Fig. 3.2.2(*a*), type 316 stainless steel and PCA exhibit quite similar behavior at 500°C. The PCA appears to have a threshold stress since the curve does not pass through the origin. However, this shift is small and might simply result from scatter of the data or from densification. Although type 316 stainless steel and PCA exhibit similar creep behavior, their behavior is significantly different from that of 204-cold-worked type 316 stainless steel, FFTF first core heat, reported by Puigh and Gilbert,[2] illustrated by the cross-hatched band in Fig. 3.2.2(*a*). The nonlinear creep behavior of this material at 500°C appears to result from thermal creep.

Similar features are demonstrated in Fig. 3.2.2(*b*) where data for 600°C are plotted. Scatter of the data for type 316 stainless steel does not permit a meaningful comparison of type 316 stainless steel and PCA at this temperature. However, both alloys appear to have lower creep rates than the FFTF first core heat of type 316 stainless steel. Again the differences are attributed to the thermal creep behavior of the FFTF first core steel.

The data presented demonstrate a significant difference between FFTF first core steel irradiated in EBR-II and type 316 stainless steel (fusion heat) and PCA irradiated in the ORR with a tailored spectrum to achieve the fusion He:dpa value. These differences can be caused either by heat to heat variations or by helium. Since helium contents are still low (67 and 87 at. ppm for type 316 stainless steel and PCA, respectively) and since the creep strain for the EBR-11-irradiated steel is nonlinear with stress, it is suggested that high thermal creep in the FFTF first core steel is more likely to account for the differences observed. Nonetheless, the results indicate clearly that further experiments are essential. The fusion program heat must be irradiated in a fast reactor such as the FFTF or ERR-11. In addition, the tubes have been reinserted into the ORR for further irradiation and examination at intervals of approximately 10 dpa.

3.2.4.5 Conclusions

Irradiation creep behavior in 20%-cold-worked type 316 stainless steel (heat X15893) and 254-cold-worked Path A PCA under irradiation in the ORR spectral tailoring experiment is similar at 500 and 600°C. A damage level of 5.1 dpa and helium levels of 67 and 87 at. ppm were attained for type 316 stainless steel and PCA, respectively. The creep rates were lower than those for FFTF first core heat irradiated in EBR-II. This difference is considered most likely to result from differences in thermal creep properties.

3.2.4.6 References

1. M. L. Grossbeck, "Irradiation Creep in Path A Alloys Irradiated to 5 dpa in the ORR-MFE-4A Spectral Tailoring Experiment," pp. 38–43 in *ADIP Semiannu. Prog. Rep. Sept. 30, 1982*, DOE/ER-0045/9, U.S. DOE, Office of Fusion Energy.

2. B. J. Puigh, E. R. Gilbert, and R. A. Chin, "An in-Reactor Creep Correlation for 20% Cold Worked AISI 316 Stainless Steel," p. 108–21 in *Effects of Radiation on Materials*, ASTM-STP-782, American Society for Testing and Materials, Philadelphia, 1982.

3.3 SWELLING BEHAVIOR OF MANGANESE - BEARING STEEL AISI 216 - D. S. Gelles and F. A. Garner (Westinghouse Hanford Company)

3.3.1 ADIP Task

ADIP Tasks 1.C.1 Microstructural Stability and 1.C.7 Microstructure and Swelling in Austenitic Alloys (Path A).

3.3.2 Objective

The object of this effort is to provide an early indication of the radiation response of low activation austenitic alloys based on manganese substitution for nickel,

3.3.3 Summary

The inclusion of 8.5 wt% manganese in AISI 216 (Fe-6.7Ni-8.5Mn-20Cr-2.7Mo-0.32Si) does not appear to alter the swelling behavior from that found to he typical of austenitic alloys with comparable levels of austentite-stabilizing elements. The swelling in AISI 216 in EBR-II is quite insensitive to irradiation temperature in the range 400 - 650°C. Microscopy reveals that this may arise from the low level of precipitation that occurs in the alloy.

3.3.4 Progress and Status

3.3.4.1 Introduction

The development of low activation alloys has heen accepted as one of the goals of the materials program of the U.S. Magnetic Fusion Energy Program. Toward this objective, irradiation nf a series of such alloys has already commenced in FFTF, utilizing the MOTA-18 experiment.[1-2] One group of these alloys is based on the substitution of manganese for nickel as an alternate Path A development approach.

In order to provide an early forecast of the hehavior of such allovs in a radiatinn environment, three steps have *been* taken. *One* involves the *use of a diffusivity-based swelling* model to predict the compositional dependence of swelling. The second involves the use of ion homhardment to provide a survey of the compositional dependence of swelling in the Fe-Cr-Mn system. The third effort centers ON the examination of manganese-stahilized alloys that. havr already heen subjected to irradiation.

Several charged particle irradiations of manganese-stahilized austenitics have heen reported in the scientific literature and show that manganese substitution does not in general confer immunity from either swelling or phase instabilities.[3-5] Only one set of neutron-induced swelling data on a manganese-bearing alloy has heen published, however.

Bates and Powell reported swelling data for a larqe range of commercial alloys irradiated in the B109 and AA-I experiments conducted in EBR-II.[6] One of the commercial alloys was annealed AISI 216 which has a coinposition (wt%) of Fe-6.7Ni-8.5Mn-20Cr-2.7Mo-0.32Si-0.07C-0.16N. As shown in Fig. 3.3.1 and Table 3.3.1. this alloy swelled more than the other alloys in the B109 exoeriment. Rates and Powell attributed this higher swelling primarily to the lower nickel content of the alloy.

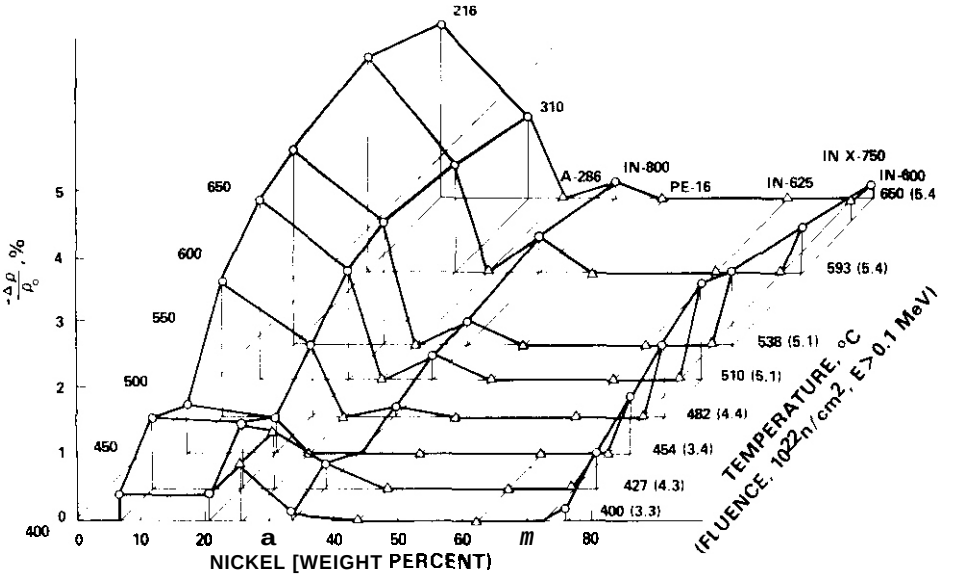

Fig. 3.3.1. Swelling vs nickel content and temperature for thr solution-trrntrd B109 allovs.[6]

Tahle 3.3.1. Density measurement results for AISI 71h specimens contained in the B-109 experiment

Specinien Identification	Irradiation Temperature (°C)	Fluence 10^{22}n/cm² (E > 0.1 MeV)	(dpa)	Swelling (%)
NM	400	3.3	16.5	0.39
NL	427	4.3	21.5	1.04
NE	454	3.4	17	0.70
NF	482	4.4	22	2.08
NK	510	5.1	25.5	2.77
NG	538	5.1	25.5	3.01
NJ	iY3	5.4	27	3.35
NH	650	5.4	27	2.68

The present report considers the response of AISI 216 from the B109 experiment in greater detail. Specimens irradiated at *417°C* and at 593°C have been examined by transmission electron microscopy to assess the consequences on void swelling and microstructural evolution of manganese substitution for nickel.

3.3.4.2 Experimental Procedure

Specimens of AISI 216 irradiated in the B109 Test at 427°C to 4.3 x 10^{22} n/cm² (E > 0.1 MeV) and at 593°C to 5.4 x 10^{22} n/cm² (E > 0.1 MeV) were obtained from ztorage. The heat treatment qiven prior to irradiation was 1066°C for 1 hour, followed by a water wench. The specimens were in the form of 3.0 mm diameter x 0.3 mm thick disks which had been sliced from the irradiated 1.3 cm long rods. Specimen preparation for transmission electron microscopy and examination followed routine procedures.

3.3.4.3 Results

AISI 216 was found to have developed microstructures during irradiation similar to those of other austenitic stainless steels. Voids were found in hoth specimens examined; the 593°C condition cnntained higher void swelling as anticipated froni the density measurements. Both Frank loops and perfect dislocation networks were found in the 427°C specimen hut only perfect dislocation networks were observed at 593°C. Only a few precipitates were found in either of the specimens. In general, these few precipitates were associated with cavities.

Examples of these microstructures are provideo in Fig. 3.3.2. Figs. 3.3.2a and 3.3.2b compare void structures in the vicinity of grain boundaries for specimens irradiated at 427 and 593°C. The grain boundaries ttna to be denudeo of voids and contain $M_{23}C_6$ particles. Away from the boundaries, the voids are uniformly aistributed. The void structures are shown at higher magnification in Figs. 3.3.2c and 3.3.2d. The voids are facetted and are in the shape of truncated octahedra, typical of austenitic steels. Several examples can be ioentified where precipitates are attached to voids. The dislocation structures are shown under dark field imaging conditions in Figs. 3.3.2e and 3.3.2f. Two of the *four* sets of Frank loops are visible as fringed features in Fig. 3.3.2e. In order to eniphasize the reduced precipitation in this alloy, micrographs of AISI 316 (20% CW) which was irradiated under identical conditions are shown in Figs. 3.3.29 and 3.3.2h. It is apparent. that the swelling is not only lower in AISI 316 but that gamma prime (Ni_3Si) and G-phase precipitates are present at higher number densities.

3.3.5 Discussion

If the results of oensity measurements for AISI 216 specimens, as given in Tahle 3.3.1, are nlotted as a function of neutron fluence, a new insight emerges. The swellinq of annealed AISI 216 appears to exhibil essentially no dependence on irradiation temperature hetween 400 and 650°C. This is consistent with the temperature-independence of swelling often observed in austenitic alloys,' although it is surprisinq that tne transient regime is insensitive over such a large regime *of* temperatiire. This insensitivity is likely due to the lack of precipitation in the alloy. The swelling curve for AISI 216 lies in the ranqe hetween that usually innabited by annealed AISI 304 ana AISI 316 as might be expected from the total Ni + Mn level of the three steels. This is only a audlitative comparison since the transient duration is affected not only by the nickel and manganese content hut, also by other factars such as the annealing temperature and tne silicon and carbon content.

It is encouraging, however, to note in a steel in which a substantial portion of the nickel has been replaceo by manganese that the swelling behavior is quite typical of the class of austenitic stainless steels as we currently understand them.' The major questions remaining to be explored, therefore, involve the radiation-induced segregation and phase evolution as well as the effect of manganese content on swelling inhibition. If, however, the manganese and nickel are eventually removed from solution by precipitation in the same manner as is nickel in 300 series alloys, manganese-stabilized alloys may exhibit a loss of austenitic stability. it is hopec that much higher levels of [manganese may provide swelling suppression similar to that observed in Fe-Cr-Ni ternary alloys with high nickel levels.

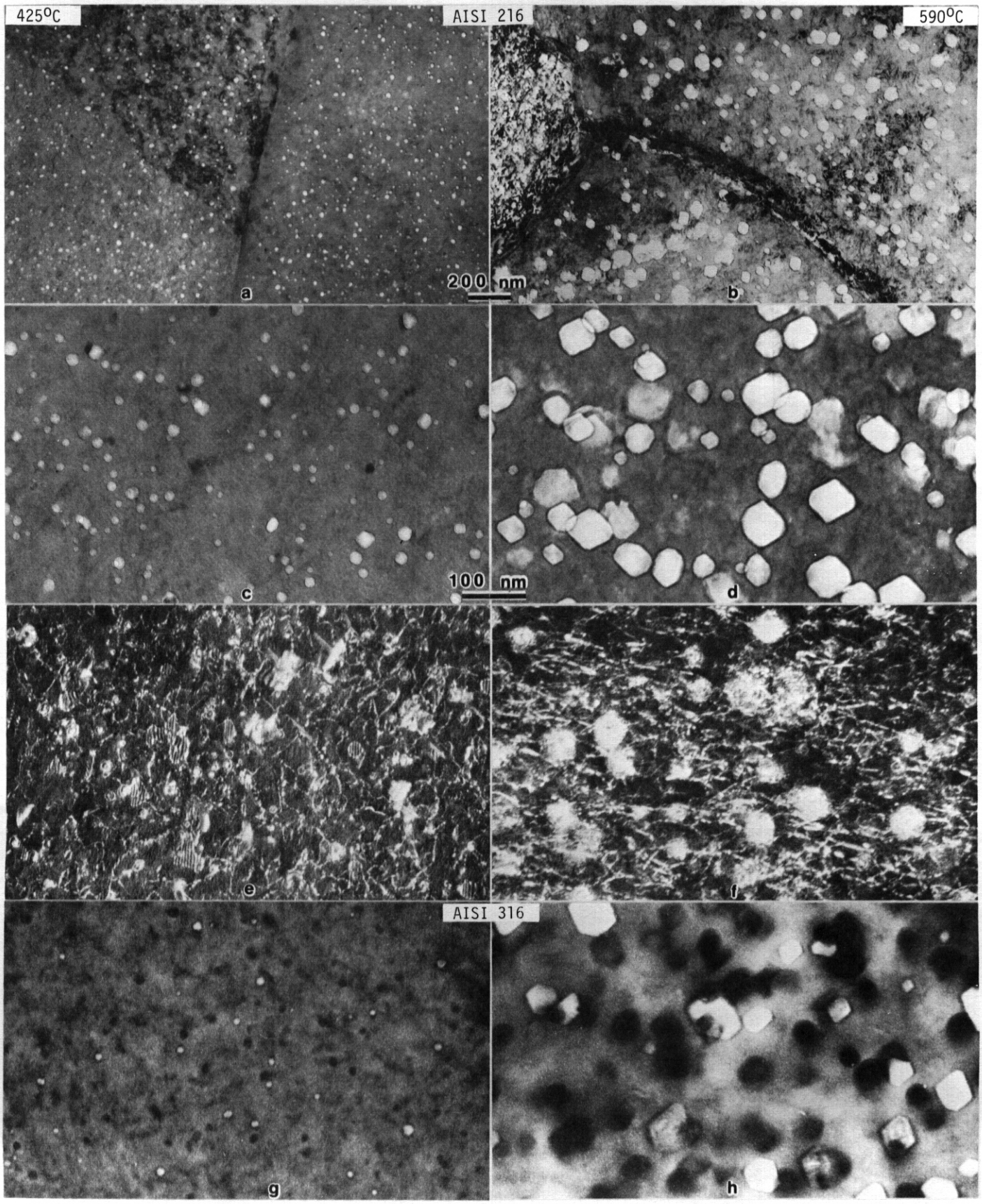

Fig. 3.3.2. Examples of microstructures observed in AISI 216 irradiated at 427 and 593°C. Figs. 3.3.2g and 3.3.2h provide a comparison with 20% cold-worked AISI 316 specimens irradiated under identical conditions. The density changes of the AISI 316 specimens were -0.13% at 427°C and 1.34% at 593°C.

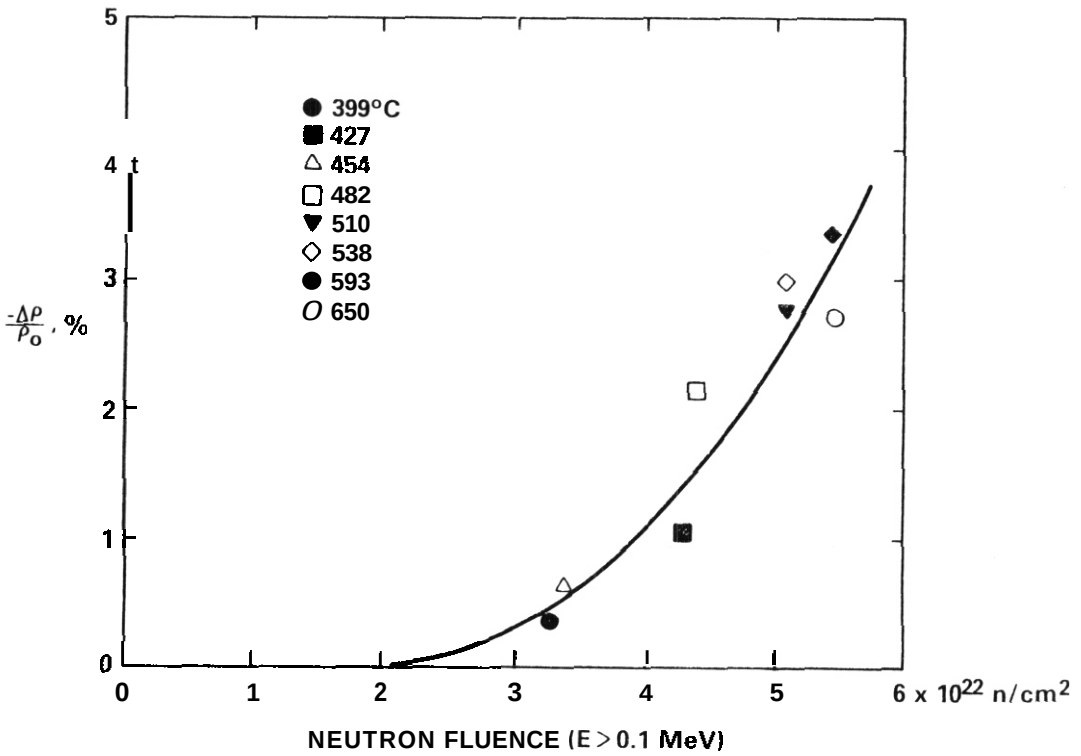

Fig. 3.3.3. Swelling in AISI 216 irradiated with the B109 test plotted as a function of fluence. NO strong dependence on irradiation temperature is observed.

3.3.6 Conclusions

Microstructural examinations of AISI 216 specimens which had been neutron irradiated at 427 and 593°C show that manganese levels of 8.5% do not alter the swelling response of the alloy compared to the behavior of other austenitic stainless steels. Post-irradiation density measurements demonstrate that swelling of this alloy is independent of temperature, in good agreement with the observed behavior of other austenitic steels. Although a substantial fraction of the nickel content has been replaced by manganese, the swelling reponse remains typical of austenitic stainless steels.

3.3.7 Future Work

This work is complete.

3.3.8 References

1. F. A. Garner, H. R. Brager and D. S. Gelles, "Reduced Activation Activities," pp. 17-18 in *DAFS Quart. Prog. Rep. Feb. 1984*, DOE/ER-0046/16, U.S. DOE, Office of Fusion Energy.

2. H. R. Brager and F. A. Garner, "Fundamental Alloy Studies," *DAFS Quart. Prog. Rep. June 1984*, DOE/ER-0046/17, U.S. DOE, Office of Fusion Energy.

3. M. Snykers and E. Ruedl, J. *Nucl. Mater.* 103 & 104, 1075 (1981).

4. D. J. Mazey, J. A. Hudson and J. M. Titchmarsh, *J. Nucl. Mater.* 107, 2 (1982)

5. R. M. Boothby, D. R. Harries and T. M. Williams, *J. Nucl. Mater.* 115, 16 (1983).

6. J. F. Bates and R. W. Powell, *J. Nucl. Mater.* 102, 200 (1981)

7. F. A. Garner, "Recent Insights on the Swelling and Creep of Irradiated Austenitic Alloys," pp. 49-61 in *DAFS Quart. Prog. Rep. Feb. 1984*, DOE/ER-0046/16, U.S. DOE, Office of Fusion Energy, (to be published in *Journal of Nuclear Materials*).

3.4 THE DEVELOPMENT OF AUSTENITIC STEELS FOR FAST INDUCED-RADIOACTIVITY DECAY — R. L. Klueh and P. J. Maziasz (Oak Ridge National Laboratory)

3.4.1 ADIP Tasks

AOIP Tasks I.A.5, Perform Fabrication Analysis, and I.C.I, Microstructural Stability.

3.4.2 Objective

During the operation of a fusion reactor, the structural material of the first wall and blanket structure will become highly radioactive from activation by the fusion neutrons. Disposal of this material after the service lifetime will be a difficult radioactive waste management problem. One way to minimize the disposal problem is to use structural materials in which radioactive isotopes induced by irradiation decay quickly to levels that allow simplified disposal techniques. We are assessing the feasibility of developing such austenitic stainless steels.

3.4.3 *Summary*

A program was started to develop austenitic steels for fusion reactors in which the induced radioactivity decays to low levels in a reasonable time. Ten small button heats of Fe-Cr-Mn-C alloys were melted, cast, and rolled. These heats will be used to determine austenite-stable compositions that can serve as a base composition for further alloying.

3.4.4 Progress and Status

During the operation of a fusion reactor, the various elements of the alloys that are proposed for the first wall and blanket structure undergo transmutation reactions when irradiated by high-energy neutrons. After the service lifetime of the reactor, these radioactive components must he properly disposed of. The complexity of this waste disposal procedure depends on the time required for the induced radioactivity to decay to levels that no longer pose a threat to people and the environment. The more rapid the decay, the simpler is the disposal task.

A U.S. Department of Energy panel studied this subject.' It was concluded that for an alloy to meet the Nuclear Regulatory Commission 10CFR61 guidelines for simplified nuclear waste storage criteria, certain alloying elements must he restricted and certain uncontrolled impurities must be eliminated. Type 316 stainless steel and the austenitic prime candidate alloy (PCA) are the austenitic steels that are currently candidates for fusion reactor structural applications. For this type of alloy to meet the 10CFR61 guidelines, nickel, nitrogen, and molybdenum would need to be severely restricted as alloying elements and niobium virtually eliminated as an impurity. Reducing nickel has the greatest impact, because its primary role is the stabilization of the austenite phase.

We previously proposed an alloy development program for fast induced-radioactivity decay (FIRD) versions of present first-wall and blanket structural candidate alloys.[2] For the austenitic alloys, manganese was proposed as a replacement for nickel, although it was recognized[2] that this may be difficult, because manganese is not as strong an austenite stabilizer as nickel. Hence, it is not possible to simply replace nickel with equal amounts of manganese. It was proposed that an effort be made to determine stable Fe-Cr-Mn-C compositions that could then be further alloyed to obtain the strength and irradiation-resistant properties required for a fusion reactor structural material.' As a start at determining the stable austenite composition, the four alloys in Table 3.4.1 were proposed.'

Table 3.4.1. Possible austenitic stainless steels for Fast Induced-Radioactivity Decay Alloy Development Program

Alloy	Chemical composition, wt %[a]			
	Cr	Mn	C	N
15 Cr-15 Mn	15	15	0.05–0.1	<0.01
15 Cr-20 Mn	15	20	0.05–0.1	<0.01
10 Cr-15 Mn	10	15	0.05–0.1	<0.01
10 Cr-20 Mn	10	20	0.05–0.1	<0.01

[a]Balance iron.

Five 600-g button heats were melted and cast in the compositions in Table 3.4.2. In addition to the four alloys listed, a lower carbon (0.05%) version of the Fe-15 Cr-15 Mn alloy was obtained. After casting, the ingots were rolled 30 to 50%. Aided by the Schaeffler diagram[3] and a determination of the magnetic character of the steels (an indication of δ-ferrite and martensite) and the fabricability, the number of alloys was expanded to a total of ten (Table 3.4.2). These steels have been rolled to thicknesses

Table 3.4.2. Goal compositions of button heats melted for Fast. Induced Radioactivity Decay Alloy Development Program

Alloy	Chemical composition, wt %[a]		
	Cr	Mn	C
PCMA-0	15	15	0.1
-1	15	15	0.05
-2	15	20	0.1
-3	10	15	0.1
-4	10	20	0.1
-5	15	15	n.Z
-6	15	20	0.2
-7	15	20	0.4
-8	20	20	0.2
-9	20	20	0.4

[a]Balance iron.

of 6.3 to 9.5 mm. Pieces of each heat are to be given the following heat treatments: (1) 24 h at 1275°C, (2) 1 h at 1150°C, (3) 8 h at 1050°C. and (4) 168 h at 800°C. Following these heat treatments, the specimens will he examined by optical metallography to determine the phases present in the microstructures.

3.4.5 Future Work

During the next reporting period, the heat-treated specimens will he examined by optical metallography. The ten heats will be rolled to 0.25- and 0.76-mm sheet to obtain transmission electron microscopy (TEM) disks and tensile specimens, respectively. Transmission electron microscopy disks are scheduled to be inserted in the Fast Flux Test Facility fusion experiment in the Materials Open Test Assembly (MOTA) in June. Although it is not expected that most of these compositions could serve as a base for further alloying, the irradiation response should provide information on the effect of manganese (as compared with nickel) on swelling and phase stability. The 0.76-mm sheet will also be used to determine the effect of manganese on compatibility with lithium.

Based on the results of the scoping tests, additional heats will be obtained as required to determine a suitable base composition for further development. Once that base is obtained, further heats will be melted that have heen further alloyed for irradiation resistance and strength. From the previous work on the development of PCA,[3] additions of titanium, silicon, and possibly tungsten as a substitute for molybdenum' are anticipated.

3.4.6 References

1. R. L. Klueh and E. E. Rloom, "Alloy Development for Fast Induced-Radioactivity Decay for Fusion Reactor Applications," pp. 11–20 in *ADIP Semiannu. Prog. Rep. Sept. 30, 1983*, DOE/ER-0045/11, U.S. DOE, Office of Fusion Energy.

2. R. W. Conn et al., *Panel Report on Low Activation Materials for Fusion Applications*, UCLA Report PPG-728, University of California at Los Angeles, June 1983.

3. P. J. Maziasz and T. K. Roche, "Preirradiation Microstructural Development Designed to Minimize Properties Degradation During Irradiation in Austenitic Alloys," *J. Nucl. Mater.* **104**, 797–802 (1982).

3.5 THE TENSILE PROPERTIES AND BEND DUCTILITY OF PCA AFTER IRRADIATION IN HFIR — D. N. Braski and P. J. Maziasz (flak Ridge National Laboratory)

3.5.1 ADIP Task

ADIP Task I.B.13, Tensile Properties of Austenitic Alloys.

3.5.2 Objective

The objective of this work is to determine the effect of neutron irradiation on the tensile properties of prime candidate alloy (PCA) irradiated in several different initial microstructural conditions.

3.5.3 Summary

Three different microstructures of PCA were irradiated in the High Flux Isotope Reactor (HFIR) at temperatures from 300 to 600°C to approximately 22 dpa and approximately 1750 at. ppm He. The B3 condition with coarse MC in the grain boundaries and cold-worked matrix resisted helium embrittlement better than the PCA-A1 (solution annealed) or PCA-A3 (25% cold worked). Disk bend ductility data were useful for screening, but correlation with tensile ductility was poor.

3.5.4 e g r e s s and Status

3.5.4.1 Introduction

Seven microstructural variants of the PCA austenitic stainless steel were previously evaluated with regard to their resistance to void swelling in the HFIR-CTR-30, -31, and -32 irradiations.' Specimens of three PCA variants were then irradiated in the HFIR-CTR-42 and -43 experiments to determine their postirradiation tensile properties and, more specifically, their resistance to helium emhrittlement. One of the variants, the PCA-B3, was designed as a modification of PCA-82. The PCA-B2 exhibited excellent performance in the disk bend tests for HFIR-CTR-30, -31, and -32 (ref. 2).

3.5.4.2 Experimental

Standard HFIR "sub-mini" tensile specimens with an 18.3-mm gage length and a 2-mm gage diameter were machined from 5-mm-diam swaged rod stock. Thin transmission electron microscopy (TEM) disks were cut, transversely, from 3-mm-diam swaged rod stock and hand ground through fino-grit papers to a thickness of 0.25 mm. Disks with the same fabrication history as the tensile specimens were used to permit a better comparison between disk bend and tensile tests. Both types of specimens were heat treated to the following conditions:

A1 — the 50% cold-swaged rod was annealed for 30 min at 1100°C,
A3 — 25% cold swaged after treatment A1,
B3 — material from the (Al) treatment was aged for R h at 800°C and then cold swaged an additional 25%.

The specimens were placed in tubes such that the difference in specimen outside diameter and tube inside diameter or "gas gap" was designed to produce temperatures from 300 to 600°C uniformly across the specimens by means of nuclear heating. The disks were placed in two small cylinders that were designed for irradiation temperatures of 500 and 600°C. Detailed calculations of the neutron fluence and materials response for these experiments are not yet available. Approximate values are used in this report. After irradiation to a damage level of approximately 22 dpa (—1750 at. ppm He), the tensile specimens were tested at their respective irradiation temperatures. Selected TEM disks were also bend tested at their irradiation temperature by the procedure developed at HEDL (ref. 3). The crosshead speed used in both tensile and bend tests was 0.51 mm/min (0.02 in./min).

3.5.4.3 Results and Discussion

The results of the postirradiation tensile tests along with those for unirradiated and thermally aged controls are given in Table 3.5.1. At the intermediate temperatures of 300 to 400°C, irradiation at the conditions of HFIR-CTR-42 and -43 had no deleterious effects on PCA-A3. In fact, at 300°C the total elongation of unirradiated PCA-A3 increased from approximately 3.5% (ref. 4) to over 5% after irradiation (Table 3.5.1), with concurrent increases in yield and ultimate tensile strengths, In contrast, the PCA-A1 specimens were "hardened" by the irradiation and demonstrated large losses of total elongation from approximately 31% (ref. 3) to 7.34. At 400 and 500°C, PCA-A3 showed increased strength due to irradiation with slight ductility losses, and PCA-A1 again exhibited strengthening along with substantial losses in ductility. After irradiation at 500°C the PCA-B3 demonstrated both strength and ductility increases compared with the unirradiated material. At 600°C, helium emhrittlement probably affected all three PCA variants, but TEM and scanning electron microscopy (SEM) will be needed for verification. The relative performance of the three PCA variants at 500 and 600°C is seen more clearly in Fig. 3.5.1. Note that total elongation has been plotted on a logarithmic scale to permit representation of the unirradiated PCA-A1 values along with the others.

Table 3.5.1. Prime candidate alloy tensile test results[a]

Specimen	Condition	Test temperature (°C)	Strength, MPa		Elongation, %	
			Yield	Ultimate	Uniform	Total
		Irradiated at test temperature				
EL4	PCA-B3	600	508	579	3.2	3.8
EK4	PCA-A3	600	539	570	1.0	1.1
EK9	PCA-A3	600	513	548	1.2	1.7
EJ11	PCA-A1	600	468	473	0.3	0.6
EL7	PCA-B3	500	659	745	5.3	8.6
EK2	PCA-A3	500	692	771	3.4	6.2
EK5	PCA-A3	500	767	842	2.0	3.9
EJ6	PCA-A1	500	765	193	1.4	3.3
EK10	PCA-A3	400	950	951	0.2	4.4
EK5	PCA-A3	400	935	938	0.3	4.1
EK8	PCA-A3	400	976	980	0.3	4.1
EJ5	PCA-A1	400	896	897	0.1	s.5
EK6	PCA-A3	300	973	973	0.2	5.3
EJ1	PCA-A1	300	851	851	0.3	1.3
		Unirradiated				
EL-46	PCA-R3	600	597	644	1.0	5.1
EL-42	PCA-R3	600	591	644	0.8	5.0
EL-40	PCA-B3	500	650	683	0.6	4.9
EL-41	PCA-B3	500	660	679	0.4	4.6
EC-68	PCA-A3	600	545	604	5.8	7.3
EC-69	PCA-A3	600	466	514	5.R	7.4
EC-67	PCA-A3	500	559	630	2.9	5.6
EC-66	PCA-A3	500	521	575	5.4	7.3
ED-86	PCA-A1	600	165	397	31.3	32.5
En-87	PCA-A1	600	175	403	27.5	31.3
ED-86	PCA-A1	500	15R	447	29.6	33.8
ED-85	PCA-A1	500	190	438	27.8	29.8
		Aged at 600°C for 5000 h				
EL10	PCA-B3	600	549	604	3.8	R.5
EL11	PCA-B3	600	539	594	2.6	7.4
EK13	PCA-A3	600	587	628	1.4	7.0
EK15	PCA-A3	600	583	624	2.7	6.9

[a]Irradiated in HFIR-CTK-42 and -43 to approximately 22 dpd (–1750 at. ppm He).

The main point of Fig. 3.5.1 is that the PCA-B3 condition exhibits superior resistance to helium embrittlement compared with the cold-worked and solution-annealed conditions. As mentioned before, *both* the strength and ductility were *increased* in PCA-B3 by the irradiation at 500°C. At 600°C, there was a slight loss of strength, hut the total elongation of 3.8% was only slightly less than the unirradiated values of 5.0 and 5.1%. It is also significant to note the improvement in uniform elongation of the irradiated PCA-B3 compared with the unirradiated material. Consideration of both strength and elongation suggests that PCA-B3 had better resistance to helium embrittlenent than PCA-A3 or -A1. Based on these and previous results, we believe that the enhanced resistance of PCA-B3 to helium emhrittlement is genuine and lies in the stability of the relatively coarse grain boundary MC particles and their interaction-with helium. Planned TEM and SEM investigations of the PCA specimens will supply more information on the microstructural aspects of helium ernbrittlement in this alloy system.

Bend tests on TEM disks were successfully used as a screenino method for the develooment of the PCA-B3 microstructure.[2] In an attempt to better correlate bend and tensile ductility, disks were cut from the same swaged material as the tensile specimens and given the same heat treatments. The results of those tests are given in Table 3.5.2. The measured deflections were converted to bend ductility in percent by nultiplying the strain ε by 100 in the expression[3]

$$\varepsilon = tw/(a^2 + 3),$$

where t and a are thickness and radius of the disk, respectively, and w is the deflection at fracture.

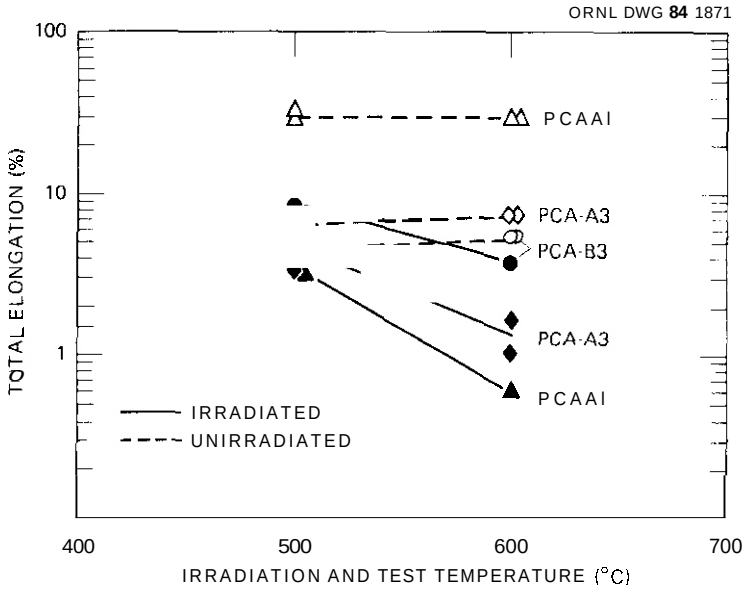

Fig. 3.5.1. Tensile ductility of unirradiated PCA and PCA irradiated in HFIR to approximately 22 dpa (–1150 at. ppm He).

Disks that were irradiated and tested at 600°C had bend ductilities ranging from 0.4 to 1.8%. The correlation of these values with the average values of tensile ductility (total elongation) was poor. Note also that, while the PCA-A1 tested at 500°C had a lower tensile ductility than the PCA-B3 at 600°C, it was bent to the 0.5-mm maximum deflection without cracking. These inconsistencies discourage one from using the bend test quantitatively. We speculate that the source of the inconsistent behavior may be related to the differences in deformation and fracture modes between the two types of test. In the past, bend tests of PCA disks that were not completely embrittled (100% intergranular fracture) yielded load-deflection curves that were very difficult to interpret with regard to bend ductility.[5]

Table 3.5.2. Prime candidate alloy disk bend test results[a]

Disk designation	Condition	Test temperature[b] (°C)	Deflection (mm)	Ductility (%)	
				Bend	Tensile
EL-1	PCA-B3	600	0.114	1.3	3.8
EK-1	PCA-A3	600	0.038	0.4	1.4
EJ-4	PCA-A1	600	0.163	1.8	0.6
EL-2	PCA-B3	500	Maximum		8.6
EK-4	PCA-A3	500	Maximum		5.1
EJ-7	PCA-A1	500	Maximum		3.3

[a]Irradiated in HFIR-CTR-42 and -43 to approximately 22 dpa (–1750 at. ppm He).

[b]Irradiated at test temperature.

3.5.5 References

1. P. J. Mariasz and D. N. Braski, "Improved Swelling Resistance for PCA Austenitic Stainless Steel under HFIR Irradiation Throuqh Microstructural Control," pp. 53–59 in ADIP *Semiannu. Prog. Rep.* Sept. 30, *1983*, DOE/ER-0045/11, U.S. DOE, Office of Fusion Energy.

2. P. J. Maziasz and D. N. Braski, "Microstructural Design of PCA Austenitic Stainless Steel for Improved Resistance to Helium Embrittlement under HFIK Irradiation," pp. 60–65 in *ADIP Semiannu. Prog. Rep. Sept. 30, 1983*, DOE/ER-0045/11, U.S. DOE, Office of Fusion Energy.

3. F. H. Huang, M. L. Hamilton, and G. L. Wire, *Nucl. Technol.* 57, 234–42 (1982).

4. D. N. Braski and P. J. Mariasz, "The Tensile Properties of Unirradiated Path A PCA," pp. 62–70 in *ADIP Semiannu. Prog. Qep. Sept. 30, 1982*, DOE/ER-0045/9, U.S. DOE, Office of Fusion Energy.

5. R. L. Klueh and D. N. Braski, "Disk-Bend Ductility Tests for Irradiated Materials," pp. 43 –51 in *ADIP Semiannu. Prog. Rep. Sept. 30, 1983*, DOE/ER-0045/11, U.S. DOE, Office of Fusion Energy.

4. PATH B: ALLOY DEVELOPMENT — HIGHER STRENGTH Fe-Ni-Cr ALLOYS

No contributions.

5. PATH C ALLOY DEVELOPMENT — REACTIVE AND REFRACTORY ALLOYS

5.1. SWELLING OF V-15Cr-5Ti ALLOY ON SINGLE- AND DUAL-ION IRRADIATION - B. A. Loomis and D. L. Smith (Argonne National Laboratory)

5.1.1 ADIP Task

ADIP Task I.A.I. Define Material Property Requirements and Make Structural Life Predications.

5.1.2 Objective

The objective of this work is to provide guidance on the applicability of vanadium-base alloys for structural conponents in a fusion reactor.

5.1.3 Summary

The effect of single ($^{58}Ni^{++}$)- and dual-ion ($^{58}Ni^{++}$ + $^{3}He^{+}$)-irradiation on the microstructure of the V-15Cr-5Ti alloy at 725°C was determined for irradiation damage levels of 125 and 205 dpa and for either the pre-implanted helium (780 appm) or simultaneously implanted helium (9.3 appm/dpa) condition. The swelling of the alloy that could be attributed to voids or cavities was negligible. The principle effect on the microstructure of the irradiation was to induce the formation of a high density of disc-like precipitates in the vicinity of grain boundaries and intrinsic precipitates and on the dislocation structure.

5.1.4 Progress and Status

5.1.4.1 Introduction

The V-15Cr-5Ti alloy is considered to be a candidate alloy for structural components in a magnetic fusion reactor (MFR). The simultaneous production of displacement damage and deposition of helium atoms within the alloy during the reactor lifetime may have a significant influence on the alloy microstructure and, therefore, on the integrity of the structural component. Observations of the microstructure in the V-15Cr-5Ti alloy after neutron or ion irradiation for damage levels up to 60 dpa have shown a rema a le absence of voids and helium-filled cavities and the presence of irradiation-induced precipitates?.' In this report, some preliminary results are presented on the microstructural changes that may be expected to occur in a V-15Cr-5Ti structural component during the lifetime (~200 dpa) of an MFR. Single ($^{58}Ni^{++}$)- and dual ($^{58}Ni^{++}$ + $^{4}He^{+}$)-ion irradiations were utilized to simulate the irradiation damage and helium production within the alloy in the environment of an MFR.

5.1.4.2 Materials and Procedure

The V-15Cr-5Ti alloy was supplied in the form of 0.81-mm thick sheet (melt number 834-6) from the Fusion Program Research Materials Inventory at Oak Ridge National Laboratory. The chemical analysis of this material is presented in Table 5.1.1. The as-received sheet was reduced in thickness to 0.25 mm and annealed at 1100°C for two hours in a system evacuated to 6.7 x 10^{-7} Pa.

Table 5.1.1. Chemical analysis of the V-15Cr-5Ti alloy

Element	Concentration (a/o)
Cr	14.1
Ti	6.6
C	0.14
O	0.10
N	0.18

Specimens of the alloy, each with a diameter of 3.05 mm, were mounted in a tungsten holder for either single-ion irradiation with 4.0-MeV $^{58}Ni^{++}$ ions, dual-ion irradiation with 3.0-MeV $^{58}Ni^{++}$ and 0.25-MeV $^{3}He^{+}$ ions or helium implantation using 0.50-MeV $^{4}He^{+}$ ions followed by irradiation with 4.0-MeV $^{58}Ni^{++}$ ions. The irradiations of the specimens at 725°C were conducted in a cryogenically pumped chamber evacuated to 1.3 x 10^{-6} Pa. The chamber was connected by cryogenically pumped, ion-bear transport tubes to the 2-MeV tandem and 0.30-Ye'/ ion accelerators at Argonne National Laboratory. A temperature of 725°C was selected for the present series of irradiations. This selection was based on the temperature for maximum void swelling in pure V.[3] Following irradiation, the specimens were sectioned from the irradiated surface to a depth of 1050 nm in the case of 4.0-MeV $^{58}Ni^{++}$ ion irradiations and G50 nm in the case of the 3.0-MeV $^{58}Ni^{++}$ ion irradiation, then thinned from the backside to perforation in an 80% CH_3OH-20% H_2SO_4 solution at ~5°C.

Deposited energy densities as a function of ion range in the alloy from a computerized TRIM code were converted to displacements per atom (dpa) and helium atom deposition using a threshold energy of 40 eV.[4] The depths in the V-15Cr-5Ti alloy for peak irradiation damage during 3.0-MeV and 4.0-MeV $^{58}Ni^{++}$ ion irradiation were computed to be 900 and 1150 nm, respectively. The depths for peak deposition of helium atoms during 0.25-MeV $^{3}He^{+}$ and 0.50-MeV $^{4}He^{+}$ ion implantation were computed to be 670 and 1110 nm, respectively. The specimens were irradiated to displacemnt damage levels of either 125 or 205 dpa at a damage rate of 5×10^{-3} dpa/s. In the case of the specimen implanted with helium prior to 4-MeV $^{58}Ni^{++}$ ion irradiation, the helium concentration was 780 appm. In the case of the dual-ion irradiated specimen, the helium implantation rate was 9.7 appm/dpa.

The microstructure of the unirradiated and irradiated alloy specimens were observed by transmission electron microscopy (TEM) in a Philips EM 400T electron microscope operated at 120 kV. The thickness of the specimens for TEM was typically 100 nm.

5.1.4.3 Experimental Results

TEM for the unirradiated alloy

The microstructure that was characteristic for the V-15Cr-5Ti alloy on insertion into the irradiation chamber is shown in Fig. 5.1.1. This microstructure is characterized by the presence of precipitates with a diameter of 2-6 μm (3.5×10^{9} particles intersected/m2) and precipitates with an average diameter of 7.5 nm and a number density of 3.6×10^{19} /m^{3}. The average grain diameter of the annealed material was 40 μm.

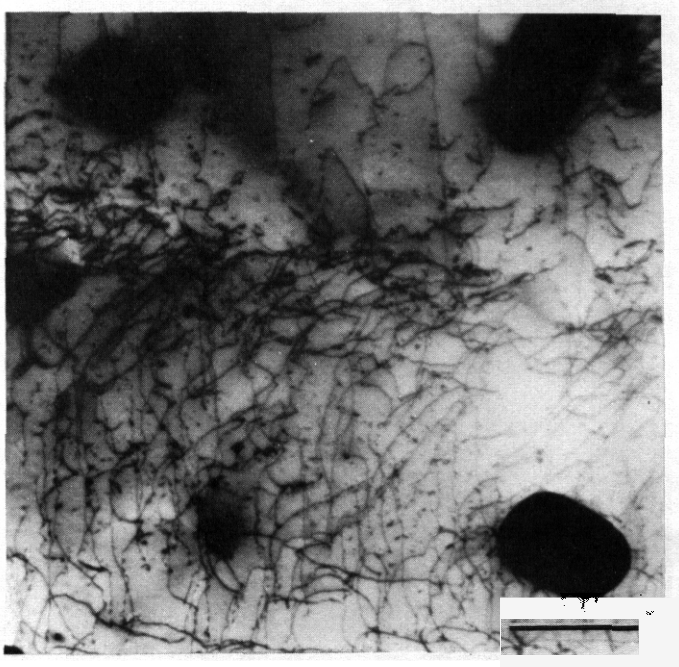

Fig. 5.1.1 Microstructure of the V-15Cr-5Ti alloy prior to irradiation (marker = 500 nm).

Since the irradiation-induced change in the microstructure of the alloy was rather subtle, it was essential to observe the microstructure in the alloy after further annealing at 725°C for the time of the irradiation, i.e. 2.5×10^{4}s (6.9 h) for 125 dpa. The microstructure of the alloy after the additional annealing is shown in Fig. 5.1.2. The microstructure is characterized by the presence within the individual grains of a large volume that has been cleared of the 7.5-nm diameter precipitates (Fig. 5.1.2a) These precipitates were transported during the additional anneaiing to the grain boundaries by interactions with the gliding dislocations (Fig. 5.1.2b).

TEM for the irradiated alloy

The microstructure in the V-15Cr-5Ti alloy after irradiation at 725°C with 4.0-MeV $^{58}Ni^{++}$ ions to 205 dpa is shown in Fig. 5.1.3. The crystallographic direction normal to the specimen surface is a <110> direction. A high density of features with a circular shape can be observed in the vicinity of the grain boundaries and the intrinsic precipitates and on the dislocations. These circular-shape features have an average diameter of 50 nm. A comparison of the microstructures in Figs. 5.1.2 and 5.1.3 show the effect of irradiation at 725°C to a damage level of 205 dpa. In the case of the circular features located on dislocations or in the vicinity of grain boundaries in the irradiated specimen, the circular shaoes appear to be contiguous with ~7.5-nm diameter precipitates. In contrast, the circular shapes in the vicinity of the intrinsic precipitates appear to contain small diameter precipitates within the circular shapes (Fig. 5.1.4). The density of the circular shapes within a 50-nm distance from the boundary of the intrinsic precipitates was ~4×10^{19}/m^{3}. The change in shape of the circular features on tilting is especially notable in Fig. 5.1.4. Also, the disappearance of the circular chapes and the appearance of white lobes at the position of the circular shapes are notable effects in Fig. 5.1.3.

The microstructure of a specimen after 4.0-MeV $^{58}Ni^{++}$ ion irradiation to 125 dpa is shown in Fig. 5.1.5. The microstructure in a specimen that was implanted with 780 appm helium (0.5-MeV $^{4}He^{+}$ ions) prior to irradiation with 4.0-MeV $^{58}Ni^{++}$ ions to 125 dpa is shown in Fig. 5.1.6. These microstructures are generally similar to the microstructure of the specimen irradiated to 205 dpa. The contiguity of the circular shapes on the dislocations is especially evident in Figs. 5.1.5 and 5.1.6. However, the average diameter of the circular features in the specimens irradiated to 125 dpa, with or without preinjection of helium, was approximately one-half the diameter in the specimen irradiated to 205 dpa.

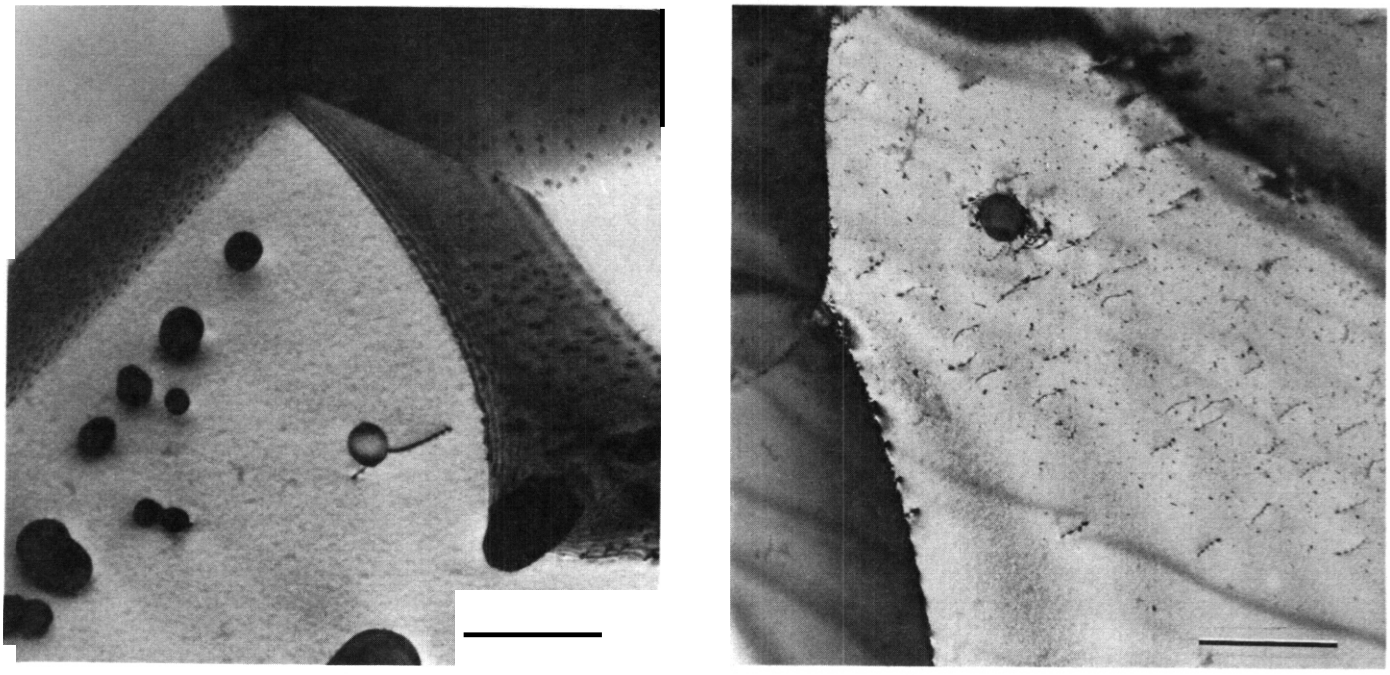

(a) (b)

Fig. 5.1.2. Microstructure of V-15Cr-5Ti alloy after additional annealing at 725°C for 2.5 x 10^4s (marker = 700 nm).

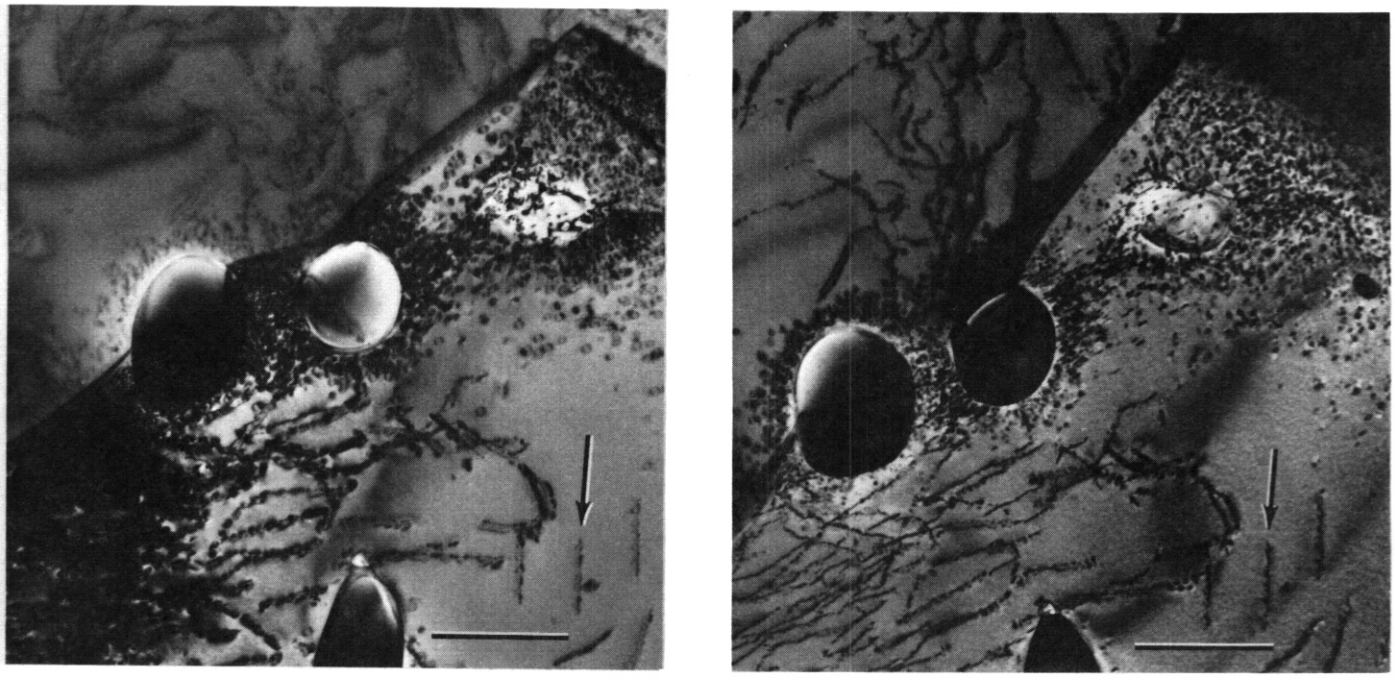

(a) (b)

Fig. 5.1.3. Microstructure of the V-15Cr-5Ti alloy after irradiation at 725°C with 4.0-MeV $^{58}Ni^{++}$ ions to 205 dpa for specimen inclinations of (a) -12.5° and (b) +3.5° (marker = 700 nm).

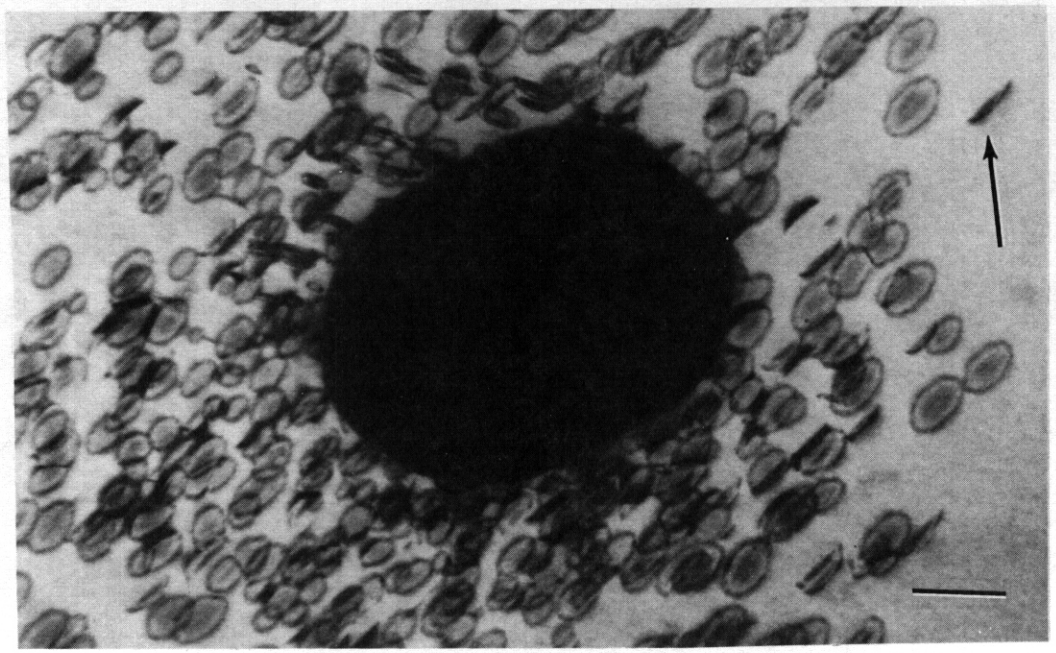

(a)

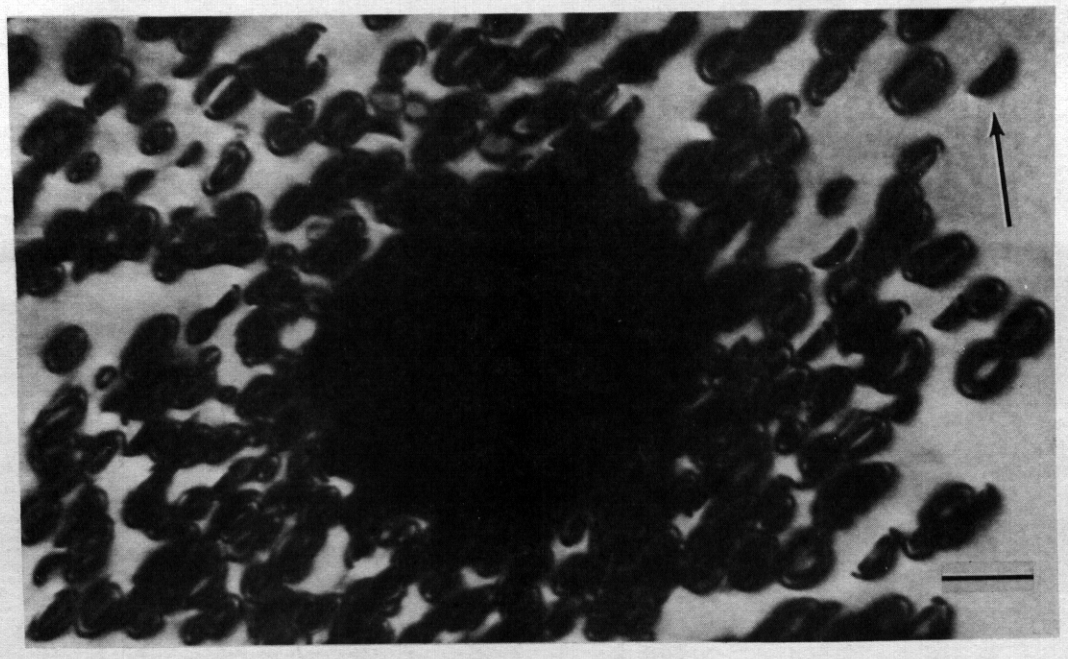

(b)

Fig. 5.1.4. Microstructure in the vicinity of intrinsic precipitates for specimen inclinations of (a) -8.0^{o} and (b) $+5.0^{o}$ from a specimen normal near to a <110> crystallographic direction (marker = 100 nm).

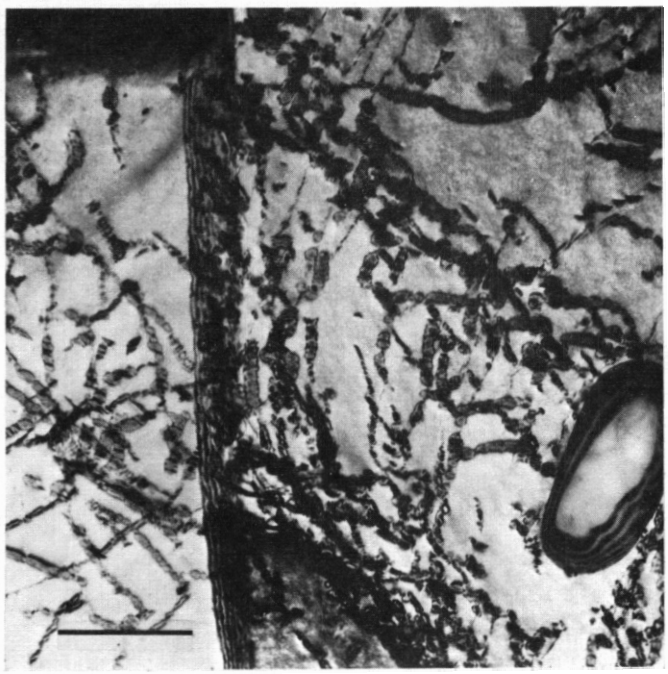

Fig. 5.1.5. Microstructure of V-15-Cr-5Ti after irradiation to 125 dpa with 4.0-Mev $^{58}Ni^{++}$ ions (marker = 400 nm).

Fig. 5.1.6. Microstructure of the V-15-Cr-5Ti after implantation with 780 appm helium and subsequent 4.0-MeV $^{58}Ni^{++}$ ion irradiation to 125 dpa (marker = 400 nm).

The microstructure of the dual-ion irradiated specimen (125 dpa, 9.3 appm He/dpa) is shown in Fig. 5.1.7. This microstructure is distinctly different from the microstructures of the single-ion irradiated specimens (Figs. 5.1.3 and 5.1.5) and the specimen implanted with helium prior to irradiation (Fig. 5.1.6).

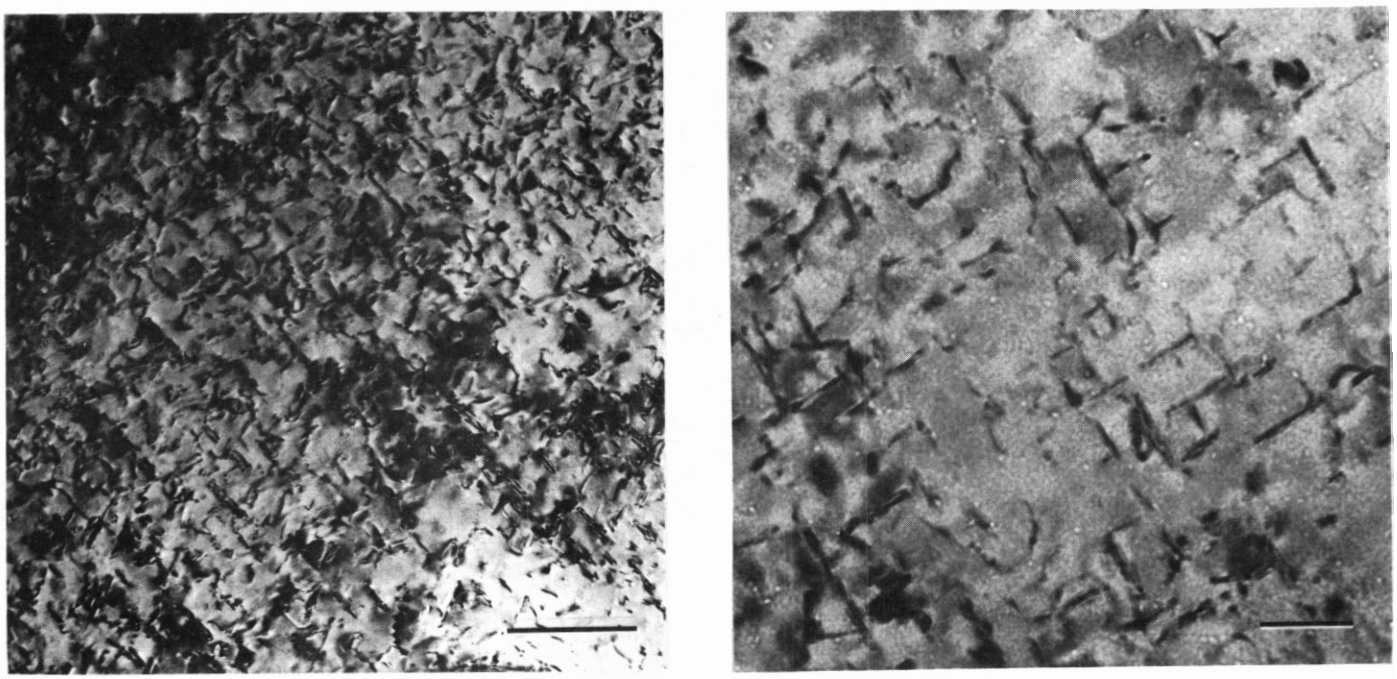

(a) (b)

Fig. 5.1.7. Microstructure of V-15Cr-5Ti alloy after irradiation to 125 dpa and simultaneous implantation of helium at a rate of 9.3 appm He/dpa (300 nm marker in (a) and 100 nm marker in (b)).

In the case of the dual-ion irradiated specimen, the features with a circular shape have an average diameter of < 8 nm and are aligned in short segments along orthogonal, <012> crystallographic directions. In addition, the presence of cavities with an average diameter of ~8 nm is clearly evident in Fig. 5.1.7.b. The number density of the cavities in this microstructure was estiiiiated to be $3 \times 10^{21}/m^3$.

5.1.5 Discussion

Swelling of the V-15Cr-5Ti alloy at 725°C was negligible at an irradiation dainage level of 125 dpa for either the pre-implanted helium (780 appm) or simultaneously implanted helium (9.3 appm/dpa) conditions. The swelling of the alloy at 725°C was also negligible on single-ion irradiation to a damage level of 205 dpa. Thus, the swelling of the V-15Cr-5Ti alloy, on the basis of these ion-irradiation results, should not be a concern in an MFR for irradiation damage levels to at least 125 dpa, which corresponds to ~11 $MW \cdot Y/m^2$.

The determination of the nature of the features with a circular shape that were profusely sited on dislocations is believed to be important for evaluation of the potential usefulness of the V-15Cr-5Ti alloy in an MFR. The interaction of these features with the dislocations may result in embrittlement of the alloy. The change in shape of the circular features (Figs. 5.1.3 and 5.1.4) together with the disappearance of the circular shapes and appearance of white lobes on TEM tilting (Fig. 5.1.3) suggest strongly that these features are thin discs of precipitate.[5] To consider the contiguous features in long stringers, e.g., in Fig. 5.1.5, to be voids is incompatible with their 25-nm diameter and the 100-nm thickness of the TEM specimen. If it is assumed that the circular features are discs of precipitate, then their thickness may be estimated from the discs on edge in Fig. 5.1.4(a). This estiinate gives a thickness value of < 10 nm.

The average diameter of the discs increased from ~25 nm to ~50 nm with an increase of the dainaye level from 125 dpa to 205 dpa. The magnitude of the increase in diameter suggests that the disc-shape precipitates were extremely effective sinks for the mobile solute atoms. The average diameter of the disc-shape precipitates in the specimen irradiated with dual-ions to 125 dpa was < 8 nni. The substantially smaller diameter of the discs in the dual-ion irradiated microstructure at 125 dpa implies that the helium atoms were extremely effective in limiting the diffusion of solute atoms.

5.1.6 Conclusions

1. Swelling of the V-15Cr-5Ti alloy at 725°C was negligible at an irradiation damage level of 125 dpa for either the pre-implanted helium (780 appm) or simultaneously implanted helium (9.3 appm/dpa) conditions. The swelling of the alloy at 725°C was also negligible on single-ion irradiation to a damage level of 205 dpa.

2. The principle effect on the microstructure of the irradiations was to induce the formation of a high density of disc-shape precipitates in the vicinity of grain boundaries and intrinsic precipitates and on the dislocation structure.

5.1.7 References

1. R. Carlander, S. D. Harkness and A. T. Santhanam, "Effects of Fast-Neutron Irradiation on Tensile Properties and Swelling Behavior of Vanadium Alloys", pp. 399-414 in *Effects of Radiation on Substructure and Mechanical Properties of Metals and Alloys*, ASTM-STP-529, American Society for Testing and Materials, 1973.

2. A. F. Bartlett, J. H. Evans, B. L. Eyre, E. A. Terry and T. M. Williams, "High Temperature Irradiation Damage Structures in Fast Reactor Irradiated Niobium and Vanadium Alluys", pp. 122-129 in *Radiation Effects and Tritium Technology for Fusion Reactors*, vol. I, J. S. Watson and F. W. Wiffen, Eds. (1976).

3. B. A. Loomis and G. Ayrault, "Cavity Formation in Single- and Dual-Ion Irradiated V-15Cr-5Ti Alloy", pp. 194-205 in *Damage Analysis and Fundamental Studies Quarterly Progress Report*, October–December 1982, DOE/ER-0046/12, U. S. Department of Energy, Office of Fusion Energy.

4. J. P. Biersack and L. G. Haggmark, "A Monte Carlo Computer Program for the Transport of Energeti Ions in Amorphous Targets", *Nuclear Instruments and Methods* 174, 257-269 (1980).

5. M. Ruhle, "Transinission Electron Microscopy of Radiation-Induced Defects", pp. 255-291 in *Radiation-induced voids in Metals*, AEC Symposium Series 26, 1972.

5.2 HELIUM DOPING OF A VANADIUM ALLOY BY A MODIFIED TRITIUM TRICK — D. N. Braski and D. W. Ramey (flak Ridge National Laboratory)

5.2.1 ADIP Task

ADIP Task I.B.15 Tensile Properties of Reactive and Refractory Alloys.

5.2.7 Objective

The goal of this work is to develop a suitable method of doping vanadium tensile specimens with helium. With a successful method, a better simulation of fusion conditions will be attained for specimens that are irradiated in the Materials Open Test Assembly (MOTA) experiment in the Fast Flux Test Facility (FFTF).

5.2.3 *Summary*

A tritium trick technique was used to implant ^3He in V-15Cr-5Ti. Modifications include wrapping specimens with tantalum foil and decay hold at 400°C. Removal of undecayed tritium at 700°C may have been excessive, because large helium bubbles in the grain boundaries severely embrittled the V-15Cr-5Ti alloy. More realistic helium distributions can probably be produced by reducing the removal temperature. The technique might facilitate the study of helium embrittlement and provide a screening method for alloy development.

5.2.4 Progress and Status

5.2.4.1 Introduction

In order to better simulate the first wall conditions that are expected with fusion reactor irradiation, it is sometimes necessary to implant helium in the test alloy before irradiation. One method of preimplanting helium is the so-called "tritium trick," where specimens are saturated with tritium, which is allowed to decay to ^3He. The tritium trick was selected as the method of implanting vanadium alloys for the MOTA experiments in the FFTF. The tritium trick technique has the advantages of being able to quickly and inexpensively dope large numbers of specimens with high concentrations of ^3He without specimen thickness limitations. This allows use of thick mechanical properties specimens.' An excellent description of the tritium trick has been presented by Remark et al.[2] A disadvantage of the technique is that, under neutron irradiation, a significant fraction of the ^3He is converted back to tritium.

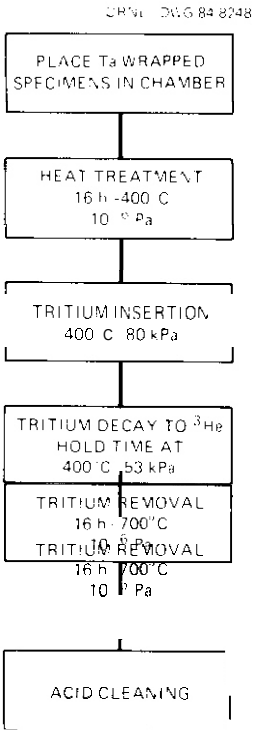

Fig. 5.2.1. Tritium trick flow chart for vanadium alloy specimens.

5.2.4.2 Experimental

Disks (3-mm diameter) and small sheet tensile specimens of the SS-3 type (gage section = 1.6 mm long × 1.5 mm wide × 0.84 mm thick) were first cleaned ultrasonically in methanol and then wrapped in three separate layers of tantalum foil (0.05 mm thick) to minimize oxygen contamination. The wrapped specimens were placed in the tritium chamber and the chamber pumped down to less than 0.5 Pa with a mechanical pump. This step is represented by the first block of the flowchart shown in Fig. 5.2.1. Next, the specimens were heated to 400°C for 16 h under a vacuum (~10^{-6} Pa) provided by *ion* pumping. This pretreatment (i.e., heating under good vacuum) has been shown to influence the metal surfaces and aid tritium takeup. The tritium was inserted at a pressure of 80 kPa (600 mm Hg) while the specimens were still at 400°C. As the tritium was absorbed by the vanadium alloy specimens (and also the tantalum foil), the chamber pressure dropped. More tritium was bled in to raise the pressure above 53 kPa (400 m Hg) and it was also absorbed. After several chargings of tritium, the system was controlled so that an equilibrium pressure of 53 kPa was established. The specimens were held at the 53 kPa pressure and 400°C to allow the absorbed tritium to decay to ^3He. The half-life for tritium decay is 12.26 years, which yields about 0.54 decay per month.[2] In this experiment, specimens were held for 20, 120, and 400 h to produce three different ^3He levels in the alloys. At the end of the decay period, undecayed tritium in the vanadium alloys was removed by reducing the chamber pressure to about 10^{-6} Pa and pumping at 700°C for 16 h. The specimens were subsequently cleaned in an acid bath consisting of one part concentrated HNO_3, one part HF, and one part H_2O, by volume, to remove tritium surface contamination. Analvsis involvinq metal solution and scintillation counting showed that the resibual radioactivity level in the alloy was only 5×10^{-4} Ci/g (<1 at. ppm tritium).

5.2.4.3 Results

The actual ^3He levels in V-15Cr-5Ti for the 20, 120, and 400 h decay times were 14, RO, and 303 at. ppm, respectively. These values were determined by Brian Oliver at Rockwell International, Canoga Park, California, using a high-sensitivity mass spectrometer system. Good ^3He homogeneity through the

thickness and across the specimens was attained, but on a microscale, larger ^3He bubbles were formed on grain boundaries than in the matrix [see Fig. 5.2.2(*a*)]. The ^3He bubbles also formed preferentially at particle-matrix interfaces [Fig. 5.2.2(*b*)]. There was no sign of tritide formation in the microstructure. The effect of the ^3He doping on the tensile properties of V-15Cr-5Ti tensile specimens (SS-3 type) is shown in Fig. 5.2.3. With no ^3He, the alloy exhibited a serrated stress-strain curve (probably caused by dynamic strain aging) and had a total elongation of approximately 24%. This value was reduced only slightly by

E-46295 E46315

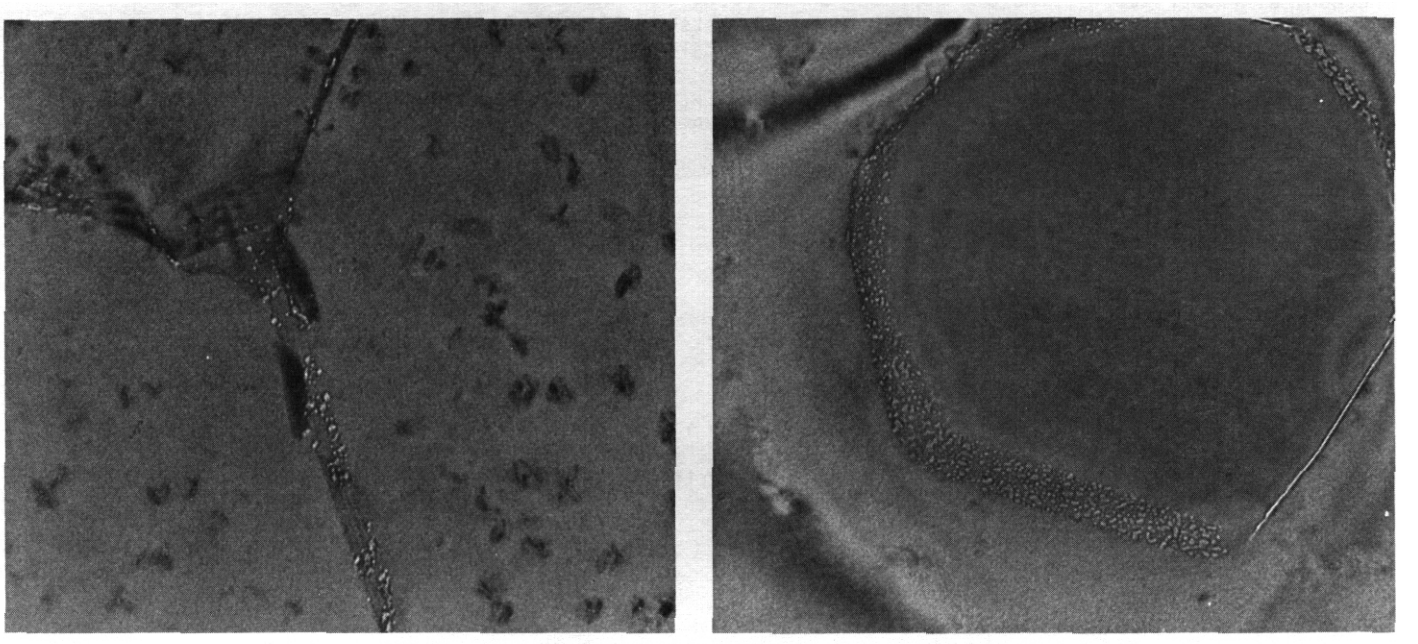

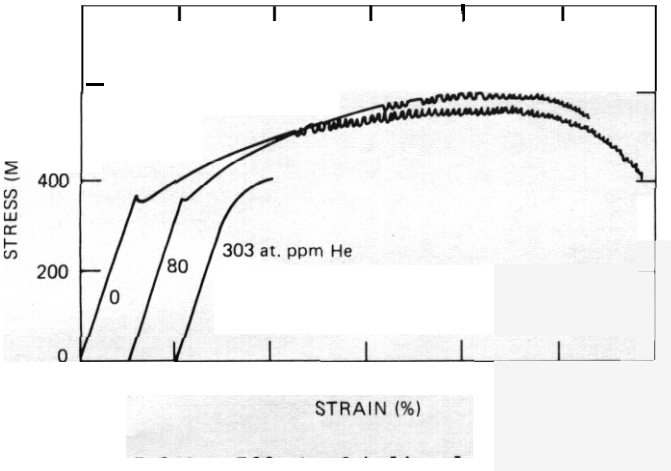

were entirely intergranular. The microstructural observation of large ^3He bubbles on the grain boundaries provides strong evidence that the helium

which hydrogen instead of tritium was used in the same system; V-15Cr-5Ti specimens showed only some minor losses in ductility after going through the same procedure used to produce 303 at. ppm ^{3}He. The measured oxygen level in V-15Cr-5Ti specimens increased by about 500 at. ppm after annealing in hydrogen, and we have assumed that the 2 to 3% losses of total elongation at 600°C were due to this additional oxygen pickup. Since the alloy also picked up about 500 at. ppm oxygen during the tritium trick, a similar ductility loss can be attributed to that treatment.

5.2.5 References

1. D. G. Atteridge et al., "Effects of Helium Implanted by Tritium Decay on the High Temperature Mechanical Properties of Niobium," pp. 307–30 in *Proc. Int. Conf. on Radiation Effects and Tritium Technology for Fusion Reactors*, Vol. II, ed. J. S. Watson and F. W. Wiffen, CONF-750989, 1975.

2. J. F. Remark et al., "Helium Charging of Metals by Tritium Decay," *Nucl. Technol.* 29, 369–77 (1976).

3. R. E. Gold, "Mechanical Property Evaluation of Path C Vanadium Scoping Alloys," pp. 291–303 in *ADIP Semiannu. Frog. Rep. Mar. 31, 1982*, DOE/ER-0045/8, U.S. DOE, Office of Fusion Energy.

5.3 ENVIRONMENTAL EFFECTS ON THE PROPERTIES OF VANADIUM-BASE ALLOYS - D. R. Diercks and D. L. Smith (Argonne National Laboratory)

5.3.1 ADIP Task

ADIP Task I.A.3, Perform Chemical and Metallurgical Compatibility Analyses.

5.3.2 Objective

The objective of this task is to experimentally evaluate the corrosion behavior of selected vanadium-base alloys in a number of aqueous, liquid metal, and gaseous environments. The results of these investigations will be utilized in the selection of appropriate vanadium-base alloys for structural applications in fusion reactors.

5.3.3 Summary

A pressurized-water refreshed autoclave system for experimentally investigating the aqueous corrosion behavior of selected vanadium-base alloys has been designed, constructed, and checked out. Test specimen material has been obtained from the ORNL Fusion Program Research Materials Inventory and sheared into corrosion coupons. A scanning Auger microprobe study of sulfur segregation in vanadium-base alloys has also been initiated.

5.3.4 Progress and Status

5.3.4.1 Aqueous Corrosion Behavior of Vanadium-Base Alloys

Blanket cooling by means of circulating pressurized water is being considered as a possible fusion reactor configuration. A water coolant offers excellent heat transfer characteristics, and it enjoys a well-developed technology from commercial fission reactor experience. However, the aqueous corrosion behavior of vanadium-base alloys, particularly in oxygenated pressurized-water systems at elevated temperatures, is not well known. Available data and information will be briefly reviewed here.

Early studies were conducted on the aqueous corrosion behavior of unalloyed vanadium at 35°C by the U. S. Bureau of Mines.[1,2] These studies determined the metal to be very resistant to corrosive attack by aerated ocean water, a 3% NaCl solution, and tap water, with observed corrosion rates of 0.018 mm/y (0.7 mils/y) or less in all three solutions. For the same solutions in the nonaerated conditions, corrosion rates were undetectable. A subsequent investigation was conducted on the susceptibility to stress-corrosion cracking of unalloyed vanadium in a variety of organic and inorganic acids and inorganic salt solutions.[3] Vanadium was found to resist stress-corrosion cracking in most of the solutions tested after 30 days of exposure at 35°C; however, U-bend specimens showed evidence of transgranular stress-corrosion cracking in 6-N HCl and 18-N H_2SO_4 solutions.

Preliminary studies of the aqueous corrosion behavior of selected vanadium-base alloys at elevated temperatures have recently been conducted at both ANL[4] and ORNL' In the first investigation, V-15Cr-5Ti and V-15Cr were exposed for about 85 h to pressurized, 250°C water containing 0.04 ppm dissolved O_2 in a refreshed autoclave system. The V-15Cr alloy specimens experienced about a 0.8 $\mu g/cm^2$ weight gain while the V-15Cr-5Ti specimens gained 23.0 $\mu g/cm^2$. In the second investigation, V-15Cr-5Ti, V-20Ti, and Vanstar-7 specimens were exposed for 100 h in 300°C water with hydrogen gas overpressures of 0 and b3 kPa (12 psi). Weight changes in all cases were less than 200 $\mu g/cm^2$, and no effect of the hydrogen overpressure on corrosion rate was observed.

The objective of the present activity is to develop a more extensive data base on the corrosion behavior of candidate vanadium-base alloys in elevated-temperature pressurized water containing controlled levels of dissolved oxygen and other impurities. As a first step, a pressurized-water refreshed autoclave system has been designed and constructed. The basic configuration of this system is shown in Fig. 5.3.1. High-purity distilled water (conductivity ~0.1 $\mu S/cm$) is Supplied to a 114-L (30-gal)-capacity Type 304 stainless steel solution-mixing tank. Here the dissolved oxygen content of the water can be controlled within a range of about 10 ppb to 40 ppm by bubbling either N_2 gas through it for deaeration or various N_2-O_2 gas mixtures for aeration. Through suitable valving, the water solution from the tank is then supplied to the autoclave by a low-capacity high-pressure pump. before entering the autoclave, the water passes through heat exchanger and preheater stages so that it enters the autoclave at approximately the desired operating temperature. The solution temperature in the autoclave is maintained within about ±1°C by a two-zone furnace and an electronic controller system. The water enters the 7.6-L (2-gal) autoclave at the bottom and exits near the top through a standpipe. A convector baffle placed in the autoclave provides proper circulation of the solution ana good uniformity of temperature (less than 2°C variation from top to bottom). The corrosion test specimens are suspended in the autoclave from a self-supporting rack.

A series of electrochemical potential electrodes, not shown in Fig. 5.3.1, is installed in the exit water line immediately in front of the heat exchanger. These electrodes include an Ag/AgCl reference electrode, a Pt counter electrode, and V-15Cr-5Ti and V-20Ti working electrodes (Vanstar 7 was not available in a suitable form for fabricating an electrode). To help gather potential data. a heating element and thermocouple are installed near the electrodes to maintain the same solution temperature as in the autoclave. The solution then passes through the heat exchanger to preheat the incoming solution to the autoclave before being discharged. A backpressure regulator installed in the discharge line maintains system pressure.

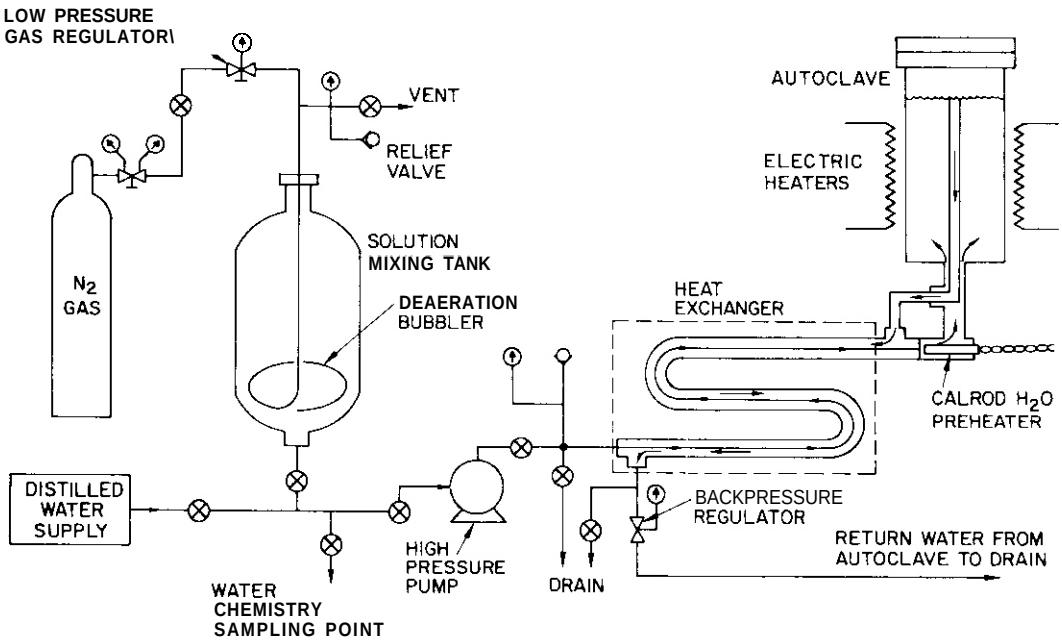

Fig. 5.3.1. Diagram of pressurized-water refreshed autoclave system to be used for ANL aqueous corrosion studies on vanadium-base alloys.

After construction of the autoclave system was completed, the system was run for two weeks at 288°C (550°F) and 8.3 MPa (1200 psi) pressure. The purpose of this run was to preoxidize the internal components of the system and to verify its long-term control stability. During and after this checkout run, minor system leaks were repaired and misadjustments in the system were corrected. The pressurized-water refreshed autoclave system is operational and the first series of corrosion tests has been initiated.

Test specimen material has been obtained from the Fusion Program Research Materials Inventory as well as from the old ANL LMFBR inventory. The material obtained from the fusion heat consists of 0.76-mm (0.030-in.)-thick sheets and 6.35-mm (0.250-in.1-diameter rods of V-15Cr-5Ti, V-20Ti, and Vanstar-7. The sheet material has been sheared into penetration and weight-change corrosion coupons and has been cleaned and weighed in preparation for the first series of exposures. The rod will be used for subsequent CERT (constant-extension rate) stress-corrosion cracking testing. The material obtained from the ANL LMFBR stocks consists of 1.52-mm (0.060-in.)-thick sheets of V-15Cr-5Ti and V-20Ti. This material has also been sheared into penetration and weight-change corrosion coupons.

5.3.4.2 Segregation of Sulfur in Vanadium-Base Alloys

Westinghouse has completed a series of post-exposure examinations of V-15Cr-5Ti sheet specimens from the ORR-MFE-2 irradiation experiment that had accumulated a damage level of approximately 5 dpa.[6] The specimens were irradiated at 375, 550, and 600°C, and the postirradiation tensile, hardness, and microstructural characteristics of the test specimens were evaluated. A number of nonirradiated control specimens were also tested. Because the specimens had been irradiated in a stagnant sodium-filled stainless steel capsule, there was concern over whether nonmetallic contamination might have occurred and affected the results of the experiment. The specimen material for this experiment was identified as being from heat HSV-207, R1301, and a bulk chemical analysis is given in Table 5.3.1.

Table 5.3.1. Bulk Chemical Analysis of V-15Cr-5Ti Material from Heat HSV-207, R1301. All compositions are given in weight percent.

Cr	13.3
Ti	4.07
O	0.103
C	0.016
N	0.0087
V	Bal.

Included in the Westinghouse examinations were a series of scanning Auger microprobe (SAM) analyses of fracture surfaces from irradiated and nonirradiated sheet specimens. The specimens were notched and subsequently fractured by impact loading in situ in the SAM chamber at room temperature. The nonirradiated specimen exhibited considerable deformation during fracture, whereas the irradiated specimen fractured at a relatively low load with little deformation. Both specimens displayed transgranular cleavage. The SAM analyses of these freshly formed fracture surfaces revealed somewhat higher levels of oxygen, carbon, and nitrogen than would be expected based upon the bulk chemical analysis of the alloy, suggesting some preferential segregation of these interstitial elements to the fracture surface. Most surprising, however, was the detection of significant levels of sulfur at the fracture surfaces. Sulfur was detected at levels of the order of 3 to 3.5 wt% on the fracture surfaces of both the irradiated and nonirradiated specimens, even though sulfur is not indicated in the bulk analysis. No explanation was offered for this unexpected finding.

In view of the relevance of the Westinghouse findings to the present vanadium alloys testing program, experiments were conducted at ANL in an attempt to duplicate the Westinghouse results. Two 44.45-mm (1.75-in.)-long miniature tensile specimens of nonirradiated V-15Cr-5Ti from heat HSV-207, R1301 were obtained fran Westinghouse. The gauge sections of these specimens were carefully cut out, notched, and mounted in the fracture stage of the SAM. Fracture was accomplished at liquid nitrogen temperature in situ. Both specimens displayed mixed intergranular/transgranular cleavage type fractures with relatively little ductility. The typical fracture surface appearance is shown in Fig. 5.3.2 with higher magnification views of transgranular and intergranular regions shown in Figs. 5.3.3 and 5.3.4, respectively.

SAM analyses were performed on both transgranular and intergranular fracture surfaces. A typical result obtained fran a region of transgranular cleavage fracture is shown in Fig. 5.3.5. Vanadium, chromium. and titanium peaks show up as expected, and a prominent carbon peak is also present (note that the vertical scale is magnified by a factor of four for Auger electron energies below 350 eV). However, no sulfur peak, normally located at –140 to 150 eV, is visible.

A similar analysis for a region of intergranular fracture is shown in Fig. 5.3.6. The same peaks seen in the transgranular region are present here, but, in addition, a very prominent sulfur peak is present. Based upon the relative peak heights present in Fig. 5.3.6 and those obtained from calibrated standards, the sulfur content present on and within a few atom layers of the intergranular fracture surface is estimated to be greater than 10 wt %. By comparison, a chemical analysis of the end pieces from the two miniature tensile specimens performed at ANL revealed the bulk sulfur content of the alloy to be less than 0.02 wt %.

The ANL analyses thus confirm a tendency for sulfur segregation in this V-15Cr-5Ti alloy. Unlike the Westinghouse results, however, segregation only to intergranular reaions was seen, with regions of transgranular cleavage fracture showing no detectable sulfur levels. In the Westinghouse study, the specimens fractured transgranularly. and relatively high sulfur levels were found at these fracture surfaces.

Follow-on studies on sulfur segregation are planned at ANL using vanadium-base alloy material obtained from the Fusion Program Research mterials Inventory as well as from the old ANL LMFBR inventory. In situ SAM fracture specimens have been fabricated fr'an alloys obtained from these two sources.

5.3.5 References

1. D. Schlain, C. B. Kenahan. and W. L. Acherman, "Corrosion Behavior of High Purity Vanadium," Corrosion 16, 114-116 (1960).

2. D. Schlain, C. B. Kenahan, and W. L. Acherman, 'Corrosion Properties of High-Purity Vanadium," J. of Less-Common Metals 3, 458-467 (1961).

3. J. P. Carter, C. B. Kenahan, and D. Schlain, "Stress Corrosion Cracking of Vanadium, Molybdenum, and a Titanium-Vanadium Alloy." U. S. Bureau Of Mines Report of Investigations 6680 (1966).

4. O. K. Chovra. D. L. Smith, and W. E. Ruther, "Environmental Effects on the Properties of Structural Alloys." pp. 497-499 in Alloy Development for Irradiation Performance: Semiannual Progress Report for the Period Ending March 31, 1982, Oak Ridge National Laboratory, DOE/ER-0045/8.

5. P. F. Tortorelli and J. H. Devan, "Compatibility of Vanadium Allovs with High-Temperature Water." pp. 201-203 in Alloy Development for Irradiation Performance: Semiannual Progress Report for the Period' Ending March 31, 1983, Oak Ridge National Laboratory, DOE/ER-0045/10.

6. R. Bajaj and R. E. Gold, "Evaluation of V-15Cr-5Ti Specimens after Neutron Irradiation in the MFE-2 Experiment, Phase 1 Final Report," Westinghouse Electric Corporation, Advanced Energy Systems Division, August 1983.

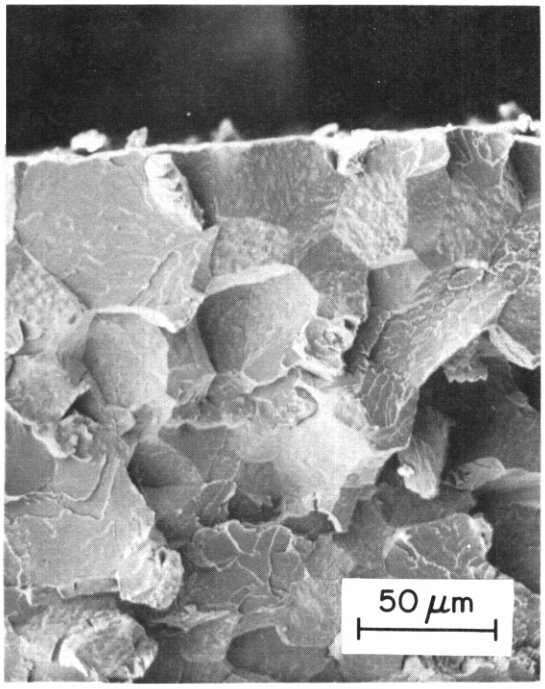

Fig. 5.3.2. Region of mixed intergranular and transgranular fracture observed in specimen fractured in situ in ANL scanning Auger microprobe.

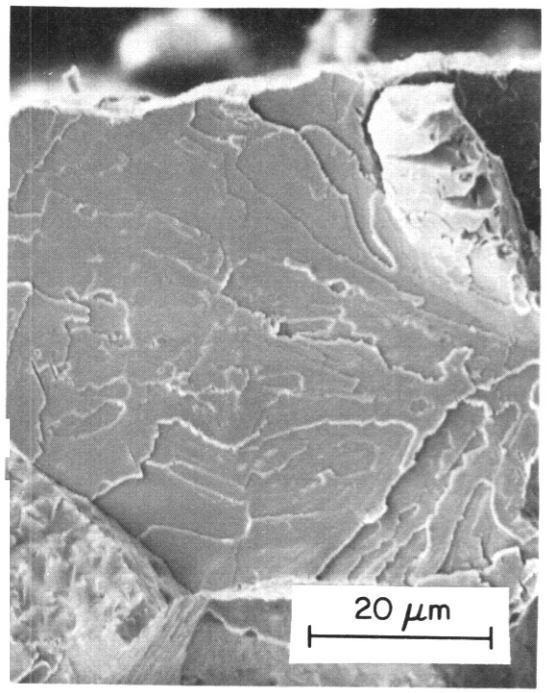

Fig. 5.3.3. Higher magnification (1500X) view of portion of fracture surface of Fig. 5.3.2, showing showing a region of transgranular cleavage fracture.

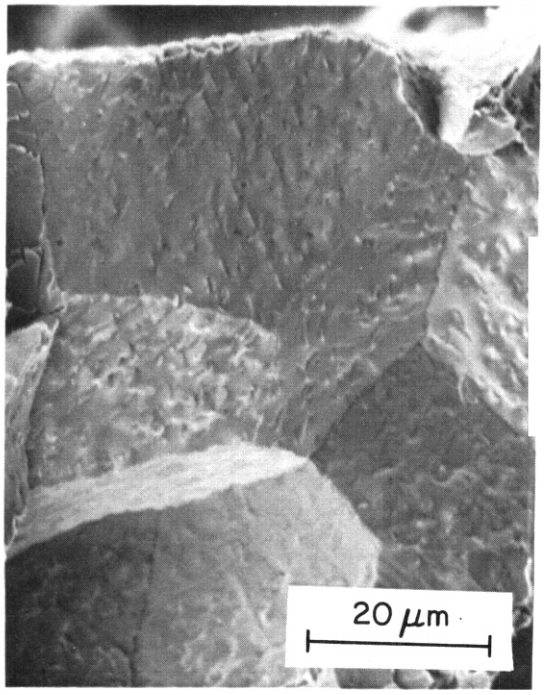

Fig. 5.3.4. Higher magnification (1500X) view of portion of fracture surface of Fig. 5.3.2, showing a region of intergranular fracture.

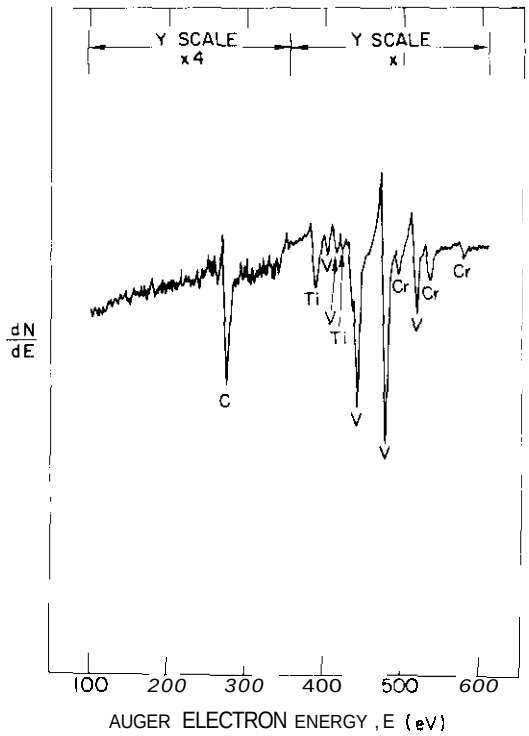

Fig. 5.3.5. Typical SAM analysis obtained from a region of transgranular cleavage fracture.

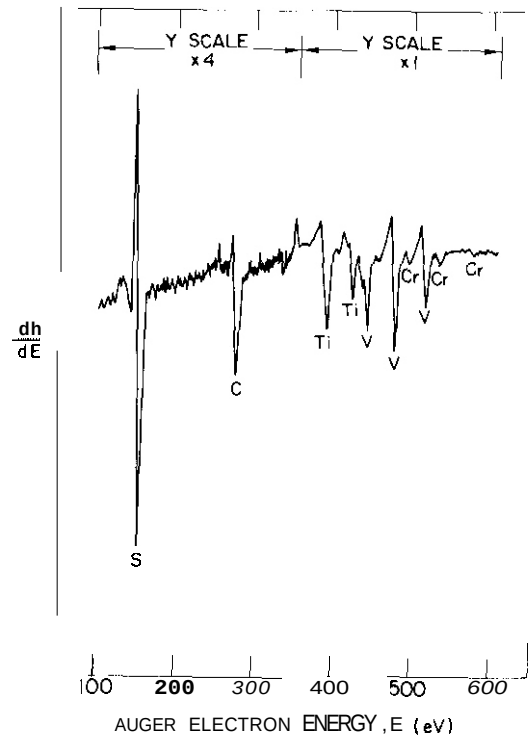

Fig. 5.3.6. Typical SAM analysis obtained from a region of intergranular fracture.

6. INNOVATIVE MATERIAL CONCEPTS

6.1 THE TENSILE PROPERTIES AND BEND DUCTILITY OF $(Fe,Ni)_3V$ LONG-RANGE-ORDERED ALLOYS AFTER IRRADIATION IN HFIR — D. N. Braski (Oak Ridge National Laboratory)

6.1.1 ADIP Task

ADIP Task I.B.13, Tensile Properties of Special and Innovative Materials.

6.1.2 Objective

The objective of this work is to determine the effect of neutron irradiation on the tensile properties and bend ductility of $(Fe,Ni)_3V$ long-range-ordered (LRO) alloys.

6.1.3 *Summary*

Several $(Fe,Ni)_3V$ LRO alloys were irradiated in HFIR-CTR-42 and -43 at 400 to 600°C, *to* approximately 10 dpa and approximately 1000 at. ppm He. Additions of cerium or carbon and the use of cold-worked microstructures did not improve the embrittlement resistance of the LRO alloys. The LRO-37-5RS alloy, with a microstructure produced by rapid solidification, exhibited the highest ductilities, and further study of the RS microstructure is warranted. The correlation between bend ductility and tensile ductility was poor.

6.1.4 Progress and Status

6.1.4.1 Introduction

Irradiation in the HFIR-CTR-30 to -32 experiments produced severe embrittlement in the $(Fe,Ni)_3V$ LRO alloys. The embrittlement was believed to be caused by one or more of the following factors: (1) helium in the grain boundaries, (2) the precipitation of VC in the grain boundaries, and (3) segregation *of* elements, such as sulfur, to the grain boundaries.' In the HFIR-CTR-42 and -43 experiments, several changes in alloy composition and/or microstructure were made to determine if a more embrittlement-resistant LRO alloy could be designed. The first alloy, LRO-42, was melted with an addition of 0.16 wt % Ce, designed to tie up any segregating elemental species. The alloy was irradiated in both the annealed and cold-worked conditions. The second alloy, LRO-37, was irradiated in two different conditions: (1) a rapidly solidified condition (LRO-37-5RS) to refine the VC particles in the microstructure, and (2) a higher carbon (0.1 wt % C) content version (LRO-37C) to increase the number of VC particles. Both tensile and disk-bend tests were performed after irradiation to determine if any of these LRO alloys resisted embrittlement better than did those previously tested.

6.1.4.2 Experimental

The composition in weight percent and condition of each LRO alloy are given in Table 6.1.1. Standard High Flux Isotope Reactor (HFIR) tensile specimens with a 18.3-mm gage length and a 2-mm gage diameter were machined from 5-mm-diam swaged stock for the LRO-42 alloy. Disks (3 mm diam × 0.25 mm thick) were cut from 3-mm-diam rods of LRO-42 and -37C and electrical discharge machined from gas-tungsten-arc (GTA) welds of LRO-37-5RS sheet material. The specimens were encapsulated in quartz tubes under 50 kPa (0.5 atm) He and

Table 6.1.1. Composition of long-range-ordered alloys

Alloy	Composition[a] (wt %)					Condition
	Ni	V	Ti	C	Ce	
LRO-42	39.7	22.8	0.3	0.01	0.16	Annealed 15 min at 1100°C. quenched into water, then 2 d at 600°C (ordered structure)
						Sane heat treatment, plus 254 cold work
LRO-37-5RS	39.6	22.5	0.3	0.03		Disks were cut from fusion zone of a gas tungsten arc weld (disordered)
LRO-37C	40.0	22.0	0.4	0.1		Ordered — same heat treatment as LRO-42 above

[a]Balance iron.

annealed as shown in Table 6.1.1. The LRO-37-5RS disks were not given an ordering anneal but would have reordered during the irradiation at elevated temperature. The specimens were irradiated at 400 to 600°C in the HFIR-CTR-42 and -43 experiments to a damage level of approximately 10 dpa and a helium level of approximately 1000 at. ppm. These values are the estimated response to the irradiation. Detailed calculation of neutron fluence and material response will be reported later. After irradiation, the tensile specimens were tested under vacuum ($<10^{-4}$ Pa) at the irradiation temperatures. The disks were bend tested[2] at their irradiation temperatures with the same test apparatus. A crosshead speed of 0.51 mm/min (0.02 in./min) was used in both types of test. Bend ductility was estimated from the expression:[2]

$$\varepsilon = tw/(a^2 + 3) ,$$

where

ε = strain,
t = disk thickness,
a = disk radius, and
w = deflection.

6.1.4.3 Results

The results of the postirradiation tensile tests are listed in Table 6.1.2. The tensile properties of an unirradiated LRO-42 control specimen that was aged at 600°C for 5000 h is also given. At 600°C, irradiation caused the yield strength to nearly double, with a drastic loss in total elongation. The identical values of uniform and total elongation indicate that virtually no necking took place prior to fracture. Note also that the ultimate tensile strength was only slightly greater than the yield strength. This type of tensile behavior would indicate that irradiation hardening had occurred, along with a mechanism that weakened the grain boundaries. It would seem that the cerium addition to LRO-42 did little to resist the embrittlement. The fracture surfaces have not yet been examined by scanning electron microscopy (SEM), but it is expected that they will be characteristic of intergranular failure because similar LRO alloys in HFIR-CTR-30 to -32 showed this type of fracture at approximately 10 dpa in HFIR (ref. 1). An embrittlement mechanism involving strengthened or hardened grain matrices and weakened grain boundaries was proposed for the path B nickel alloys.[3] The effect of irradiation in the 25%-cold-worked LRO-42 is shown in the data at 500°C; as expected, the stronger and less ductile behavior was exhibited by the cold-worked specimens.

Table 6.1.2. Tensile test results for LRO-42 irradiated in HFIR-CTR-42 and -43 (~10 dpa)

Specimen	Condition	Test temperature (°C)	Stress (MPa)		Elongation (%)	
			Yield	Ultimate tensile	Uniform	Total
		Irradiated at test temperature				
VH-1	Annealed	600	912	926	0.3	0.3
VJ-2	254 cold worked	500	1241	1386	1.5	1.5
VJ-3	254, cold worked	500	1361	1390	1.7	1.7
VH-2	Annealed	500	961	1128	2.9	2.9
VJ-4	254, cold worked	400	1143	1269	1.7	2.3
		Aged at 600°C for 5000 h				
VH-3	Annealed	600	534	1014	15.4	24.0

The results of the disk-bend tests for all four LRO alloys are given in Table 6.1.3. Although the number of specimens was limited, there is a clear indication that the LRO-37 in the rapidly solidified condition offered considerably more resistance to embrittlement than did the other LRO alloys. The addition of cerium or carbon or using a cold-worked microstructure was not effective in reducing embrittlement. At 600°C the LRO-37-5RS disk exhibited a 0.178-mm deflection and 2.0% bend ductility, and at 500°C it went to the "maximum" deflection of 0.51 mm without fracturing. These bend ductilities are also greater than any of those measured for LRO alloys in the HFIR-CTR-30 to -32 experiments.' The effect of the rapid solidification is to refine the VC particle size and distribute the particles on matrix dislocations as well as on the grain boundaries, as shown in Fig. 6.1.1. In this case, the microstructure was produced by rapid melting and cooling of the metal in a welding process,[4] but it could just as well be produced by other rapid

solidification techniques. A special technique such as rapid solidification is needed to refine the VC particle size because, unlike TiC particles in austenitic stainless steel, VC is too stable to be dissolved by a high-temperature solution annealing treatment. In any case, the performance of the LRO-37-5RS is encouraging and further study of the RS microstructure is certainly warranted. The correlation between bend ductility and tensile ductility was poor.

Table 6.1.3. Disk bend test results on long-range-ordered alloys irradiated in CTR-42 and -43 (~10 dpa)

Disk	Alloy	Condition	Irradiation and test temperature (°C)	Deflection (mm)	Ductility (%)	
					Bend	Tensile
VL-1	LRO-37-5RS	Weld zone	600	0.178	2.0	
VK-1	LRO-37C	High C	600	0.051	0.6	
VK-2	LRO-37C	High C	600	0.025	0.3	
VH-1	LRO-42	Annealed	600	0	0	0.3
VH-2	LRO-42	Annealed	600	0.013	0.1	
VJ-1	LRO-42	25% Cold worked	600	0	0	
VJ-5	LRO-42	25% Cold worked	600	0	0	
VL-4	LRO-37-5RS	Weld zone	500	Maximum		
VK-4	LRO-37C	High C	500	0.038	0.4	
VK-5	LRO-37C	High C	500	0.019	0.2	
VH-5	LRO-42	Annealed	500	0.025	0.3	2.9
VH-6	LRO-42	Annealed	500	0.028	0.3	
VJ-2	LRO-42	25% Cold worked	500	0.019	0.2	1.5
VJ-4	LRO-42	25% Cold worked	500	0.030	0.3	1.7

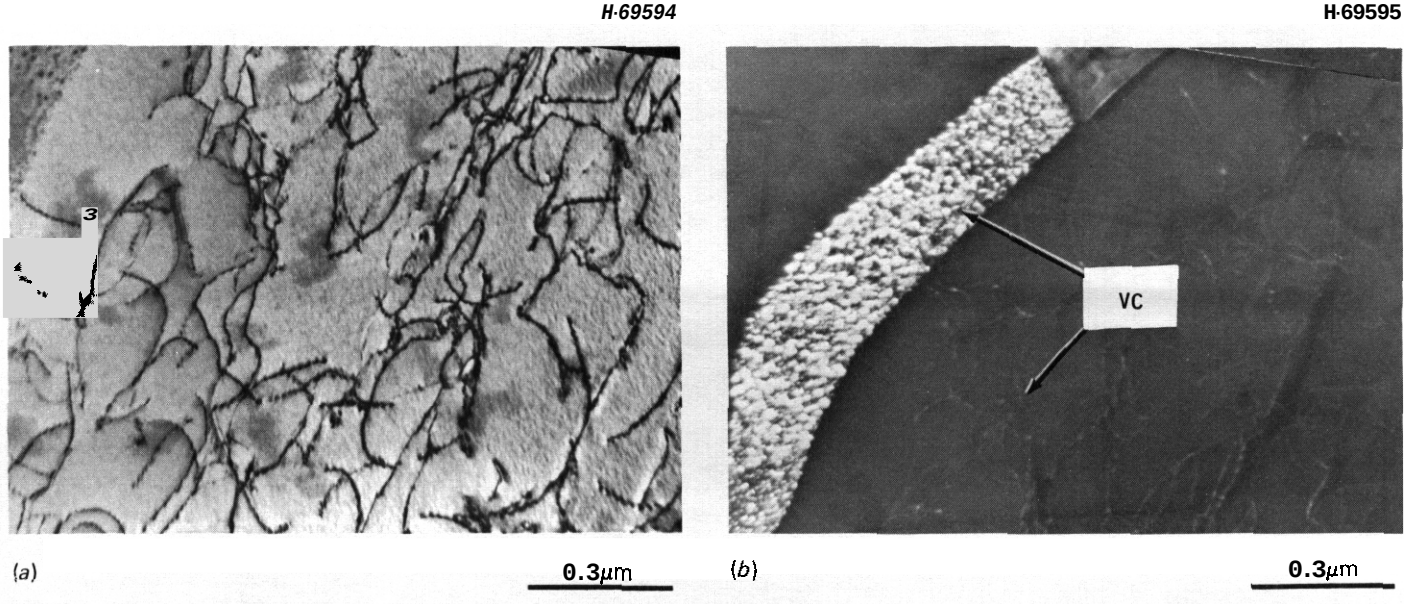

Fig. 6.1.1. Microstructure of LRO-37-5RS (after reordering heat treatment) showing small VC particles decorating a grain boundary and matrix dislocations. (a) Bright-field. (b) Precipitate dark-field.

6.1.4.4 References

1. D. N. Braski, "Bend Ductility of Iron-Base Long-Range-Ordered Alloys after Irradiation in HFIR," pp. 94–98 in *ADIP Semiannu. Prog. Rep. Mar. 31, 1983*, DOE/ER-0045/10, U.S. DOE, Office of Fusion Energy.

2. F. H. Huang, M. L. Hamilton, and G. L. Wire, *Nucl. Technol.* 57, 234–42 (1982).

3. W. J. S. Yang and M. L. Hamilton, "The Ductility Behavior of Irradiated Path B Alloys," pp. 90–119 in *ADIP Semiannu. Prog. Rep. Sept. 30, 1982*, DOE/ER-0045/9, U.S. DOE, Office of Fusion Energy.

4. D. N. Braski and S. A. David, "Microstructure of Welds in an Iron-Base Long-Range-Ordered Alloy," pp. 144–57 in *ADIP Semiannu. Rog. Rep. Sept. 30, 1982*, DOE/ER-0045/9, U.S. DOE, Office of Fusion Energy.

7.1 POSTIRRADIATION FRACTURE TOUGHNESS TESTS OF ESR ALLOY HT-9 AND MODIFIED 9Cr-1Mo ALLOY FROM UBR REACTOR EXPERIMENTS

J. R. Hawthorne, J. R. Reed and J. A. Sprague (Naval Research laboratory)

7.1.1 ADIP Task

The Department of Energy (DOE)/Office lor Fusion Energy (OPE) has stated the need to investigate ferritic alloys under the ADIP program task. Ferritic Steels Development (Path E).

7.1.2 Objectives

Alloy HT-9 and Modified 9Cr-1Mo are being evaluated for potential applications as first wall materials in magnetic fusion reactors. Objectives of the current research task were to test fatigue-precracked Charpy-V (PCC_V) specimens from representative plates irradiated in the UBR reactor at 149°C or 300°C, and, to compare the results against postirradiation notch ductility data developed previously for the materials. Both plates represent electroslag relined (ESR) melt processing.

7.1.3 Summary

PCC, specimens of Alloy HT-9 and Modified 9Cr-1Mo alloy were irradiated at 300°C and 149°C, respectively, to ~0.8 X 10^{20} n/cm^2, E >0.1 MeV. During this period, postirradiation tests for fracture toughness were completed and results compared to notch ductility determinations from standard Charpy-V (C_V) specimens irradiated in the same reactor experiments. Fracture surface examinations by SEM are also reported.

7.1.4 Progress and Status

7.1.4. 1 Introduction

The ferritic stainless steel compositions, HT-9 and 9Cr-1Mo (Mod.), are being assessed for possible first wall applications in magnetic fusion reactors by the Magnetic Fusion Materials Program and for duct applications in liquid metal fast breeder reactors by the Cladding/Duct Alloy Development Program of the Department of Energy. For these proposed uses, fracture resistance properties before and after elevated temperature irradiation are being investigated. Specimen typrs include C_V specimens for notch ductility determinations and PCC_V specimens for dynamic fracture toughness (K_J) determinations. Tensile property changes with irradiation are being established concurrently for use in fracture resistance assessments.

Previous reports [1,2] described experimental tests of the postirradiation notch ductility of HT-9 plates representing ESR and Argon-Oxygen Decarburized (AOD) melt processing, and an ESR 9Cr-1Mo (Mod.) plate. The HT-9 plates were irradiated at 93, 149, 288C and 300°C; the 9Cr-1Mo (Mod.) plate was irradiated at 149°C only. Plate compositions and heat treatments are listed in Tables 7.1.1 and 7.1.2, respectively. irradiation details are given in ref. 2.

The C_V upper shelf energy level (LT orientation) of the ESR HT-9 plate was found to be about 70 percent higher than that of the AOD HT-9 plate but lower than that of the 9Cr-1Mo (Mod.) plate (by ~80 J). The 41 J transition temperatures of the three materials, however, were nearly the same (-40, -23, -32°C respectively). Comparable radiation embrittlement sensitivities were observed for the HT-9 plates for both the low and high exposure temperatures, revealing a non-dependence on the method of melt processing. On the other hand, the C_V data showed the 9Cr-1Mo (Mod.) plate to have better radiation resistance at 149°C than the Alloy HT-9 plate. The difference can be attributed to relative alloying level, impurity content (especially phosphorus content) or the general dissimilarity in microstructure (see Fig. 7.1.1).

7.1.4.2 Dynamic Fracture Toughness Tests

Preirradiation fracture toughness determinations for the HT-9 and 9Cr-1Mo (Mod.) material? are illustrated in Figs. 7.1.2 and 7.1.3. The determinations were computed from energy absorbed to maximum load corrected for specimen and machine compliance, and were developed using J-integral assessment procedures. It is recognized that J-integral determinations based on maximum load imply an absence of stable (rising load) crack extension. Where this is not the case, K_J values so determined would tend to overestimate the K_J at crack initiation. The 100 MPa√m temperature was arbitrarily selected to index the toughness transition.

A major difference between materials is observed relative to the correlation of notch ductility and fracture toughness. In the Alloy HT-9, the upswing in toughness with temperature coincides approximately with the upswing in C_V energy absorption. On the other hand, the upswing in toughness for the 9Cr-1Mo (Mod.) begins well above tire temperature marking the rise in C, energy absorption. As one result[2], C_V energy values of 120 J are not indicative of a high toughness level is is the case with the Alloy HT-9. In Fig. 7.1.2, a 120 J energy level for the 9Cr-1Mo (Mod.) material is seen to correspond to a toughness

Table 7.1.1 Compositions (wt-%) of Alloy HT-9 and Modified Alloy 9Cr-1Mo Materials

Material	C	Si	Mn	P	S	Cr	Mo	Ni
ESR HT-9[a] (Code ES)	0.20	0.17	0.57	0.016	0.003	12.10	1.04	0.51
AOD HT-9[b] (Code 9TH)	0.20	0.24	0.57	0.018	0.007	11.64	1.01	0.52
9Cr-1Mo(Mod.)[c] (Code VS)	0.081	0.11	0.37	0.010	0.003	8.61	0.89	0.09

Material	V	W	N	Al	Ti	Cu	Cb/Ta	B
ESR HT-9	0.28	0.45	0.027	0.006	0.001	0.07	<0.001	<0.001
AOD HT-9	0.30	0.57	0.044	0.009	<0.01	0.04	0.01	0.001
9Cr-1Mo(Mod.)	0.209	<0.01	0.055	0.007	0.004	0.04	0.072	<0.001

[a] ESR Melt No 9-607 R2 (Universal Cyclops)

[b] AOD Melt No 9-607 (Electralloy)

[c] ESR Melt No 30176-1 (Cartech)

Table 7.1.2 Material Heat Treatments and Tensile Strengths

Material	Thickness	Yield Strength[a]	Tensile Strength[a]	Heat Treatment
ESR HT-9	15.9 mm	552 MPa	770 MPa	1050°C ± 14°C - 0.5h;
(Code ESR)	(0.6 in.)	(80.1 ksi)	(111.7 ksi)	780°C - 4h, air cool
AOD HT-9	15.9 mm	561 MPa	779 MPa	1050°C - 0.5h, air cool;
(Code 9TH)	(0.6 in.)	(81.4 ksi)	(113.0 ksi)	780°C - 2.5h, air cool
9Cr-1Mo(Mod.)	25.4 mm	633 MPa	752 MPa	1038°C - 1h, air cool;
(Code VS)	(1.0 in.)	(91.8 ksi)	(109.1 ksi)	760°C - 1h. air cool

[a] Ambient temperature tests; 5.74 mm or 6.40 mm gage diameter specimens

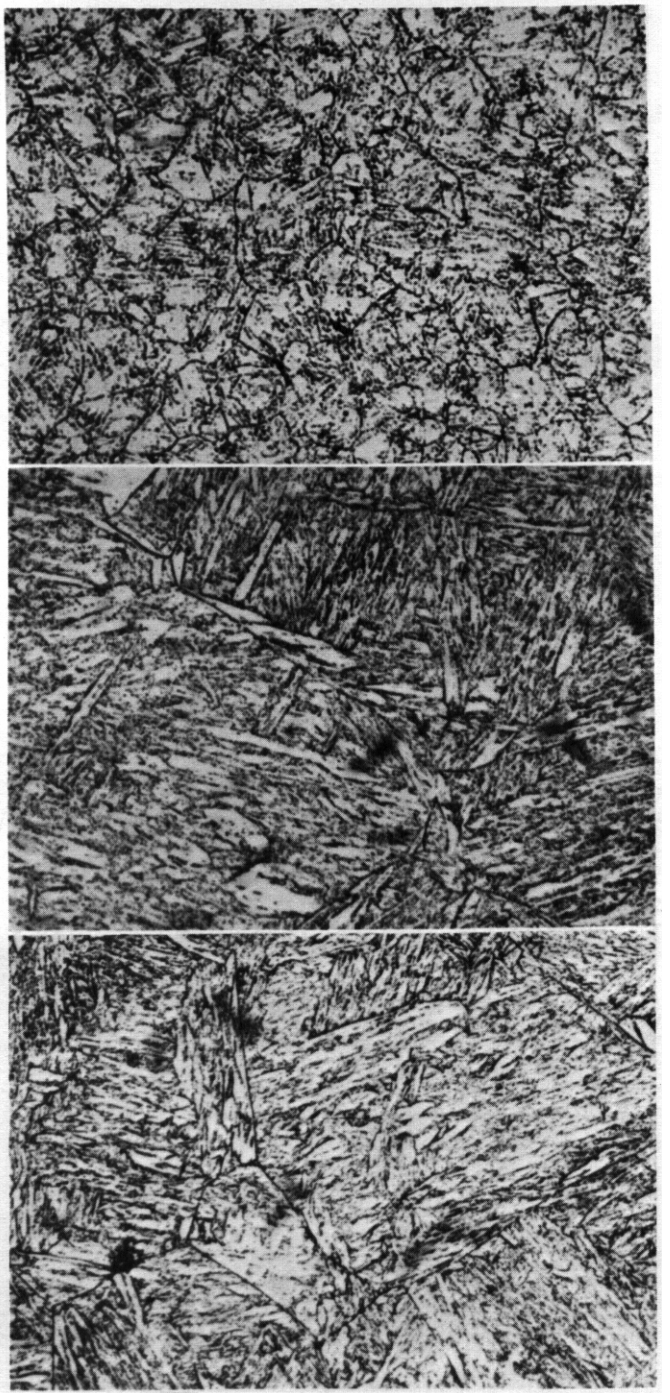

Fig. 7.1.1 Microstructures of the test plates.
Modified Alloy 9Cr-1Mo (upper panel)
ESR Alloy HT-9 (center panel)
AOD Alloy HT-9 (lower panel).

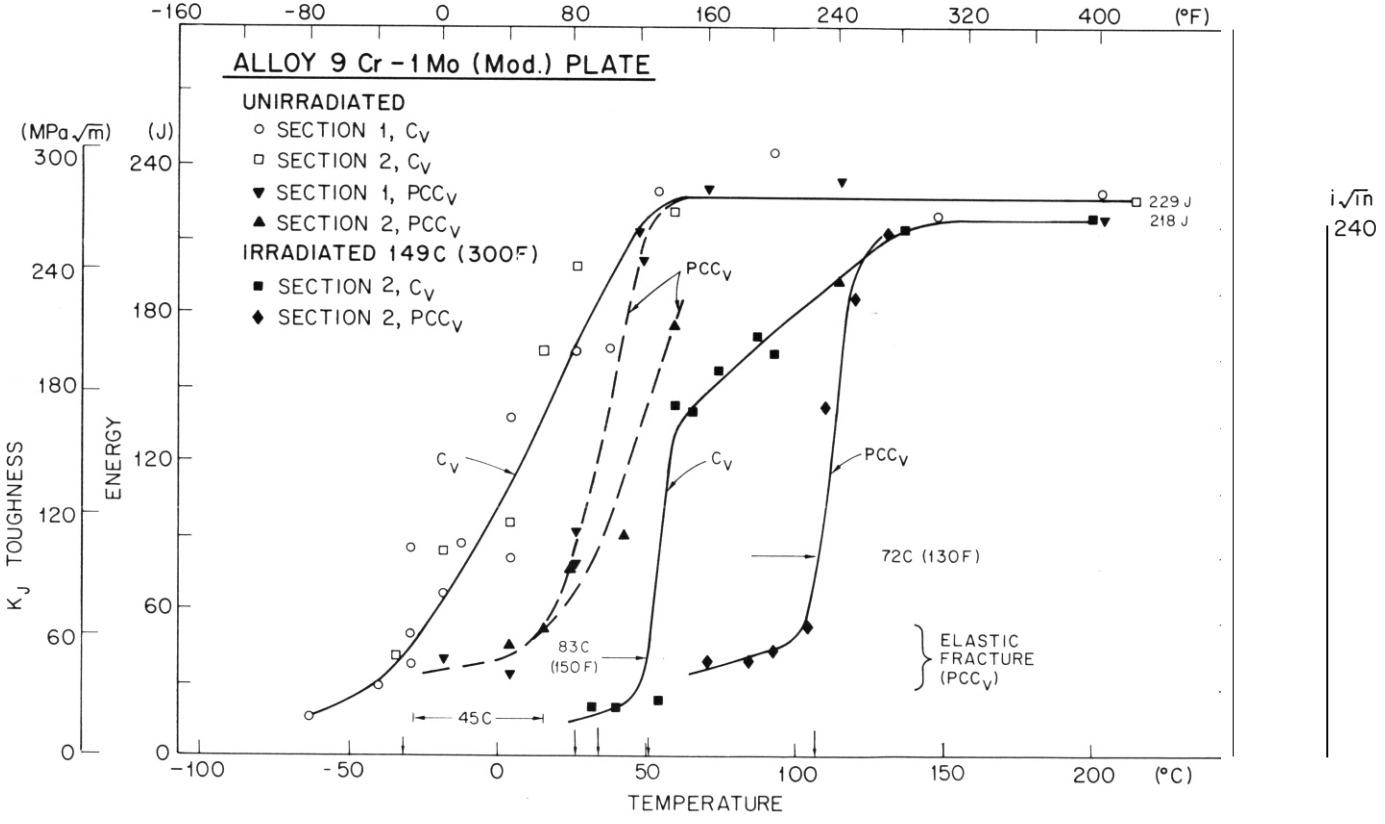

Fig. 7.1.2 Trends in C_V notch ductility and K_{Jd} fracture toughness (PCC_V method) for the Alloy 9Cr before irradiation. Data for two sections of the parent plate are shown.

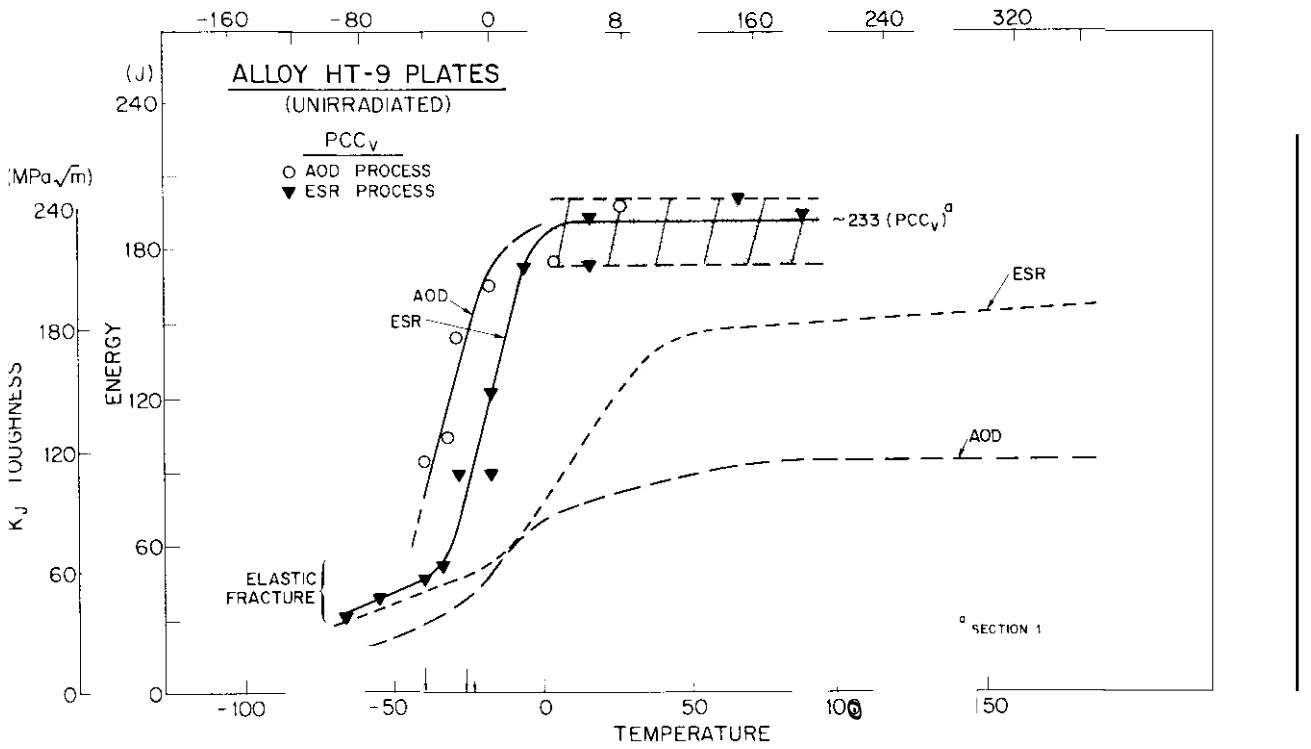

Fig. Trends in C_v notch ductility and K_{Jd} for the two Alloy HT-9 plates (unirradiated condition)

of ~33 MPa√m (low).

Postirradiation fracture toughness and notch ductility determinations for the 9Cr-1Mo (Mod.) plate are reported in Fig. 7.1.4. The irradiation at 149°C produced only a small decrease in upper shelf properties but a large elevation of the brittle/ductile transition indices. The increase in 100 MPa√m temperature and the increase in the 41 J temperature are about the same; accordingly, the C_v and PCC_v methods are comparable in their independent assessment of the irradiation effect. By the same token, the preirradiation temperature difference between the 100 MPa√m and 41 J indices was retained after irradiation. The importance of this observation to the projection of postirradiation fracture resistance is obvious, Also, while the 41 J temperature remains well below 149°C, the postirradiation 100 MPa√m temperature has been elevated to within 42°C of the simulated service temperature. The indicated toughness reserve against further neutron effects, in turn, is not nearly as great as that suggested by the notch ductility properties alone.

Figure 7.1.5 provides a fracture toughness vs. notch ductility comparison for the 300°C irradiated ESR Alloy HT-9 plate. The radiation-induced increase in the 100 MPa√m temperature is somewhat less (by ~17°C) than the increase in the 41 J temperature. With the AOD plate, the 100 MPa√m temperature elevation was the greater of the two shifts but some uncertainity exists in its exact postirradiation transition temperature due to the data scatter and the few test points (see Fig. 7.1.6). On balance, it can be concluded that C_v performance for this alloy is a relatively good indicator of PCC_v performance for both "irradiated and irradiated conditions. In particular, the upturn in toughness with temperature for this alloy is coincident with the "toe" of the C_v curve (i.e., starts at 38-41 J) and attains a maximum well before the onset of the C_v upper shelf regime.

There is no question that the upper shelf toughness levels of the two HT-9 plates after irradiation are essentially the same, in spite of their obvious difference in C_v upper shelf energy levels. Thus, initiation toughness for this composition does not appear to be a function of melt processing (AOD vs. ESR).

7.1.4.3 Fractographic Examinations

7.1.4.3.1 General Observations

The expected transitions in failure mode with temperature (and therefore C_v energy or K_{Jd}) were observed for most cases in this study. Failures ranged from predominantly cleavage at lower-shelf temperatures through mixed-mode fractures in the transition regimes to failure dominated by microvoid coalescence at the upper-shelf temperatures. Representative fracture surfaces from upper-and lower-shelf tests of ESR HT-9 and 9Cr-1Mo (Mod.) alloys are shown in Fig. 7.1.7. A mix of irradiated and non-irradiated specimens are shown; appearances are representative of both conditions.

At lower-shelf test temperatures, the fracture surfaces of 9Cr-1Mo (Mod.) specimens exhibited larger cleavage facets with less tearing between the facets than was observed for the HT-9. This can be seen by comparing Figs.7.1.7(a) and 7.1.7(c) where the C_v energy values of both Specimens were 41 J (30 ft-lb.). At upper-shelf temperatures, the populations of primary dimples were qualitatively the same, with the higher upper-shelf energy of the 9Cr-1Mo being reflected in greater deformation between primary dimples. The energy absorption for Fig. 7.1.7(d) was 217 J; that for Fig. 7.1.7(b) was 115 J. The primary generic difference between the pre-cracked and blunt-notch specimens was seen on the lower shelf, well below the transition temperature. Here a 0.4-0.6 mm region of ductile failure by microvoids was observed behind the blunt notch followed by failure of the remainder of the specimen by cleavage. In contrast, the stress concentration provided by the sharp fatigue pre-crack allowed the nucleation of cleavage fracture without this initial ductile failure. Amplifications of, and exceptions to these general observations are discussed in the following paragraphs.

7.1.4.3.2 Allay HT-9

Consistent with the trends in fracture energy, the principal difference between AOD and ESK plates, both in the non-irradiated and irradiated condition, was in upper-shelf Fracture appearance. The ESR material exhibited none of the surface roughness and secondary cracking of the AOD heat, which previously was associated with the ferrite stringers (Ref. 4). Among specimens of the ESR material, no differences in fracture appearance were detected between TL and LT orientations, or, between non-irradiated and irradiated conditions for either upper- or lower-shelf temperature regimes. Following irradiation none of the materials exhibited the fracture-surface roughness or secondary cracking on the scale of the prior austenite grain size which was reported by Smidt, et al (5) fur a HT-9 rod material irradiated at 427°C. Presumably the lower fluence and irradiation temperature of the present set of experiments produced less irradiation-enhanced segregation to prior austenite boundaries.

7.1.4.3.3 Modified 9Cr-1Mo

The most notable observation of the fractography of this alloy was that the fracture modes of

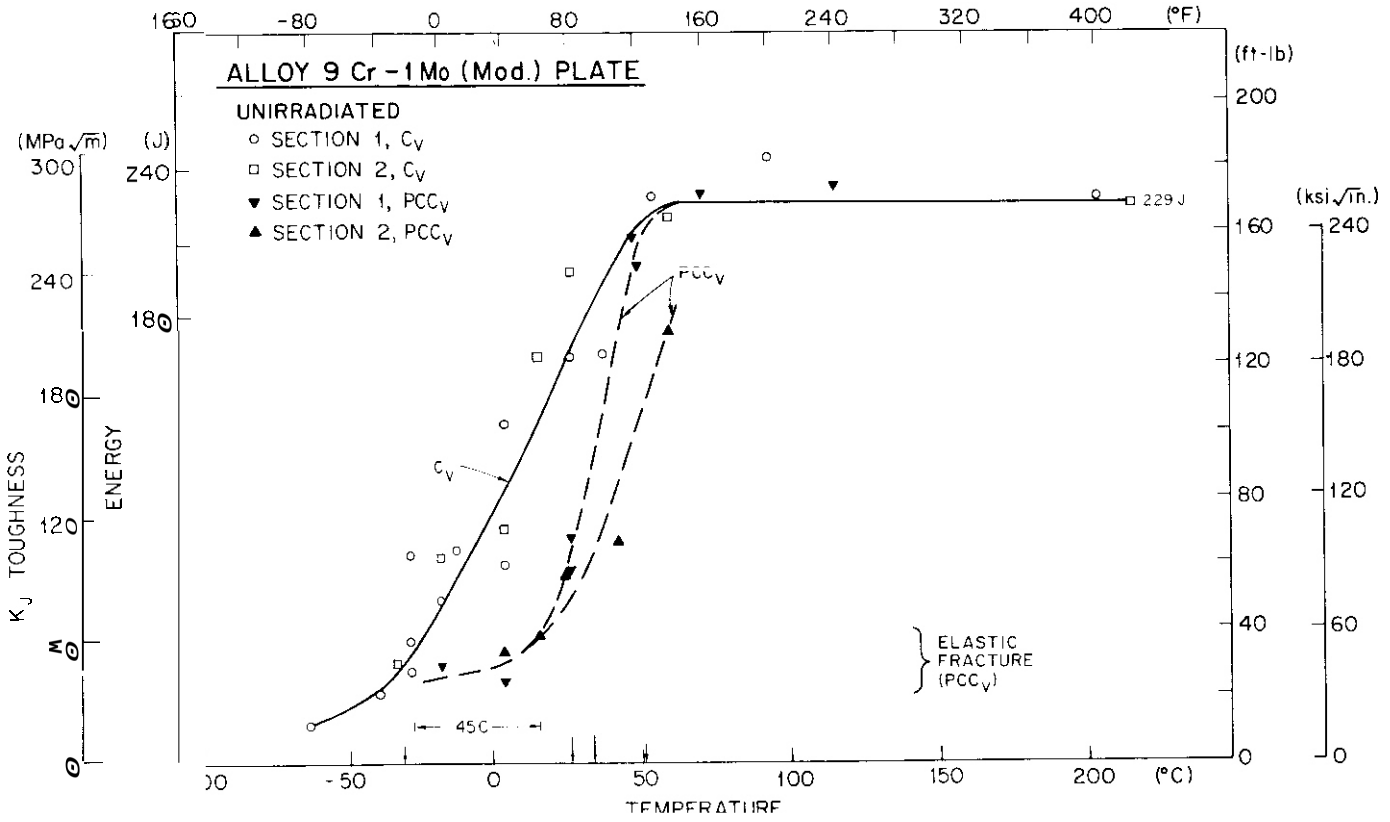

Fig. 7.1.4 C_V notch ductility and K_{Jd} fracture toughness trends for the Alloy 9Cr-1Mo (Mod.) plate before and after 149C irradiation to ~0.9 X 10^{20} n/cm^2, E > 0.1 MeV or ~5x10^{-2} dpa.

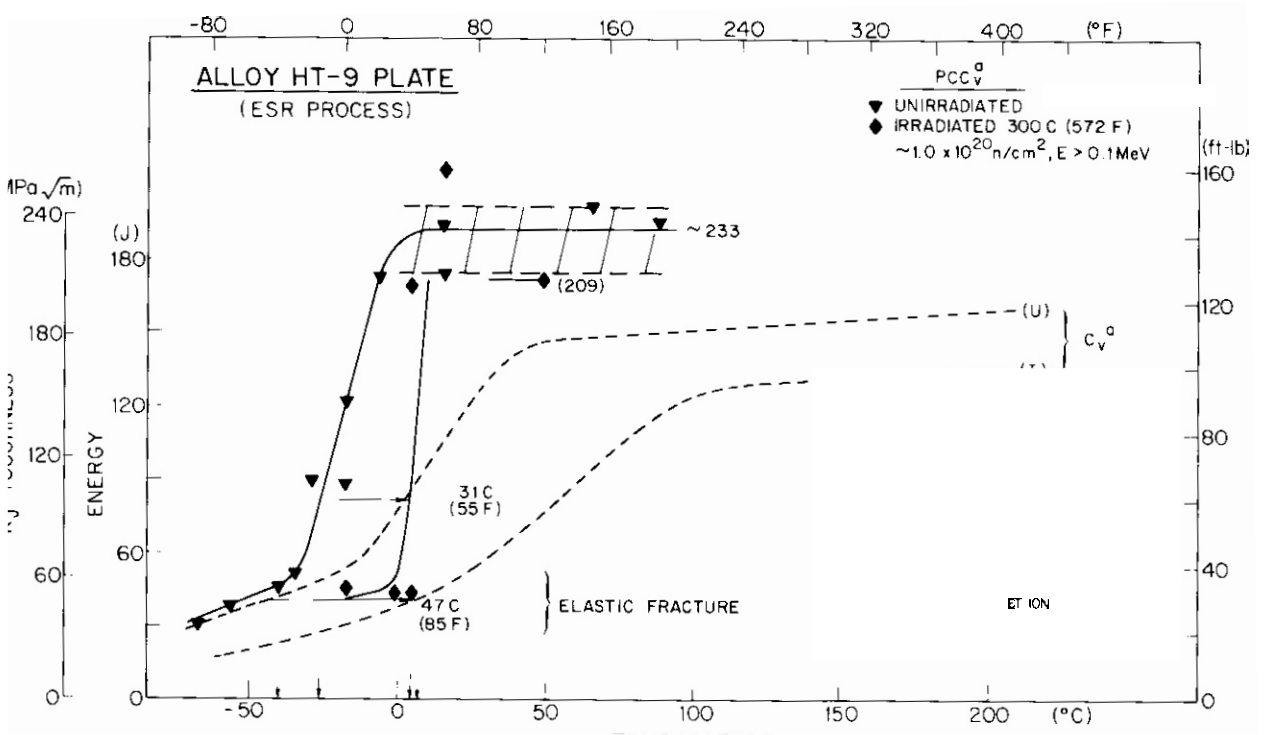

Fig. 7.1.5 Dynamic fracture toughness (K_{Jd}) of the ESR Alloy HT-9 plate before and after irradiation at 300C.

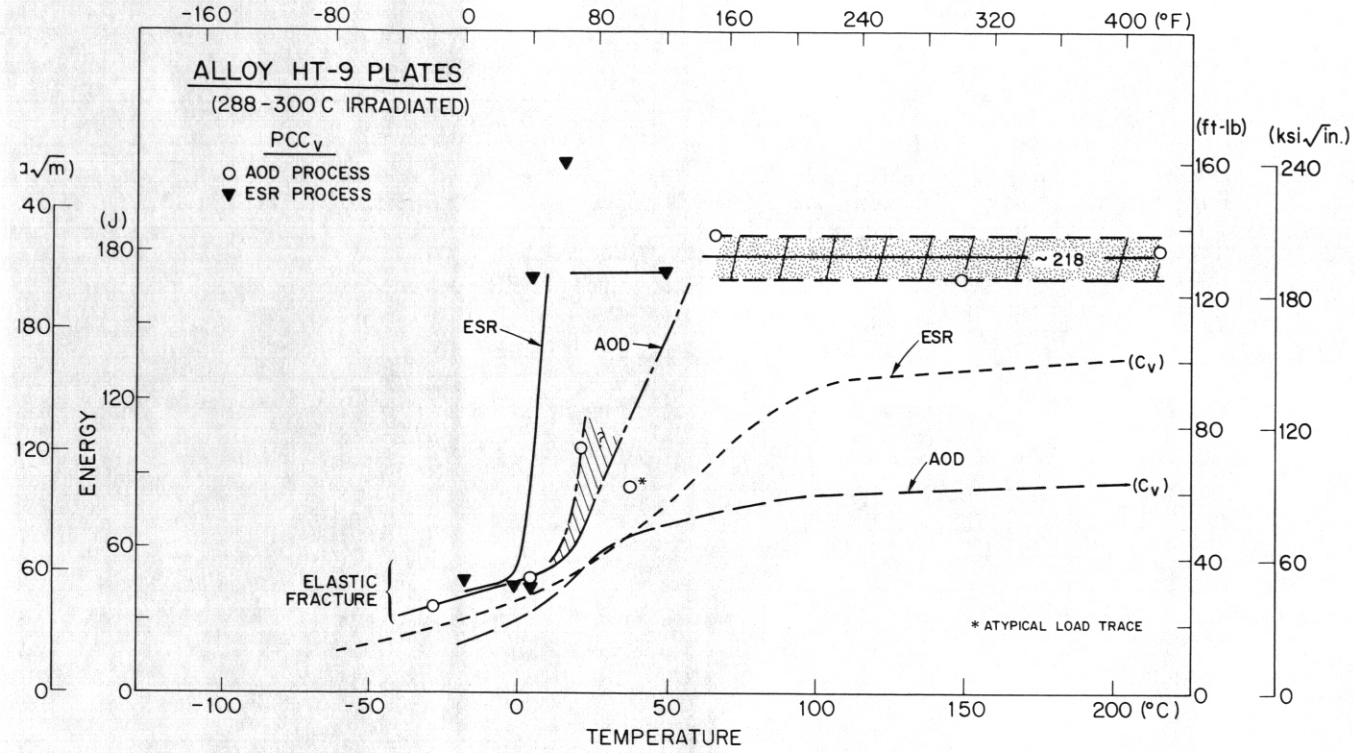

Fig. 7.1.6 Postirradiation dynamic fracture toughness (K_{Jd}) of the ESR Alloy HT-9 plate vs. the AOD Alloy HT-9 plate (288C or 300C irradiation). Postirradiation C_v trends are also shown.

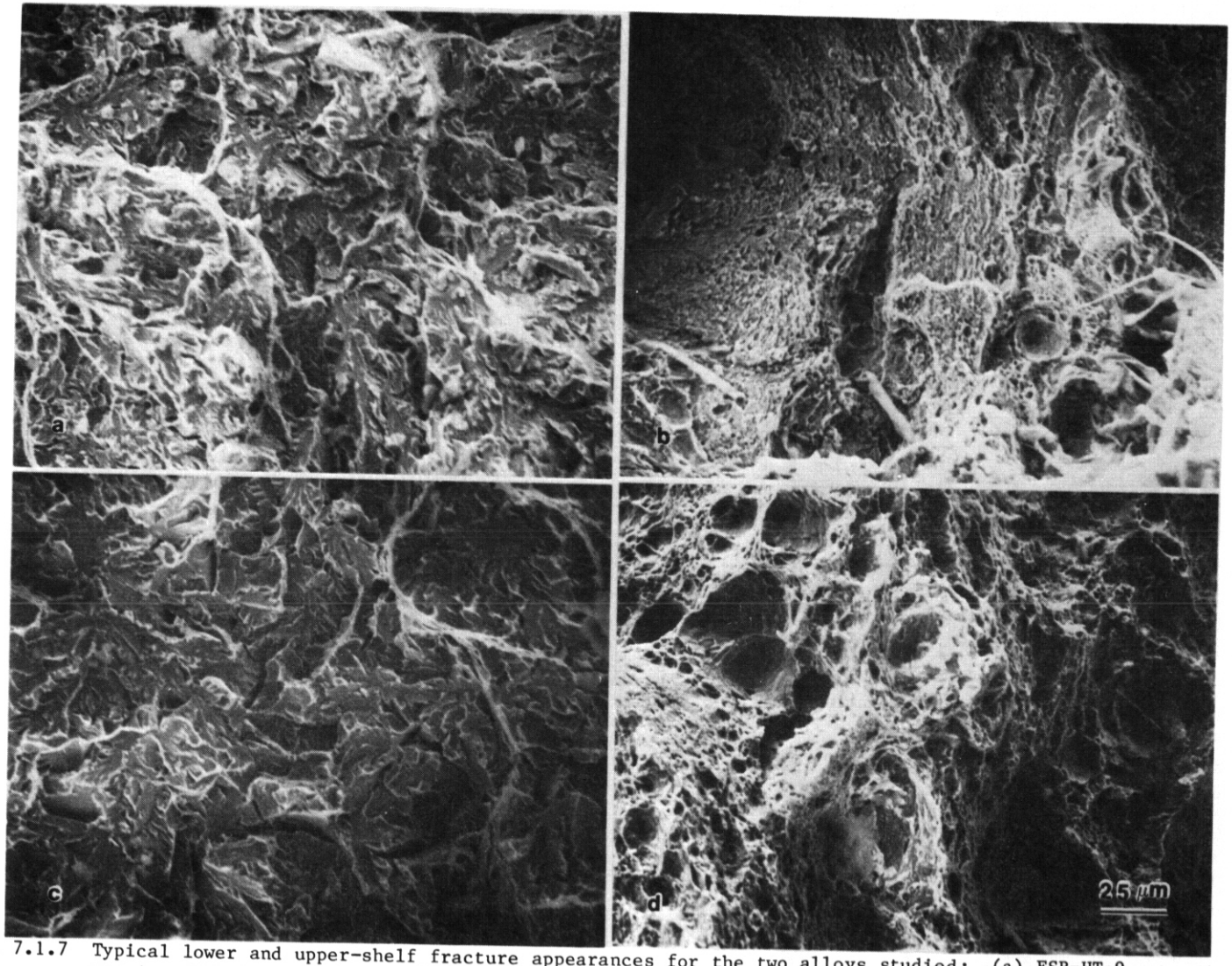

Fig. 7.1.7 Typical lower and upper-shelf fracture appearances for the two alloys studied: (a) ESR-HT-9, non-irradiated, tested at -40°C (lower shelf); (b) ESR HT-9, irradiated at 149°C, tested at 204°C (upper shelf); (c) 9Cr-1Mo (Mod.), non-irradiated, tested at -34°C (lower shelf); (d) 9Cr-1Mo (Mod.), irradiated at 149°C, tested at 138°C (upper shelf).

pre-cracked and blunt-notch specimens followed the two distinct trends found for the K_{Jd} vs. C_v energy transitions. This is illustrated in Fig. 7.1.8. The fracture regions shown are approximately 1 mm behind the notch (C_v) or pre-crack (PCC_v) of the non-irradiated specimens tested at 15°C, and for specimens of this alloy irradiated at 149°C and fractured at 88-93°C. For both pairs of specimens, the blunt-notch failure is predominantly by microvoid coalescence, whereas the pre-cracked specimen failure is by cleavage. The difference in fracture mode mirrors the difference observed between C_v energy and K_{Jd} transitions in this alloy, and implies that cleavage nucleation is more sensitive to crack-tip acuity for this alloy than for HT-9. With the HT-9, differences in transition temperature for fracture energy and failure mode were not observed.

A further observation, not fully investigated due to a lack of specimens, relates to the ductile failure mode shown in Fig. 7.1.8(b). In the central region of the fracture surface (inside of the shear lips), the ductile failure extended only 2.5 mm back from the machined notch. Beyond this distance, there was a 3 x 4 mm region of nearly pure cleavage. Since the C_v energy of this specimen was 164 J (120 ft.-lb.), this large amount of cleavage was a bit surprising. No such region of pure cleavage was observed in the irradiated C_v (Modified 9Cr-1Mo) specimen of Fig. 7.1.8(c). Thus, one can only speculate at present whether the part-through transition to cleavage is solely related to the notch sensitivity of this alloy.

7.1.5 Discussion

The agreement in radiation embrittlement sensitivity of the ESR and AOD Alloy HT-9 plates in the range of 288°C to 300°C is not surprising since they originated from the same melt. Primary composition differences (see Table 7.1.1) are in nitrogen, tungsten and silicon contents. Copper, phosphorus and nickel contents, on the other hand, are essentially the same. These latter elements have been shown, through pressure vessel steel studies to have a highly detrimental effect on 288°C radiation resistance (refs 6,7,8,9).

The difference in upper shelf energy levels of the two HT-9 plates is believed related, in part, to the fissures present in the AOD specimen surfaces but absent in the ESR specimen fractures. Testing of larger specimens such as compact tension (CT) types, would help qualify the role of these artifacts. Noting the similarity of K_{Jd} upper shelf levels of the two plates, comparable J_{Ic} properties but greatly different tearing modulus values would be projected for CT specimen (J-R curve) tests. A modification of the effects of specimen thickness by the presence of plate-like fissures is also a possibility; that is, secondary cracking normal to the fracture plane would alter material constraint in the Z-direction.

Table 7.1.1 does provide a clue to the radiation sensitivity difference between the 9Cr-1Mo (Mod.) plate (low) and the HT-9 plates (high). Phosphorus and nickel contents are much lower for the former material. Also, a coupled effect of material composition and material microstructure may be involved. Examination of additional melts of both compositions with phosphorus level varied, would be beneficial to their overall qualification for radiation applications.

The temperature difference between the notch ductility and toughness transitions for the 9Cr-1Mo (Mod.) plate is not readily explained. On one hand, experimental comparisons of 41 J vs. 100 MPa$\sqrt{m}$ transition temperature elevations for a spectrum of 288°C irradiated pressure vessel steels depict good (~1:1) correspondence (ref. 6). On the other hand, certain ship hull steels (ABS grade CS) and 2 1/4Cr-1Mo steels have drop weight test, nil-ductility transition temperatures within the C_v upper shelf temperature regime (refs. 10,11). The latter behavior would be consistent with the trend observed here for the 9Cr-1Mo (Mod.). Some insight into the nature of the C_v vs. PCC_v difference was obtained by the SEM examinations. However, additional heats will have to be examined to determine the consistency of the relationship and its dependence on the 9Cr-1Mo heat treatment condition.

7.1.6 Conclusions

Primary observations and conclusions reached from this experimental study are:

(1) The modified Alloy 9Cr-1Mo plate was more resistant to 149°C irradiation than the ESR Alloy HT-9 plate. The difference can be attributed to their dissimilarities in chemical composition, especially phosphorus content, and/or microstructure.

(2) Both alloys were not unduly embrittled by a fluence of ~1 x 10^{20} n/cm^2 (E >0.1 MeV) at 149°C and do show a capability for higher fluence service at this and more elevated temperatures.

(3) Alloy HT-9 plates representing ESR vs. AOD processing of one parent melt, have essentially the same radiation embrittlement sensitivity at 300°C and at lower exposure temperatures. For the AOD plate of this study, the 41 J transition temperature elevation by 93°C irradiation was about three times that produced by 288°C irradiation to the same fluence (~1 x 10^{20} n/cm^2).

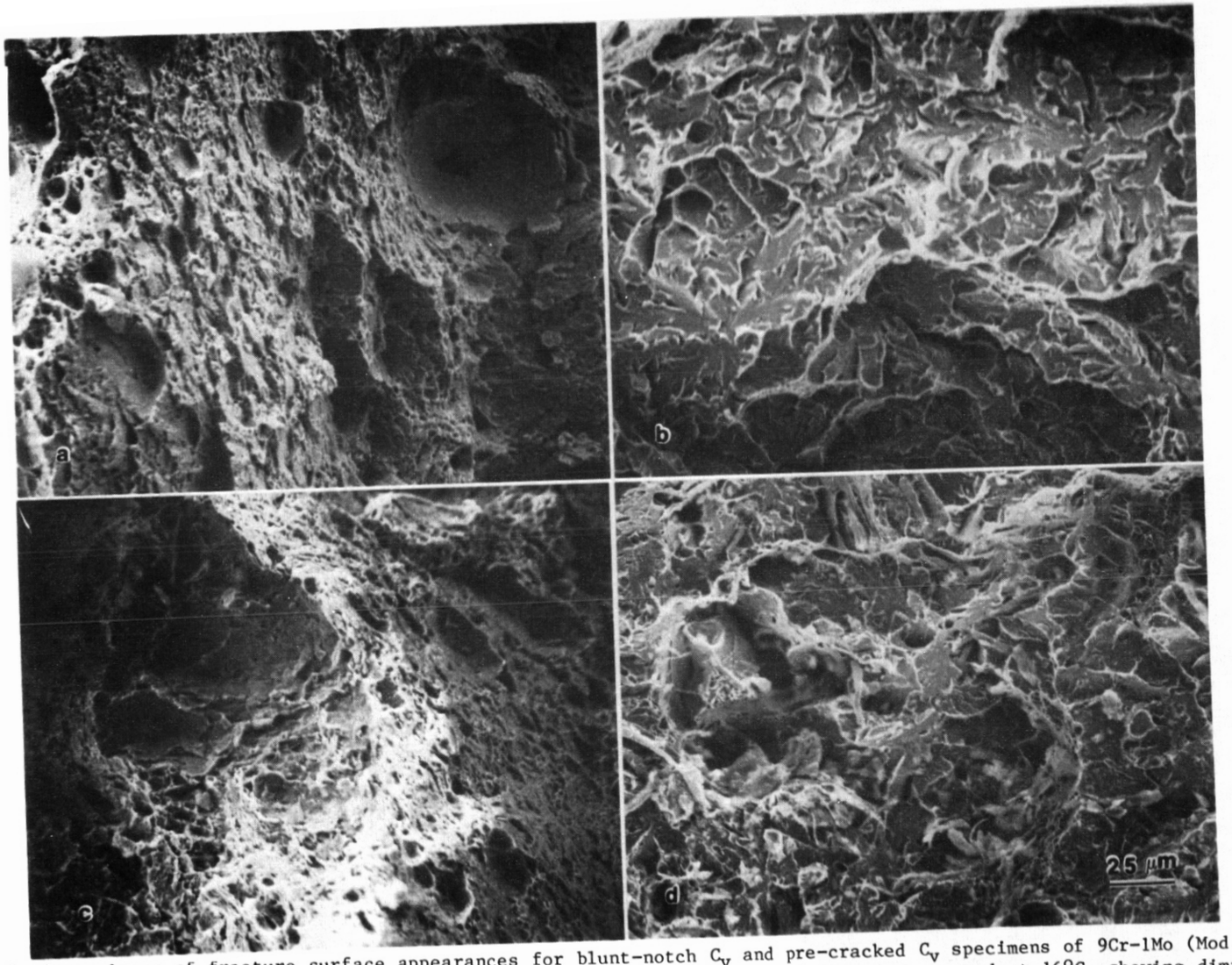

Fig. 7.1.8 Comparisons of fracture surface appearances for blunt-notch C_v and pre-cracked C_v specimens of 9Cr-1Mo (Mod.) tested at similar temperatures near ductile-brittle transition: (a) non-irradiated C_v tested at 16°C, showing dimpled rupture; (b) non-irradiated PCC_v, tested at 16°C, showing predominant cleavage; (c) 149°C irradiated C_v, tested at 88°C, showing dimpled rupture; (d) 149°C irradiated PCC_v, tested at 93°C, showing predominant cleavage.

(4) Alloy HT-9 in plate form appears unacceptable for 93°C high fluence service **unless** the component design requires only elastic fracture resistance.

(5) All three test materials exhibited good retention of C_v upper shelf and K_{Jd} upper shelf toughness following irradiation to $\sim 1 \times 10^{20}$ n/cm^2, E >0.1 MeV.

(6) **The** upswing in K_{Jd} toughness with temperature coincides with the upswing in C_v notch ductility for Allay HT-9 but not for the modified Alloy 9Cr-1Mo. For the latter, the toe **of** the K_{Jd} transition **was** 45°C higher in temperature than the toe of the C_v energy curve. The data indicate the modified 9Cr-1Mo composition is highly sensitive to specimen notch acuity.

(7) The C_v and PCC_v data show a general agreement of these test methods in their independent assessments of radiation-induced embrittlement. Differences between the K_{Jd} 100 MPa$\sqrt{m}$ and 41 J transition temperature elevations by irradiation **were** observed (Alloy HT-9) but do not show a consistent trend vs. test method.

(8) PCC_v specimens of modified Alloy 9Cr-1Mo can fail predominantly by cleavage at temperatures where C_v specimens fail predominantly by shear. SEM observations did not discern other major differences in fracture mode characteristics among the materials in unirradiated or irradiated conditions.

7.1.7 References

[1] J. R. Hawthorne, "Postirradiation Notch Ductility and Fracture Toughness Behavior of AOD Heat of Alloy HT-9," in Alloy Development for Irradiation Performance, Semi-Annual Progress Report far period ending March 32, 1982, DOE/ER-0045/8, Sept. 1982.

[2] J. R. Hawthorne, "Postirradiation Notch Ductility Tests of ESR Alloy HT-9 and Modified 9Cr-1Mo Alloy from UBR Reactor Experiments," in Alloy Development for Irradiation Performance, Semi-Annual Progress Report for period ending Sept. 30, 1983, DOE/ER-0045/11.

[3] J. R. Hawthorne, J. R. Keed **and** J. A. Sprague, "Fracture Resistance of Two Ferritic Stainless Steels After Intermediate Temperature Irradiation," Twelfth Symposium on Effects of Radiation on Materials, **June** 18-20, 1984, Williamsburg, VA.

[4] Gelles, D. S. and Hu, W. L., "Fractographic Examination of HT-9 and 9Cr-1Mo Charpy Specimens Irradiated in the **AD-2** Test," Alloy Development for Irradiation Performance, Semiannual Progress Report for Period Ending Sept. 30, 1982, Department of Energy DOE/ER-0045/9, Feb 1983, pp. 178-219.

[5] Smidt Jr., F. A., Hawthorne, J. R. and Provenzano, V., "The Fracture Resistance of HT-9 After Irradiation at Elevated Temperature," Proceedings, Symposium on Effects of Radiation on Structural Materials, ASTM STP 725, Feb 1980, p. 269.

[6] Hawthorne, J. R., "Status of Knowledge of Radiation Embrittlement Resistance in USA **Reactor** Pressure Vessel Steels, NUREG/CR-2511, **Nuclear** Regulatory Commission, Feb. 1982.

[7] Potapovs, U. and Hawthorne, J. R., "**The** Effect of Residual Elements on 550F Irradiation Response of Selected **Pressure** Vessel Steels and Weldments," NUCLEAR APPLICATIONS, 6 **(No.** 1), 1969, p. 27-46.

[8] Hawthorne, J. R., "Significance of Nickel and Copper Content to Radiation Sensitivities and Postirradiation Heat Treatment Recovery of Reactor Vessel Steels," Effects of Radiation on Materials, Eleventh Conference, ASTM STP 782, American Society for Testing and Materials, 1982, pp. 375-390.

[9] Hawthorne, J. R., "Evaluation of Reembrittlement Rate Following Annealing and Related Investigations on RPV Steels," MEA-2032, Materials Engineering Associates, Inc., October 1983.

[10] Hawthorne, J. R. and **Loss,** F. J., "Fracture Toughness Characterization of Shipbuilding Steels," NRL Report 7701, Naval Research Laboratory, July 10, 1974.

[11] Pellini, W. S., "Advances in Fracture Toughness Characterization Procedures and in Quantitative Interpretations to Fracture-Safe Design for Structural Steels," NRL Report 6713, Naval Research Laboratory, April 3, 1968.

7.2 ELEVATED-TEMPERATURE TENSILE PROPERTIES OF 9 Cr-1 MoVNb STEEL IRRADIATED IN THE EBR-II AO-2 EXPERIMENT — R. L. Klueh and J. M. Vitek (Oak Ridge National Laboratory)

7.2.1 AOIP Task

AOIP tasks are not defined for Path E Ferritic Steels in the 1978 program plan.

7.2.2 Objective

The goal of this project is to measure the tensile properties of 9 Cr-1 MoVNb steel irradiated at elevated temperatures in EBR-II. In the future, the results will be compared with elevated-temperature irradiations of this steel in the High Flux Isotope Reactor (HFIR), where much more helium is produced in irradiations to the same dpa level.

7.2.3 Summary

Tensile specimens of normalized-and-tempered 9 Cr-1 MoVNb steel were irradiated in EBR-II to 10 to 12 dpa at *390* to 550°C. Tests were conducted at room temperature and at the irradiation temperature on irradiated and unirradiated Specimens. Irradiation at 390°C increased the yield stress and ultimate tensile strength. No change in strength was observed for irradiation at 450, 500, and 550°C.

7.2.4 Progress and Status

The tensile specimens described in this report were irradiated in EBR-II as part of the large AD-2 experiment conducted by HEOL (ref. 1). The experiment included 12 Cr-1 MoVW, 9 Cr-1 MoVNb, and 2 1/4 Cr-1 Mo steels, with specimens for the determination of tensile properties, impact properties, fracture toughness, fatigue, and crack growth. Disks of each material were also included to determine microstructural effects of irradiation.

7.2.5 Experimental Procedure

The 9 Cr-1 MoVNb steel (heat 30182) used in this experiment was obtained from the Carpenter Technology Corporation and had the composition given in Table 7.2.1 (ref. 1). The specimens were fabricated from an ESR ingot that had been rolled to 0.76-mm sheet. The sheet was heat treated as follows: 1 h at 1038°C, air cool; 1 h at 760°C, air cool.

Sheet tensile specimens in this experiment were of an SS-1 type, with a reduced gage section 20.3-mm long by 1.5-mm wide by 0.76-mm thick (Fig. 7.2.1). The specimens were machined with their gage lengths perpendicular to the rolling direction of the sheet.'

Specimens were irradiated in capsules designed to maintain temperatures of 390, 450, 500, and 550°C. Four specimens were irradiated at 390 and 500°C, three at 550°C, and one at 450°C. Irradiation was in row 4 of EBR-II. All but two of the specimens were in level 7 of the capsules' and were exposed to approximately 2.1 × 10^{26} neutrons/m^2 (>0.1 MeV), which produced a displacement damage of about 10 dpa. One

Table 7.2.1. Chemical composition of 9 Cr-1 MoVNb steel (heat 30182)

Element	Composition (wt %)		Element	Composition (wt %)	
	Carpenter Technology	HEOL Overcheck		Carpenter Technology	HEOL Overcheck
C	0.086	0.08	cu	0.03	0.03
Mn	0.37	0.37	Al	0.014	0.009
P	0.012	0.011	B	<0.001	<0.001
S	0.003	0.004	As		(0.001
Si	0.16	0.19	Sn		0.002
Ni	0.11	0.090	Zr		(0.001
Cr	8.44	8.47	N		0.054
Mo	0.89	0.88	O		0.008
V	0.24	0.21	Pb		<0.001
Nb	0.08	0.07	Sb		(0.001
Ti	(0.02	0.001	W		<0.001
co	0.02	0.017	Fe		Balance

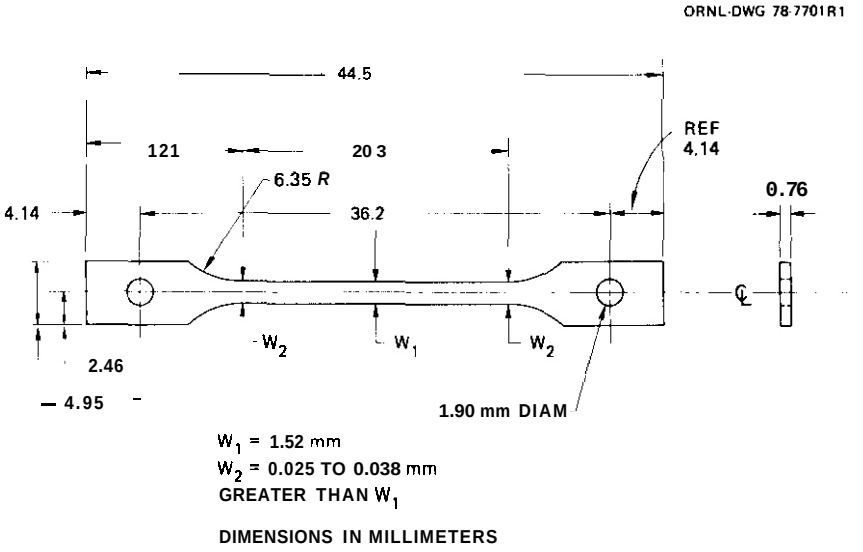

Fig. 7.2.1. Geometry of SS-1 tensile specimens used in these experiments.

specimen each at 390 and 500°C was exposed to approximately 2.5 × 10^{26} neutrons/m^2, which produced a displacement damage of approximately 12 dpa. The uncertainty in fluence has been estimated as ±10% and the temperature uncertainties as 390 ± 10°C, 450 ± 15°C, 500 ± 20°C, and 550 ± 30°C (ref. 2).

After irradiation, tensile tests were conducted at the irradiation temperature and, where specimens were available, at room temperature. As-heat-treated as well as thermally aged control samples were also tested to separate the effect of irradiation from thermal-aging effects. Thermal aging was at the irradiation temperature for 5000 h — the approximate time of the irradiation. The tensile tests were made in a vacuum chamber on a 44-kN-capacity Instron universal testing machine at a crosshead speed of 8.5 μm/s, which results in a nominal strain rate of 4.2 × 10^{-4}/s.

7.2.6 Results

The microstructure of the normalized-and-tempered 9 Cr-1 MoVNb steel was tempered martensite (Fig. 7.2.2). The prior austenite grain size was estimated as being between ASTM numbers 8 and 10; the microhardness was 221 DPH (1000 g load). Thermal aging for 5000 h produced little change in the optical microstructure, the microhardness. or the amount of precipitate present (as determined by electrolytic extraction). After 5000 h at 550°C, the microhardness was 218 DPH. Before aging, approximately 2.0 *wt* % precipitate was extracted; after 5000 h at 550°C, approximately 2.1% precipitate was extracted.

The tensile results for the as-heat-treated, thermally aged, *and* irradiated 9 Cr-1 MoVNb steel are given in Tables 7.2.2 to 7.2.4. In Figs. 7.2.3 and 7.2.4, the tensile properties for these three conditions are compared for tensile tests conducted at the irradiation temperature. Because of the limited number of control specimens provided,' only a few room-temperature tests were conducted.

Fig. 7.2.2. Microstructure of normalized-and-tempered 9 Cr-1 MoVNb steel used in these experiments.

Irradiation at 390°C resulted in hardening *as* measured by both the 0.2% yield stress and the ultimate tensile strength (Fig. 7.2.3). At 450, 500, and 550°C, no change in yield stress or ultimate tensile strength occurred that could be attributed to irradiation or thermal aging. There was essentially no difference in the strength at any of these three temperatures.

Table 7.2.2. Tensile properties of unirradiated 9 Cr-1 MoVNb steel

Test temperature (°C)	Strength (MPa)		Elongation (%)	
	Yield	Ultimate	Uniform	Total
22	547	697	7.3	11.9
400	474	553	2.5	5.9
500	438	517	3.6	7.2
550	440	497	3.6	10.3

Table 7.2.3. Tensile properties of 9 Cr-1 MoVNb steel aged for 5000 h

Temperature ("C)		Strength (MPa)		Elongation (%)	
Aging	Test	Yield	Ultimate	Uniform	Total
400	400	460	555	3.3	6.0
450	450	473	570	3.0	5.6
500	500	451	522	2.9	6.1
550	550	414	467	2.9	7.8

Table 7.2.4 Tensile properties of irradiated 9 Cr-1 MoVNb steel

Temperature (°C)		Strength (MPa)		Elongation (%)	
Irradiation	Test	Yield	Ultimate	Uniform	Total
390	22	881	933	3.6	7.0
390	400	781	808	1.4	4.1
450	450	480	575	3.6	6.9
500	22	558	712	7.9	12.4
500	500	445	536	3.3	6.8
550	22	544	697	6.1	10.0
550	550	429	495	3.1	9.9

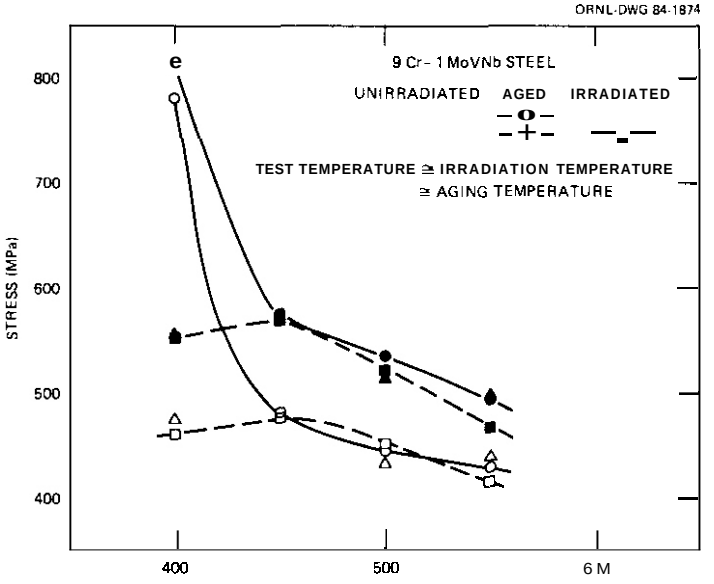

Fig. 7.2.3. The 0.2% yield stress and ultimate tensile strength of 9 Cr-1 MoVNb steel as a function of test temperature for irradiated specimens, as-heat-treated controls, and thermally aged controls. The test temperature equals the irradiation and aging temperatures: specimens were aged 5000 h.

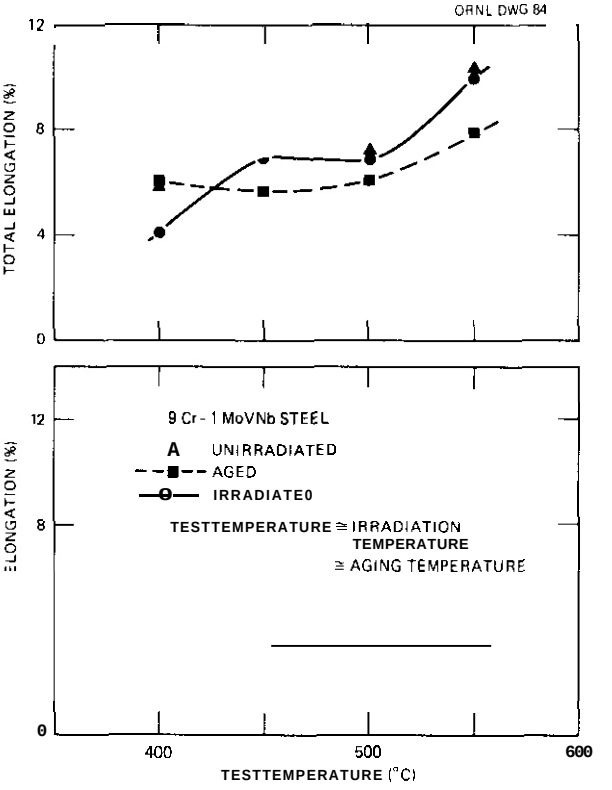

Fig. 7.2.4. The uniform and total elongations of 9 Cr-1 MoVNb steel as a function of test temperature for irradiated specimens, as-heat-treated controls, and thermally aged controls. The test temperature equals the irradiation and aging temperatures: specimens were aged 5000 h.

The effect of irradiation on ductility reflected the effect on strength (Fig. 7.2.4). The uniform and total elongations of the specimen irradiated at 390°C were slighly less than those of the unaged and aged controls. At the three highest irradiation and test temperatures, however, there appeared to be no effect of irradiation.

Irradiation in EBR-II at 390°C also caused hardening in 12 Cr-1 MOVW steel[3] and 2 1/4 Cr-1 Mo steel.[4] For the 12 Cr-1 MOVW, the irradiated and unaged controls had similar strengths when irradiated and tested at 450, 500, and 550°C; no data were reported on thermally aged controls.[3] The strength of the 2 1/4 Cr-1 Mo steel was decreased by thermal aging at all four temperatures. The strength of the irradiated and aged 2 1/4 Cr-1 Mo steel specimens were similar at 450 and 500°C. However, at 550°C, irradiation led to an enhanced softening over that caused by thermal aging.[4]

In the next ADIP semiannual report, the tensile data for the 12 Cr-1 MoVW steel aged specimens will be reported, and the results for the irradiated specimens, unaged controls, and thermally aged controls for the 2 1/4 Crl Mo, 9 Cr-1 MoVNb, and 12 Cr-1 MoVW steels will be compared in more detail.

7.2.7 References

1. R. J. Puigh and N. F. Panayotou, "Specimen Preparation and Loading for the AD-2 Ferritics Experiment," pp. 260–93 in *ADIP Quart. Prog. Rev. June 30, 1980,* DOE/ER-0045/3, U.S. DOE. Office of Fusion Energy.
2. R. J. Puigh, HEDL, private communication to R. L. Klueh, ORNL, Oct. 19, 1983.
3. R. L. Klueh and J. M. Vitek, "Elevated-Temperature Tensile Properties of 12 Cr-1 MoVW Steel Irradiated in the ERR-11, AD-2 Experiment," pp. 104–7 in *ADIP Semiannu. Prog. Rep. Mar. 31, 1983,* DOE/ER-0045/10, U.S. DOE, Office of Fusion Energy.
4. R. L. Klueh and J. M. Vitek, "Elevated-Temperature Tensile Properties of 2 1/4 Cr-1 Mo Steel Irradiated in the EBR-II, AD-2 Experiment," pp. 95–102 in *ADIP Semiannu. Prog. Rep. Sept. 30, 1983,* DOE/ER-0045/11, U.S. DOE, Office of Fusion Energy.

7.3 FRACTURE TOUGHNESS OF IRRADIATE0 HT-9 - F. H. Huang (Westinghouse Hanford Company)

7.3.1 ADIP Task

The Department of Energy/Office of Fusion Energy (DOE/OFE) has cited the need to investigate ferritic alloys under the ADIP program task Ferritic Steels Development (Path E).

7.3.2 Objective

The objective of this work is to evaluate the effects of neutron irradiation, grain size and welding on the fracture toughness of HT-9 irradiated to a fluence of 5.5 x 10'' n/cm². The goal is to characterize the fracture behavior of fusion first wall ferritic materials.

7.3.3 *Summary*

Compact tension specimens of HT-9 from the AD-2 recon experiment were tested at 205°C. Specimens Of base metal have two different grain sizes: ASTM 8-9 and ASTM 3-4. One specimen of weld metal was also tested at 205°C. Test results showed that the fracture toughness of HT-9 with a larger grain size was lower and the toughness degradation due to high fluences was more severe for the HT-9 weld metal than for the base metal.

7.3.4 Introduction

The AD-2 experiment has been designed to study the mechanical properties, particularly the fracture and weld properties, of ferritic alloys such as Hi-9 and 9Cr-1Mo which are candidate materials for the first wall or blanket of a fusion reactor. Subsized specimens were used to save irradiation space and to meet requirements for testing prototypic component thickness.

The number of specimens required to ohtain fracture toughness data was reduced **by** using single specimen electropotential techniques. Results of fracture toughness tests on unirradiated HT-9 using the technique have been reported.'

Some of the fracture toughness specimens from the AD-2 experiment were irradiated to a fluence of 3 x 10'' n/cm², the rest were reconstituted to a fluence of 6 x 10^{22} n/cm². Specimens were given various austenitizing and tempering treatments to give different grain sizes. The purpose was to study the effect of grain size on the degree of temper embrittlement. The experiment also included fracture toughness specimens machined from HT-9 welded material to investigate the properties of the fusion metal and the heat affected zone.

Unirradiated weld specimens and those irradiated to a fluence of 3 x 10^{22} n/cm² were already tested and results reported.',' Only a few specimens of base metal from the AD-2 experiment were tested, and more are to be tested at a later date.

7.3.5 Progress and Status

7.3.5.1 Experimental Procedure

The base metal specimens were machined directly from the 33.3 mm diameter, heat number 91354, bar stock. The bar stock was hot worked after soaking at 1149°C for a minimum of one hour, tempered at 750°C for one hour, and air cooled. The prior austenitic grain size of the compact tension specimens fabricated from slices of the bar stock (Fig. 7.3.1a) was ASTM 8-9. This treatment was designated TMT h3 in the AD-2 experiment. An additional heat treatment: 1050°C/0.5 h/AC + 780°C/2.5 h/AC was given to these TMT #3 specimens to increase the grain size to ASTM 3-4, it was designated TMT **114.**

The weld specimen was fabricated from 6.35 mm thick welded plates as shown in Fig. 7.3.1b. The notch orientation of the weld specimen is parallel to the fusion line of the welded material. Details of AD-2 specimen fabrication were reported in Reference 4. The configuration of the 2.54 mm thick circular compact tension specimen and the test procedures for in-cell fracture toughness using electropotential techniques were given in References 2 and 3.

Irradiated specimens were first precracked using the electropotential technique to monitor the precrack length. After the test, they were heat tinted and broken at room temperature for crack extension measurements. During the precracking and test a constant DC current of 13 amp was applied to the specimen, and the potential output and the load-time were recorded.

7.3.5.2 Results and Discussion

The load and electropotential output versus displacement curves of irradiated Hi-9 are plotted in Fig. 7.3.2. The values of J were calculated from load versus displacement records, and the crack extensions were obtained from electropotential via the electropotential calibration curves. Figs. 7.3.3 and 7.3.4 show J versus Δa curves for irradiated HT-9 base and weld metal tested at 205°C. The critical fracture toughness, J_{IC}, was determined from J versus Δa curves and the blunting lines and are listed in Table 7.3.1. Also given in Table 7.3.1 are the values of tearing modulus (T).

The effect of grain size on the fracture toughness of HT-9 irradiated at 390°C can be seen in Fig. 7.3.5. Since there were only two grain sizes, the relationship between fracture toughness and grain size

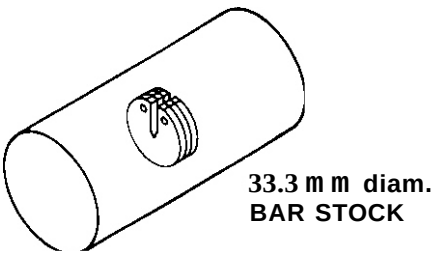

(a)

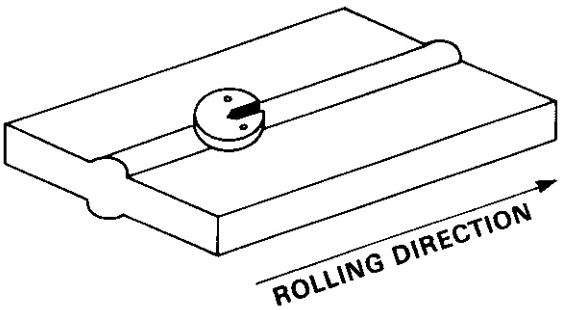

(b)

Fig. 7.3.1a. Processing of HT-9 specimens from alloy stock.

Fig. 7.3.1b. Orientation of fracture toughness specimen with respect to weld material.

was not established in detail. However, it is clear that the toughness with an ASTM grain size of 8-9 is higher than that with an ASTM grain size of 3-4. A material with smaller grain size is expected to exhibit a greater plastic deformation and therefore a higher fracture toughness.

Experimental evidence shows that a decrease in grain size lowers the ductile-brittle transition temperature for Fe-25Cr ferritics[5] and fracture appearance transition temperature for 2-1/4Cr-1Mo steel.' Materials having second phase particles may be tougher than a solid solution, because the particles generally retard grain growth. In HT-9, small quantities of titanium, aluminum and tantalum tend to form carbides and act as grain refiner, promoting a higher-fracture toughness. The effect of irradiation temperature on the fracture toughness is also shown in Fig. 7.3.5. The effect is insignificant as indicated by the only two data points.

As they usually contain defects, welds are expected to be more susceptible to fracture than the base metal. Fracture toughness tests on HT-9 welds irradiated to a fluence of 3 x 10^{22} n/cm² (E > 0.1 MeV) were performed and results reported.[3] It was found that the fracture toughness was not degraded but the ability of HT-9 weld to resist crack propagation was impaired severely after irradiation. As the fluence was increased to about 6 x 10^{22} n/cm², the trend was reversed, the toughness was reduced significantly (Fig. 7.3.6) while the resistance to crack propagation was slightly increased (Fig. 7.3.7). Fractography on lower fluence specimens showed that irradiation has not affected the fracture mode on a coarse scale. The fracture mode of HT-9 weld may be changed after irradiation to a fluence of 6 x 10^{22} n/cm². This will be confirmed by scanning electron microscope fractography.

The 2.54 mm thick specimens tested in this work are small compared to the conventional one (25 mm thick). The intention of using small specimen and a single specimen method was to economize irradiation space. However, while a small specimen size is desirable, invalid data produced by an undersized specimen are not favorable. Experimental results',' have shown that the specimen size used in this work is satisfactorily optimized for data validity. Since the post-irradiation fracture toughness was reduced and the yield stress was increased by irradiation, the thickness criterion for a valid J_{IC} test was met for the 2.54 mm thick specimens used in irradiated testing.

7.3.6 Conclusions

(1) The fracture toughness of HT-9 with a grain size of 3-4 is lower than that of HT-9 with a grain size of 8-9.

(2) Irradiation temperature has a weak effect on the toughness hut a strong effect on the tearing modulus of HT-9.

(3) The fracture toughness of HT-9 weld metal was degraded by 40% as the fluence was increased from 3 to 6 x 10^{22} n/cm².

7.3.7 Future Work

Fracture toughness tests on irradiated specimens of HT-? from the AD-2 experiment will be continued.

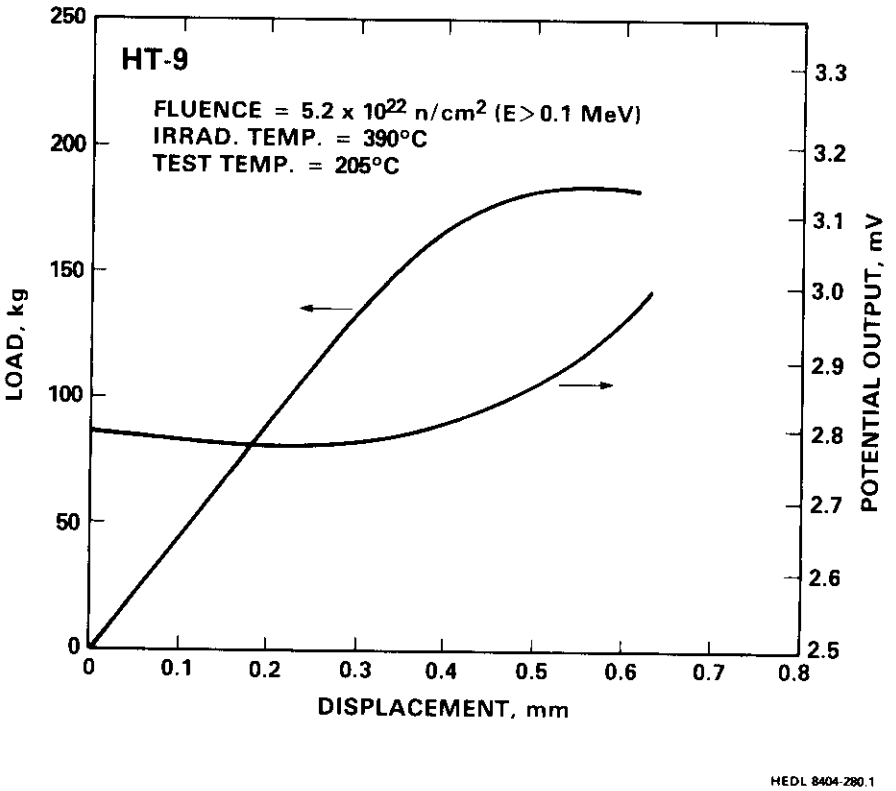

Fig. 7.3.2. Potential output and load versus displacement curves for irradiated HT-9.

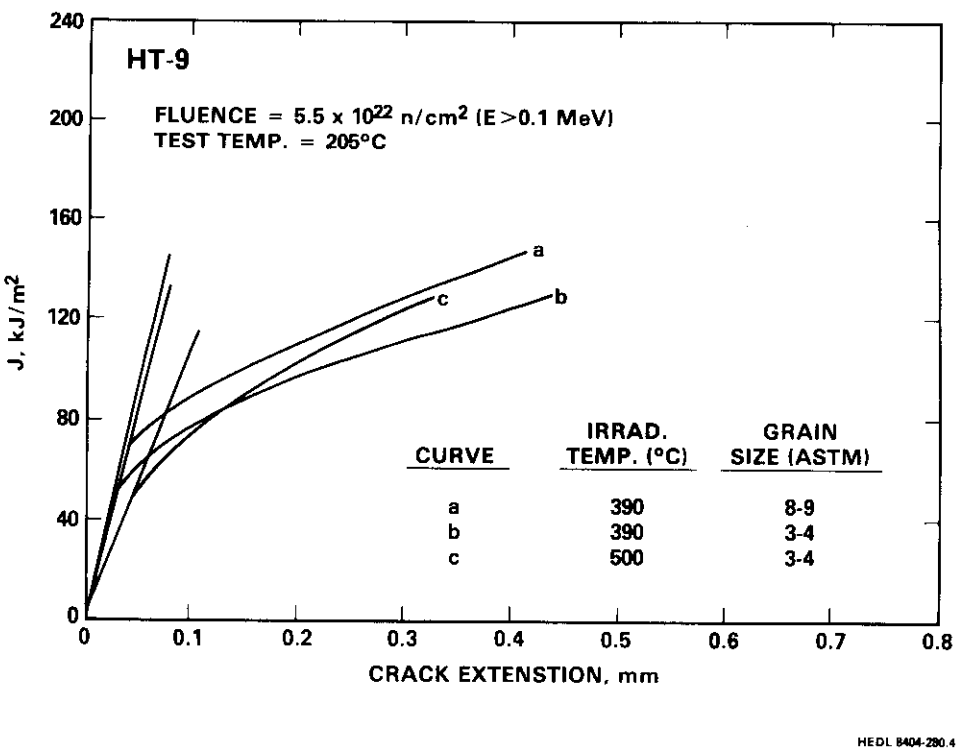

Fig. 7.3.3. J versus Δa curves obtained via electropotential calibration curves for irradiated HT-9.

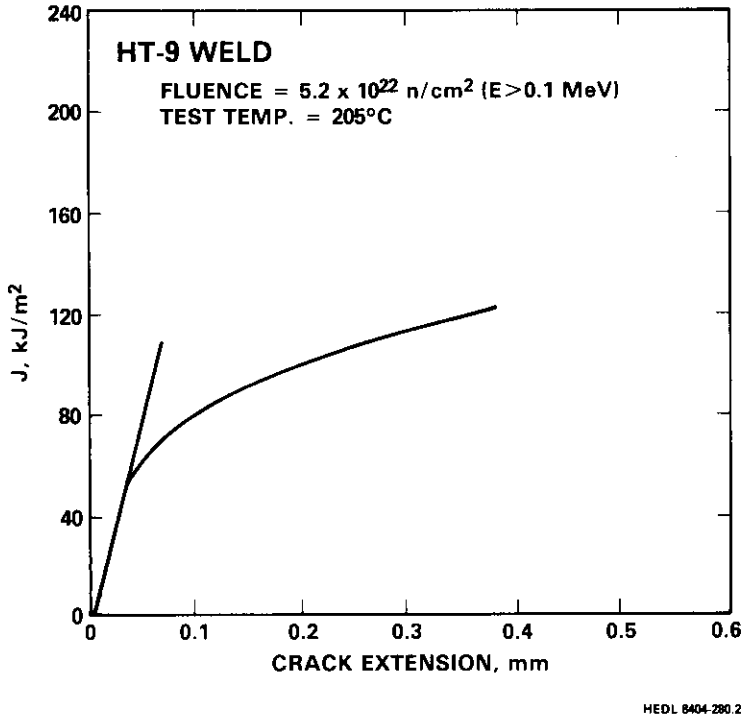

Fig. 7.3.4. J versus Δa curves obtained via an electropotential calibration curves for irradiated HT-9 weld.

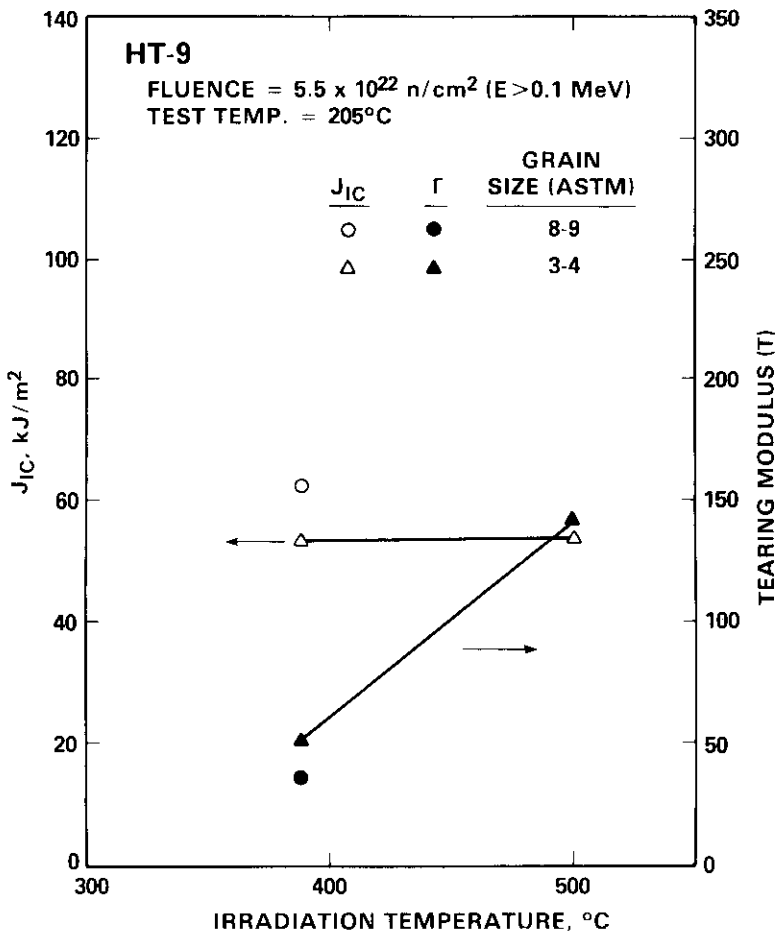

Fig. 7.3.5. Irradiation temperature dependence of fracture toughness and tearing modulus for irradiated HT-9 with different grain size.

Table 7.3.1. Fracture toughness test results of HT-9 base and weld metals

Material	Irradiation Temp. (°C)	Fluence (10^{22} n/cm²)	J_{IC} (kJ/m²)	Tearing Modulus	Grain Sire (ASTM)
Base	390	5.5	62.1	37	8-9
Rase	390	5.2	53.0	54	3-4
Base	500	5.2	54.2	140	3-4
Weld	390	5.2	57.8	44	-

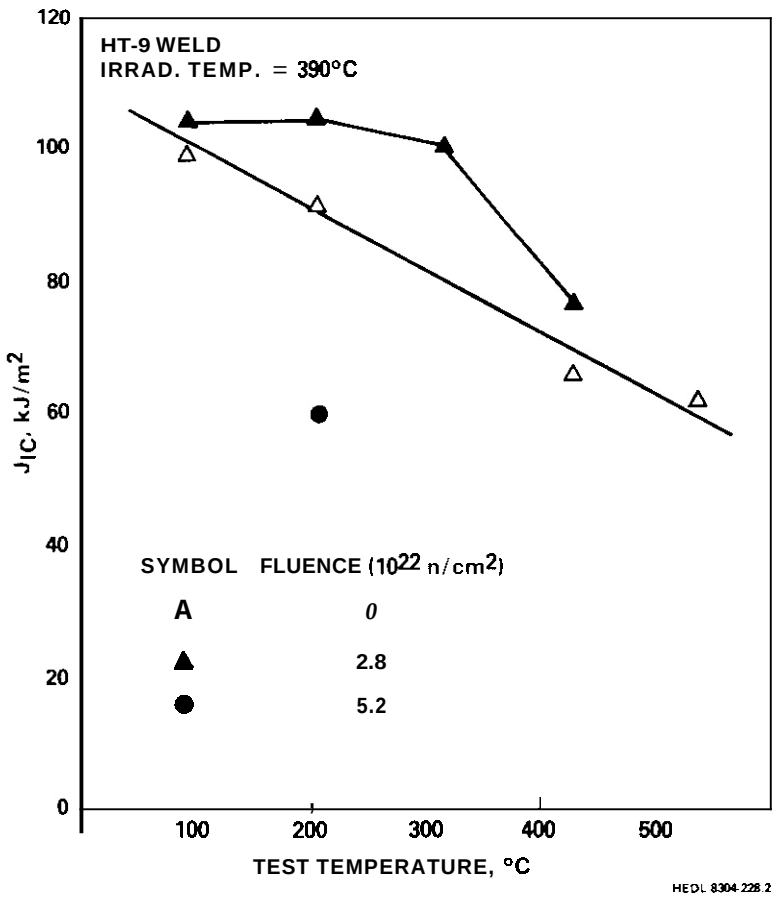

Fig. 7.3.6. Temperature dependence of fracture toughness for irradiated and unirradiated HT-9 weld metal.

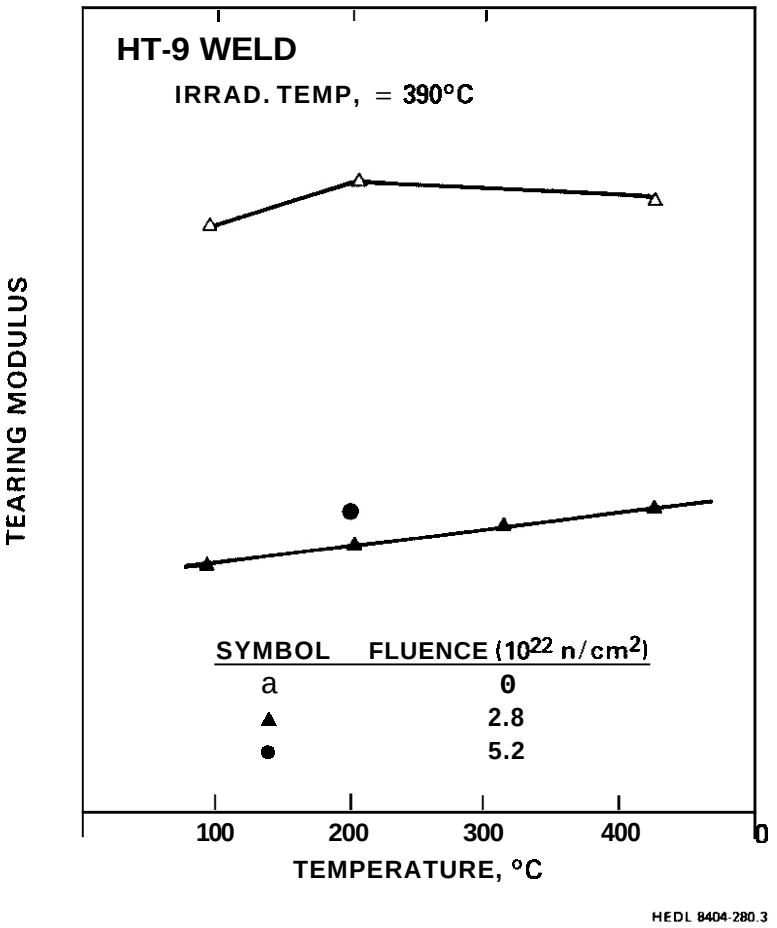

Fig. 7.3.7. Temperature dependence of tearing modulus for irradiated and unirradiated HT-9 weld metal.

7.3.8 References

1. F. H. Huang and G. L. Wire, "Fracture Toughness Testing of Ferritic Alloys Using Electropotential Techniques," *J. Nucl. Mater.* 104, 1511-1516 (1982).

2. F. H. Huang, "Fracture Toughness of Unirradiated HT-9 and Modified 9Cr-1Mo Welds," pp. 221-229 in *ADIP Semiann. Prog. Rep. Sept.* 30, *1982,* DOE/ER-0045/9, U.S. DOE, Office of Fusion Energy.

3. F. H. Huang and D. S. Gelles, "Fracture Toughness of Irradiated HT-9 Weld Metal," pp. 125-130 in *ADIP Semiann. Prog. Rep. March 31, 1983,* DOE/ER-0045/10, U.S. DOE, Office of Fusion Energy.

4. R. J. Puigh and N. F. Panayotou, "Specimen Preparation and Loading for the AO-2 Ferritics Experiment," pp. 260-293 in *ADIP Quart. Prog. Rep. Sept. 30, 1980,* DOE/ER-0045/4, U.S. DOE, Office of Fusion Energy.

5. A. Plumtree and R. Gullberg, "The Influence of Interstitial Content on the Ductile-Brittle Transition Temperature of Fe-25Cr Ferritic Stainless Steels," *J. Test. Eval.* 2(5), 331-336 (1974).

6. C. J. McMahon Jr., D. H. Gentner and A. H. Ucisik, "An Investigation of the Effects of Grain Size and Hardness in Temper-Embrittled 2-1/4Cr-1Mo Steel," *J. Eng. Muter. Tech.* 106, *66-70* (1984).

7. F. H. Huang and D. S. Gelles, "Influence of Specimen Size and Microstructure on the Fracture Toughness of a Martensitic Stainless Steel," *Eng. Fract. Mech.* 19(1), *1-20* (1984).

8. F. H. Huang, "Use of Subsized Specimens for Evaluating the Fracture Toughness of Irradiated Materials," presented at ASTM Symposium on the Use of Nonstandard Subsized Specimens for Irradiated Testing, Albuquerque, NM. Sept. 23, 1983, to be published by American Society for Testing and Materials.

7.4 VARIATION OF POSTIRRADIATION STRENGTH PROPERTIES OF FERRITIC STEELS WITH IRRADIATION TEMPERATURES — J. M. Vitek and R. L. Klueh (Oak Ridge National Laboratory)

7.4.1 ADIP Task

AOIP Tasks are not defined for Path E Ferritic Steels in the 1978 Program Plan.

7.4.2 Objective

The objective of this work is to combine currently available postirradiation strength data in the fusion program on ferritic steels to determine the effect of irradiation temperature on the strength properties.

7.4.3 *Summary*

Data on postirradiation strength properties have been plotted as a function of irradiation temperature, and a consistent trend has been observed for the three ferritic steels under investigation.

7.4.4 Progress and Status

7.4.4.1 Introduction

Several experiments have been conducted evaluating the postirradiation strength properties of ferritic steels for a variety of irradiation temperatures. Many of these data were recently compiled into plots of strength versus irradiation temperature for each of the three ferritic steels under investigation — 2 1/4 Cr-1 Mo, 9 Cr-1 MoVNb, and 12 Cr-1 MoVW (ref. 1). However, several objections arise regarding the methods used in this analysis. First, the plots combine postirradiation hardness test results with postirradiation yield strength properties. This is inappropriate since the former involves significant plastic deformation while the latter relates to primarily elastic deformation. Instead, a valid comparison would be between the ultimate tensile strengths and hardness. This view is supported by the fact that conversion tables relate ultimate tensile strength to hardness, and not yield strength to hardness.'

Second, it is invalid to correlate hardness ratios with strength ratios as done earlier,' since the conversion between strength and hardness is not linear. For example, post- and preirradiation hardness values for 9 Cr-1 MoVNb were 25.3 and 15.2, respectively, yielding a hardness ratio of 1.66 whereas conversion to tensile strengths and then taking the ratio of post- to preirradiation values results in a ratio of only 1.25.

Finally, since all hardness measurements were made at room temperature, regardless of the irradiation temperature, any comparison with tensile data should be with tensile data taken at room temperature. Inclusion of data from elevated-temperature tests is inappropriate and complicates any correlation.

The earlier data, where appropriate, were replotted in an effort to achieve a consistent and valid correlation of tensile and hardness results taken on several alloys irradiated under a variety of conditions. These results are presented in this report.

7.4.4.2 Results and Discussion

The data base in this study is taken from various sources as listed in Table 7.4.1. These include all the appropriate data previously used'.'" as well as recently acquired data.[8-11] The results are plotted in Fig. 7.4.1 for the three ferritic alloys — 12 Cr-1 MoVW, 9 Cr-1 MoVNb, and 2 1/4 Cr-1 Mo. These curves present the ratio of post- to preirradiation strength versus the irradiation temperature for tests at room temperature. Where hardness data were used, the hardness values were first converted to ultimate tensile strengths.[2]

Several points are worthy of discussion. First, all three steels show basically the same degree of hardening at low irradiation temperatures, and this hardening remains nearly constant to about 400°C. With irradiation temperatures of 500°C or higher, some softening is found. The temperature of reversal from hardening to softening is essentially the same for all three alloys.

The scatter in Fig. 7.4.1 is considerably less than that shown earlier.' With the more consistent curves, the change in room-temperature strength properties with irradiation seems to be much more predictable and furthermore seems to be similar for all three alloys. Much of the scatter that remains, particularly in Fig. 7.4.1(*a*), is due to tensile strength properties of 12 Cr-1 MOVW with two different heat treatments irradiated in ERR-I1 AD-2.

Table 7.4.1. Sources of data used in Fig. 7.4.1

Symbol	Test type	Irradiation experiment	References
▬	Tensile	HFIR-CTR-33	3, 4, 5
▬	Tensile	EBR-II X-322	6
■	Tensile	EBR-II-AD-2	8, 9, 10
▲	Tensile	HFIR-MFE-RB1	11
O	Hardness	HFIR-MFE-RR1	1
□	Hardness	EBR-11-AD-2	7

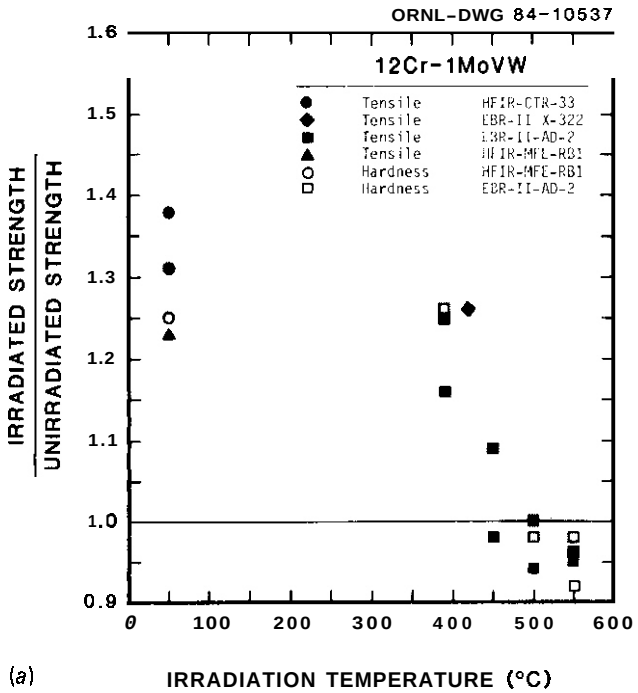

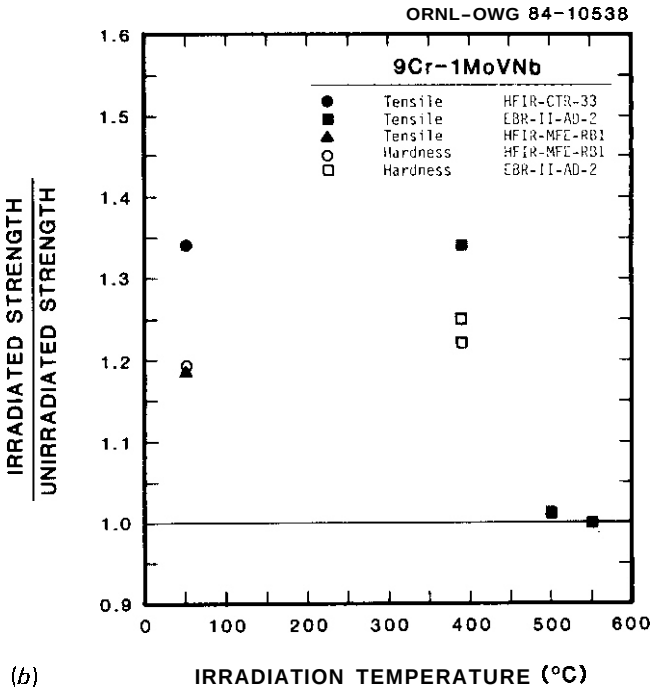

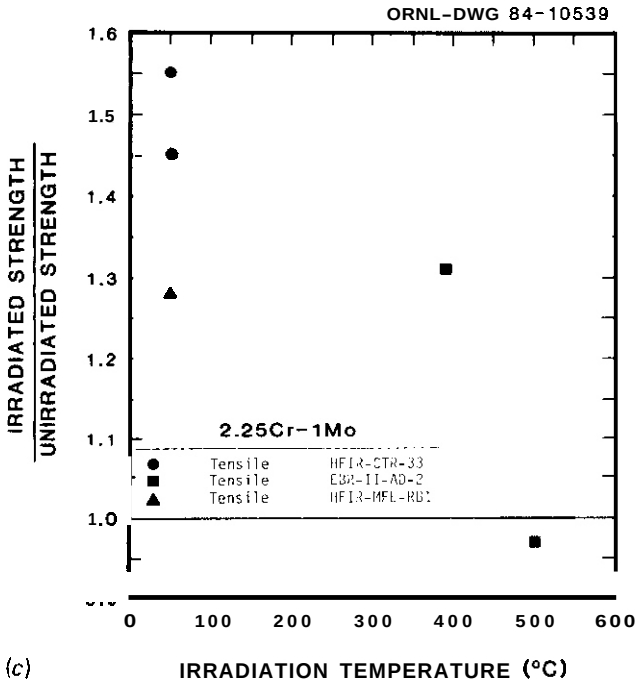

Fig. 7.4.1. Ratio of irradiated to unirradiated strength plotted against irradiation temperature for *(a)* 12 Cr-1 MoVW, *(b)* 9 Cr-1 MoVNb. and *(c)* 2 1/4 Cr-1 Mo. All strength values are from room-temperature tests.

Gelles et al. suggested' that the Charpy properties were not saturated in the HFIR-MFE-RBI experiment, irradiated to an approximate damage level of 5 dpa. The large difference in strength ratios between hardness results from HFIR-MFE-RBI and yield strength values from HFIR-CTR-33 was taken as additional evidence that saturation was not achieved in HFIR-MFE-RB1. However, this discrepancy is substantially reduced when hardness is properly compared with ultimate tensile strength. The difference between strength ratios from HFIR-MFE-RB1 irradiated samples (≈5 dpa) and those irradiated in HFIR-CTR-33 (≈10 dpa) is not really any greater than the scatter found elsewhere. In addition, the fact that strength ratios from hardness measurements of RB1-irradiated samples were lower may not relate to saturation effects since lower values from hardness readings were also found in Fig. 7.4.1(*b*) for samples irradiated at 390°C in EBR-II to identical fluences. Furthermore, recent tensile results indicate the same postirradiation properties are found for specimens from HFIR-MFE-RE1 (ref. 11) and HFIR-CTR-33. (The same ratios are not found since initial properties differed.) Therefore, it is likely that tensile property saturation is near, if not already achieved. Nonetheless, there is a chance that saturation of tensile properties has not been achieved in HFIR-MFE-RB1.

This would be indicated by the fact that tensile property ratios for HFIR-MFE-RB1 irradiated samples are consistently lower than ratios for HFIR-CTR-33 samples. In the case that saturation has not been reached, Fig. 7.4.1 indicates that all the alloys fall equally short of saturation.

The strength properties plotted in Fig. 7.4.1 cannot be readily associated with impact behavior since impact properties are related to yield strength behavior. However, it is not clear that similar curves plotting the relative increase in yield strength against irradiation temperature are particularly useful in predicting Charpy impact properties. This is because the unirradiated yield strength values vary considerably with heat treatment, and taking ratios of post- to preirradiated properties may be misleading. In fact, the justification for using relative strengths as an indication of saturation is not obvious. Because of variations in the initial material conditions, equivalent relative strength increases may be a misleading indicator with regard to saturation. Relative strength increases were used previously[3-5] in comparing somewhat different alloys with similar microstructures but significantly different initial strengths. However, the use of such relative increases for a given alloy with different unirradiated strengths (and presumably different microstructures) may not be appropriate. The examination of other possible means of reflecting saturation in strength properties will be the subject of future work.

7.4.5 References

1. D. S. Gelles et al., "Effect of HFIR Irradiation at 55°C on the Microstructure and Toughness of HT-9 and 9 Cr-1 Mo," pp. 115–27 in *ADIP Semiannu. Prog. Rep. Sept. 30, 1983,* DOE/ER-0045/1, U.S. DOE, Office of Fusion Energy.
2. *Metals Handbook,* Vol. 1, Properties and Selection, p. 1234, American Society for Metals, Metals Park, Ohio, 1961.
3. R. L. Klueh, J. M. Vitek, and M. L. Grossbeck, "Effect of Low Temperature Irradiation with (n,α) Helium Production on Tensile Properties of 12 Cr-1 MoVW-Type Steels," *J. Nucl. Mater.* 1036104, 887–91 (1981).
4. R. L. Klueh, J. M. Vitek. and M. L. Grossbeck, "Nickel-Doped Ferritic (Martensitic) Steels for Fusion Reactor Irradiation Studies: Tempering Behavior and Unirradiated and Irradiated Tensile Properties," pp. 648–64 in *Effects of Irradiation on Materials: Eleventh Conference,* ASTM-STP-782, ed. H. R. Brager and J. 5. Perrin, American Society for Testing and Materials, Philadelphia, 1982.
5. R. L. Klueh and J. M. Vitek, "Tensile Properties of Ferritic Steels after Low-Temperature HFIR Irradiation," pp. 275–83 in *ADIP Semiannu. Frog. Rep. Sept. 30, 1981,* DOE/ER-0045/7, U.S. DOE, Office of Fusion Energy.
6. F. A. Smidt, Jr., J. R. Hawthorne, and V. Provenzano, "Fracture Resistance of HT-9 after Irradiation at Elevated Temperature," pp. 269–84 in *Effects of Radiation on Materiats: Tenth Conference,* ASTM-STP-725, ed. D. Kramer, H. R. Brager, and J. S. Perrin, American Society for Testing and Materials, Philadelphia, 1981.
7. D. S. Gelles and W. L. Hu, "Fractographic Examination of HT-9 and 9 Cr-1 Mo Charpy Specimens Irradiated in the AD-2 Test," pp. 178–219 in *ADIP Semiannu. Prog. Rep. Sept. 30, 1982,* DOE/ER-0045/9, U.S. DOE, Office of Fusion Energy.
8. R. L. Klueh and J. M. Vitek, "Elevated Temperature Tensile Properties of 12 Cr-1 MoVW Steel Irradiated in the ERR-11, AD-2 Experiment," pp. 104–7 in *ADIP Semiannu. Prog. Rep. Mar. 31, 1983,* DOE/ER-0045/10, U.S. DOE, Office of Fusion Energy.
9. R. L. Klueh and J. M. Vitek, "Elevated-Temperature Tensile Properties of 9 Cr-1 MoVNb Steel Irradiated in the EBR-II AD-2 Experiment," Sect. 7.2 of this report.
10. R. L. Klueh and J. M. Vitek, "Elevated Temperature Tensile Properties of 2 1/4 Cr-1 Mo Steel Irradiated in the EBR-II, AD-2 Experiment," pp. 95–102 in *ADIP Semiannu. Prog. Rep. Sept. 30, 1983,* DOE/ER-0045/11, U.S. DOE, Office of Fusion Energy.
11. R. L. Klueh, Oak Ridge National Laboratory, unpublished results.

7.5 EVALUATION OF FERRITIC ALLOY Fe-2-1/4Cr-1Mo AFTER NEUTRON IRRADIATION - MICROSTRUCTURAL DEVELOPMENT

D. S. Gelles (Westinghouse Hanford Company)

7.5.1 ADIP Task

The Department of Energy (DOE) Office of Fusion Energy (OFE) has cited the need to investigate ferritic alloys under the ADIP Program task, Ferritic Steels Development (Path E). The tasks involved are akin to task number 1.C.2, Microstructures and Swelling in Austenitic Alloys and task number 1.C.1, Microstructural Stability.

7.5.2 Objective

The objective of this work is to provide guidance on the applicability of martensitic stainless steels for fusion reactor structural components.

7.5.3 *Summary*

Microstructural examinations are reported for nine specimen conditions of 2-1/4Cr-1Mo steel which had been irradiated bv fast neutrons over the temoerature ranae 390 to 510°C. Two heats of material were involved, each with a different preirradiation heat treatment, one irradiated to a peak flunce of 5.1 x 10^{22} n/cm² (E > 0.1 MeV) or 24 dpa and the other to 2.4 x 10^{23} n/cm² (E > 0.1 MeV) or 116 dpa. Void swellina is found following irradiation at 400°C in both conditions and to 480°C in the higher fluence conditions. Concurrently dislocation structure and precipitation formed. Peak void swelling, void density, aislocation density and precipitate number density developed at the lowest temperature, ~400°C, whereas mean void size, and mean precipitate size increased with increasing irradiation temperature. The examination results are used to provide interpretation of in-reactor creep, density change and post irradiation tensile behavior.

7.5.4 Progress and Status

7.5.4.1 Introduction

The Electric Power Research Institute of Palo Alto, CA has funded a program entitled Evaluation of Irradiation Metal Samples for Use in Fusion Components under contract RP-1597-1 with McDonnell Douqlas Astronautics Company. Westinghouse Hanford Company has been a participant in that program under contract Y3E052R entitled Evaluation of Ferritic Alloy Fe-2-1/4Cr-1Mo After Neutron Irradiation - Irradiation Creep and Swelling. The second phase of that effort has now been completed. In order to disseminate the results of that effort to the fusion materials community in the shortest possible time, a version of the summary report is being included in the Alloy Development for Irradiation Performance Semiannual Progress Report. This report provides results of microstructural examinations on irradiated 2-1/4Cr-1Mo steel.

Previous experiments in this series have provided irradiation creep,' irradiation induced density change' and postirradiation tensile properties' for 2-1/4Cr-1Mo. Pressurized tube specimens in a normalized and tempered bainitic condition were measured for diameter changa following irradiation at 390, 480 and 570°C to 5.5 x 10^{22} n/cm² (E > 0.1 MeV) or 26 dpa.' It was found that the creep rate was greatest at 570°C but the creep rate at 390°C was slightly higher than at 480°C. Based on diameter change measurements on unstressed pressurized tubes, void swelling of about 0.3% was predicted and creep at 390°C was in part attributed to swelling enhanced creep.

Density change measurements were made on slug specimens in an unusual heat treatment condition following irradiation at 400, 425, 450, 480. 510 and 540°C to fluences hetween 1.55 x 10^{23} n/cm² and 2.41 x 10^{22} n/cm² (E > 0.1 MeV) or 74 to 116 dpa.' The heat treatment condition was complex and was believed to have contained tempered proeutectoid ferrite, overtempered bainite, proeutectoid ferrite and untempered bainite. This condition was found to be highly resistant to irradiation induced swelling. The peak density change, 0.28% swelling, occurred following irradiation at 400°C to 1.6 x 10^{23} n/cm² or 77 dpa. This peak was attributed to void swelling whereas a lesser peak of 0.22% swelling at 540°C was attributed to orecioitation causes.

Miniature sheet tensile specimens in a normalized and tempered bainitic condition were irradiated at 390, 450, 500 and 550°C to about 1.9 x 10^{22} n/cm² (E > 0.1 MeV) or 9 dpa. Following irradiation, tensile tests were conducted at the irradiation temperature and in a few cases at room temperature.' Thermal control specimens aged far 5000 hours to duplicate the irradiation condition were also tested. The results showed that thermal aging reduced strength moderately for all testing conditions but that reactor irradiation increased yield strength by 25% at 390°C and decreased yield strength by 40% at 550°C for tests run at the irradiation temperature. These results were interpreted as follows. Reductions in strength due to thermal aging at 390 and 450°C were attributed to loss of interaction solid-solution hardening (ISSH), whereas at 500 and 550°C a combination of loss of ISSH and precipitate coarsening were responsible. Similar explanations were used to explain effects of irradiation at 450 and 500°C hut the increase in strenqth following 390°C irradiation was attributed to the development of dislocation-loop structure and the decrease in strength following irradiation at 550°C was concluded to he due to the enhanced kinetics of the precipitation coarsening reaction during irradiation.

The present effort is intended to support the previous studies by providing microstructural information on several specimens *of* interest. The specimens examined were either sections from the density change

specimens or were unstressed disks which matched the irradiation conditions of the pressurized tube specimens. The disk specimens had been irradiated to twice the exposure received by the tensile specimens. Therefore, microstructural information from these specimens should he able to answer several questions raised in previous work. For example, is the mechanism, swelling enhanced creep, applicable in pressurized tubes irradiated to only 25 dpa? Could a density change peak at 540°C be due to void swelling? Is the explanation for post irradiation tensile behavior reasonable?

The present effort is also applicable to a companion study of irradiation effects in 2-1/4Cr-1Mo. A task paralleling the irradiation effects data base development is to provide a hasis for extrapolating that data base to irradiation regimes and doses which more closely duplicate fusion first wall conditions.' The objectives of that task are threefold: 1) to compare microstructural evolution under ion homhardment with that under neutron bombardment in order to accurately model void, dislocation and precipitate evolution during irradiation, 2) to develop theoretical models to predict radiation damage and, 3) to generate lifetime dnalyses of Tokamak and Tamdem Mirror Ferromagnetic Reactor Structures. Therefore, the present microstructural studies are expected to provide both a basis for comparison of microstructural evolution between ion and neutron bombardment and quantitative information which should be directly applicable to theoretical model calculations.

7.5.4.2 Experimental Procedures

Specimens of 2-1/4Cr-1Mo selected for microstructural examination were obtained from three irradiation tests. Details regarding alloy chemistry and specimen fabrication have been previously described.' Two heats of material are involved and alloy chemistries are reproduced in Table 7.5.1. Heat treatment conditions are given in Table 7.5.2. All tests were irradiated in the Experimental Breeder Reactor (ERR-11) located in Idaho Falls, Idaho. The first test designated AAI contained rod specimens 1.25 cm x 0.3 cm in diameter. Details of the irradiation test are given in Reference 1. The second test called AAXIV Phase 2 contained, among other conditions, both pressurized tubes and disk specimens of 2-1/4Cr-1Mo. The disk specimens were 0.03 cm x 0.3 cm in diameter and were included to provide specimens for microstructural examination to match irradiation conditions for mechanical properties samples. However, the disk specimens were not in the same pin as the pressurized tubes. The disks were contained in pins 8326 and B326a. Pin 8326 received an accumulated fast fluence of 2.6 x 10^{22} n/cm² (E > 0.1 MeV) or 12.5 dpa and was a weeper design which allowed flowing sodium coolant from the reactor to directly contact the specimens. The design temperature was 400°C and thermal expansion devices (TEDs) indicated that the actual temperature was 395 % 5°C. Disk specimens were then reconstituted into pin B236a. Pin B326a received an accumulated fast fluence of 2.5 x 10^{22} n/cm² (E > 0.1 MeV) or 12 dpa and was of 07 design which employed gas gap regulation of gama heating losses in order to obtain the desired temperature in an internal subcapsule. The design temperature was 412°C but TEDs indicate that the actual temperature was 425 + 10°C. Therefore, the temperature is given as 410 ± 20°C for the entire AAXIV Phase 2 irradiation experiment. The specimens irradiated in the third test, designated AD2, involved pins 8317, B318, 8321, B317a, B318a and B319a. Each was a 87 design and the accumulated fast fluence was estimated at 6.1 x 10^{22} n/cm² (E > 0.1 MeV) or 29 dpa. Design temperatures were 400, 450 and 500°C but TED results are not yet available for verification. The disk specimen conditions do not exactly match the tensile specimen conditions irradiated in the same experiment. The disk specimens were more central in the reactor core and therefore received a higher neutron flux by ahout 25%. Specimens selected for examination are listed by sample identification number in Tahle 7.5.3.

Specimens were prepared for transmission electron microscopy as follows. Rod specimens were sliced into disks 0.025 cm x 0.3 cm in diameter using a slow speed saw with diamond impregnated blades. All specimens were briefly electropolished in a 5% perchloric acid, 95% butanol solution at 30 V to remove surface corrosion. At least two foils of each condition were prepared. Thin foil specimens were then produced using a Metalthin twin jet electropolishing machine which was located in a radiation shielded facility equipped with manipulators. The polishing solution was the same with polishing conditions at 65 V and moderate pump speed. As is often found to be the case for lower chromium alloys, surface staining was often found to be a problem in which case, a very brief "flash polish" was helpful.

Microstructural examinations were performed for the most part on a JEOL 1200EX electron microscope operating at 120 KeV. One specimen of 94L6 was also examined on a JEOL 100 CX electron microscooe operating at 100 KeV. The general procedure involved examination of a number of areas of interest, and then following a known tilt of the specimen, a reexamination of those areas. This generally provided void and precipitate information, and in several cases dislocation structure information in areas for which foil thickness could be measured stereoscopically. Thickness determination required measurement of the maximum parallax, ΔH, for the area of interest on a stereo viewer and then computation of the foil thickness from the relationship

$$t = \frac{\Delta H}{2M \sin(\theta/2)} \qquad (1)$$

where t is the foil thickness, M is the magnification of the images and θ is angle of tilt between the images.

Quantitative measurements of void, precipitate and dislocation structures employed a measurement device coupled directly to a minicomputer. With the push of a foot pedal, a void imaqe width in the <110> direction, a precipitate diameter (or length in the case of rod specimens) or a dislocation intersection with a line grid was input to the computer. The computer was programed to accept a large number of measurements and given the foil thickness, compute the size distributions, total volume fraction and numher densities for the input data on request. For void swelling, the program accounted for the faceted nature of the void shape and was able to allow large variation in truncation in a given area of interest with a maximum error

Table 7.5.1 Chemical analysis of 2-1/4Cr-1Mo heats as supplied by the vendors (in weight percent)

Element	Rod Specimens Heat 38649	Disk Specimens Heat C4337-14S
C	0.12	0.093
Mn	0.42	0.52
P		0.011
S		0.011
Si	0.21	0.17
Ni	0.16	0.40
Cr	2.17	2.15
Mo	0.93	0.95
cu		0.16
Al		0.003
Fe	bal	bal

Table 7.5.2. Heat treatments given rod and disk specimens prior to irradiation

Specimen Type	Heat #	Heat Treatment*
Rod Specimens	C4337-14S	1010°C/1 hr/WQ + 843°C/2 hr/WQ
Disk Specimens	38649	900°C/30 min/AC + 700°C/1 hr/AC

*Temperature/time at temperature/cooling procedure where AC = air cooled, WQ = water quenched

Table 7.5.3. Irradiation conditions of specimens selected for microstructural examination

ID	Experiment	Irradiation Temperature °C	Irradiation Fluence x 10^{22} n/cm²	(dpa)
94M6	AAI	400	16.0	(76)
94L6	AAI	425	20.7	(99)
94E7	AAI	450	15.5	(74)
94F6	AAI	480	19.8	(95)
94K6	AAI	510	24.1	(116)
NUYL	AAXIV	410 ± 20	5.1	(24)
31CP	ADZ	390	5.0	(24)
31CV	AD2	450	5.0	(24)
31CR	ADZ	500	5.0	(24)

due to truncation of 20%. As each feature was measured on a 3X print, the apparatus pin pricked the feature to prevent counting the same feature twice.

7.5.4.3 Results

Reporting of the results of microstructural examinations will be divided into three sections. First the microstructures of the AAI specimens will he described. Then the microstructure of the normalized and tempered bainite (AAXIV and ADZ) will be described. Finally the results of quantitative measurements for both specimen conditions will be given.

AAI Specimens

The heat treatment given the AAI specimens (Table 7.5.2) produced a complex microstructure. The material was in the form of 1.2 cm thick plate when heat treated and the water quenches called for at the end of each treatment step would have resulted in cooldown within about 100 seconds. Primarily upper bainite with no proeutectoid ferrite is expected when cooling from the austenite region under such conditions as can be shown from the continuous cooling transformation (CCT) diagram' given in Fig. 7.5.1. The first step of the treatment, normalization at 1010°C for one hour followed by a water quench should produce ~75% upper bainite with the remainder lower bainite and martensite. Reheating to 843°C put the specimens in the two phase region (between the Ac_1 at 740°C and the Ac_3 at 880°C). Therefore, austenite formed and some ferrite was retained. However, all carbides should be dissolved. Water quenching should again cause the austenite to transform primarily to upper bainite with no proeutectoid ferrite formed during cooling. The microstructure produced by this treatment is shown in Figs. 7.5.2 and 7.5.3. Fig. 7.5.2 gives optical metallography at a series of magnifications for the preirradiation structure. The structure is fine (prior austenite grain size ASTM #8) with at least two phases easily identified: a bainite structure similar to lath martensite which appears as gray regions with internal linear structure and nonequiaxed ferrite which appears as white, substructure-free, regions. Fig. 7.5.3 provides examples of transmission electron microscopy for this structure. Three distinctly different regions can he identified. Large precipitate-free regions with low dislocation densities are regions which were retained ferrite at 843°C. The remaining structure was austenite at 843°C which transformed to bainite on cooling. Both upper and lower bainite are present. In upper bainite, the carbide particles frequently form in elongated configurations between the hainite (ferrite) grains whereas in lower bainite the carbides tend to precipitate at an inclined angle to the major growth direction, or longitudinal axis, of the bainitic ferrite grains.[5] In Fig, 7.5.3, examples of retained ferrite, upper bainite and lower bainite have been labeled. Therefore, post irradiation microstructural examination of AAI conditions should include each of these regions.

Specimen 94M6, irradiated at 400°C to 1.6 x 10^{23} n/cm² (E > 0.1 MeV) or 76 dpa was found to retain the preirradation microstructure but void swelling, dislocation network evolution and precipitation occurred as a result of irradiation. An example of the microstructure at low magnification is shown in Fig. 7.5.4. At the upper right a retained ferrite region is shown in dislocation contrast. Small voids can he seen but the precipitate structure is not very apparent. In comparison, at the lower right a region corresponding to upper bainite can be seen in heavy strain contrast. The void density is lower, and elongated carbide particles separating bainite plates can be seen. At the lower left a region of lower bainite is present. The precipitate particles are larger and more numerous than in the retained ferrite region, and the void density appears to be lower. Examples of the three structures are shown at higher magnifications in Fig. 7.5.5. The most notable differences between them are in precipitate size and distribution and void distribution. Precipitate number density is greatest in the retained ferrite region and lowest in the upper hainite region. However, both the upper bainite and lower bainite regions contain the elongated precipitate particles characteristic of the retained ferrite region. It is anticipated that such particles have formed during irradiation whereas the larger particles originated in the preirradiation heat treatment. Voids are uniformly distributed in retained ferrite regions and lower bainite regions whereas they are non-uniformly distributed in the upper bainite region. Some areas in the upper bainite region contain very few voids.

One area of retained ferrite in specimen 94M6 was used to examine the irradiation induced dislocation network in detail. An area oriented near [011] was imaged using g = $01\bar{1}$, 211 and 200 for dislocation contrast as shown in Fig. 7.5.6. Comparison of the images from g = $01\bar{1}$ and 200 reveals that few dislocations appear in both micrographs. This indicates that these dislocations are predominantly of a<100> character because if they were of type a/2 <111>, then all would show up for $\bar{g}$ = 200 and half would show up for g = $01\bar{1}$. A table which can be used to demonstrate this point is provided in Table 7.5.4. For those $g \cdot \bar{b}$ products equal to zero, dislocations of that Burgers vector should be invisible whereas products which are nonzero should allow visibility. Note that for $\bar{g}$ = 200 only dislocations with Burgers vector a[100] should be visible; a[010] and a[001] should be invisible. (However, all a/2 [111] should be visible.) From Fig. 7.5.6 it can be shown that perfect dislocation loops are present, that they tend to be on {001} planes and that they are pure edge in character. Many examples of a<001> dislocation segments can also be found. Therefore. the dislocation structure is in the process of transferring from a loop dominated structure to a network dominated structure.

Specimen 94L6, irradiated at 425°C to 2.1 x 10^{23} n/cm² (E > 0.1 MeV) or 99 doa in many ways resembled specimen 94M6 irradiated at 400°C. Regions of retained ferrite, upper bainite and lower bainite could be identified, and void swelling was present. However, the amount of swelling was reduced due to reduced void number densities and voids were absent in upper bainite regions. Also the precipitates in retained ferrite regions were larger so that differentation between retained ferrite and lower bainite regions was much more [illegible] An example of the structure at low magnification is shown in Fig. 7.5.7. The central reoinn [illegible] bainite and by comparison with Figs. 7.5.3 and 7.5.4 it is

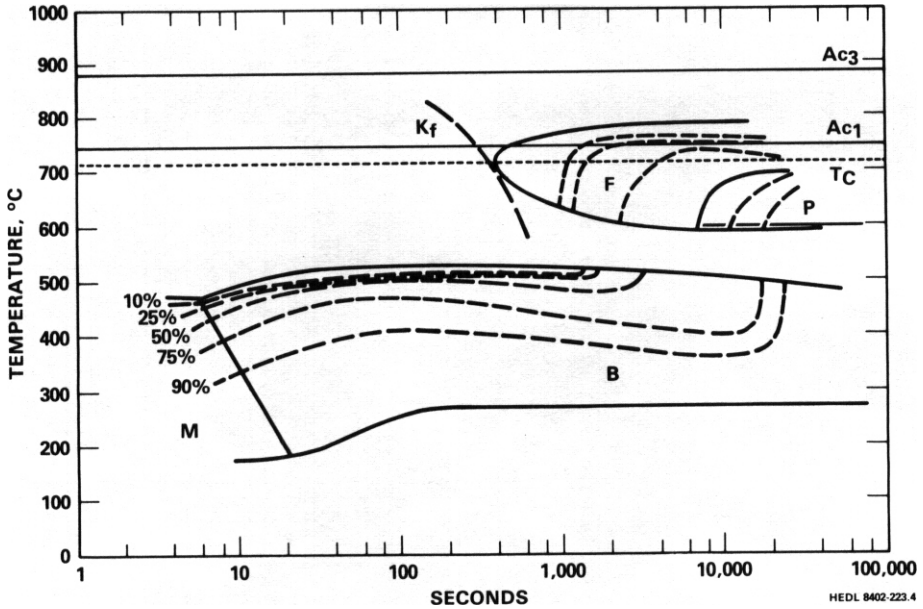

Fig. 7.5.1. Continuous cooling transformation diagram for 0.1 percent carbon 2-1/4Cr-1Mo steel, ASTM grain size 7. F = polygonal ferrite, P = pearlite, B = bainite, M = martensite.

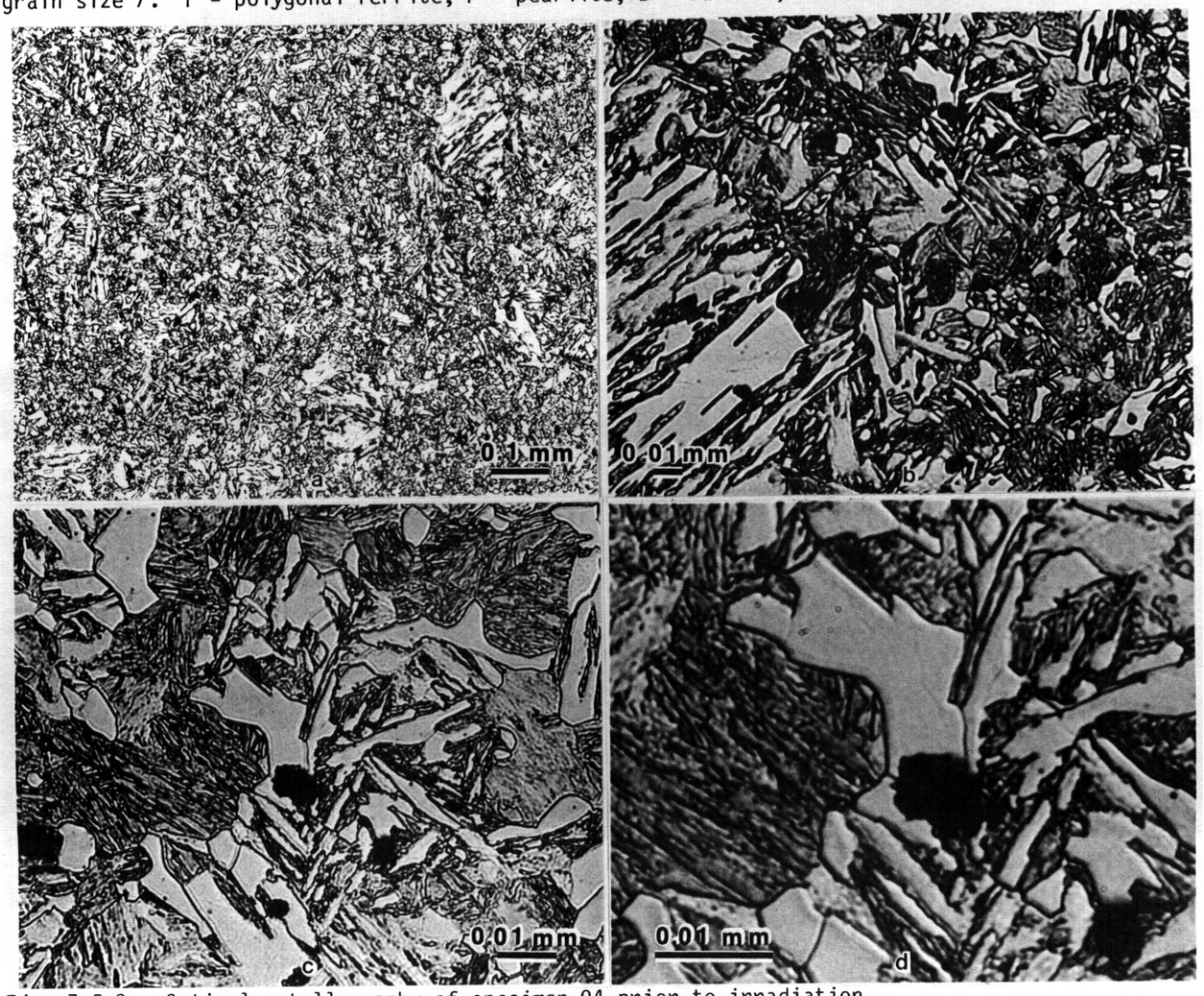

Fig. 7.5.2. Optical metallography of specimen 94 prior to irradiation.

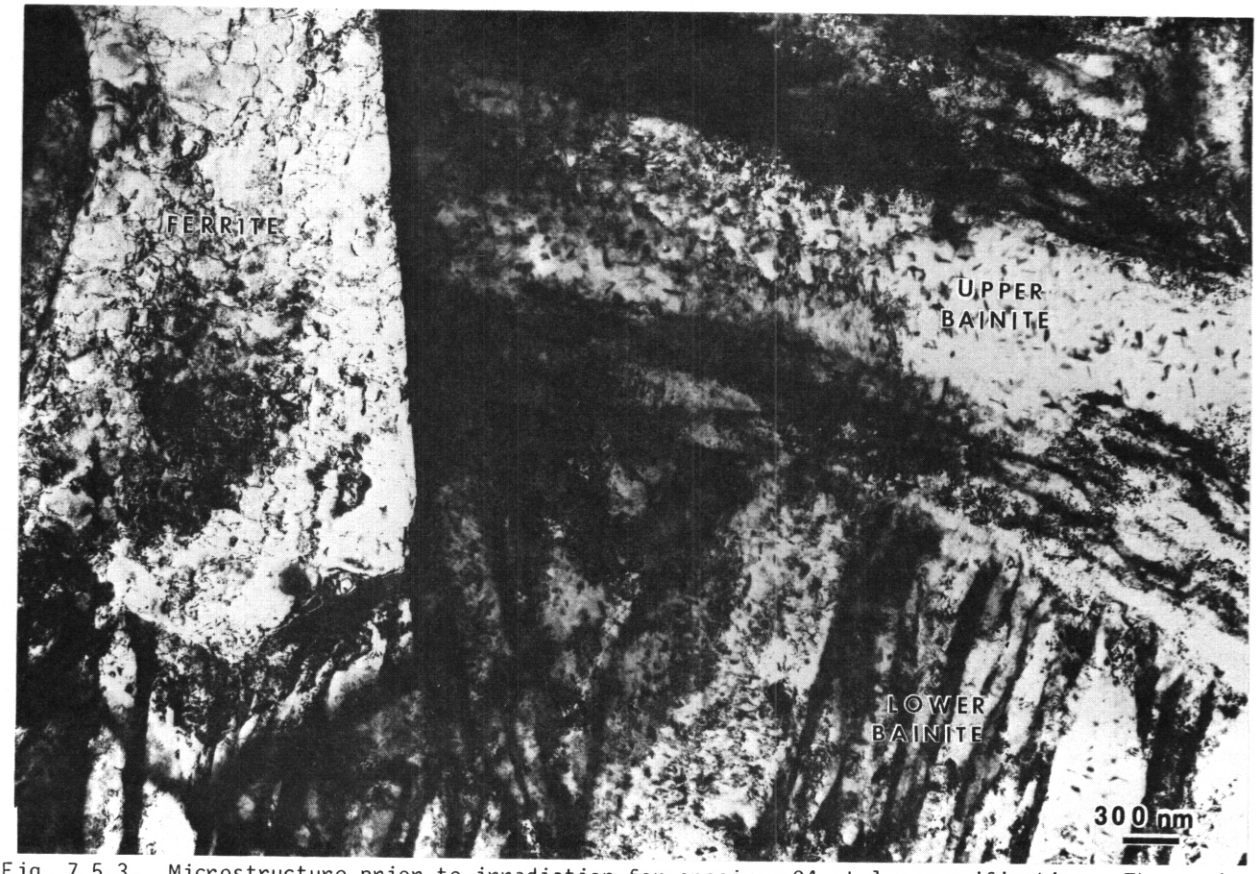

Fig. 7.5.3. Microstructure prior to irradiation for specimen 94 at low magnification. The various regions are labeled.

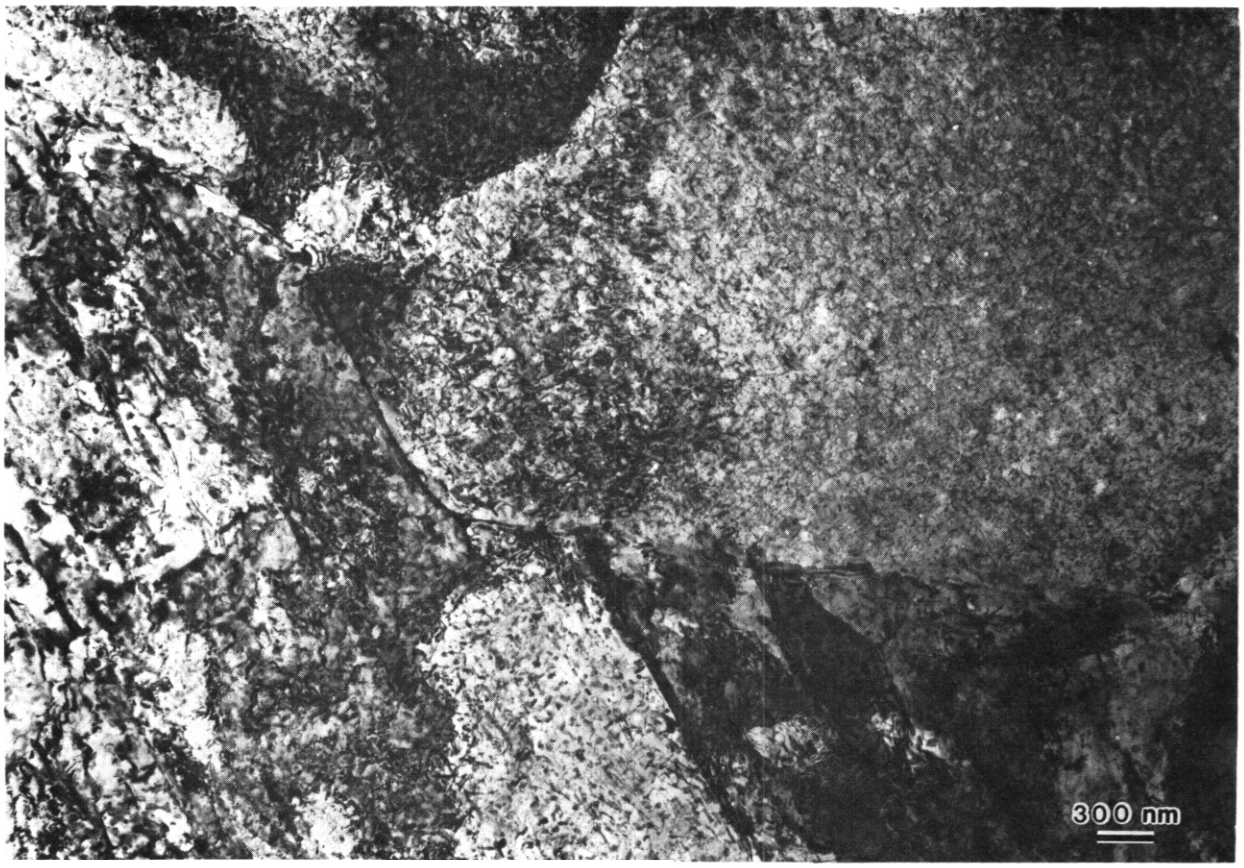

Fig. 7.5.4. Microstructure in specimen 94M6 irradiated at 400°C to 1.6 x 10^{23} n/cm² (E > 0.1 MeV) at low magnification.

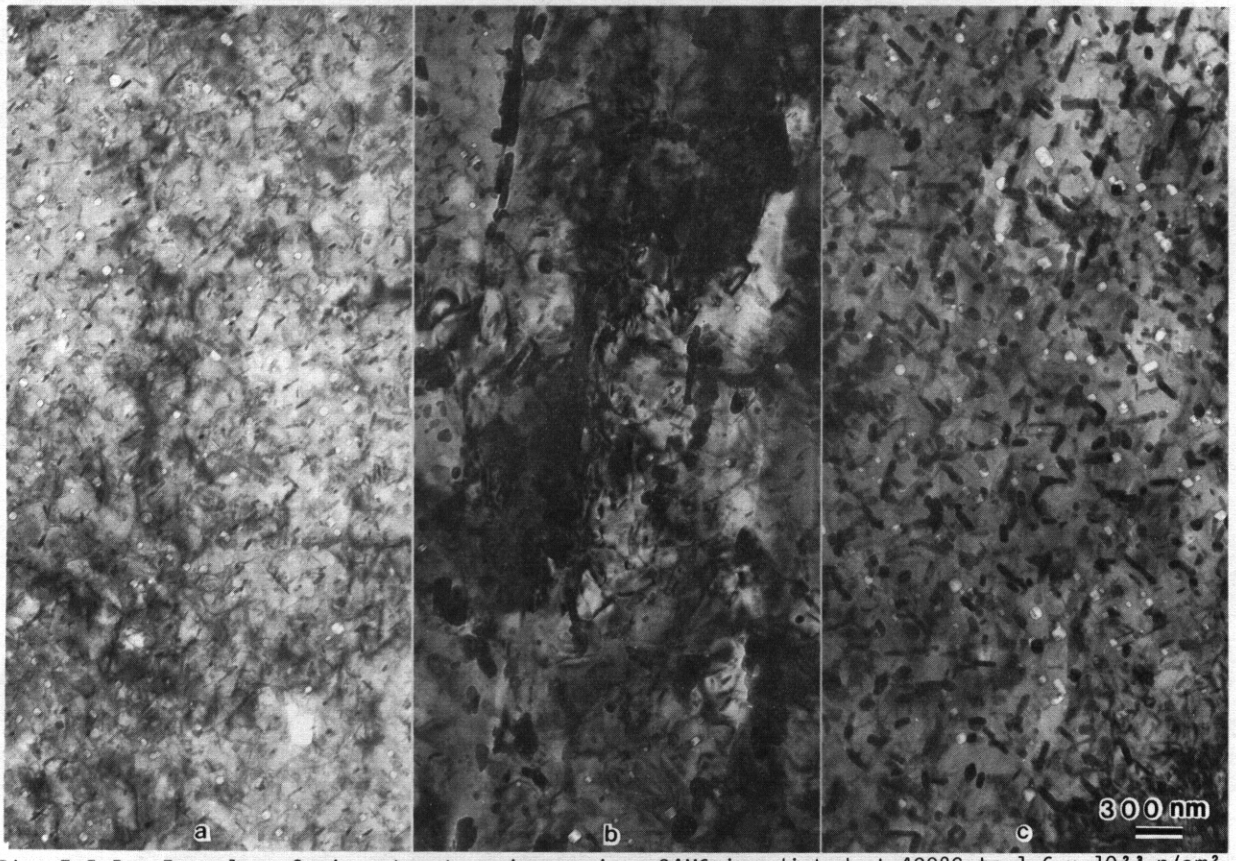

Fig. 7.5.5. Examples of microstructure in specimen 94M6 irradiated at 400°C to 1.6 x 10^{23} n/cm^2 (E > 0.1 MeV) showing a) ferrite, b) upper bainite and c) lower bainite.

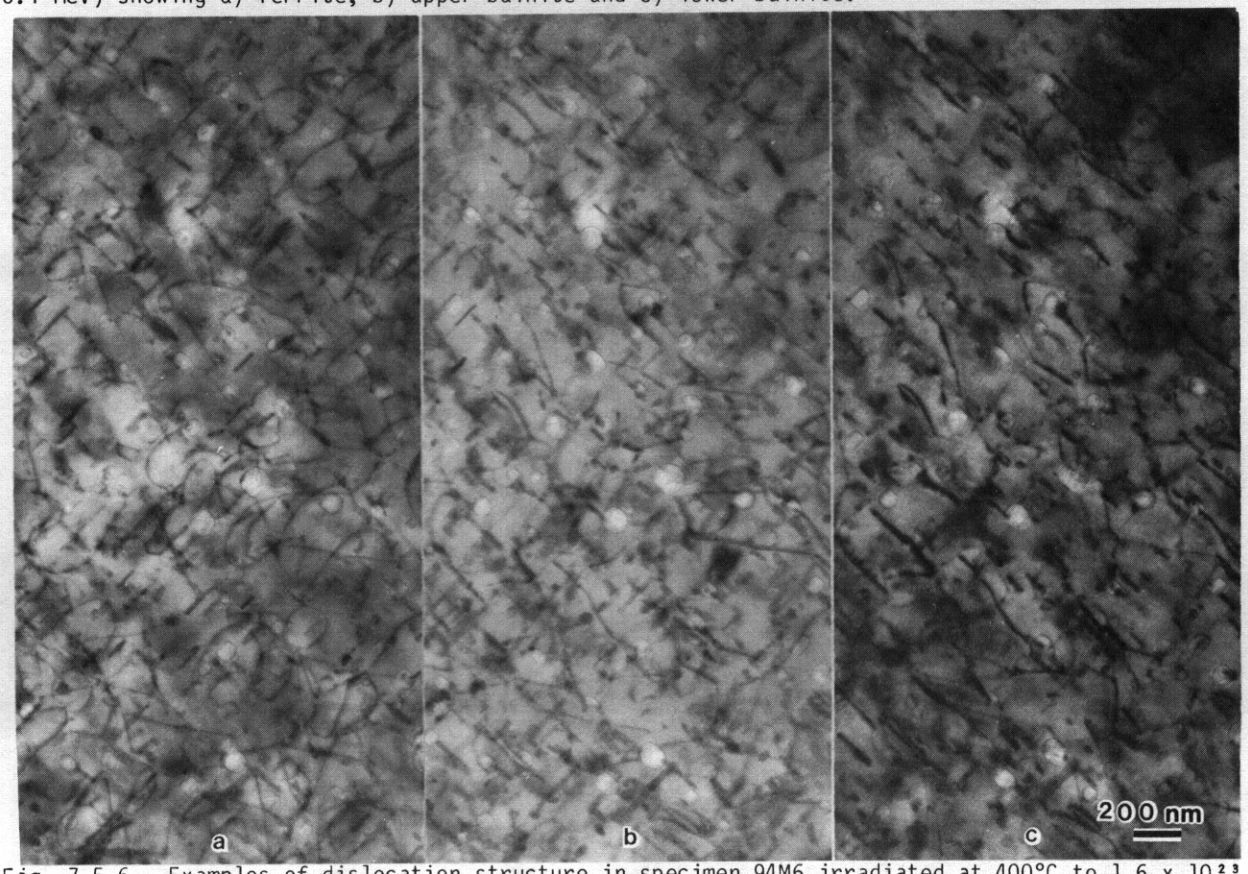

Fig. 7.5.6. Examples of dislocation structure in specimen 94M6 irradiated at 400°C to 1.6 x 10^{23} n/cm^2 (E > 0.1 MeV) showing the same area under a) g = 011, b) g = 211 and, c) g = 200 contrast conditions.

Table 7.5.4. The $\bar{g}\cdot\bar{b}$ imaging criterion for various imaging conditions and burgers vectors possible in 2-1/4Cr-1Mo steel

	$\bar{b}$						
$\bar{g}$	$\frac{a}{2}[111]$	$\frac{a}{2}[\bar{1}11]$	$\frac{a}{2}[1\bar{1}1]$	$\frac{a}{2}[11\bar{1}]$	$a[100]$	$a[010]$	$a[001]$
200	1	1	1	1	2	0	0
020	1	1	1	1	0	2	0
002	1	1	1	1	0	0	2
$01\bar{1}$	0	0	1	1	0	1	1
$\bar{1}10$	0	1	1	0	1	1	0
$10\bar{1}$	0	1	0	1	1	0	1
$11\bar{2}$	0	1	1	2	1	1	2
$1\bar{2}1$	0	1	2	1	1	2	1
$\bar{2}11$	0	2	1	1	2	1	1
$2\bar{1}1$	1	1	2	0	2	1	1
$21\bar{1}$	1	1	0	2	2	1	1
$1\bar{1}2$	1	0	2	1	1	1	2
$12\bar{1}$	1	0	1	2	1	2	1

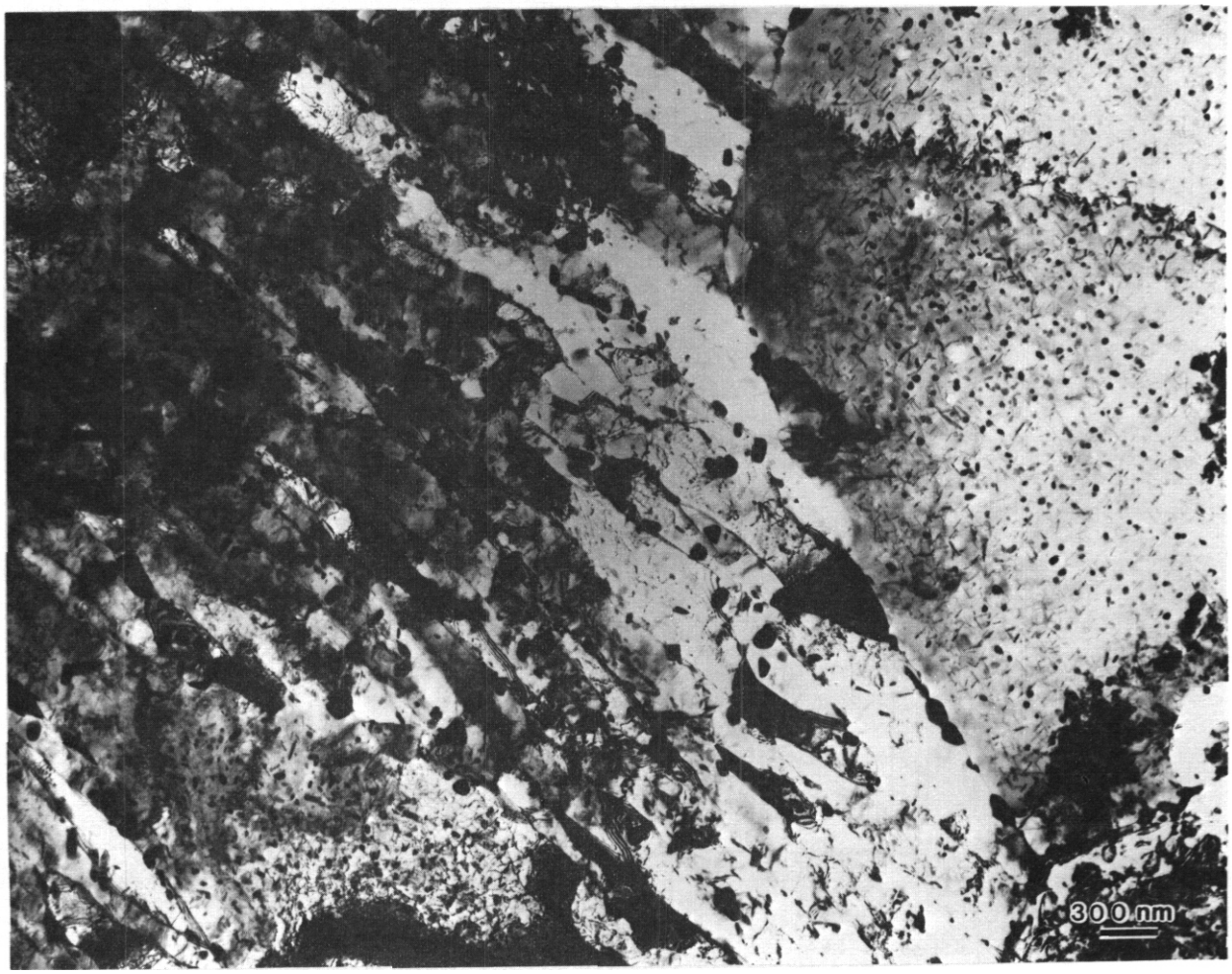

Fig. 7.5.7. Microstructure of specimen 94L6 irradiated at 425°C to 2.1 x 10^{23} n/cm^2 (E > 0.1 MeV) at low magnification.

the carbide particles at bainite plate boundaries has occurred. In the right side of Fig. 7.5.7 is a region of retained ferrite and at the lower right, a region can be seen of lower bainite which appears to be in dislocation contrast. The precipitate structure in these two regions appear similar in size. Examples of structures are shown at higher magnification in Fig. 7.5.8. In Fig. 7.5.8a, an example is given of non-uniform void development within a retained ferrite region and similar conclusions can be made from Fig. 7.5.8c, a lower bainite region. This comparison also shows that swelling in retained ferrite is higher and that the precipitate structures appear very similar.

Specimens 94E6 and 94F6 irradiated at 450°C to 1.6×10^{23} n/cm² and 480°C to 2.0×10^{23} n/cm² respectively, were quite similar. In fact, due to foil preparation difficulty which resulted in surface pitting, insufficient thin area was available in these specimens for low magnification micrographs which provide a better understanding of this complicated microstructure. However, it was possible to show that retained ferrite regions did contain voids in both cases. The void density was low and not all regions contained voids. In comparison, no voids were identified in upper bainite or lower bainite regions. Also, lower bainite regions appeared to contain more rod shaped precipitates than had been found for lower irradiation temperatures. (However, this generalization may be incorrect due to poor sampling procedures.) Examples of these structures in 94E6 and 94F6 are given in Figs. 7.5.9 and 7.5.10, respectively.

Specimen 9LK6, irradiated at 510°C to 2.4×10^{23} n/cm² was the only specimen in this series of AAI specimens which did not contain voids. The structure was overaged compared to the lower irradiation temperature conditions and grain growth in the upper bainite regions was apparent. A low magnification example of this structure is shown in Fig. 7.5.11. A small grain of retained ferrite can be seen in the right portion of this figure, two regions of lower bainite appear at the lower edge of the micrograph and the central portion is an upper bainite region. Comparisons with the preirradiation structure in Fig. 7.5.3 and the 400°C irradiation condition in Fig. 7.5.4 show why the strength of this material is not maintained at 510°C in-reactor. Examples of the structure of the 510°C sample at higher magnification are shown in Fig. 7.5.12. Both the retained ferrite and lower bainite are shown in dislocation contrast. The dislocation density is low in both cases.

AAXIV and AD2 Specimens

Descriptions of microstructural observations on specimens from the AAXIV and AD2 tests are combined because the irradiation experiments were designed to be almost identical. The same heat of 2-1/4Cr-1Mo was used with the same heat treatment. The irradiation temperatures were similar (the AAXIV test did not include a 500°C condition) and the goal fluences were both 6×10^{22} n/cm². As an objective of this part of the experiment is to determine the effect of irradiation on microstructure for a standard heat treatment condition in order to provide interpretation of in-reactor creep and tensile test response, the series of specimens chosen provides the most complete set available for microstructural examination.

The heat treatment given this material was intended to provide a fully tempered bainite structure. Air cooling (from 900°C) was expected to result in cooling rates slower than for the AAI material but fast enough to avoid proeutectoid ferrite (i.e., in less than 1000 seconds) as shown in Figs. 7.5.13 and 7.5.14. The microstructure was found to be lower bainite and consisted of large bainite plates with large needle shaped M_7C_3 precipitate particles within the bainite plates and blocky M_6C or $M_{23}C_6$ particles on or near grain boundaries. Examples of the structure in specimen NU which was heat treated with the specimens irradiated in the AAXIV test as revealed by optical metallography are given in Fig. 7.5.13 and as found by transmission electron microscopy are shown in Fig. 7.5.14. In Fig. 7.5.14, a grain boundary node can be seen towards the right of the micrograph. Needle shaped carbide particles are found to be non-uniformly distributed in the structure. The microstructure in specimen 31, heat treated with the specimens irradiated in the AD2 test was found to be very similar to specimen NU. A comparison is provided in Fig. 7.5.14c showing the dislocation and precipitate structure for specimens NU and 31 at higher magnifications. A good example of subgrain dislocation cell walls can be seen at the upper part of Fig. 7.5.14c.

Specimens NUYL irradiated at 410°C to 5.1×10^{22} n/cm² and 31CP irradiated at 390°C to 5.0×10^{22} n/cm² were found to contain very similar microstructures. In both cases, a high density of uniformly distributed small voids was found and small spherical particles had developed between the rod shaped carbide particles which were present prior to irradiation. The major difference between these structures was in the size of the particles which formed during irradiation. Examples of the microstructure of specimen NUYL are shown in Figs. 7.5.15 and 7.5.16 and those of specimen 31CP are shown in Figs. 7.5.17 and 7.5.18. Fig. 7.5.15 shows a prior-austenite grain boundary node approximately in the center of the micrograph with several subgrain (bainite) boundaries in the field of view. The grain at the bottom is in heavy strain contrast and therefore somewhat obscured. The larger precipitate particles which can be seen at grain boundaries and within grains were created prior to irradiation. The structure which formed during irradiation between these particles is shown at higher magnification in Fig. 7.5.16. Fig. 7.5.16a provides an example of void and precipitate development near grain boundaries and Fig. 7.5.16b shows a region in strain contrast in order to image the dislocation structure. The voids are found to be faceted and to form quite close to grain boundaries. The dislocation structure consists of a dislocation network as opposed to individual dislocation loops. However, on a finer scale a high density of equiaxed particles can be seen. Fig. 7.5.17 shows similar features at low magnification in specimen 31CP. A contorted grain boundary runs across the micrograph and a region at the upper right is obscured by strong strain contrast. Some large pits can be seen (one right in the center of the micrograph) and should be ignored because they are specimen preparation artifacts. Fig. 7.5.18 shows this structure at higher magnification. The void density in specimen 31CP as shown in Fig. 7.5.18a appears to be higher than specimen NUYL and the precipitates formed during irradiation appear to be smaller. Fig. 7.5.18b provides an example toward the bottom of a small region in dislocation contrast. Again a dislocation network rather than a dislocation loop structure is found.

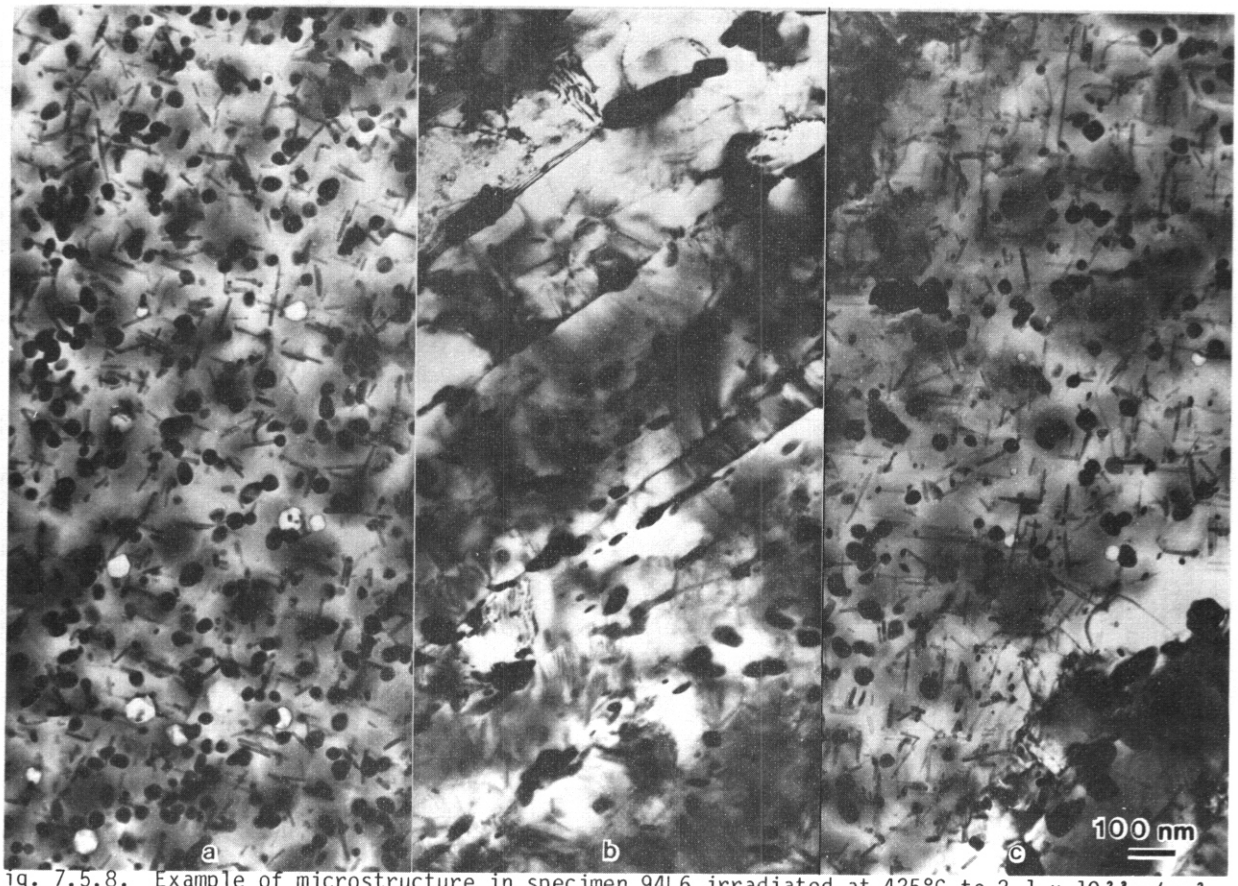

Fig. 7.5.8. Example of microstructure in specimen 94L6 irradiated at 425°C to 2.1 x 10^{23} n/cm^2 (E > 0.1 MeV) showing a) ferrite, b) upper bainite and, c) lower bainite.

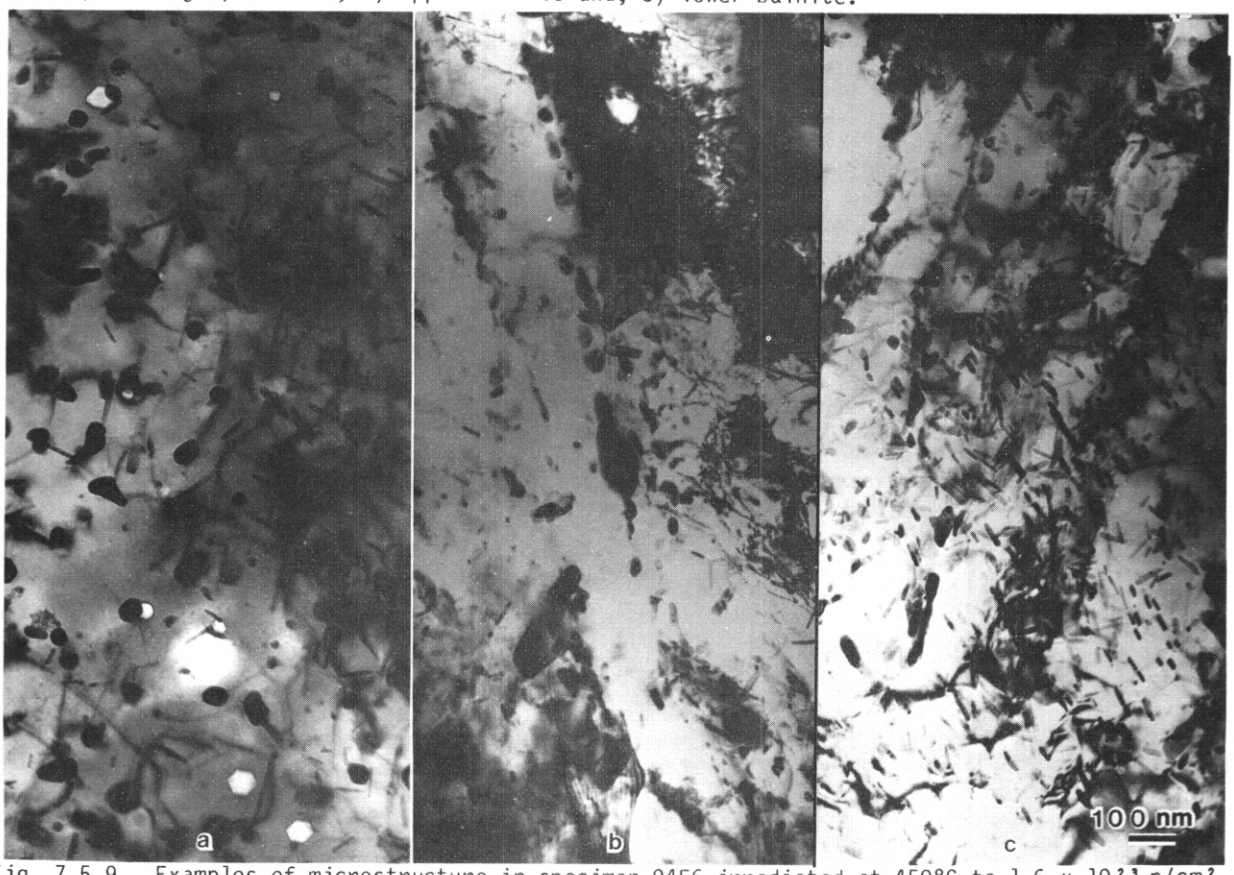

Fig. 7.5.9. Examples of microstructure in specimen 94E6 irradiated at 450°C to 1.6 x 10^{23} n/cm^2 (E > 0.1 MeV) showing a) ferrite, b) upper bainite and c) lower bainite.

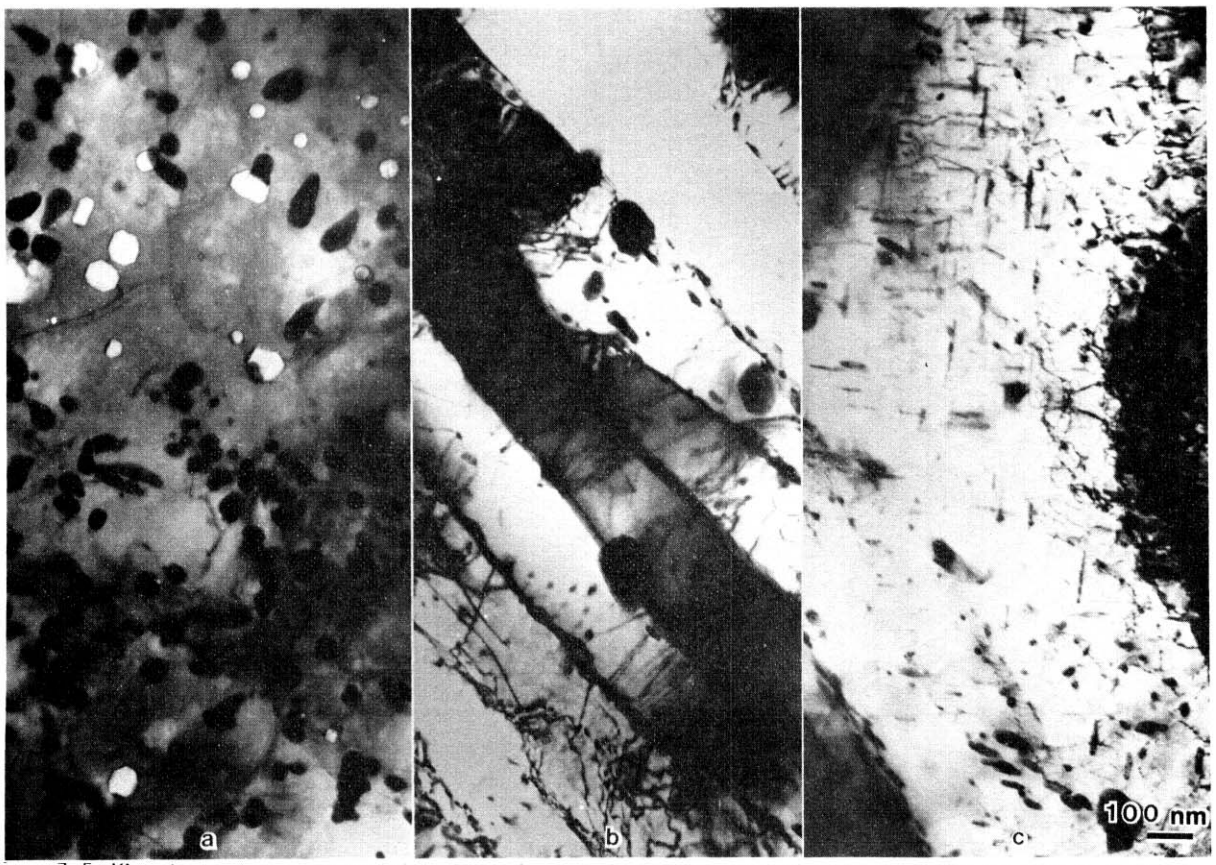

Fig. 7.5.10. Examples of microstructure in specimen 94F6 irradiated at 480°C to 2.0 x 10^{23} n/cm² (E > 0.1 MeV) showing a) ferrite, b) upper bainite and c) lower bainite.

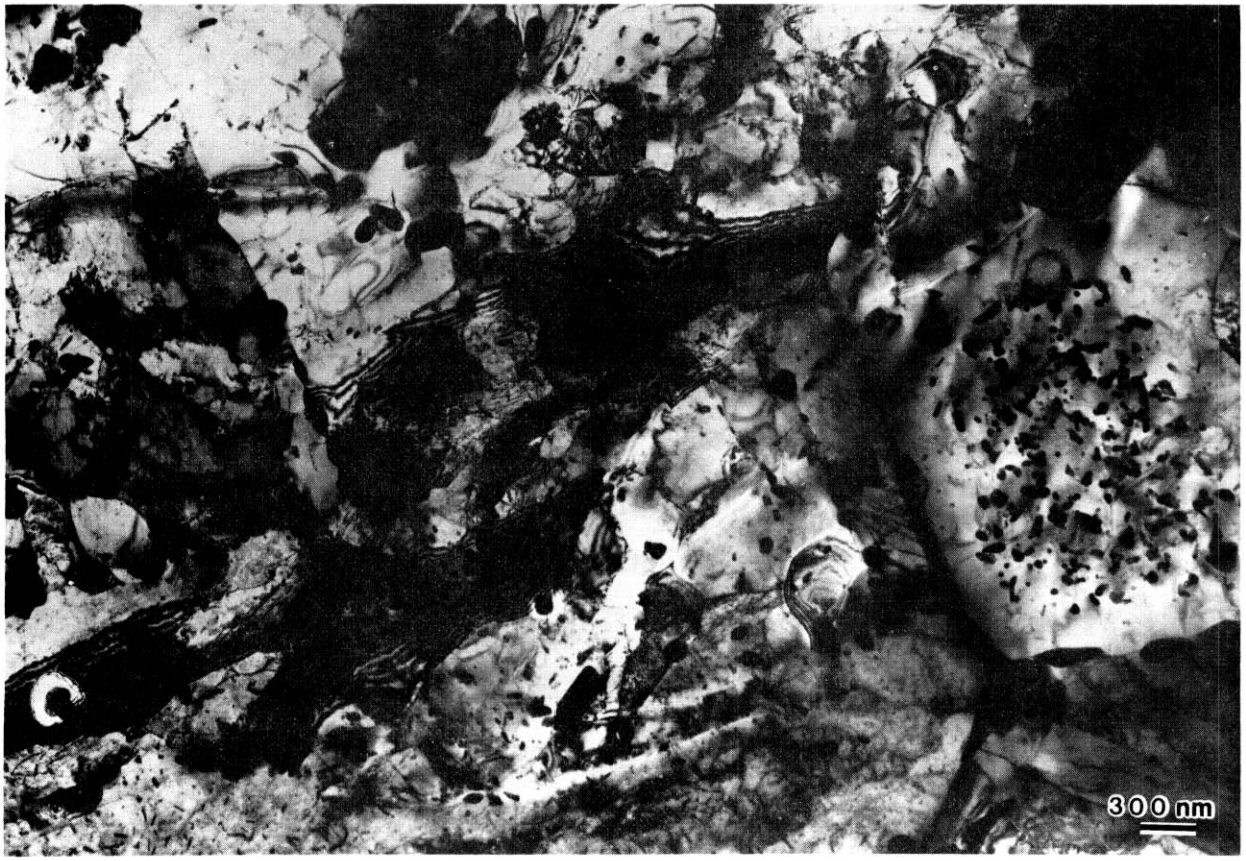

Fig. 7.5.11. Microstructure of specimen 94K6 irradiated at 510°C to 2.4 x 10^{23} n/cm² (E > 0.1 MeV) at low magnification.

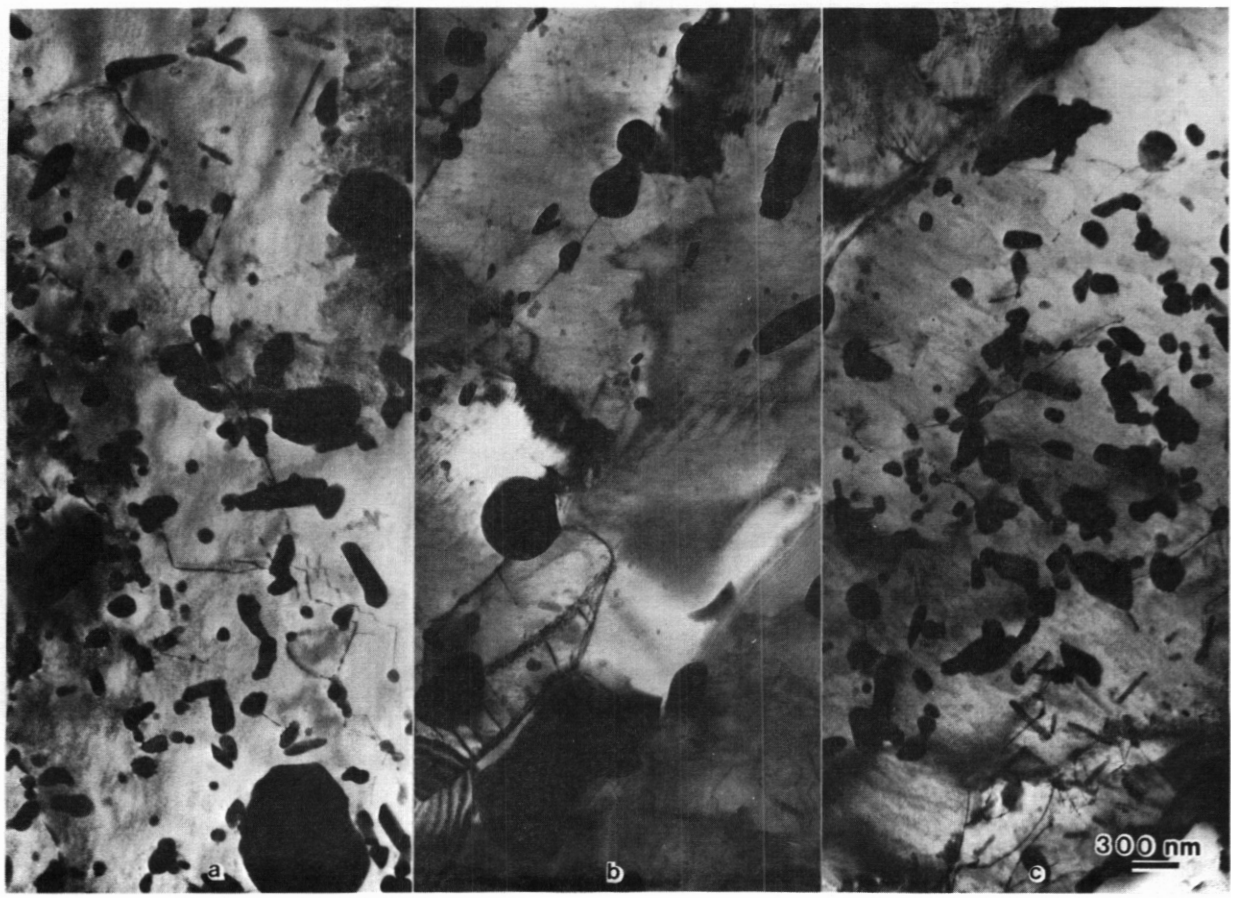

Fig. 7.5.12. Examples of microstructure in specimen 94K6 irradiated at 520°C to 2.4 x 10^{23} n/cm² (E > 0.1 MeV) showing a) ferrite, b) upper bainite and c) lower bainite.

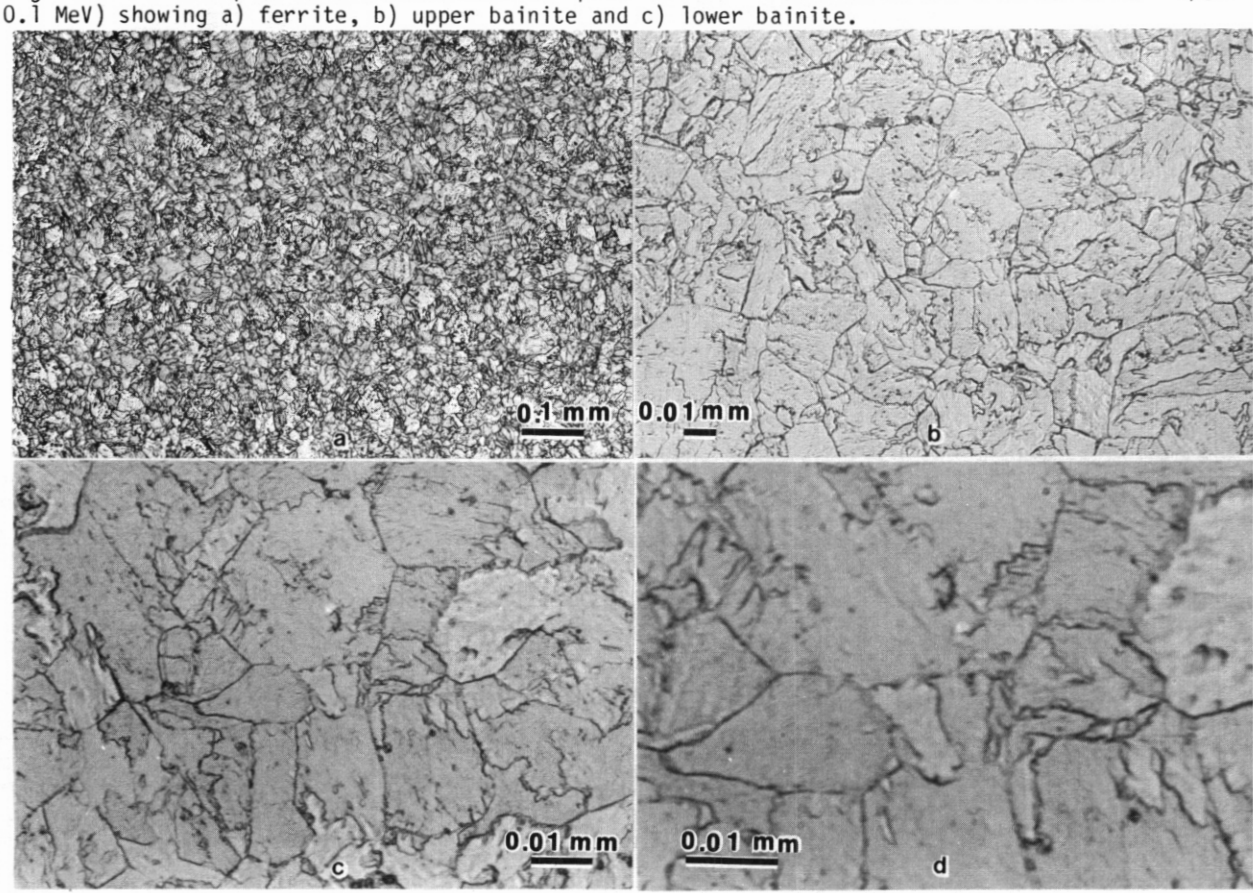

Fig. 7.5.13. Optical metallography of specimen NU prior to irradiation. Specimen 31 was similar.

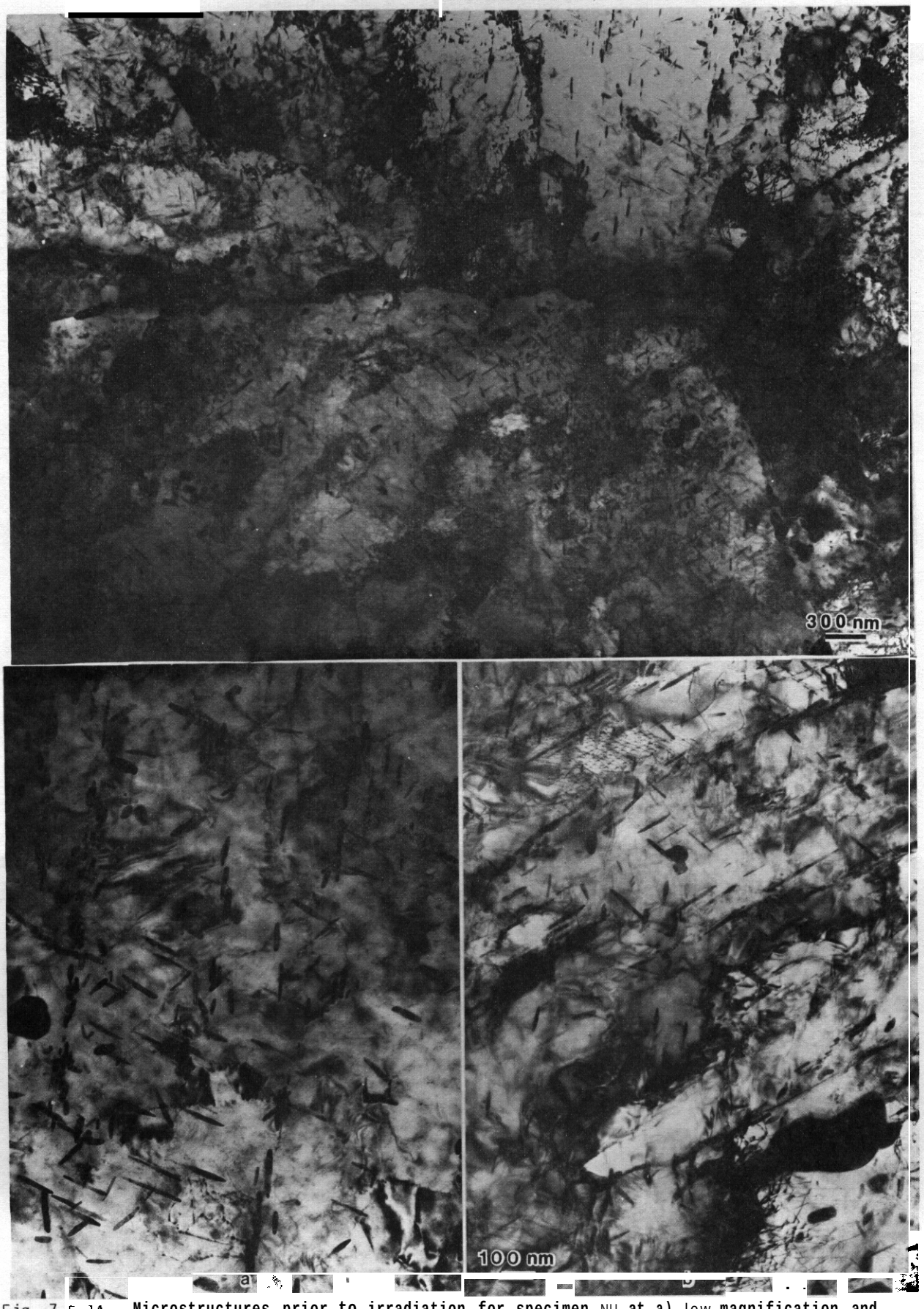

Fig. 7.5.14. Microstructures prior to irradiation for specimen NU at a) low magnification and b) intermediate magnification and for specimen 31 at c) intermediate magnification.

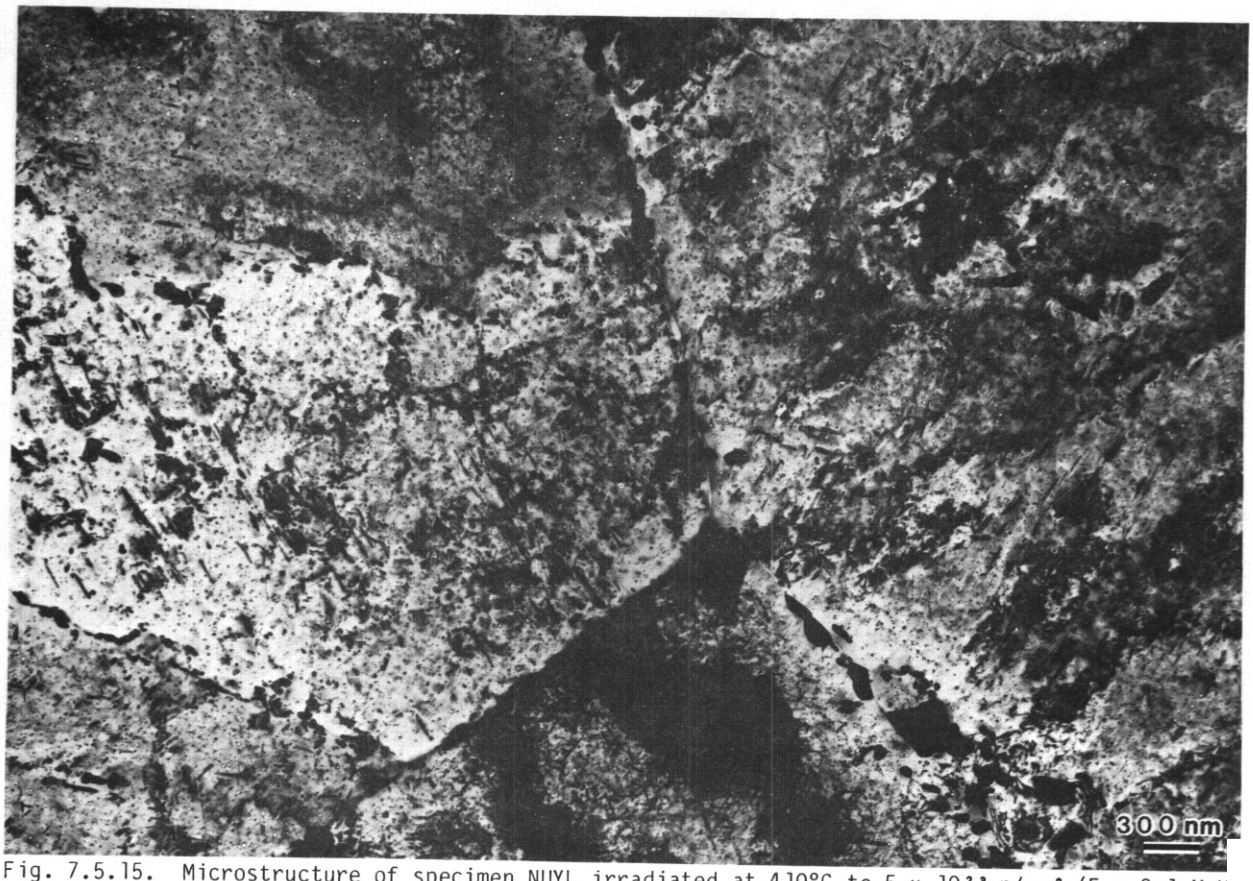

Fig. 7.5.15. Microstructure of specimen NUYL irradiated at 410°C to 5 x 10^{23} n/cm² (E > 0.1 MeV at low magnification.

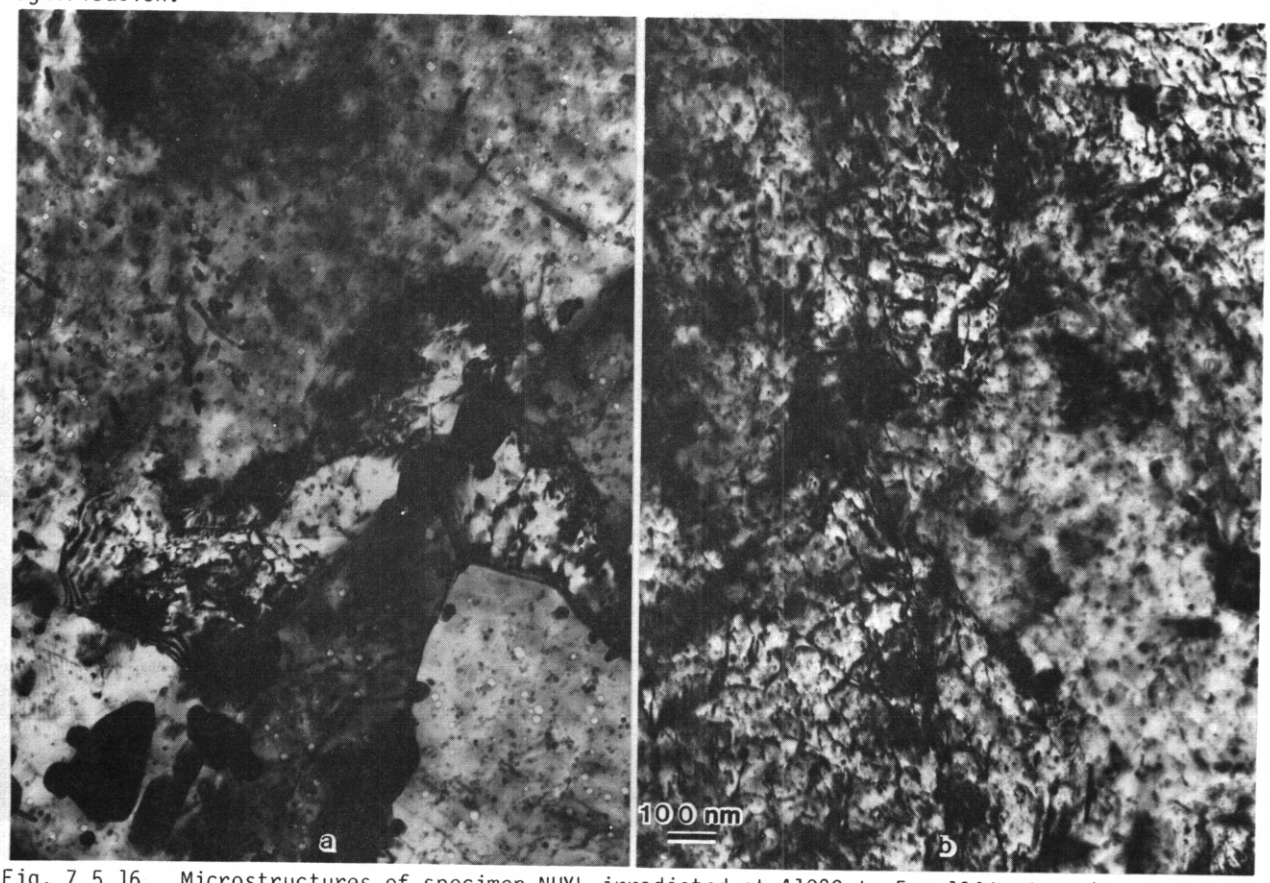

Fig. 7.5.16. Microstructures of specimen NUYL irradiated at 410°C to 5 x 10^{23} n/cm² (E > 0.1 MeV) showing examples of a) void and b) dislocation structure. Note the fine precipitate in the background.

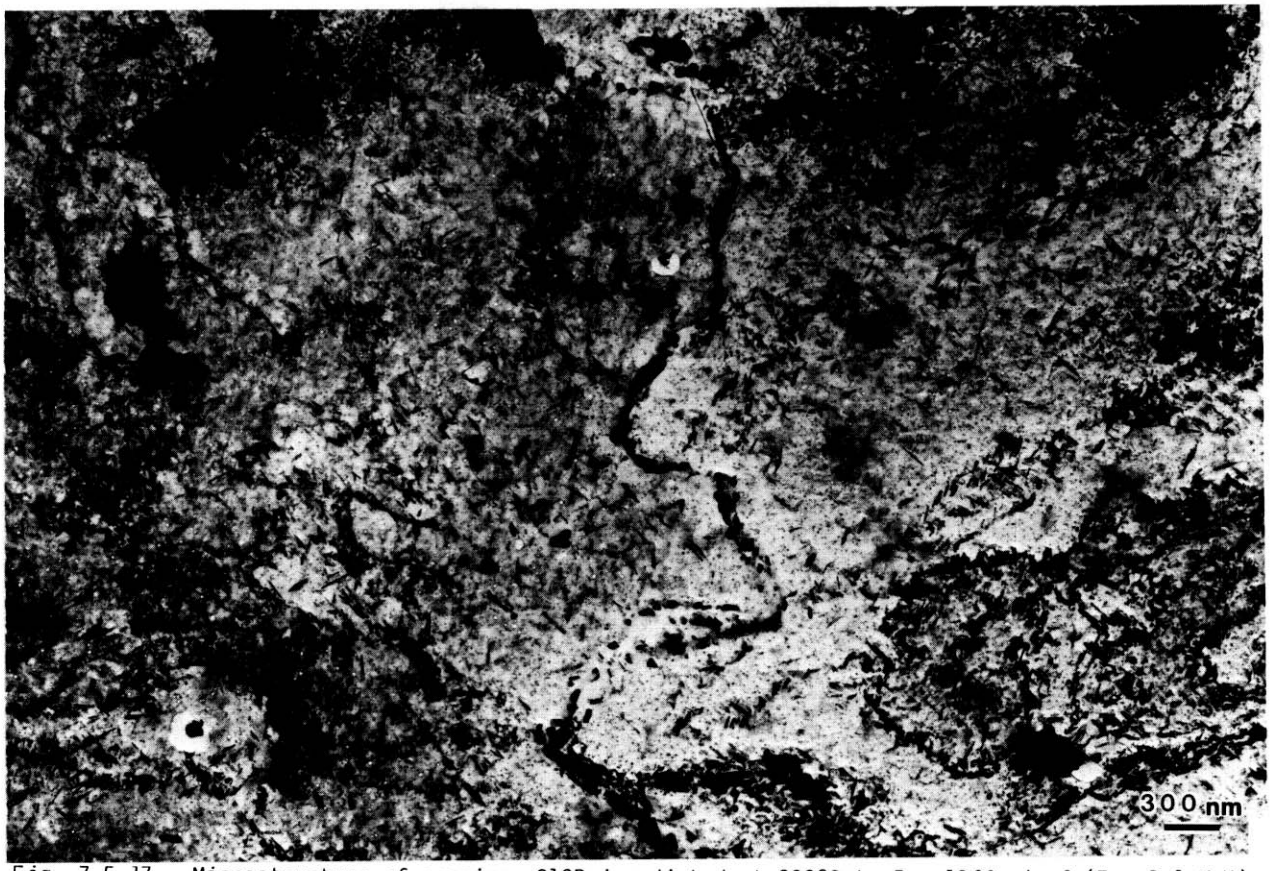

Fig. 7.5.17. Microstructure of specimen 31CP irradiated at 390°C to 5 x 10^{22} n/cm² (E > 0.1 MeV) at low magnification.

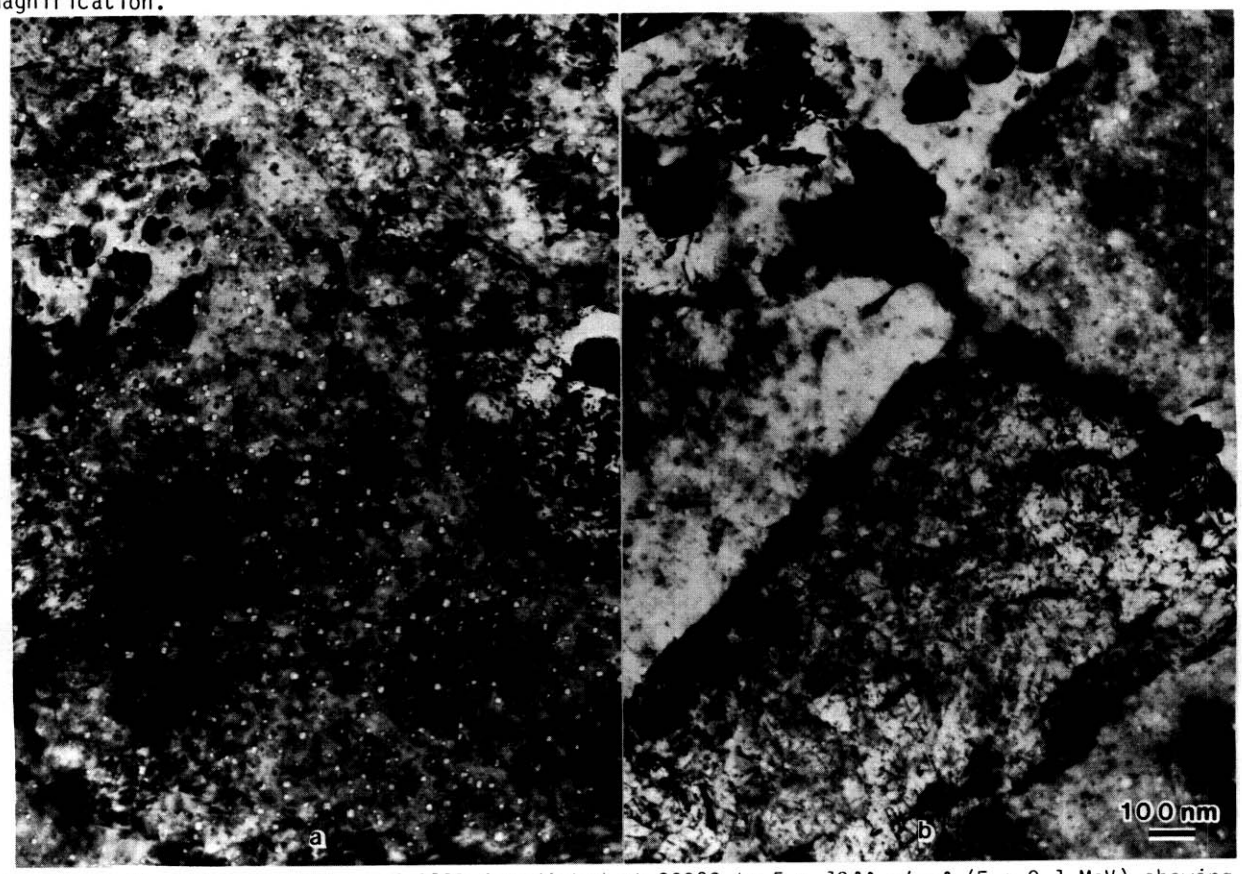

Fig. 7.5.18. Microstructure of 31CP irradiated at 390°C to 5 x 10^{22} n/cm² (E > 0.1 MeV) showing examples of a) void and b) dislocation structure.

The microstructure of specimen 31CV irradiated at 450°C to 5.0 X 10^{22} n/cm² was quite different. No voids were found. Precipitates which formed during irradiation could be identified but the density was lower than the 400°C sample and the dislocation structure consisted of a loose tangle with no loops. This microstructure is shown at low magnification in Fig. 7.5.19. Effects of irradiation are difficult to identify. However, at higher magnification, as shown in Fig. 7.5.20, a low density of precipitate particles can be seen and examples of a dislocation network can be found.

Specimen 31CR irradiated at 500°C to 5.0 X 10^{22} n/cm² was not very different. No voids were found. The precipitate structure may have contained somewhat more acicular precipitate (a tendency which can also be observed in AAI specimens irradiated at ~500°C) but this may be a consequence of statistical uncertainty and not a true effect. An example of this structure is given in Fig. 7.5.21 showing a prior austenite grain boundary node at low magnification and examples at higher magnification are given in Fig. 7.5.22. Fig. 7.5.22b shows a region in strong strain contrast. Examples of subgrain boundary development can be found in several places.

Quantitative Microstructural Measurements

The preceeding results have shown that the major consequences of fast neutron irradiation on 2-1/4Cr-1Mo microstructures are the formation and development of voids, precipitates and dislocations. Voids were only found for irradiation temperatures below 500°C with swelling apparently at a maximum for the lowest temperature examined, 400°C. In both heat treatment conditions new precipitates formed during irradiation. This was most noticeable at the lowest irradiation temperature, 400 to 450°C whereas at a higher temperature it was often not possible to easily differentiate between precipitates which formed during irradiation and those which were present prior to irradiation and only grew during irradiation. Both equiaxed and rod-shaped precipitates were present, but no attempt was made in this study to identify either the crystal structures or compositions of these phases. A possible identification is Mo_2C for the rod shaped precipitates and M_6C or $M_{23}C_6$ for the equiaxed precipitates. However, it is conceivable that equiaxed precipitates of two types coexist. Dislocation structures which developed due to the agglomeration of irradiation induced point defects could be identified only at 400°C. At higher temperatures, a dislocation network was formed which was difficult to distinguish from the dislocation structure present prior to irradiation or the scale of the dislocation structure was obscured by the precipitate structure. The intent of this section is to present results of quantitative measurements of voids, precipitates and dislocations made from micrographs of these structures.

The results of quantitative measurements on micrographs of AAI specimens are given in Table 7.5.4 and similar measurements on AAXIV and AD2 specimens which were examined are provided in Table 7.5.5. Both tables ioentify the micrograph negative number from which measurements were made, provide swelling, number density and mean diameter for void populations, volume fraction, number density and mean diameter for equiaxed particles, number density and mean particle length for rod shaped particles and dislocation density. In many cases, micrographs did not provide clear images of all the features of interest in a single micrograph. Therefore, features which were out of contrast were not measured and there are gaps in the tables. In Table 7.5.4, measurements are reported for the three microstructural areas of interest: ferrite, upper bainite and lower bainite. However, because of difficulty differentiating between ferrite and lower bainite following irradiation at higher temperature, lower bainite results are reported as measurements in ferrite. This is the case for 94E6, 94F6 and 94K6.

The results of Tables 7.5.4 and 7.5.5 may be interpreted as follows. Void swelling as high as 0.5% was measured in specimen 94M6 irradiated in AAI at 400°C but large variations in swelling were found from area to area with median values of 0.22% in ferrite, 0.06% in lower bainite and 0.045% in upper bainite. Void densities in this specimen condition were on the order of 1 x 10^{15} cm^{-3} in ferrite, 3 X 10^{14} cm^{-3} in lower bainite and 1.3 X 10^{14} cm^{-3} in upper bainite. Void densities were similar in specimens NUYL and 31CP in the bainitic condition, 2 x 10^{15} cm^{-3}, but swelling was lower, with peak swelling measured of 0.23% and median swelling measured of 0.10% following irradiation at 400°C. Fig. 7.5.23 has been constructed to show the temperature dependence of void development. Fig. 7.5.23a gives the swelling as a function of irradiation temperature for ferrite in AAI specimens. Results for AD2/AAXIV specimens at 400 and 450°C are also given. Swelling is highest at 400°C but void measurements indicate a secondary peak occurs at 480°C in the AAJ specimen condition. Density change measurements did not show this secondary peak. It is therefore possible that the peak appears due to area to area variation and a resultant statistical bias in measurement which arose due to specimen preparation difficulties. Further examinations would be required to eliminate this possiblity. The void density results shown in Fig. 7.5.23b also show a secondary maximum at 480°C but the void density is much higher at 400°C.

Precipitate development follows similar trends. With increasing temperature, precipitate number density decreases and mean precipitate size, or length for rod shaped precipitates increases. However estimates of precipitate volume fraction for spherical precipitates does not vary systematically with temperature. This is believed to be a consequence of precipitates present prior to irradiation in the area of interest which are included in some measurements. The results of precipitate measurements in AD2/AAXIV specimens and in ferrite in AAI specimens are shown in Fig. 7.5.24. Comparison of Figs. 7.5.22 and 7.5.24 indicates that precipitate size and number densities of spherical precipitates are at least as large as those for voids.

Dislocation densities are found to be between 10^{9} and 10^{11} cm/³. The AD2/AAXIV condition was somewhat higher than the AAI condition but both followed the same trend with temperature: as irradiation temperature was increased the dislocation density decreased. Fig. 7.5.25 has been prepared to demonstrate this behavior.

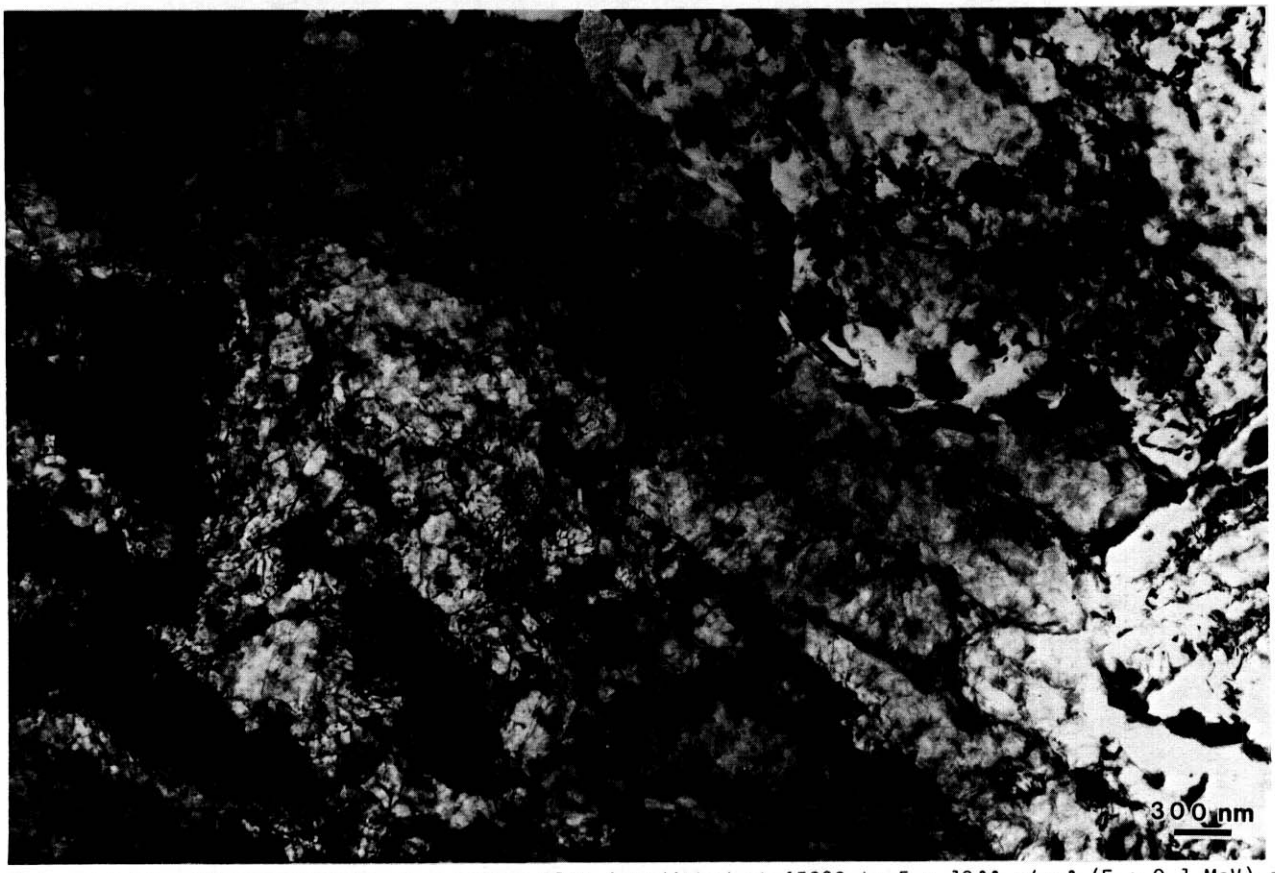

Fig. 7.5.19. Microstructure of specimen 31CV irradiated at 450°C to 5 x 10^{22} n/cm² (E > 0.1 MeV) at low magnification.

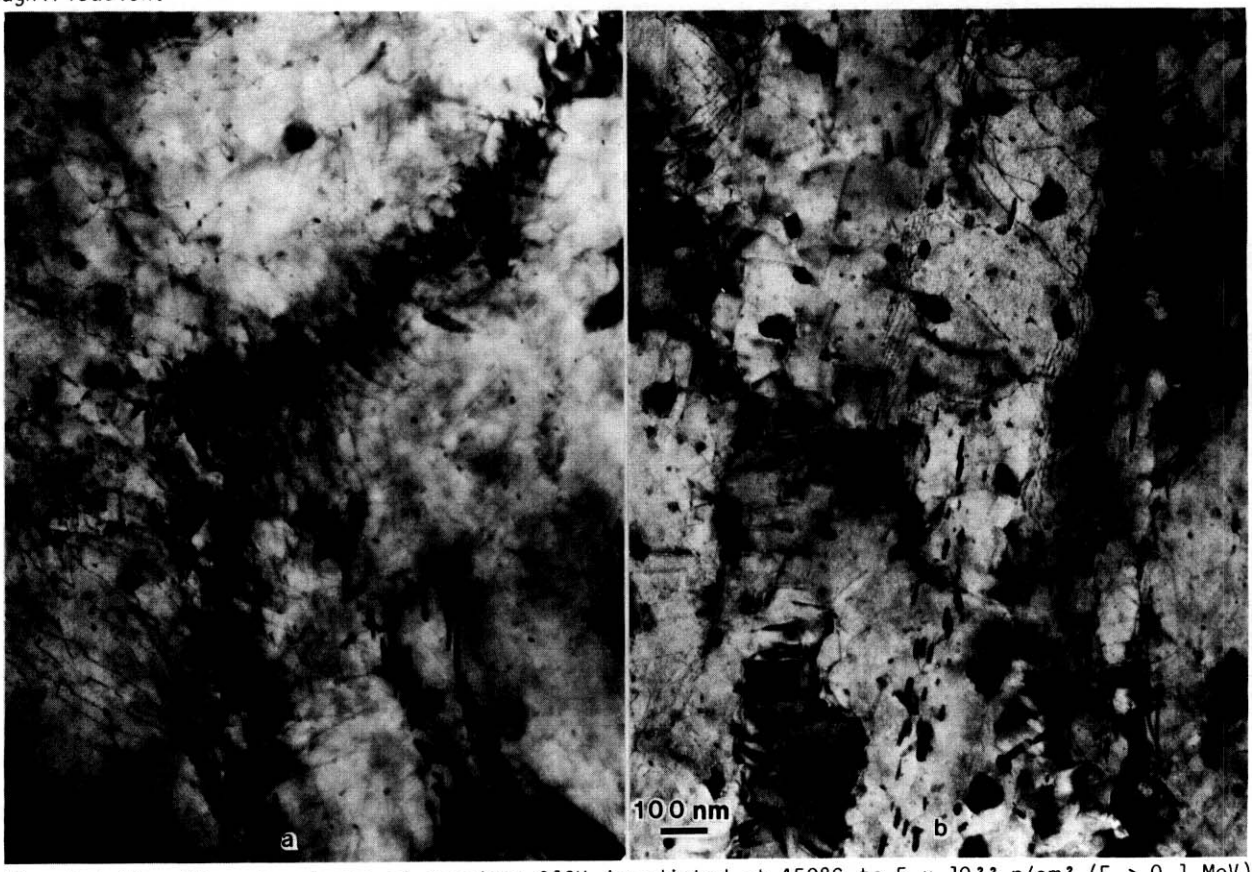

Fig. 7.5.20. Microstructures of specimen 31CV irradiated at 450°C to 5 x 10^{22} n/cm² (E > 0.1 MeV) showing two regions in precipitate and dislocation contrast.

Fig. 7.5.21. Microstructure of specimen 31CR irradiated at 500°C to 5 x 10^{22} n/cm² (E > 0.1 MeV) at low magnification.

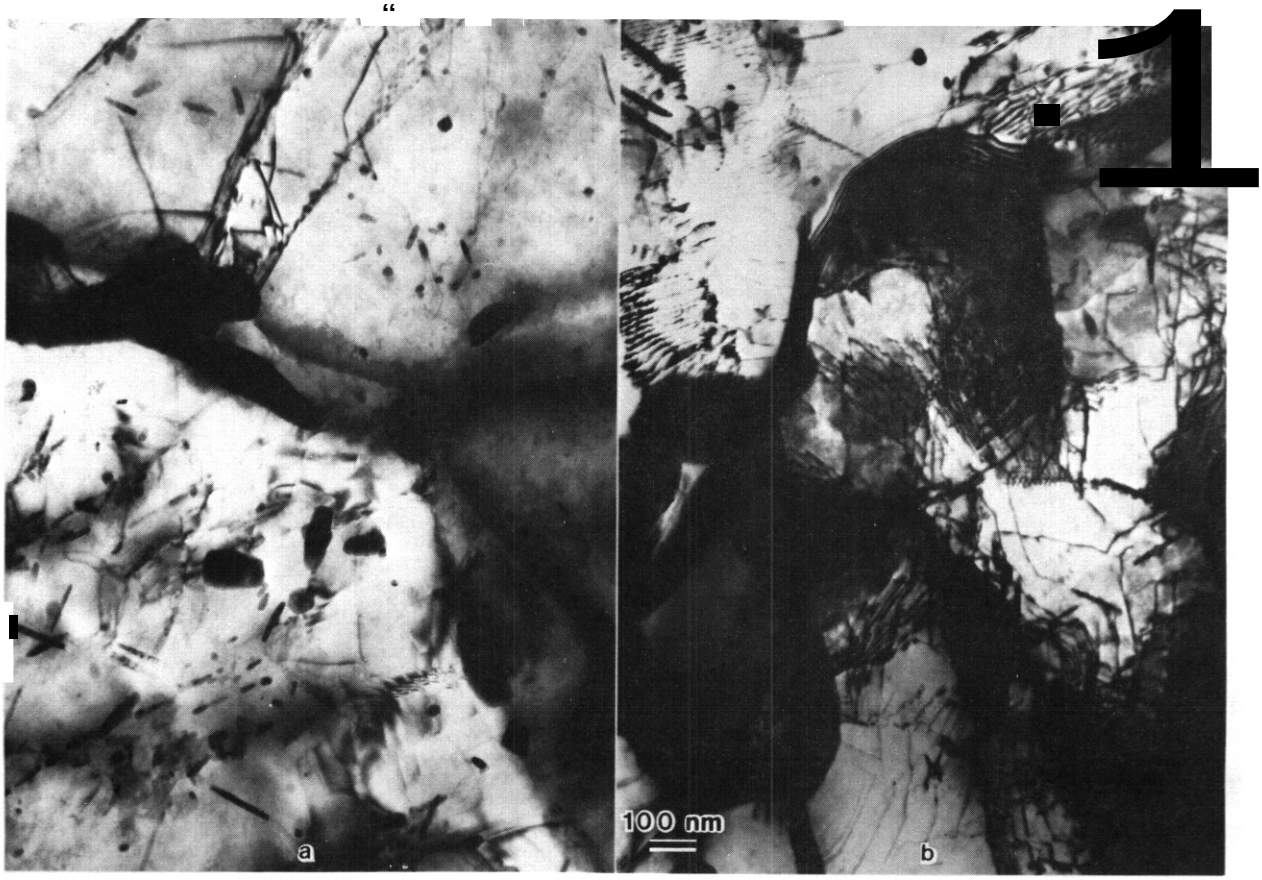

Fig. 7.5.22. Microstructure of specimen 31CR irradiated at 500°C to 5 x 10^{22} n/cm² (E > 0.1 MeV) showing a) precipitate structure and b) dislocation structure.

Table 7.5.4. o quantitative microstructural measurements for AAI specimens

Structure		Voids			Precipitates/Spheres			Rods		Dislocations
		Swelling $\Delta V/V_0$, %	Density #/cm³	Mean Diameter nm	Volume %	Density #/cm³	Mean Diameter nm	Density #/cm³	Mean Length nm	Density #/cm²
Ferrite		0.47	1.05×10^{15}	16.2	1.61	1.5×10^{15}	17.8	1.13×10^{15}	28.2	
		0.35	1.5×10^{15}	15.4	1.95	9.7×10^{14}	25.6	9.9×10^{14}	32.7	
		0.26	1.14×10^{15}	16.7						1.7×10^{10}
	30	0.38	1.24×10^{15}	17.0	0.13	9.1×10^{14}	11.5	2.8×10^{15}	27.0	3.2×10^{10}
	28	0.19	1.18×10^{15}	13.1	1.72	1.9×10^{15}	23.3	3.3×10^{15}	28.4	
	39	0.24	1.08×10^{15}	15.6	1.58	8.1×10^{14}	23.6	2.2×10^{15}	27.9	4.1×10^{10}
	37	0.21	0.93×10^{15}	16.5	0.74	9.6×10^{14}	23.2	1.3×10^{15}	31.5	
	30	0.13	0.93×10^{15}	14.2					33.3	
	36	0.06	0.52×10^{15}	12.7	0.68	8.67×10^{14}	15.6	9.6×10^{14}	30.7	
	31	0.12	1.5×10^{15}	10.3				8.1×10^{14}	25.9	
	11	0.22	1.1×10^{15}	15.5	1.6	9.5×10^{14}	23.0	1.2×10^{15}	28.0	3×10^{10}
Bainite	36	0.063	2.9×10^{14}	16.0	1.83	9.7×10^{14}	27.4	4.1×10^{16}	44.2	
	36	0.031	2.4×10^{14}	13.0	1.99	5.3×10^{14}	36.3	3.0×10^{16}	46.7	
	35	0.060	4.7×10^{14}	12.0						4.9×10^{10}
	35	0.041	6.3×10^{14}	8.3						
	35	0.067	2.8×10^{14}	14.8	1.42	6.6×10^{14}	22.5	1.9×10^{15}	23.3	
	37				3.83	1.5×10^{15}	32.2	9.4×10^{15}	30.5	
	11	0.06	3×10^{14}	13.0	1.9	8×10^{14}	30.0	7×10^{14}	37.0	5×10^{10}
Upper Bainite	39	0.026	9.3×10^{13}	16.3	4.4	8.4×10^{16}	38.5	4.6×10^{14}	33.7	
	39	0.039	1.3×10^{14}	18.4	8.5	6.7×10^{14}	42.2			
	30	0.065	2.2×10^{14}	11.6	7.4	9.6×10^{14}	38.6			
	30	0.060	1.8×10^{14}	15.2		4.7×10^{14}	43.4	2.6×10^{14}	35.0	
	36	0.009	1.2×10^{14}	10.8	2.3	5.7×10^{14}	32.5	4.0×10^{14}	30.4	
	11				12.0	5.8×10^{14}	45.9			
	38	0.048	9.3×10^{13}	16.4	11.3	4.2×10^{14}	46.9			
	11	.045	1.3×10^{14}	16.0	8.0	6.0×10^{14}	42.0	4.0×10^{14}	33.0	N.M.

Table 7.5.4. (Cont'd)

[illegible]	Structure	Negative Number	Voids: Swelling $\Delta V/V_0$, %	Voids: Density #/cm³	Voids: Mean Diameter nm	Precipitates/Spheres: Volume %	Precipitates/Spheres: Density #/cm³	Precipitates/Spheres: Mean Diameter nm	Rods: Density #/cm³	Rods: Mean Length nm	Dislocations: Density #/cm²
[illegible]	Ferrite	237	0.098	3.8×10^{13}	38.5	1.59	5.6×10^{15}	36.9*		36.9	1.3×10^{10}
		239	0.088	7.6×10^{13}	17.7	1.63	1.34×10^{15}	22.0	1.35×10^{15}	40.2	
		254	0.107	3.1×10^{13}	34.6	1.31	8.6×110^{14}	24.8	1.29×10^{15}	40.0	1.2×10^{10}
		259	0.074	4.5×10^{13}	27.7	1.32	7.7×10^{14}	26.2	1.16×10^{15}	40.5	2.9×10^{9}
		276	0.055	4.8×10^{13}	23.4	2.16	9.6×10^{14}	24.0	1.17×10^{15}	40.0	1.5×10^{10}
		273	0.000	0							1.5×10^{10}
		15929	0.000	0	---	2.10	5.2×10^{14}	36.6	9.1×10^{14}	58.3	1.5×10^{10}
		Median	.075	4.0×10^{13}	28.0	1.6	8.0×10^{14}	25.0	1.2×10^{15}	40.0	1.5×10^{10}
	Lower Bainite	251	0.027	4.5×10^{13}	22.7	2.6	1.5×10^{15}	24.2	1.3×10^{15}	47.9	8.1×10^{9}
	Upper Bainite	237	0.007	1.9×10^{13}	13.8	9.0	5.2×10^{14}	37.3			
		273	0.00	0	----	8.8	5.7×10^{14}	35.5	9.5×10^{13}	41.0	
		Median	0.004	1×10^{13}	13.8	8.9	5.5×10^{14}	36.0	1×10^{14}	41.0	N.M.
94b	Ferrite	173	0.021	2.3×10^{13}	47.7	3.7	3.8×10^{14}	41	6.0×10^{14}	41.0	5.4×10^{9}
			0.000	0	---						1.4×10^{10}
		192	0.031	1.6×10^{13}	30.0	2.7	6.6×10^{14}	35	3.5×10^{15}	60.2	
			0.000	0	---				2.8×10^{15}	41.4	
		Median	0.01	8×10^{12}	38	3.2	7.5×10^{14}	38	6×10^{14}	41.0	9×10^{9}
	Upper Bainite	173	0	0	---	1.5	1.1×10^{15}*	22.8*	6.1×10^{14}	26.2	
94b	Ferrite	213	0.214	6.1×10^{13}	45.1	4.5	3.6×10^{14}	52.9			6.1×10^{9}
		217	0.020	2.3×10^{13}	42.0	4.6	1.9×10^{14}	59.3			
		212	0.161	4.6×10^{13}	41.0	6.2	4.0×10^{14}	56.1			
		214									3.2×10^{9}
			0.16	5×10^{13}	42	4.5	4×10^{14}	56			[illegible]
	Upper Bainite	237	0	0	---				1. [illegible] 10	42.3	
[illegible]	Ferrite	371	0	0	---	7.6	9.4×10^{14}	50.4			
		367	0	0	---	9.8	7.5×10^{14}	47.6			4.6×10^{9}
		367	---	---	---	---	1.9×10^{14}	65.3			5.0×10^{9}
		Median	0	0		8.5	7.5×10^{14}	50	4×10^{14}	70	5×10^{9}
	Upper Bainite	375	0	0		4.9	2.2×10^{14}	37.1	4.9×10^{13}	48.9	

[illegible] N.M. Not Measured

Table 7.5.5. Summary of quantitative microstructural measurement for AAXIV and AD2 specimens

Specimen	Negative Number	Voids: Swelling $\Delta V/V_0$, %	Voids: Density #/cm³	Voids: Mean Diameter nm	Precipitates/Spheres: Volume %	Precipitates/Spheres: Density #/cm³	Precipitates/Spheres: Mean Diameter nm	Rods: Density #/cm³	Rods: Mean Length nm	Dislocations: Density #/cm²
NUYL	314	.065	7.4×10^{14}	11.7	0.53	4.9×10^{15}	11.5	3.1×10^{14}	31.1	N.M.
31CP	338									4.4×10^{10}
	336	.11	2.1×10^{15}	9.6	0.1	3.0×10^{15}	8.1	1.6×10^{15}	34.5	
	336	.12	1.7×10^{15}	10.3	8.0	6.3×10^{15}	10.1	1.02×10^{15}	45.5	
	347	.23	2.7×10^{15}	10.1	3.3	4.5×10^{15}	13.7			
	median	.1	2×10^{15}	10	2.	5×10^{15}	11	1×10^{15}	31	4×10^{10}
31CV	469	0	0		2.0	1.2×10^{15}	22.5	8.8×10^{14}	31.3	3.4×10^{10}
	465	0	0		2.2	1.15×10^{15}	21.3	2.5×10^{14}	69.2	
		0	0		2.	1.2×10^{15}	22	5×10^{14}	50	3×10^{10}
31CR	478	0	0		3.2	4.5×10^{14}	35.0	5.2×10^{14}	56.5	
	497	0	0		1.7	3.9×10^{14}	32.8	5.0×10^{14}	84.7	
	483	0	0			2.6×10^{14}	46.1	2.6×10^{14}	102.	
	median	0	0		2.5	4×10^{14}	35.	5×10^{14}		

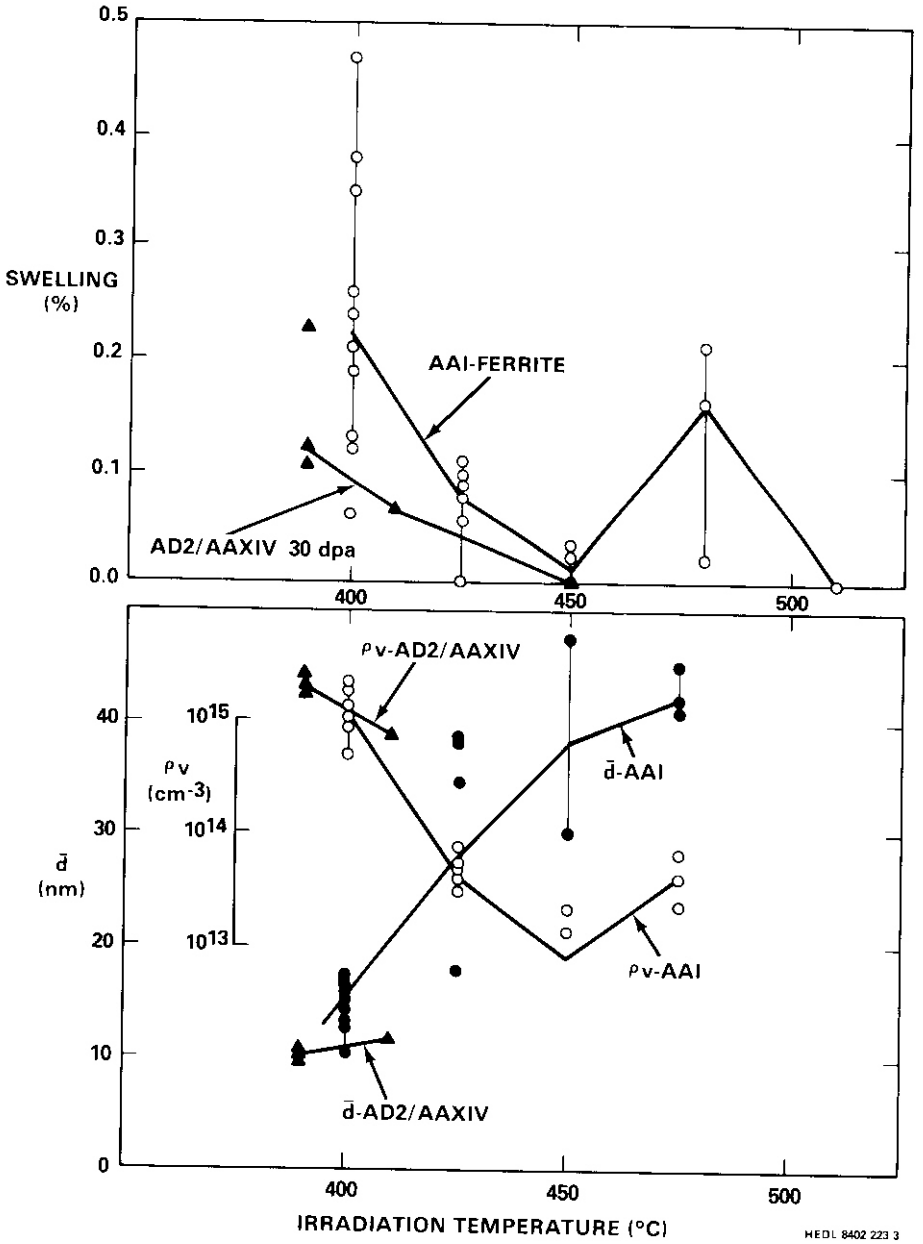

Fig. 7.5.23. Void measurements in ferrite AAI and AD2/AAXIV specimen conditions as a function of temperature. Only results for ferrite in AAI specimens are shown.

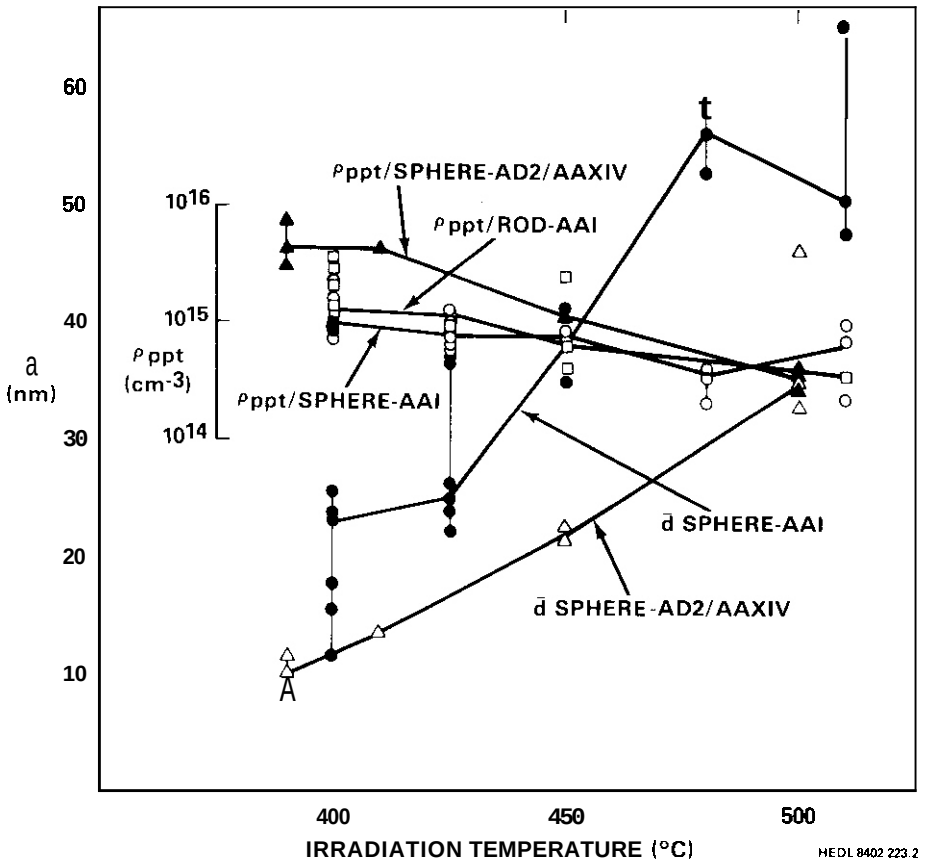

Fig. 7.5.24. Measurements of precipitates in ferrite in AAI and AD2/AAXIV specimen conditions as a function of temperature.

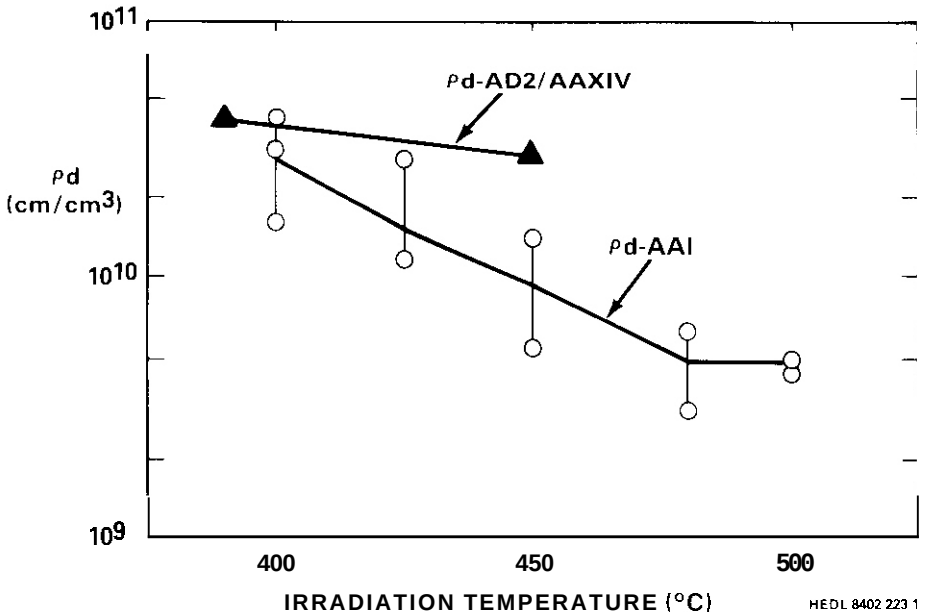

Fig. 7.5.25. Measurements of dislocation density plotted as a function of irradiation temperature.

7.5.4.4 Discussion

The present results provide information which answers several questions concerning the behavior of irradiated 2-1/4Cr-1Mo steel hut which also raises several further questions. It is now demonstrated that void swelliny, dislocation loop development and precipitation occur aS a result of fast neutron irradiation in the temperature range 400 to 480°C in 2-1/4Cr-1Mo steel. The purpose of this discussion will be to summarize these results and to assess the implications of these results on the intrepretation of in-reactor creep, density change dnd post irradiation tensile behavior

Effects of Irradiation on Microstructure

Fast neutron irradiation of 2-1/4Cr-1Mo produces microstructural features which are similar to those found in other steels'. For example, the AAI material has now been examined following irradiation at throe fluence levels, 5 x 10"" n/cm², 1.8 x 10²³ n/cm² and 2.5 x 10"" n/cm².[6] It is found that for irradiation at 425°C, precipitation and dislocation evolution occur rapidly, by 5 x 10²² n/cm² but void formation is only found after 1.6 x 10²³ n/cm² and further void development after 2.1 x 10²³ n/cm² is found to have produced little further swelling.' The peak swelling temperature is at 400°C or below and density measurements show an increase in swelling of only 0.16% from 1.4 x 10²² n/cm² to 1.6 x 10²³ n/cm² at 400°C.' Therefore, 2-1/4Cr-1Mo is highly swelling resistant but swelling does occur in the alloy.

The onset of swelling occurred at much lower fluence for specimens in hoth the AD2 and AAXIV tests. The reason for this difference cannot be determined at this time: several possibilies exist. However, it is likely to be a consequence of either differences in heat treatment procedure or heat-to-heat variation. Heat treatment differences provide the possible correlation that more carbon in solution delays the onset of swelling whereas compositional differences such as nickel or minor impurity effects may have controlled the swelling response. Examination of alternate heat treatment conditions included in the AD7 test may provide the answer.

Implications for Irradiation Creep Modeling

The present results validate two assumptions drawn in the companion study of irradiated pressurized tubes.' That study concluded that at 480°C and below, effects of irradiation controlled behavior where at 570°C the thermal creep contributions were significant. The study also concluded that in-reator creep at 390°C was increased compared with that at 480°C, probably due to swelling enhanced creep. The microstructural results of this study have shown void swelling in 2-1/4Cr-1Mo at temperatures as high as 480°C whereas no irradiation induced microstructure could he identified in a specimen irradiated at 510°C. Therefore, the transition from irradiation induced microstructure controlled to thermally controlled behavior occurs at ~500°C for 2-1/4Cr-1Mo. Also, void swelling is found in disk specimens which correspond to the same condition of composition and irradiation history as the pressurized tubes irradiated at 390°C. Therefore, swelling enhanced in-reactor creep compared to the 480°C condition and void swelling causes for diameter change in unstressed tubes can be validated.

Interpretation of Density Change Measurements

Microstructural examinations reveal two mechanisms which can cause the density changes observed in irradiatea AAI specimens. Void swelling can contribute to density change for irradiation temperatures of 480°C or below. Void volume fraction is greatest at the lowest irradiation temperature examined, 400°C, hut the accumulated swelling is low, on the order of 0.2% or less even at 400°C. Concurrently, precipitation occurs during irradiation. Precipitation can he expected to lead to changes in density and effects as large as 0.2% are not unreasonable. Therefore, density change measurements for 2-1/4Cr-1Mo specimens irradiated in the AAI test are expected to include contributions due to void swelling and precipitation. However, further work will he required in order to determine which precipitate phases have formed, whether those phases also form during thermal aging and whether those phases can explain the differences between density change measurements and void swelling measurements.

Interpretation of Tensile Test Results

The present microstructural results demonstrate that interpretation of postirradiation tensile tests for 2-1/4Cr-1Mo speciinens must include effects due to irradiation induced (or enhanced) precipitate development. The precipitate structures represent the most densely packed obstacles for dislocation motion in specimens irradiated at 400°C. Therefore, they likely control plastic flow behavior. Void may contribute but are expected to liave a smaller effect; the number density is lower, and it is likely that the lower fluence condition of the tensile specimens (compared to those used for microstructural examination) will contain NO void swelling whereas irradiation induced precipitates will be present. Dislocation loops will also contribute to plastic flow behavior. The present quantitative microstructural measurements can provide a basis for comparing the effect of these different microstructural components on strength. However, such a coinparsion is considered to be beyond the scope of the present effort.

Microstructural studies confirm that irradiation at 550°C leads to decreases in post irradiation strength as a consequence of overaging of the precipitate structure and the concurrent loss of ISSH. However, because microstructural comparisons with thermally aqed specimens have not yet been made, the reason for strength differences between specimens thermally aqed and irradiated at 550°C cannot be identified.

Possibilities are that different precipitation reaction sequences apply for the two environments or that the kinetics are different.

7.5.5 Conclusion

A series of nine specimen conditions of 2-1/4Cr-1Mo have been examined by transmission electron microscopy following irradiation by fast neutrons over the temperature range 390 to 510°C. Irradiation was found to produce void swelling, precipitation and dislocation network development at temperatures of 480°C or below whereas at 500°C and above, behavior can best be described as precipitate averaging. Void swelling varied as a function of irradiation temperature, preirradiation microstructure and possibly heat treatment or composition differences with peak swelling on the order of 0.2% found following irradiation at 400°C. The dislocation structure in a retained ferrite grain following irradiation at 400°C was found to contain predominantly a<100> dislocations with some a/2<111> dislocations also present.

Quantitative measurements have been made of void, precipitate and dislocation structures in the various distinctly different microstructural regions. Precipitates which formed during irradiation are shown to be a dominant feature which should affect properties.

7.5.6 References

1. D. S. Gelles and R. J. Puigh, "Evaluation of Ferritic Alloy Fe-2-1/4Cr-1Mo After Neutron Irradiation - Irradiation Creep and Swelling," pp. 82-94 in *ADIP Semiann. Prog. Rep. Sept. 30, 1983*, DOE/ER-0045/11, U.S. DOE, Office of Fusion Energy.

2. R. L. Klueh and J. M. Vitek, "Elevated - Temperature Tensile Properties of Irradiated 2-1/4Cr-1Mo Steel Irradiated in the EBR-II, AD-2 Experiment," pp. 95-102 in *ADIP Semiann. Prog. Rep. Sept. 30, 1983*, DOE/ER-0045/11, U.S. DOE, Office of Fusion Energy.

3. Electric Power Research Institute Project RP1597-2 on Radiation Damage and Performance Analysis of Ferromagnetic Steels for Fussion Application with the Fission Engineering Program, Nuclear Engineering Department, University of Wisconsin, Madison, WI.

4. T. Wada and G. T. Eldis, "Transformation Characteristics of 2-1/4Cr-1Mo Steel," pp. 343-363 in *Applications of 2-1/4Cr-1Mo Steel for Thick-Wall Pressure Vessels*, ASTM STP 755, G.S. Sandahl and M. Semchysher, Eds, American Society for Testing and Materials (1982).

5. F. B. Pickering, "The Structure and Properties of Bainite in Steel," pp. 109-129 in *Transformation and Hardenability in Steel*, Climax Molybdenum Company of Michigan, Ann Arbor, MI, (1967).

6. D. S. Gelles, "Microstructural Examination of Several Commercial Ferrite Alloys Irradiated to High Fluence," *J. Nucl. Mater.* 103 & 104, 975-979 (1981).

7.6 MICROSTRUCTURAL EXAMINATION OF SEVERAL COMMERCIAL ALLOYS IRRADIATED TO VERY HIGH NEUTRON FLUENCE — D. S. Gelles (Hanford Engineering Development Laboratory)

No contribution.

7.7 ALLOY DEVELOPMENT FOR IMPROVED SWELLING RESISTANCE IN FERRITIC STEELS — J. M. Vitek and R. L. Klueh (flak Ridge National Laboratory)

7.7.1 ADIP Task

ADIP tasks are not defined for Path E Ferritic Steels in the 1978 program plan.

7.7.2 Objective

The objective of this work is to investigate the factors that result in different swelling characteristics of ferritic steels. These results should pave the way for improved swelling-resistant ferritic steels.

7.7.3 *Summary*

Eleven button melt heats of ferritic steel have been produced and are being processed to sheet form. Transmission electron microscopy (TEM) disks of these heats will be irradiated in the High Flux Isotope Reactor (HFIR), and their postirradiation evaluation is expected to provide insight toward improving the swelling resistance of ferritic steels.

7.7.4 Progress and Status

7.7.4.1 Introduction

Several studies have been conducted to evaluate the swelling response of 9 Cr-1 MoVNb and 12 Cr-1 MoVW to irradiation. These investigations have been on EBR-II irradiated specimens' as well as HFIR-irradiated disks.[2] In the latter case, the simultaneous production of helium with irradiation damage indicated that the presence of helium enhances swelling. Regardless of which reactor was used for the irradiation, and even though the swelling observed was minimal, an apparent trend existed. The 9 Cr-1 MoVNb alloy showed a greater tendency for swelling than 12 Cr-1 MoVW.

Rased on this evidence, a series of alloys was designed to address the question of what accounts for the swelling variation. By learning more about the alloy-dependent characteristics of swelling in ferritic steels, it is hoped an even more swelling-resistant alloy can be developed.

7.7.4.2 Alloy Design Considerations

Although the 9 Cr-1 MoVNb and 12 Cr-1MoVW alloys are similar in structure and composition, several features are different. An attempt was made to separate these variations and produce alloys that consider one alteration at a time. Eleven different alloy compositions were designed *in* an effort to make specific comparisons possible. The nominal alloy composition variations are given in Table 7.7.1.

"Standard" 9 Cr-1 MoVNb and 12 Cr-1 MOVW alloys were included to ensure that the differences observed previously still existed in the small-scale button melts. These alloys are alloys B and F, respectively.

Several elemental variations were considered. These included:

effect of Cr in 9 Cr-1 MoVNb — alloys B and L
in 12 Cr-1 MoVW — alloys D and F
effect of W in 12 Cr-1 MoVW — alloys F and H
effect of Ni in 9 Cr-1 MoVNb — alloys B and C
in 12 Cr-1 MoVNb — alloys F, J, and K
effect of C in 9 Cr-1 MoVNb — alloys B and I
in 12 Cr-1 MoVW — alloys F and G
effect of Nb in 9 Cr-1 MoVNb — alloys B and E

Table 7.7.1. Nominal compositional variations (wt %) of experimental heats

Heat ID	Cr	Mo	Ni	C	Nb	W
B	9	1	0.1	0.1	0.06	
C	9	1	0.4	0.1	0.06	
D	9	1	0.4	0.2		0.5
E	9	1	0.1	0.1		
F	12	1	0.4	0.2		0.5
G	12	1	0.4	0.1		0.5
H	12	1	0.4	0.2		
I	9	1	0.1	0.2	0.06	
J	12	1	0.5	0.2		0.5
K	12	1	0.6	0.2		0.5
L	12	1	0.1	0.1	0.06	

Several compositional variations are expected to have side effects. For example, it is known[2] that not only are the carbide levels different in 9 Cr-1 MoVNb and 12 Cr-1 MoVW, but their distributions also vary somewhat. The 9 Cr-1 MoVNb alloy has a much greater concentration of carbides at prior austenite grain boundaries. This is likely to be due to the presence of niobium in 9 Cr-1 MoVNb. Hence the effect of carbon level is being evaluated in both alloys, so that presumably both carbide distributions will be included. For a fixed carbon level, the effect of carbide distribution is expected to be covered by the niobium comparison.

With irradiation in HFIR, the amount of helium produced during irradiation is related to the nickel content. Therefore, a comparison of different nickel contents will also include a comparison with different helium levels. To separate these effects somewhat, the effect of multiple element variation but with constant helium levels will be possible by comparing alloys C and F.

7.7.4.3 Alloy Preparation and Evaluation

An 18-kg (40-lb) master alloy, with the minimum alloy content common to all alloys, was procured from Combustion Engineering to provide a common basis for all the alloy button melts, so only minor further alloy additions were needed. The eleven button melts are being melted and rolled down to 2.25-mm (0.010-in.) sheet. Each button melt will consist of approximately 0.5 kg (1 lb) of material.

These alloys are intended to provide information on the swelling response of ferritic steels. This will be accomplished by irradiating TEM disks in HFIR at the peak swelling temperature of 400°C to a damage level of 50 dpa. The HFIR-CTR-49 experiment, described elsewhere in this report, will be used. In order not to delay the start of this experiment, and until more information is available on the heat treatment response of these alloys, a standard heat treatment of 1050°C/0.5 h/AC + 760°C/1 h/AC will be used for all alloys.

The influence of heat treatment on swelling behavior will not be addressed in this study. However, the effect of heat treatment variations on the swelling response of ferritics will be examined for the standard 9 Cr-1 MoVNb and 12 Cr-1 MoVW alloys by irradiating these materials in the HFIR-CTR-50 experiment to 100 dpa at 400°C.

7.1.5 References

1. D. S. Gelles and L. E. Thomas, "Microstructural Examination of HT-9 and 9 Cr-1 Mo Contained in the AD-2 Experiment," pp. 373–61 in *ADIP Semiannu. Prog. Rep. Mar. 31, 1982*, DOE/ER-0045/8, U.S. DOE, Office of Fusion Energy.

2. J. M. Vitek and R. L. Klueh, "Microstructure of 9 Cr-1 MoVNb and 12 Cr-1 MoVW Ferritic Steels after Irradiation at Elevated Temperatures in HFIR," pp. 108–14 in *ADIP Semiannu. Prog. Rep. Sept. 30, 1983*, DOE/ER-0045/11, U.S. DOE, Office of Fusion Energy.

7.8 The Influence of Step Austenitizing Treatment on the Toughness and Tensile Ductility of Hydrogen Charged HT-9, W. M. Garrison, Jr. (SNL-L), J. M. Hyzak (SNL-L)

7.8.1 AOIP Task

The Department of Energy (DOE) Office of Fusion Energy (OFE) has cited the need for these data under the ADIP Program Task, Ferritic Alloy Development (Path E).

7.8.2 Objective

The goal of this study is to evaluate the hydrogen compatibility of the 12Cr-1Mo ferritic/martensitic steel HT-9 for use in first wall and blanket structures. This report summarizes data on the effect of internal hydrogen on the room temperature tensile properties of this ESR processed 12Cr-1Mo steel.

7.8.3 Summary

Prior research on the tensile behavior of the quenched and tempered steel HT-9 has shown that the steel exhibits marked susceptibility to hydrogen embrittlement and hydrogen induced intergranular fracture (1,2). The severity of the embrittlement can be significantly reduced and the intergranular fracture mode entirely eliminated by swaging and retempering the steel (3). These improvements are attributed to a reorientation of the prior austenite grain boundaries with respect to the tensile axis and to reduced carbide and impurity coverages of grain boundary interfaces.

The swaging results suggest that the hydrogen compatibility of HT-9 could be increased by reducing the grain size. To assess the role of grain size, two different austenitizing treatments were employed. The first employed reductions in austenitizing temperature to refine the prior austenite grain size. To assess the roles of microstructural features other than grain size, a two step austenitizing treatment was used. In these treatments specimens were quenched from a fixed initial austenitizing temperature which determines the austenite grain size to a second, lower, austenitizing temperature. The second austenitizing temperature will redistribute the carbides and grain boundary segregants. As the same temperatures were used in varying the austenitizing temperature and the second austenitizing temperature in the step treatments, comparison of the two treatments should provide some insight as to the role of grain size in the hydrogen embrittlement of this steel.

The major effects of lowering the austenitizing temperature from 1050° C are to increase the hydrogen charged tensile ductility and to reduce the yield strength. Decreasing the austenitizing temperature from 1050° to 900° C increases the hydrogen charged tensile ductility from 13% to 47% and decreases the yield strength from 110 ksi to 72 ksi. Decreasing the second austenitizing temperature in the step treatment does not lower the yield strength as much as lowering the austenitizing temperature. Therefore, at the same austenitizing and second austenitizing temperatures, the carbide morphologies are not the same and comparison of the two heat treatments cannot be used to define the role of grain size.

7.8.4 Progress and Status

7.8.4.1 Introduction

Previous work has shown that the introduction of 6 wppm hydrogen by cathodic charging reduces the tensile reduction in area of HT-9 from about 59% to 13% and alters the fracture mode from ductile rupture to one substantially intergranular along prior austenite grain boundaries (1,2). The susceptibility of HT-9 to hydrogen induced embrittlement and grain boundary fracture can be virtually eliminated by swaging and retempering the quenched and tempered structure (3). The improved hydrogen compatibility of swaged and retempered HT-9 is attributed to both a reorientation of prior austenile grain boundaries with respect to the tensile axis and to reductions in the coverage of the grain boundaries by both carbides and impurities. The success of the swaging treatment suggests that heat treatments designed to both vary the prior austenite grain size and the extent of carbide and impurity coverages of these boundaries might be employed to improve the hydrogen compatibility of the HT-9 and to define the relative importance of grain boundary carbides and segregants in causing the embrittlement.

Two types of variations in heat treatment were employed. In the first, austenitizing temperatures were varied; the austenitizing temperatures used were 1050° C, the customary austenitizing temperature, 1000° C, and 950° C. Lowering the austenitizing temperature will reduce the austenite grain size.

The second neat treatment variation utilized a step austentitizing treatment in which specimens were held at 1050° C and then transferred to a furnace at a temperature of either 1000° C, 950° C or 900° C. The initial austenitizing temperature will fix the grain size, while the second austenitizing temperature will change carbide and segregant distribution.

7.8.4.2 Experimental Procedure

The 12Cr-1Mo steel used in this study was 1.59 cm thick ESR processed plate with chemical composition:

C	Cr	Mo	V	W	Si	Mn	S	P
0.20	12.1	1.04	0.28	0.45	0.17	0.57	.003	.016

The transverse tensile properties were determined for the following two types of austenitizing treatments. For the first, specimen blanks were austenitized for 45 minutes, air cooled, tempered at 750° C for one hour and then water quenched; austentizing temperatures of 10500, 1000°, 950° and 900° C were used. For the second type of austenitizing treatment specimens were austenitized at 1050° C for 45 minutes, immediately transferred to another furnace at the second austenitizing temperature and held for 45 minutes. The second austenitizing temperatures were 1000°, 950°, and 900° C. The specimens were then air cooled, tempered for one hour at 750° C and then water quenched.

Round tensile specimens were then machined from the heat treated specimen blanks. The tensile specimens had a gage diameter and length of 0.28 cm and 2.0 cm respectively.

Tensile specimens were cathodically charged with hydrogen at room temperature at a current density of 0.006 A/cm^2 for 2.5 hours in a 4% sulphuric acid solution containing 5 mg/of sodium arsenate as a recombination poison. When charged for 2.5 hours the quenched-and-tempered material austenitized at 10500 C and tempered contained 6-8 wppm of hydrogen as measured by a LECO hydrogen determinator. After charging, the specimens were immediately plated with 0.004 cm of copper and then equilibrated 24 hours before testing. All tensile tests were run at room temperature at an initial strain rate of 0.025/min.

The extent of carbide grain boundary coverage was determined from carbon replicas of polished specimens etched with Vilella's reagent. Micrographs of prior austenite grain boundaries were taken and the total length of the boundary and the total distance between carbides were measured for each. The ratio of the grain boundary length containing carbides to the total grain boundary length was taken as the fraction of the grain boundary area covered by carbides (4). A minimum of ten acceptable micrographs were used to determine an average carbide grain boundary coverage for each condition. An acceptable micrograph was one in which the grain boundary carbide images were clearly defined along their entire circumference.

7.8.4.3 Results

The effects of variations in austenitizing temperature on the mechanical properties of HT-9 are summarized in Table I. Reducing the austenitizing temperature did not markedly change the uncharged tensile ductility and Charpy impact energy but significantly lowered the yield strength and increased the tensile ductility after hydrogen charging. The yield strength is 110 ksi after austenitizing at 1050° C, and decreases to 72 ksi on austenitizing at 900° C. The tensile ductility after hydrogen charging is 13% after austenitizing at 1050° C, increases as the austenitizing temperature is lowered and is 47.8% after austenitizing at 900° C. The intergranular fracture mode observed on an austenitizing at 10500 C disappears at the austenitizing temperature is decreased (Figure 1).

The effects of the two-step austenitizing treatment are summarized in Table 2. These treatments do not significantly alter the uncharged tensile ductility. Lowering the second austenitizing temperature does reduce the yield strength but not as markedly as simply decreasing the austenitizing ,temperature. Reducing the second austenitizing temperature does not improve the hydrogen tensile ductility; however, it does result in a significant drop in the Charpy impact toughness. The Charpy impact toughness of HT-9 is reduced from 86 ft-lbs to 44 ft-lbs when the second austenitizing temperature is 900° C.

7.8.4.4 Discussion

The significant result is that as the austenitizing temperature is lowered, the hydrogen charged tensile ductility increases and brittle intergranular fracture is eliminated. This probably is due in part to a marked reduction in grain size. The grain size is about 150 µm after austenitizing at 10500 C and about 15 µm after austenitizing at 1000° C (Figure 2). The grain size does not seem to decrease appreciably on decreasing the austenitizing temperature below 1000° C. Therefore, the increase in hydrogen tensile ductility observed as the austenitizing temperature is lowered below 1000° C is probably associated with the reduction in yield strength. The reduction in yield strength is due to the reduced solubility of the alloy carbides associated with lower austenitizing temperatures.

The step austenitizing treatments were employed to eliminate grain size variations but allow variations in other microstructural features such as carbide solubility and distribution as well as the extent of impurity segregation. The results of the step austenitizing treatments could then be compared with those from the variations in austenitizing temperature to provide some insight as to the role of grain size. This comparison would be valid if the carbide distribution established at a particular austenitization temperature and the same second austenitizing temperature were identical. However, this is not the case, as these temperatures have very different yield strengths.

While this comparison cannot be made, it is clear that lowering the second austenitizing temperature in the step treatments results in additional grain boundary susceptibility to fracture. While not reflected in the hydrogen charged tensile ductility this is reflected on the Charpy results. The Charpy impact toughness decreases as the second austenitizing temperature is reduced and the fracture becomes increasing intergranular. This increased tendency for intergranular fracture cannot be attributed to changes in the fraction of the prior austenite grain boundaries covered by carbides. The extent of this coverage remains about 85% for the four step austenitizing treatments used.

7.8.5 Conclusions

The use of lower austenitizing temperatures increases the hydrogen charged tensile ductility of HT-9.

Step austenitizing treatments do not alter the hydrogen compatibility of HT-9, but reducing the second temperature in these treatments does reduce the Charpy impact toughness.

7.8.6 References

1. J. M. Hyzak and W. M. Garrison, Jr., "Hydrogen Embrittlement of ESR Processed 12Cr-1Mo Steel," ADIP Semiannual Progress Report, DOE/ER-0045/8, March 1982, pp. 401-413

2. J. M. Hyzak and W. M. Garrison, Jr., Topical Conference on Ferritic Alloys for Use in Nuclear Energy Technologies, June 19-23, 1983, Metallurgical Society of AIME, in press.

3. W. M. Garrison. Jr.., and J. M. Hyzak. "The Influence of Prior Cold Work on the Hydrogen Charged Tensile Fracture of a 12Cr-1Mo Steel", ADIP Semiannual Progress Report, DOE/ER-0045/10, March 31, 1983, pp. 147-154

4. E. E. Underwood, "Surface Area and Length in a Volume," Quantitative Microscopy, R. T. De Hoffand, F. N. Rhines eds., pp. 77-127, McGraw-Hill Book Company, 1968.

Table 1

Effect of Austenitizing Temperature on Mechanical Properties

Austenitizing Temperature (°C)	Yield Strength (ksi)	Charpy Toughness (ft-lbs)	% Reduction in area Uncharged'	Charged
1050	110	86	59	13
1000	92	90	65.6	20.7
950	84	87	68.7	40
900	72	83	63.5	47.8

Table 2

Effect of Step Austenitizing Treatment on Mechanical Properties

Second Temperature (°C)	Yield Strength (ksi)	Charpy Toughness (ft-1bs)	%Reduction in area uncharged	charged
1050	110	86	59	13
1000	103	80	62.4	7.3
950	96	65	59.9	9.2
900	96	44	60.4	6.2

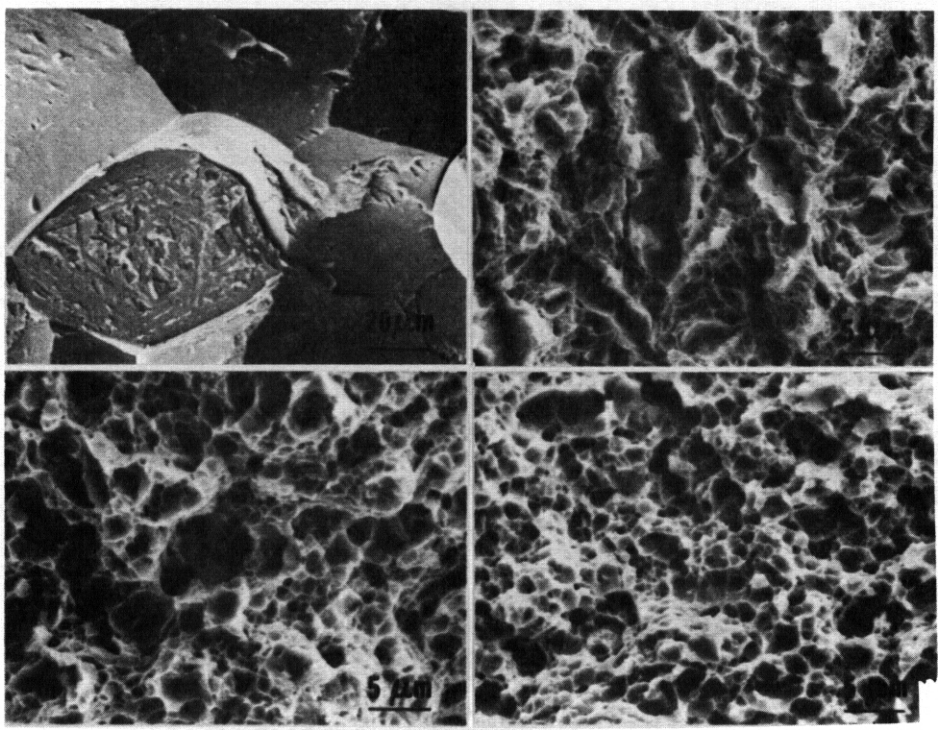

Figure 1
Fractographs of hydrogen charged HT-9 tensile specimens austenitized at
a) 10500 C, b) 10000 C, c) 950° C, and d) 9000 C.

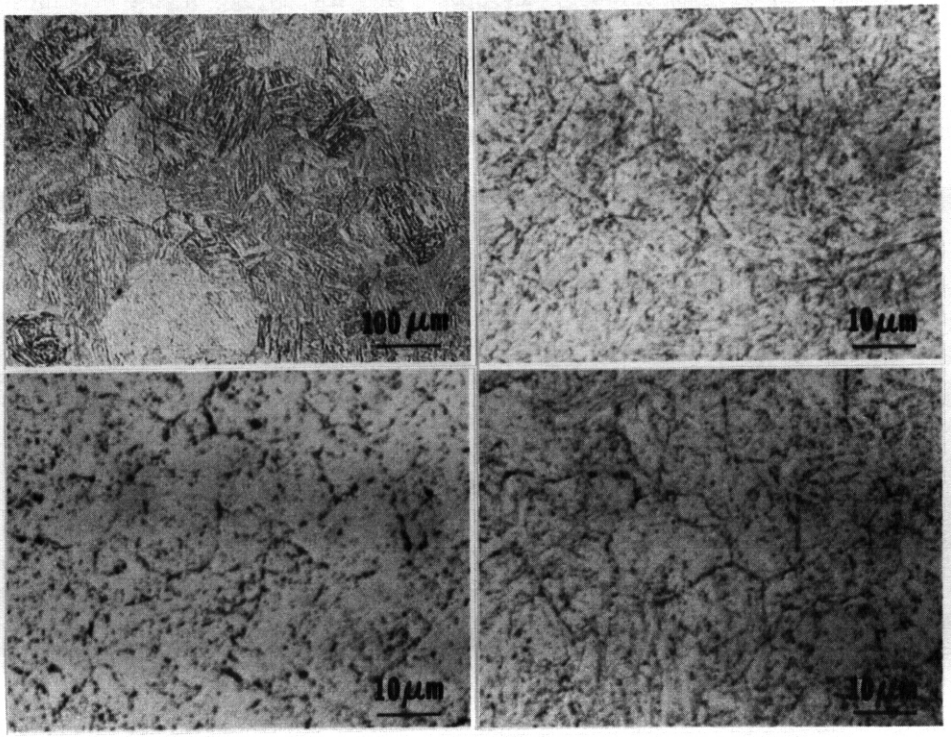

Figure 2
Optical micrographs-of HT-9 austenitized at
a) 10500 C, b) 10000 C, c) 9500 C, and d) 900° C.

7.9 HYDROGEN-INDUCED DUCTILITY LOSSES IN THE HEAT-AFFECTED ZONE OF HT 9 WELDMENTS - J. C. LIPPOLD AND J. M. HYZAK. SANDIA NATIONAL LABORATORIES, LIVERMORE

7.9.1 ADIP Task

The Department of Energy (DOE)/Office of Fusion Energy (OFE) has cited the need to investigate ferritic alloys under the ADIP program task, Ferritic Steels Development (Path E).

7.9.2 Objective

Results reported previously have demonstrated the deleterious effect of internal hydrogen on the tensile ductility of quench-and-tempered HT 9. The goals of this task are to determine if similar degradation in ductility occurs in the weld heat-affected zone (HAZ) and to study the effect of postweld heat treatment on the hydrogen-charged tensile behavior.

7.9.3 *Summary*

The effect of internal hydrogen introduced by cathodic charging on the tensile behavior of simulated HAZ microstructures has been evaluated. The loss in ductility of the HAZ after a postweld heat treatment at 750°C *is* equivalent to that observed in the quench-and-tempered base material. A postweld heat treatment at 600°C results in tensile ductilities which are inferior to those of the base metal at comparable charging levels.

7.9.4 Progress and Status

7.9.4.1 Introduction

Previous work [1-4] has shown that hydrogen introduced by cathodic charging severely reduces the tensile ductility of quench-and-tempered (Q/T) HT 9. The reduction in area (RA) decrease associated with internal hydrogen is summarized in Figure 7.9.1 for both the AOD-melted and ESR versions of the National Fusion Heat [5]. Therm-mechanical treatment has been shown to influence the behavior of HT 9 in hydrogen. For example, cold swaging and retempering the initial Q/T material was found to substantially improve the hydrogen charged tensile ductility relative to the Q/T microstructure [4]. In addition, this treatment was effective in suppressing the intergranular fracture mode which accompanied the loss in ductility. More recently, the austenitizing temperature has been shown to influence the ductility of HT 9 in hydrogen [6]. The relationship between heat treatment and resistance to hydrogen embrittlement is not straigntforward, but appears to be controlled by the amount and morphology of the carbides and segregation of impurities to prior austenite grain boundaries [2,3,7].

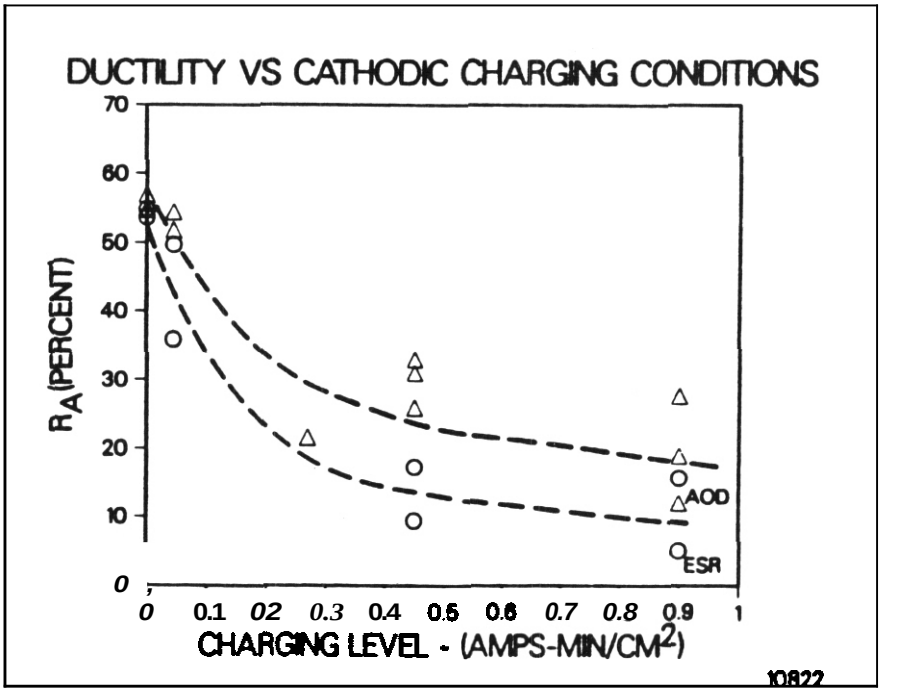

Figure 7.9.1. Reduction in Area [RA] versus Hydrogen Charging Level [current density X time] for ESR and AOD Processed 12Cr-1Mo steel [Ref. 2].

Within the heat-affected zone (HAZ) of HT 9 weldments, the region which experiences a thermal excursion into the temperature range between the alloy melting point (fusion line) to the lower critical temperature (Ac_1) is austenitized and subsequently forms untempered martensite upon cooling. Since the austenitizing temperature varies as a function of distance from the fusion line, the prior austenite grain size and carbide distribution changes significantly across this region. Previous investigations 18.91 have shown that during welding the region adjacent to the fusion line consists of a two phase mixture of austenite and delta ferrite. The delta ferrite forms along the austenite grain boundaries and is retained as the surrounding microstructure transforms to martensite upon cooling. Adjacent to this region, the HAZ exhibits a coarse prior austenite grain size and a microstructure which is essentially free of carbides. As the distance from the fusion line increases, the prior austenite grain size gradually decreases and the volume fraction of undissolved carbides increases.

It is evident from the above discussion that a complex microstructural gradient exists in the HAZ Of HT 9 following welding. This microstructural complexity is exacerbated when a postweld heat treatment (PWHT) is employed to temper the martensite. As a result, predicting the hydrogen compatibility of the HAZ relative to the base metal is nearly impossible. The purpose of this study is to assess the hydrogen-charged tensile behavior oF the HAZ and compare the behavior with that of the Q/T base material.

7.9.4.2 Experimental Procedure

The material used in this investigation was in the form of 10 mm (~3/8 in.) thick plate. This plate was a part of the orignial National Fusion Heat which was melted using the argon-oxygen decarburization (AOD) process [5]. The chemical composition of the material is listed in Table 7.9.1. The heat treatment consisted of austenitizing at 1040°C for 0.5 hours, air cooling, and then tempering at 750°C for one hour. The tempered hardness of the plate was on the order of R_C 22-24.

Table 7.9.1

Chemical Composition of HT 9 (AOD)

C	Cr	Ni	Si	Mn	Mo	V	W	N	P	S
0.20	11.64	0.52	0.24	0.57	1.01	0.30	0.57	.044	.018	.007

HAZ Microstructure Simulation

The microstructural gradient which exists over the narrow extent of the veld HAZ [2-3 mm] poses the problem of unambiguously evaluating individual microstructures within the HAZ. In this study, as in previous investigations-C10.11], the Cleeble has been successfully used to simulate the desired microstructure in a bulk sample. Specimen blanks 9.5 mm [3/8 in.] square and 100 mm long were machined from the Q/T plate. These blanks Were then thermally cycled in the Cleeble to simulate two distinct HAZ microstructures, designated HAZ#1 and HAZ#2. The thermal cycles used to produce these microstructures are illustrated in Figure 7.9.2.

The HAZ#1 cycle achieved a peak temperature of 1350°C and reproduced the two-phase microstructure which is adjacent to the fusion line in actual weldments. The HAZ#2 cycle [peak temperature 1150°C reproduced the coarse prior austenite grain structure farther from the fusion line. The Gleeble simulations were performed in such a manner that a uniform microstructural region approximately 30 mm long was produced along the axis of the specimen. Tensile bars were then machined from these samples such that the gage Section of the tensile bar contained the uniform microstructure.

A number of the HAZ #1 and #2 samples were subjected to a PWHT at either 600°C or 750°C. The specimens were tempered at these temperatures for 1 hour and then water quenched.

Cathodic Charging

Tensile specimens were cathodically charged with hydrogen using the charging conditions listed in Table 7.9.2. Charging was performed in a 4% sulfuric acid solution containing 5 mg/liter of sodium arsenate as a recombination poison. After charging, the specimens were immediately plated with 0.04 mm of copper to prevent egress of the hydrogen. The charged/plated samples were equilibrated for 24 hours at room temperature and then tensile tested using an extension rate of 0.51 mm/min [0.02 in/min].

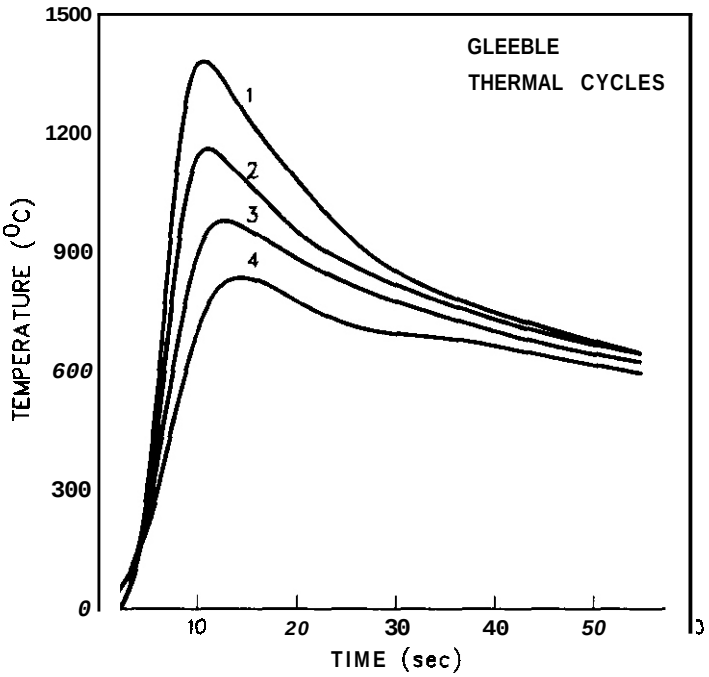

Figure 7.9.2. Gleeble thermal cycles used to simulate the HT 9 HAZ microstructures.

Table 7.9.2

Cathodic Charging Conditions

Condition	Current Density [amps/cm^2]	Time [min]
1	0.003	15
2	0.006	15
3	0.006	150

7.9.4.3. Results

The hardness Of the various HAZ/PWHT combinations are listed in Table 7.9.3. Note that the initial hardness of the HAZ #1 microstructure is slightly lower than that of HAZ #2. This differential is probably due to the small amount of ferrite interspersed within the martensite. There is essentially no difference in hardness between the HAZ microstructures following the PWHT at a given temperature [600 or 750°C].

Table 7.9.3

Hardness of HAZ Microstructures

HAZ Region	PWHT [°C for 1 hr]	Hardness [R_c]
	none	47–49
	600	37–38
	750	24–25
	none	49–51
2	600	38–39
	750	21–22

Results of the tensile tests of the individual HAZ/PWHT combinations are listed in Table 7.9.4. HAZ #1 and #2 samples which were not subjected to a PWHT were tested at only one charging level. In general, the individual HAZ/PWHT combinations were tested in the uncharged condition and at three charging levels.

Table 7.9.4

Tensile Test Results *

PWHT [°C]	Y.S., MPa [ksi]	U.T.S., MPa [ksi]	R.A. [%]	Charging Condition **
none	1448 I2101	1889 [274]	3.1	uncharged
	-	745 [108]	0.0	2
	1048 [152]	1262 [183]	62.7	uncharged
	1117 I1621	1296 [188]	42.0	1
600	1089 11581	1214 [176]	25.3	2
	-	965 [140]	4.8	3
	676 [98]	875 [127]	58.0	uncharged
	703 [102]	869 [126]	60.3	1
750	690 [100]	875 11271	42.7	2
	696 [101]	862 [105]	17.1	3
	1393 [202]	1882 [273]	3.1	uncharged
none	-	1227 [178]	0.0	1
	1145 [166]	1317 [191]	59.5	uncharged
600	1130 I1641	1276 [185]	55.0	1
	1117 [162]	1227 [178]	5.6	2
	696 [101]	882 [128]	55.8	uncharged
	738 [107]	896 [130]	58.5	
750	730 [106]	910 11321	41.8	2
	738 [107]	890 [129]	35.0	3

* all values are the average of two tests except for samples without PWHT
** see Table 7.9.2 for charging condition

In both the HAZ #1 and #2 microstructures the ductility decreases as the internal hydrogen level increases. At the highest charging level [Condition 31 the ductility drops precipitously, particularly in samples which were given *a* PWHT at 600°C. The HAZ #1 and li2 samples subjected to the 750°C PWHT exhibited nearly equivalent hydrogen-charged tensile behavior.

The ductility **loss** *of* the HAZ microstructures relative to the Q/T AOD base material is shown in **Figure** 7.9.3. After a PWHT at 600°C the hydrogen-charged ductility **is** dramatically less than that of the Q/T base material [Fig. 7.9.3a]. A PWHT at 750°C restores the ductility to a level which is at least equivalent or, in the case *of* HAZ #2, superior to the base material ductility [Fig. 7.9.3b].

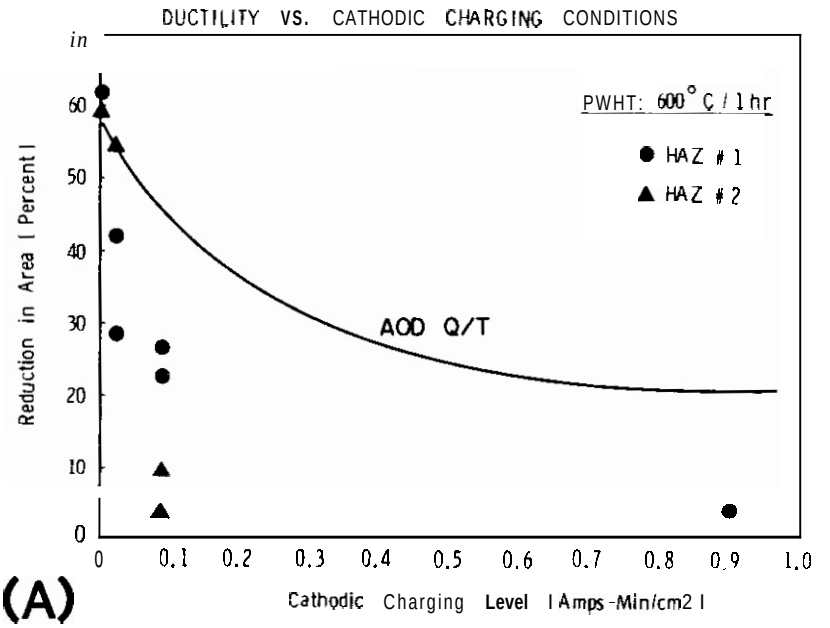

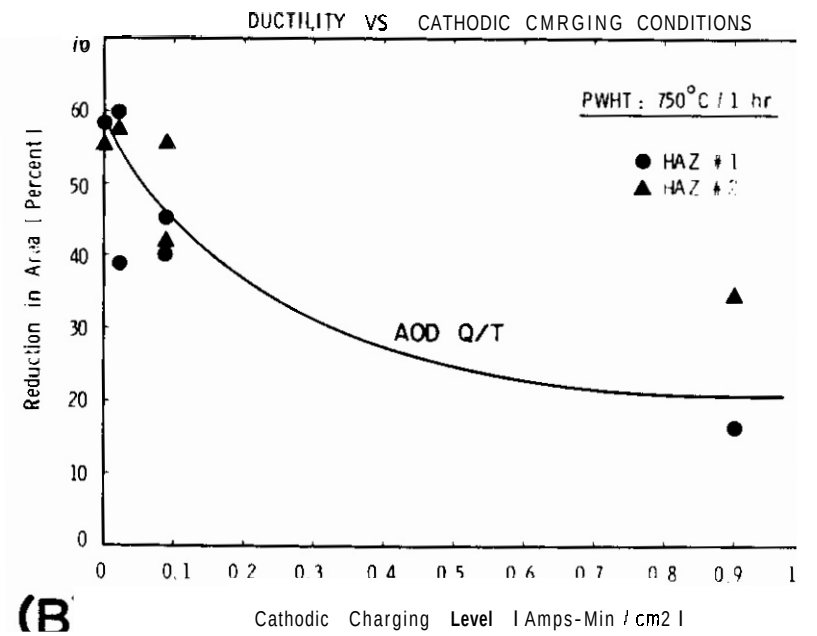

Figure 7.9.3. Reduction in Area RA] versus Hydrogen Charging Level for the Simulated HAZ microstructures relative to the AOD Q/T behavior. A, 600° C PWHT; B. 750° C PWHT.

Fractography

Macrofractographs of both a HAZ #1 and #2 tensile sample charged with Condition 1 [Table 7.9.2] are shown in Figure 7.9.4. The tensile bars were given a PWHT at 750°C. The RA of both samples was on the order of 60%[Table 7.9.41 and they exhibit a CUP-cone type failure. Secondary cracking on the fracture surface is both radial and vertical in Fig. 7.9.4. The Vertical cracks are associated with ferrite and/or sulfide stringers in the original plate; Cracking of this type is also observed in the uncharged HAZ tensile samples and in the Q/T AOD base material [1,3].

As the ductility decreases with the increase in internal hydrogen concentration. the tendency for the radial and orientation-type cracking is reduced. At the highest charging level [Condition 31 the macroscopic fracture surfaces are relatively flat and the degree of surface cracking along the gage length increases significantly.

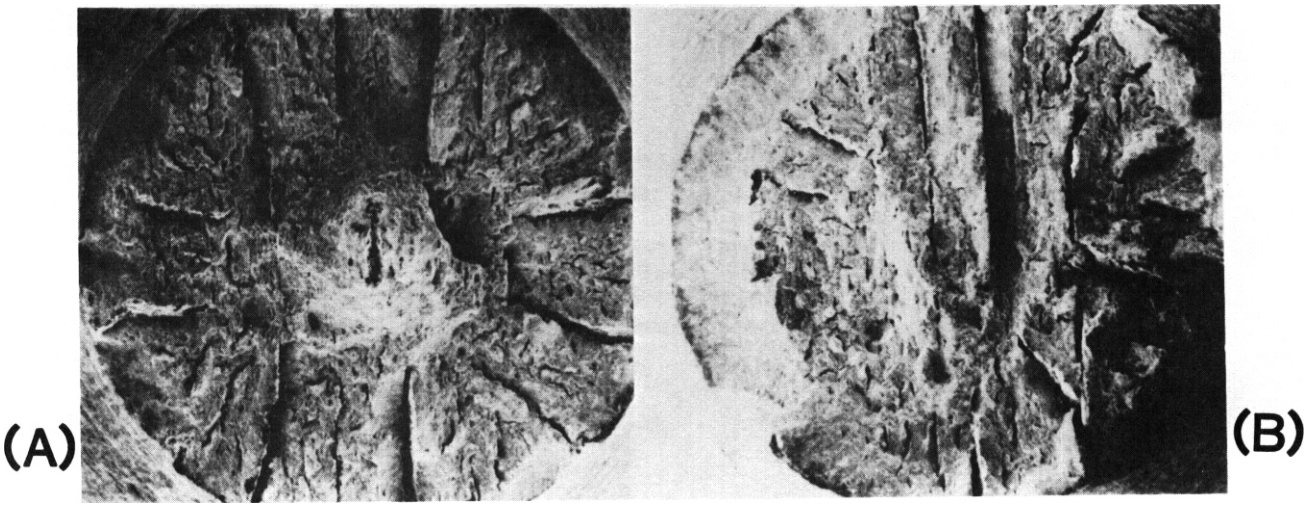

Figure 7.9.4 Macrofractographs of tensile samples charged to Condition 1. A. HAZ #1; B, HAZ #2

HAZ microstructures which have been given a PWHT [either 600 or 750°C] and are tested in the uncharged condition or at the lowest charging level [Condition 1] generally exhibit a ductile dimple failure mode. As the hydrogen concentration in the samples increases. the fracture mode shifts to quasi-cleavage, whereby fracture occurs along martensite lath boundaries. Ultimately, at the highest charging level, failure is by an intergranular mode along prior austenite grain boundaries. The quasi-cleavage failure mode is evident in a HAZ #1/750°C sample which was charged using Condition 2 [Figure 7.9.51. Failure is primarily along lath boundaries with some evidence of secondary cracks along grain boundaries. The smooth feature running vertically in Figure 7.9.5 is a region along a ferrite Stringer where localized melting occurred during the HAZ #1 thermal cycle.

The tendency for hydrogen to promote intergranular fracture is demonstrated in Figure 7.9.6. HAZ #1 microstructures subjected to a 600°C PWHT and tested in either the charged [condition 21 or uncharged condition are contrasted. Note that the uncharged sample fails by ductile rupture [Fig. 7.9.6a] while the charged sample exhibits a large degree of intergranular failure [Fig. 7.9.6b]. Again. the vertical crack associated with the fracture surface in Figure 7.9.6b is the result of localized melting along stringers during the HAZ #1 thermal cycle.

The effect of the PWHT temperature on the fracture mode was relatively subtle at the lowest charging levels [Conditions 1 and 2]. The fracture morphology of HAZ #2 samples given a PWHT at either 600 or 750°Cand charged to the same level [Condition 2] are contrasted in Figure 7.9.7. Both fractures occur primarily by quasi-cleavage, although some intergranular fracture is evident on the 600°C PWHT Surface. Secondary cracking along prior austenite grain boundaries is more pronounced in the 750°C sample. Typically, the secondary cracking along grain boundaries is more prevalent in HT 9 tensile samples [either charged or uncharged] which exhibit reasonable ductility. As the ductility decreases, the overall fracture tends to be flatter and the secondary cracking is suppressed. The large difference in RA ductility between the 600 and 750°C samples in Figure 7.9.7 [5.6 and 41.8 %, respectively] corroborates this hypothesis.

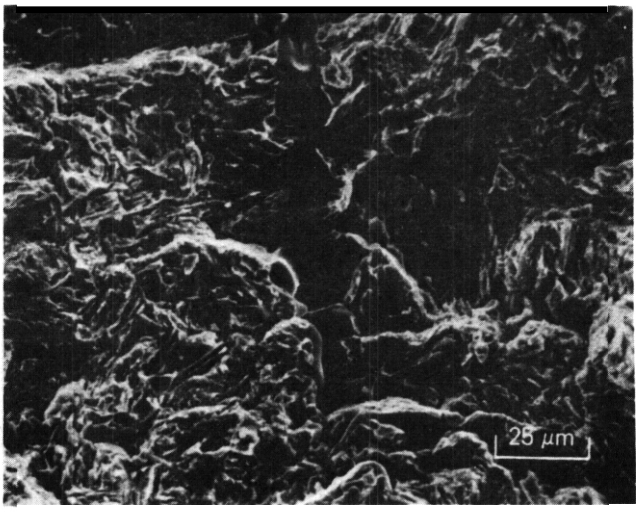

Figure 7.9.5. Fracture surface of HAZ #1/PWHT 750° C sample charged at Condition 2. Arrows indicate melted region along ferrite stringer.

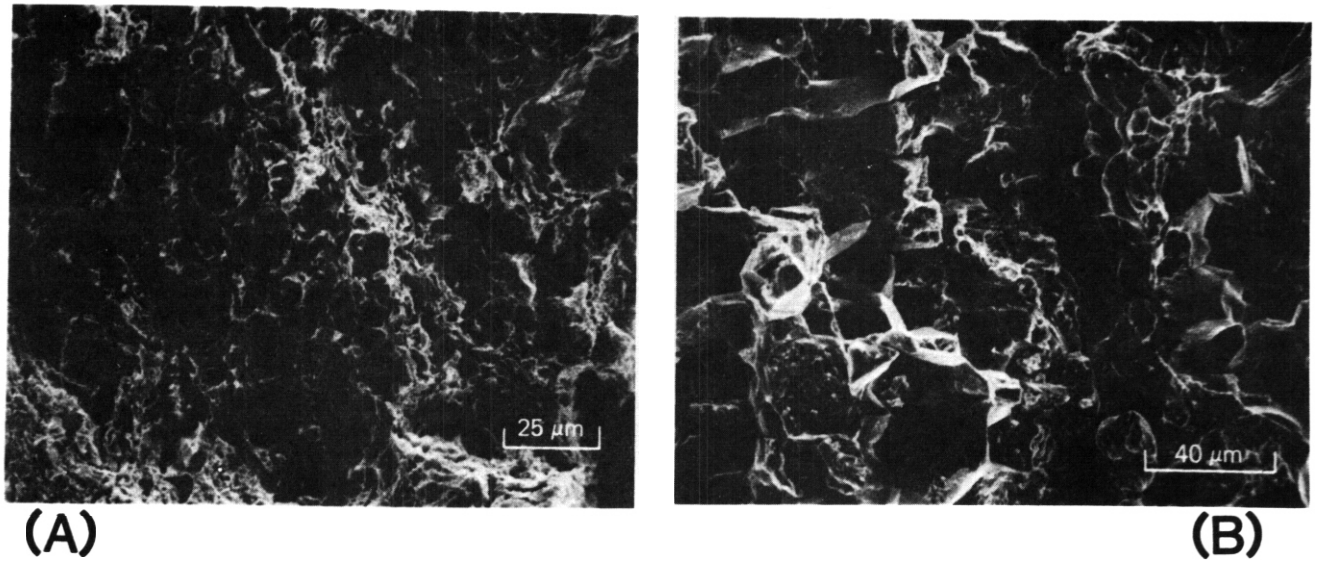

Figure 7.9.6. The effect of hydrogen charging on the fracture mode of the HAZ #1 microstructure which has been subjected to a 600° C PWHT. A. uncharged; B, charged to Condition 2.

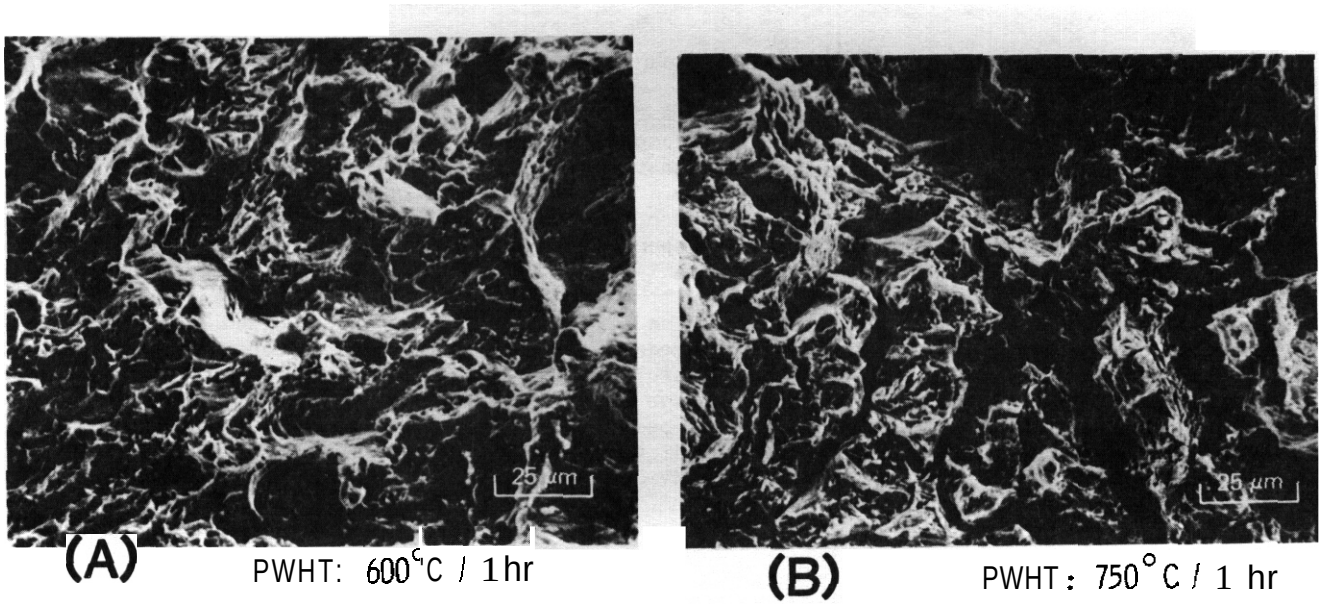

Figure 1.9.7. The effect of PWHT on the fracture mode of the HAZ #2 microstructure charged to Condition 2. A. 600° C/ 1 hr: B, 750° C/ 1 hr.

7.9.4.4 Discussion

The first wall of MFE reactors will be subject to a build-up of internal hydrogen over the course of its operating lifetime. The hydrogen results from both direct injection from the plasma and transmutation of alloying elements [n,p reactions]. The actual concentration of hydrogen in the first wall is difficult to calculate, but it is reasonable to expect that the hydrogen [tritium] inventory may be relatively large. The hydrogen concentration in HT 9 after charging at Condition 3 is on the order of 5-10 wppm [12]. Thus, the hydrogen levels which were attained in this and previous investigations [1-4,6,7] are probably in the range of those which will actually be present in the first Wall of fusion reactors. Unfortunately, there are several important differences between the laboratory tests reported here and actual reactor conditions. First, the steady-state first wall temperature will be in the range of 100-400°C; the elevated temperature should reduce the susceptibility to hydrogen-induced ductility loss relative to room temperature behavior [13]. Second, a significant amount of radiation damage occurs during the reactor lifetime. This damage results in the production of internal defects and subsequent hardening of the structure. Thus, radiation damage would be expected to contribute to the susceptibility to hydrogen embrittlement. Finally, the actual thermo-mechanical history of the first wall is difficult to model: it is likely that the simple tensile tests performed in this investigation are not truly representative of the conditions which will be experienced in service.

Effect of HAZ Microstructure

The two HAZ microstructures which were evaluated in this investigation were selected due to their potential susceptibility to hydrogen embrittlement relative to the other HAZ regions [10,11]. The HAZ #1 microstructure contains a two-phase mixture of delta ferrite and untempered martensite after welding. The tempering time is sufficiently short to prevent transformation of the ferrite. although significant carbide precipitation occurs along the ferrite-martensite interface due to the enrichment of chromium and molybdenum in the ferrite. The HAZ #2 microstructure exhibited the highest hardness in the HAZ of HT 9 and contained the coarsest prior austenite. Garrison and Hyzak [6] have shown that the susceptibility to hydrogen-induced ductility loss in Q/T base material is related to the grain size: as the prior austenite grain size increases the ductility decreases and the tendency for intergranular fracture increases.

Despite the difference in microstructure. the simulated HAZ tensile Samples showed little variation in hydrogen-charged ductility at equivalent PWHT temperatures. When the microstructures were subjected to a 750°C PWHT. for example, there is essentially no difference in their tensile behavior [Fig. 7.9.3a], particularly at the lowest charging levels [Conditions 1 and 21. After a 600°C PWHT the relative difference between the two microstructures is greater [Fig. 7.9.3b]. This differential may be due in part to the variation in carbide precipitation kinetics at 600°C or to the difference in prior austenite grain size. The formation of delta ferrite along austenite grain boundaries at high temperatures in the HAZ #1 region tends to pin these boundaries, thus resulting in a finer grain size than that of the lower temperature HAZ #2 microstructure.

Effect of PWHT

The PWHT temperature exerts the greatest influence on the hydrogen-charged tensile ductility of the HAZ in HT 9 weldments. A PWHT at 600° C is not sufficient to restore the HAZ ductility to the level of the surrounding Q/T microstructure [Fig. 7.9.3a]. At this PWHT temperature the microstructure is much harder istrongerl than the Q/T base material due to the incomplete tempering of the martensite. The resultant fracture occurs either by quasi-cleavage along martensite lath boundaries at the low charging levels or by an intergranular mode at higher charging levels [Fig. 7.9.6b].

After a PWHT at 750°C the mechanical properties of the HAZ approach those of the Q/T base material. At this temperature the hardness of the martensite approachs that of the base material [Table 7.9.31. The resultant hydrogen-induced ductility loss is comparable to that of the Q/T microstructure. The fracture behavior also mirrors the base material; at the lowest charging levels failure is by a mixed quasi-cleavage/ductile rupture mode. At the highest charging level, failure occurs by a mixed cleavage/intergranular mode. The shift to the intergranular mode at the higher hydrogen concentrations has been associated with both the extent of grain boundary carbide coverage and the degree of impurity segregation to these boundaries [3,4,7]. With the exception of the delta ferrite in the HAZ #1 microstructure. both HAZ regions resemble Q/T microstructures which have been austenitized at a high temperature. Since the 750° C PWHT is essentially the same as the base metal tempering temperature, it is not surprising that the hydrogen-charged tensile ductility and fracture behavior of the HAZ and Q/T base metal are similar.

7.9.5 Conclusions

1. Hydrogen-induced tensile ductility losses in the HAZ of HT 9 weldments after a PWHT at 750°C are equivalent to those exhibited by the Q/T base material [AOD].

2. A PWHT at 600° C results in hydrogen-charged tensile ductilities which are significantly less than those of the Q/T base material at comparable hydrogen concentrations.

3. The variation in microstructure within the HAZ had Only a small effect on the Susceptibility to hydrogen embrittlement for a given PWHT.

4. At the highest hydrogen charging levels, HAZ tensile samples subjected to a 750° C PWHT failed by a mixed quasi-cleavage/intergranular fracture mode. At the lowest charging levels failure occurred in a cleavage/ductile rupture mode.

5. After a 600°C PWHT. HAZ tensile samples exhibited varying degrees of intergranular failure at the lowest hydrogen charging levels.

7.9.6. References

1. J.M. Hyzak and W.M. Garrison, "The Effect of Hydrogen Charging on the Tensile Properties of HT 9 Base Metal". ADIP Progress Report DOE/ER-0045-7, Sept. 1981, pp. 186-203.

2. J.M. Hyzak and W.M. Garrison, "Hydrogen Embrittlement of ESR Processed 12Cr-1Mo Steel", ADIP Progress Report DOE/ER-0045-8, March 1982. pp. 401-413.

3. J.M. Hyzak and W.M. Garrison, "The Effect of Internal Hydrogen on the Tensile Behavior of a 12Cr-1Mo-0.3V Steel", Topical Conference on Ferritic Alloys for Use in Nuclear Energy Technologies. June 1983, Snowbird. Utah. TMS/AIME, in press.

4. W.M. Garrison and J.M. Hyzak. "The Influence of Prior Cold Work on the Hydrogen Charged Tensile Fracture of a 12Cr-1Mo Steel", ADIP Progress Report DOE/ER-0045-10, March 1983. pp. 147-154.

5. T.A. Lechtenberg, "The Procurement and Characterization of the ESR National Fusion Program Heat of 12Cr-1Mo Steel", ADIP Progress Report DOE/ER-0045-8, March 1982. pp. 363-369.

6. W.M. Garrison and J.M. Hyzak, "The Influence of Step Austenitizing Treatment on the Toughness and Tensile Ductility of Hydrogen Charged HT 9". ADIP Progress Report DOE/ER-0045-12, March 1984. this report.

7. J.M. Hyzak and W.M. Garrison, "Grain Boundary Segregation and Embrittlement in a 12Cr-1Mo Steel Resulting from Cooling Rate Variations", ADI? Progress Report DOE/ER-0045-11, Sept. 1983, pp. 148-151.

5. J.C. Lippold, "Weldability of HT 9: The Autogenous CTA Process", ADI? Progress Report DOE/ER-0045-2, July 1980, pp. 98-108.

9. J.C. Lippold, "Transformation and Tempering Behavior of HT 9 Weldments", Proc. of the Second Topical Conference on Fusion Reactor Materials, August 1981, Seattle, WA. pp. 1127-1133.

10. J.C. Lippold, "The Effect of Postweld Heat Treatment on the Toughness of the Heat-Affected Zone in a 12Cr-1Mo-0.3V Martensitic Stainless Steel", ADIP Progress Report DOE/ER-0045-8, March 1982. pp. 388-398.

11. J.C. Lippold, "The Toughness of Simulated Heat-Affected Zone Microstructures in a 12Cr-1Mo-0.3V Martensitic Stainless steel", ADIP Progress Report DOE/ER-0045-8, March 1982, pp. 371-387.

12. J.M. Hyzak, unpublished research performed at Sandia National Laboratories, Livermore, 1983.

13. J.M. Hyzak and R.E. Stoltz. "Hydrogen Compatibility of HT 9 Martensitic Stainless Steel", Proc. of the Second Topical Conference on Fusion Reactor Materials. ANS/ASM, Seattle, WA, August 1981. pp. 877-881.

7.10 THE DEVELOPMENT OF FERRITIC STEELS FOR FAST INDUCED-RADIOACTIVITY DECAY — R. L. Klueh and J. M. Vitek (Oak Ridge National Laboratory)

7.10.1 ADIP Tasks

ADIP Tasks I.A.5, Perform Fabrication Analysis, and I.C.l, Microstructural Stability.

7.10.2 Objective

During the operation of a fusion reactor, the structural material of the first wall and blanket structure will become highly radioactive from activation by the high-energy fusion neutrons. A difficult radioactive waste problem will be involved in the disposal of this material after the service lifetime is complete. One way to minimize the disposal problem is the use of structural materials in which the induced radioactive isotopes decay rather quickly to levels that allow for simplified disposal techniques. We are exploring the development of ferritic steels to meet this objective.

7.10.3 Summary

In the 2 1/4 Cr-1 Mo, 9 Cr-1 MoVNb, and 12 Cr-1 MoVW steels currently of interest as structural materials for fusion reactors, the molybdenum will form long-lived isotopes that will make such alloys difficult to dispose of after reactor operation. As an alloying element, tungsten is often similar to molybdenum. To determine if tungsten can replace molybdenum in the ferritic steels of interest, eight 18-kg heats of chromium-tungsten steels have been prepared and are being investigated.

7.10.4 Progress and Status

The safety and environmental concerns that result from the radioactivity induced in the first wall and blanket structure during operation of fusion reactors were previously discussed.' This problem can he minimized by the use of structural materials that form radioactive isotopes that rapidly decay to levels that allow for simplified waste-disposal procedures. For a steel to have "fast" induced-radioactivity decay (FIRD) characteristics, the Mo, Nb, Ni, N, and Cu must be minimized.[2]

The chromium-molybdenum steels are currently the ferritic steels of most interest for fusion reactor applications. These include 2 1/4 Cr-1 Mo, 9 Cr-1 MoVNb, and 12 Cr-1 MoVW steels. Because of the molybdenum in all three steels and the niobium in the 9 Cr-1 MoVNb steel, they are non-FIRD alloys. In the previous report, tungsten was proposed as a substitute for molybdenum and tantalum as a substitute for niobium.' A series of experimental steels was proposed to examine such elemental substitutions (Table 7.10.1). The compositions for this series of steels were based on variations of the three steels currently of interest in the fusion reactor materials program. The compositions were also chosen to develop information on the effect of Cr, W, and V on the properties of this class of steels. Studies of the unirradiated and irradiated properties of these alloys should also prove useful in understanding the chromium-molybdenum steels.

Eight heats of Cr-W, Cr-V, and Cr-W-V steels similar to those given in Table 7.10.1 were prepared by Combustion Engineering, Inc., Chattanooga, Tennessee. The only difference from Table 7.10.1 is that no 2 1/4 Cr-0.5 V steel was melted. It was replaced by a 9 Cr-2 W-0.25 V-0.07 Ta steel. The melt compositions are given in Table 7.10.2. In addition to the nominal Cr, V, W, C, and Ta given in Table 7.10.1, the concentrations of other elements such as Mn, P, Si, etc., were adjusted to levels typical of commercial practice (Table 7.10.2).

All the heats were prepared as air-melted heats, which were then electroslag remelted (ESR) to obtain about 18 kg of usable material. The ESR ingot was hot rolled to 15.9- and 3.2-mm-thick plates. The 15.9-mm plate will be heat treated and used for making standard Charpy V-notch specimens to determine the impact behavior of these materials. The 3.2-mm plate is to be further rolled into 0.25- and 0.76-mm sheet for transmission electron microscopy (TEM) and tensile specimen fabrication, respectively.

Table 7.10.1. Possible ferritic steels for Fast Induced-Radioactivity Decay alloy development program

Alloy	Chemical composition[a] (wt %)			
	Cr	V	W	C
2 1/4 Cr-1/4 V	2–2.5	0.25		0.1–0.15
2 1/4 Cr-1/2 V[b]	2–2.5	0.5		0.1–0.15
2 1/4 Cr-2 W	2–2.5		2	0.1–0.15
2 1/4 Cr-1 W-1/4 V	2–2.5	0.25	1	0.1–0.15
2 1/4 Cr-2 W-1/4 V	2–2.5	0.25	2	0.1–0.15
5 Cr-2 W-1/4 V	5	0.25	2	0.1–0.15
9 Cr-2 W-1/4 C[c]	9	0.25	2	0.1–0.15
12 Cr-2 W-1/4 C	12	0.2	2	0.1–0.15

[a]Balance iron.

'Alloys with 0.08 and 0.154, C should be tested.

[c]An alloy with 0.12% Ta should be considered to-complete the analogy with 9 Cr-1 MoVNb steel.

7.10.5 Future Work

To determine the tempering characteristics of these new steels, pieces of the 15.9-mm plate from each heat were normalized and are being tempered for 2 h at 600, 650, 700, 750, and 780°C. After the tempering treatments, hardness measurements will be

Table 7.10.2. Composition of Fast Induced-Radioactivity Decay ferritic steels

Element	Chemical composition[a] (wt %)							
	2 1/4 Cr-1/4 V, heat 3785	2 1/4 Cr-1 W-1/4 V, heat 3786	2 1/4 Cr-2 W, heat 3787	2 1/4 Cr-2 W-1/4 V, heat 3788	5 Cr-2 W-1/4 V, heat 3789	9 Cr-2 W-1/4 V, heat 3790	9 Cr-2 W-1/4 V-Ta, heat 3791	12 Cr-2 W-1/4 V, heat 3792
C	0.11	0.10	0.11	0.11	0.13	0.12	0.10	0.10
Mn	0.40	0.34	0.39	0.42	0.47	0.51	0.43	0.46
P	0.015	0.015	0.016	0.016	0.015	0.014	0.015	0.014
S	0.006	0.006	0.005	0.006	0.005	0.005	0.005	0.005
Si	0.17	0.13	0.15	0.20	0.25	0.25	0.23	0.24
Ni	0.01	0.01	<0.01	<0.01				
Cr	2.36	2.30	2.48	2.42	5.00	8.73	8.72	11.49
Mo	0.01	<0.01	<0.01					
V	0.25	0.25	0.009	0.24	0.25	0.24	0.23	0.23
Nb	<0.01	<0.01	<0.01					
Ta	<0.01	<0.01	<0.01				0.075	
Ti	<0.01	<0.01	<0.01					
Co	0.005	0.006	0.008					
cu	0.02	0.025	0.03					
A1	0.02	0.02	0.02	0.021	0.03	0.03	0.03	0.028
B	<0.001	<0.001	0.001					
W		0.93	1.99	1.98	2.07	2.09	2.09	2.12

[a]Balance iron.

obtained and selected specimens will be examined by optical metallography. Once the 0.25-mm sheet is obtained, TEM disks will be punched and heat treated. Disks from each of the heats will be included in the FFTF fusion experiment in the Materials Open Test Assembly (MOTA) in June 1984. Tensile specimens will also be obtained. Unirradiated tensile and impact properties will be obtained to determine the effect of the Cr, W, V, and Ta and to determine a suitable heat treatment for each steel.

7.10.4.4. References

1. R. L. Klueh and E. E. Rloom, "Alloy Development for Fast Induced-Radioactivity Decay for Fusion Reactor Applications," pp. 11–20 in *ADI? Semiannu. Prog. Rep. Sept. 20, 1983*, DOE/ER/0045/1, U.S. DOE, Office of Fusion Energy.
2. R. W. Conn et al., *Panel Report on Low Activation Materials for Fusion Applications*, UCLA Report PPG-728, University of California at Los Angeles, June 1983.

8. STATUS OF IRRADIATION EXPERIMENTS AND MATERIALS INVENTORY

8.1 IRRADIATION EXPERIMENT STATUS AND SCHEDULE — M. L. Grossbeck (Oak Ridge National Laboratory)

A large number of planned, in-progress, and completed reactor irradiation experiments support the ADIP program. Table 8.1.1 summarizes the parameters that describe completed experiments. Experiments that have been removed from the reactor only recently, are currently undergoing irradiation, or are planned for future irradiation are included in the schedule bar charts of Table 8.1.2.

Experiments were under way during the reporting period in the Oak Ridge Research Reactor (ORR) and the High Flux Isotope Reactor (HFIR), which are mixed-spectrum reactors, and in the Fast Flux Test Facility (FFTF), which is a fast reactor.

During this reporting period the HFIR reflector change was successfully completed on schedule. The irradiation of HFIR-CTR-47 and -48 was interrupted but continued on schedule upon startup on January 4, 1984. Three HFIR capsules began irradiation, all of which were part of international cooperative programs. The experiment HFIR-CTR-52 contained fatigue specimens from the European Community (EC). This was part of a joint program conducted under Annex II of the IEA Implementing Agreement on Fusion Energy. The experiments HFIR-JP-I and -2 were the first irradiation experiments conducted under a joint program between the U.S. and Japan. The experiments in the first phase of this program are shown in Table 8.1.2. A fusion irradiation experiment in the FFTF Materials Open Test Assembly (MOTA) facility also began irradiation during this reporting period. Emphasis in this experiment has been placed on vanadium alloys, but path A and E alloys are also included. Controls for the ORR-MFE-4 experiment and low activation alloys are among those included.

The spectral tailoring experiment, ORR-MFE-4 was due to be examined in FY 84 at 10 dpa, but it was decided to postpone examination until early in FY 86 at a damage level of 15 dpa. This will permit comparison with the FFTF experiment.

Table 8.1.1. Descriptive parameters for completed ADIP program fission reactor irradiation experiments

Experiment	Major objective	Alloy	Temperature (°C)	Displacement damage (dpa)	Helium (at. ppm)	Duration (months)	Date completed
			Experiments in ORR				
ORR-MFE-1	Scope the effects of composition and microstructure on tensile, fatigue, and irradiation creep	Paths A, R, C	250–600	2	≤10	4	6/78
ORR-MFE-2	Scope the effects of composition and microstructure on tensile, fatigue, and irradiation creep	Paths A, B, C	300–600	6	≤60	15	4/80
ORR-MFE-5	In-reactor fatigue crack growth	Path A	325–460	1	<10	2	2/81
			Experiments in EBR-II				
Subassembly X-264	Effect of preinjected helium on microstructure, tensile prnperties, and irradiation creep	316, PE-16, V–20% Ti, V–15% Cr–5% Ti, Nb–1% Zr	500–825	8	2–200	4	1/77
AA-X Subassembly X-287	Effect of preinjected helium on microstructure, tensile properties, and irradiation creep	316, PE-16, V–20% Ti, V–15% Cr–5% Ti, Nb–1% Zr	400–700	20	2–200	23	12/78
Subassembly X-217D	Stress relaxation	Titanium alloys	450	2		1	1/78
Pins B285, B286, and B284	Swelling, fatigue crack growth, and tensile properties	Titanium alloys	370–550	25		14	9/79
			Experiments in HFIR				
HFIR-CTR-3	Swelling and tensile properties	PE-16, Inconel 600	300–700	4.39	350–1800	3	2/75
HFIR-CTR-4	Swelling and tensile properties	PE-16	300–700	2.2–4.5	100–350	2	3/77

Table 8.1.1. (Continued)

Experiment	Major objective	Alloy	Temperature (°C)	Displacement damage (dpa)	Helium (at. ppm)	Duration (months)	Date completed
HFIR-CTR-5	Swelling and tensile properties	PE-16, Inconel 600	300–700	4.3–9	350–1800	3	4/75
HFIR-CTR-6	Swelling and tensile properties	PE-16, Inconel 600	300-700	4.3–9	350-1800	3	4/75
HFIR-CTR-7	Swelling and tensile properties	PE-16	300-700	9–18	1250–3000	7	8/77
HFIR-CTR-8	Swelling and tensile properties	PE-16	300–700	9–18	1250-3000	7	8/77
HFIR-CTR-9	Swelling and tensile properties	316, 316 + Ti	280–680	10–16	400–1000	6	5/77
HFIR-CTR-10	Swelling and tensile properties	316, 316 t Ti	280–680	10–16	400-1000	6	5/77
HFIR-CTR-11	Swelling and tensile properties	316, 316 + Ti	280–680	10–16	400-1000	6	5/77
HFIR-CTR-12	Swelling and tensile properties	316, 316 + Ti	280–680	7–10	200–500	4	2/77
HFIR-CTR-13	Swelling and tensile properties	316, 316 + Ti	280–680	7–10	200-500	4	2/77
HFIR-CTR-14	Fatigue	316	430	9–15	400–1000	7	17/77
HFIR-CTR-15	Fatigue	316	550	6–9	200–400	4	10/78
HFIR-CTR-16	Weld characterization, swelling, and tensile properties	316, PE-16, Inconel 600	55	6-9	150–2700	4	8/77
HFIR-CTR-17	Weld characterization	316	280–620	7–13	180–460	5.5	10/77
HFIR-CTR-18	Swelling and tensile properties	316, PE-16	280–700	17–27	1600-5600	12	6/78
HFIR-CTR-19	Weld characterization	316	280–620	7–10	200–500	4	12/77
HFIR-CTR-20	Fatigue	316	430	6–9	200–400	4	1/78
HFIR-CTR-21	Fatigue	316	550	9–15	400-1000	7	7/78
HFIR-CTR-22	Fatigue	316	430	6–9	200–400	4	3/78
HFIR-CTR-23	Fatigue	PE-16	430	69	370-1000	3.5	7/79
HFIR-CTR-24	Temperature calibration and tensile properties	316	300–620	2.2	30	1	12/78
HFIR-CTR-26	Swelling and tensile properties	316	284–620	30	1900	10	4/80
HFIR-CTR-27	Swelling and tensile properties	316	284–620	56	3500	18	1/81
HFIR-CTR-28	Swelling and tensile properties	316	370-560	30	1900	10	17/80

Table 8.1.1. (Continued)

Experiinent	Major objective	Alloy	Temperature (°C)	Displacement damage (dpa)	Helium (at. ppm)	Duration (months)	Date completed
HFIR-CTR-29	Swelling and tensile properties	316	370–560	56	3500	18	8/81
HFIR-CTR-30	Swelling, microstructure, and ductility	Paths A, B, C, D, E	300–600	40	≤15,000	14	11/8/81
HFIR-CTR-31	Swelling, microstructure, and ductility	Paths A, 8, C, 0, E	300–600	20	≤7500	8	5/28/81
HFIR-CTR-32	Swelling, microstructure, and ductility	Paths A, 8, C, D, E	300–600	10	≤3000	4	12/81
HFIR-CTR-33	Swelling, tensile properties, weld characterization	Paths A and E	55	10	≤510	4	10/80
HFIR-CTR-34	Charpy	Path E	300, 400	10	0–75	4	5/82
HFIR-CTR-35	Charpy	Path E	300, 400	10	0–75	4	5/82
HFIR-CTR-39	Swelling and tensile	Path E	300–500	12	0–90	5	10/82
HFIR-CTR-40	Swelling and tensile	Path E	300–500	12	0–90	5	12/82
HFIR-CTR-41	Swelling and tensile	Path E	300–500	12	0–90	5	1/83
HFIR-MFE-RB1	Swelling, microstructure, crack growth, fracture toughness, Charpy, tensile, and fatigue	Path E	55	10	90	8	7/82
HFIR-MFE-RB2	Swelling, microstructure, crack growth, fracture toughness, Charpy, tensile, and fatigue	Path E	55	20	200	17	7/83
HFIR-MFE-T1	Swelling, tensile fatigue	Path E	55	30	≤300	12	8/10/82
HFIR-MFE-T2	Swelling, tensile fatigue	Path E	55	9	≤75	3	5/3/81
HFIR-MFE-T3	Impact properties	Path E	55	10	<85	4	12/24/81

Table 8.1.2. Objectives and schedule for current and planned ADIP program reactor irradiation experiments

Experiment designation	Major objective
A. Oak Ridge Research Reactor	
ORR-MFE-4	Effect of irradiation on tensile, fatigue, and irradiation creep of path A PCA (Prime Candidate Alloy) and path B base research alloys. Spectral tailoring to maintain correct He/dpa ratio. Irradiation on continuing basis. 330–600°C (1)
ORR-MFE-6J	Swelling, tensile, irradiation creep fatigue, crack growth, and microstructure of Path A alloys. 60 and 200°C. Evaluated at 10 to 15 dpa intervals. Employs spectral tailoring to achieve fusion He:dpa valve.
ORR-MFE-75	Similar to ORR-MFE-6J but 300 and 400°C.
B. Experimental Breeder Reactor (EBR-II)	
Experiment plan depends on alloy availability. EBR-II space not yet identified.	Effect of irradiation on swelling, tensile, fatigue, and crack growth properties of V and Nb scoping alloys. 370, 450, 550, and 650°C. Position in reactor not finalized, therefore no fluence estimate. (3)

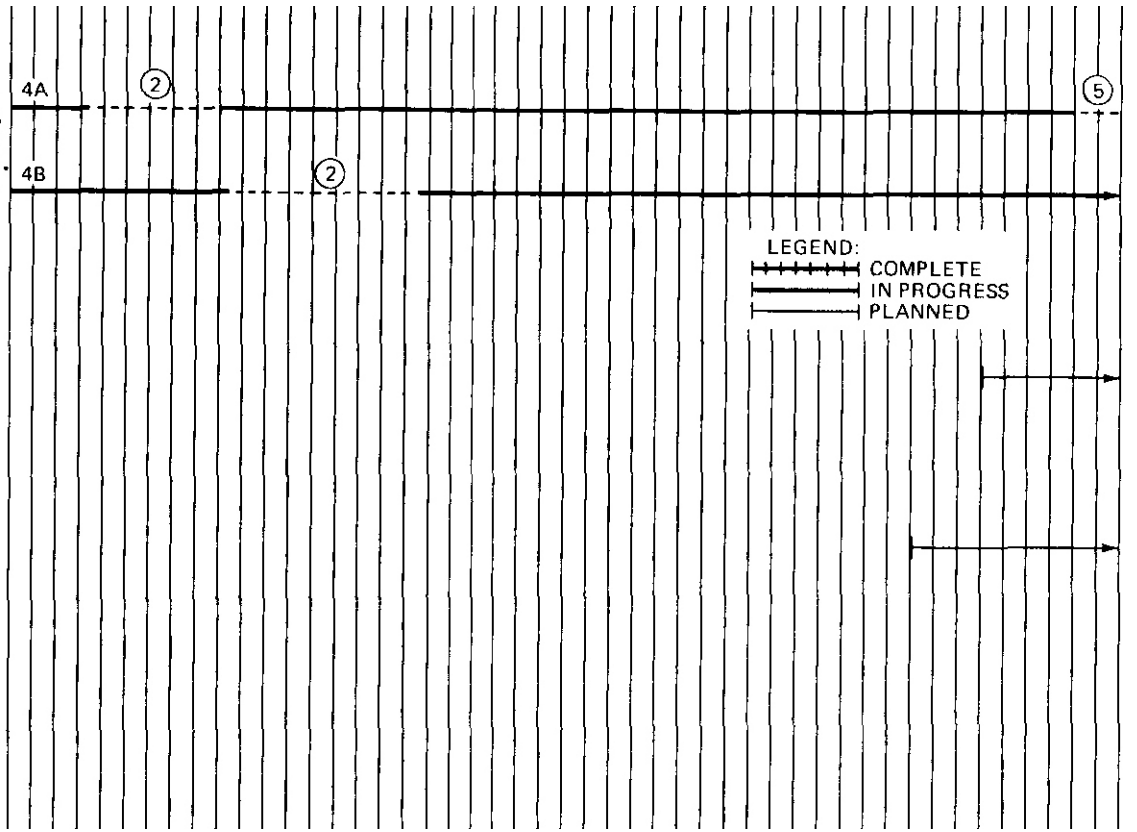

(1) MFE-4A operates at 330 and 400°C. MFE-4B will operate at 60 and 600 C

(2) Removed from reactor for reencapsulation.

(3) Delayed for undetermined period.

(4) Interim examination. Experiment out of reactor. Reencapsulated in subassembly X-344B.

(5) Remove from reactor for 15 dpa specimen discharge.

(6) Remove for specimen discharge.

(7) HFIR shut down for reflector replacement

(8) The HFIR-JP experiment series is a joint program shared by the U.S. and Japan Fusion Reactor Materials activities.

Table 8.1.2. (Continued)

Experiment designation	Major objective
AD-2 (6 pins in separate subassemblies of row 4)	To supplement present EBR-II data on ferritic alloys with data on crack growth, fatigue, and fatigue toughness. Temperature 390, 450, 500, and 550°C. 15 and 30 dpa.
C. Fast Flux Test Facility (FFTF)	
FFTF MOTA Fusion Experiment	Microstructural and mechanical properties of Path A, C, and E alloys.
D. High Flux Isotope Reactor (HFIR)	
HFIR-CTR-36	Fatigue properties of path A alloys. 30 dpa, 2000 ppm He.
HFIR-CTR-42	Swelling, tensile properties of path A alloys. 20 dpa, 1100 ppm He, 300 to 600°C.
HFIR-CTR-43	Swelling, tensile properties of path A alloys. 20 dpa, 1100 ppm He, 300 to 600°C.
HFIR-CTR-44	Swelling, tensile properties of path A alloys. 10 dpa, 500 ppm He, 250 to 400°C. Joint experiment of U.S., European Community, and Japan.
HFIR-CTR-45	Similar to HFIR-CTR-44.
HFIR-CTR-46	Impact properties of path E alloys. 10 dpa, 75 ppm He, 300 and 400°C.

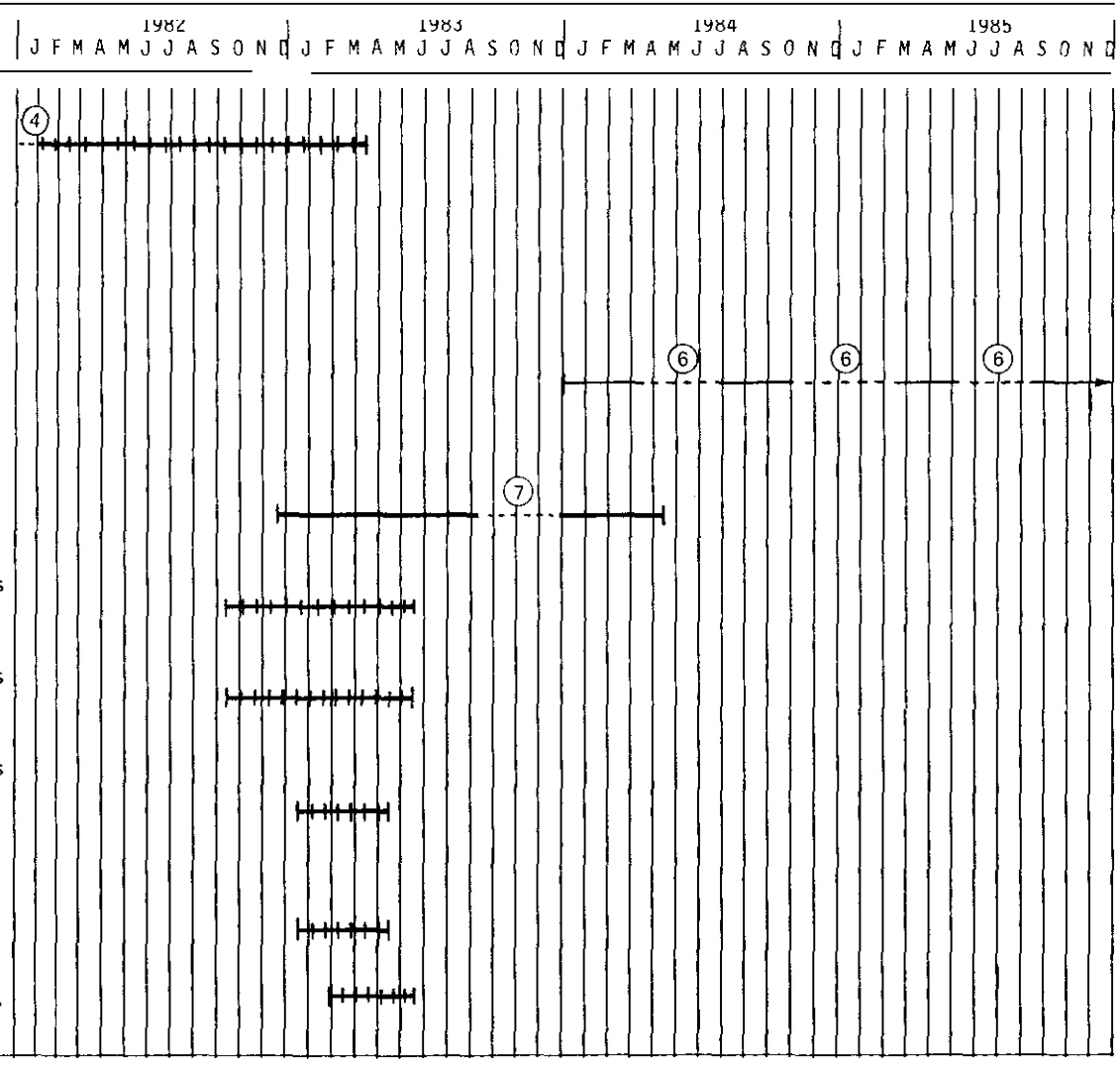

Table 8.1.2. (Continued)

Experiment designation	Major objective
HFIR-CTR-47	Impact properties of path E alloys. 40 dpa, 400 ppm He, 300 and 400°C.
HFIR-CTR-48	Similar to HFIR-CTR-47.
HFIR-CTR-49	Tensile properties and microstructure of path E alloys. 50 dpa, 70 to 500 ppm He, 300 to 500°C.
HFIR-CTR-50	Tensile, swelling, microstructure of path A and E alloys, 100 dpa, 150 to 6000 ppm He, 400, 600°C.
HFIR-CTR-51	Swelling, tensile properties of low-activation alloys. 20 dpa, 300–600°C
HFIR-CTR-52	Fatigue properties of 316 SS 10 dpa, 500 ppm He 430°C. Joint experiment with European community and Japan.

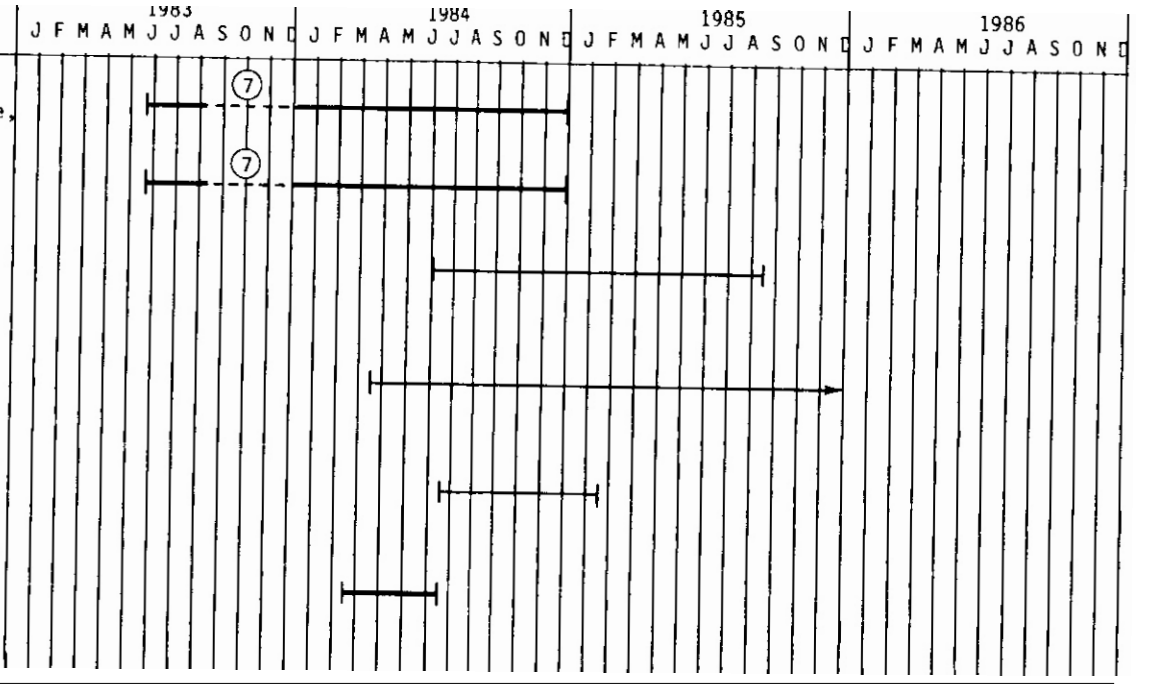

Table 8.1.2. (Continued)

Experiment designation	Major objective
HFIR-JP-1 (8)	Swelling, tensile and fatigue properties, and microstructure of path A alloys. 300–600°C, 30 dpa, 2000 ppm He.
HFIR-JP-2	Similar to HFIR-JP-1 but to 50 dpa, 3500 ppm He.
HFIR-JP-3	Similar to HFIR-JP-1.
HFIR-JP-4	Swelling, tensile properties, and microstructure of path A alloys. 55°C, 50 dpa, 2000 ppm He.
HFIR-JP-5	Similar to HFIR-JP-2.
HFIR-JP-6	Similar to HFIR-JP-1.
HFIR-JP-7	Similar to HFIR-JP-1.
HFIR-JP-8	Similar to HFIR-JP-2.

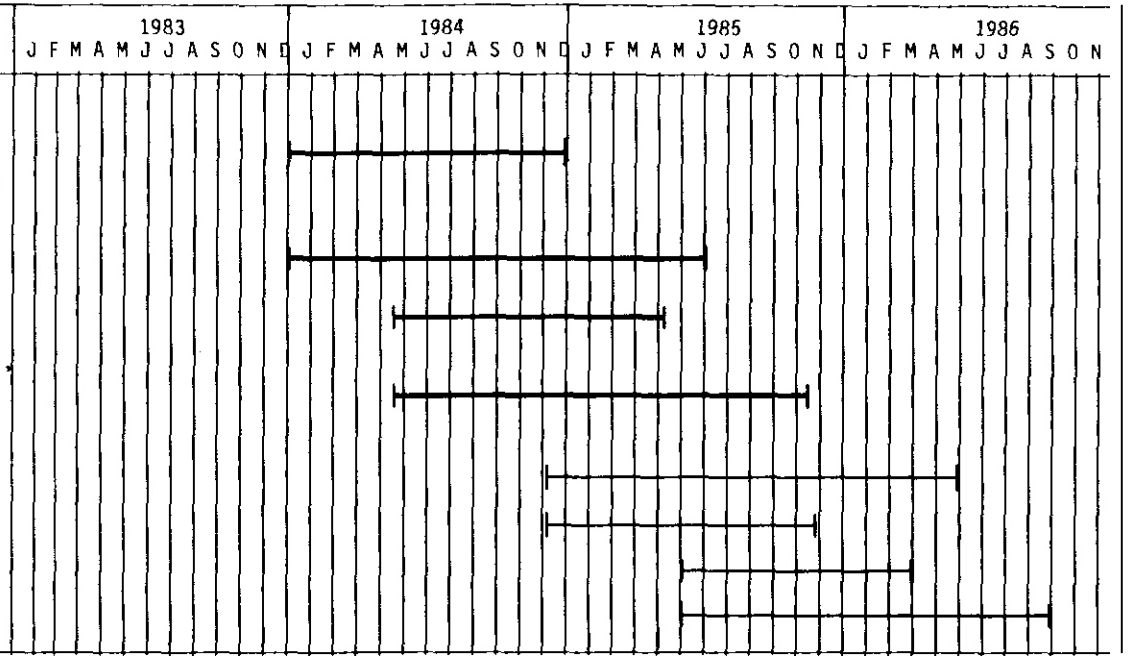

8.2 FUSION PROGRAM RESEARCH MATERIALS INVENTORY — T. K. Roche, F. W. Wiffen (Oak Ridge National Laboratory), J. W. Davis (McDonnell Douglas Company), and T. A. Lechtenberg (GA Technologies)

8.2.1 ADIP Tasks

ADIP Task I.D.l, Materials Stockpile for MFE Programs.

8.2.2 Objective

Oak Ridge National Laboratory maintains a central inventory of research materials to provide a common supply of materials for the Fusion Reactor Materials Program. This will minimize unintended material variations and provide for economy in procurement and for centralized record keeping. Initially this inventory is to focus on materials related to first-wall and structural applications and related research, but various special purpose materials may be added in the future.

The use of materials from this inventory for research that is coordinated with or otherwise related technically to the Fusion Reactor Materials Program of DOE is encouraged.

8.2.3 Materials Requests and Release

Materials requests shall be directed to the Fusion Program Research Materials Inventory at ORNL (Attention: F. W. Wiffen). Materials will be released directly if (a) the material is to be used for programs funded by the Office of Fusion Energy, with goals consistent with the approved Materials Program Plans of the Materials and Radiation Effects Branch and (b) the reouested amount of material is available without compromising other intended uses.

Materials requests that do not satisfy both (a) and (b) will be discussed with the staff of the Reactor Technologies Branch, Office of Fusion Energy, for agreement on action.

8.2.4 Records

Chemistry and materials preparation records are maintained for all inventory material. All materials supplied to program users will be accompanied by summary characterization information.

8.2.5 Summary of Current Inventory and Material Movement During Period October 1, 1983 through March 31, 1984

A condensed, qualitative description of the content of materials in the Fusion Program Research Materials Inventory is given in Table 8.2.1. This table indicates the nominal diameter of rod or thickness of sheet for product forms of each alloy and also indicates by weight the amount of each alloy in larger sizes available for fabrication to produce other product forms as needed by the program. There was no material added to the inventory during this reporting period. Table 8.2.2 gives the materials distributed from the inventory.

Alloy compositions and more detail on the alloys and their procurement and/or fabrication are given in this and earlier ADIP progress reports.

Table 8.2.1 Summary status of materials available in the fusion program research materials inventory

Alloy	Product form			
	Ingot or bar weight (kg)	Rod diameter (mm)	Sheet thickness (mm)	Thin-wall tubing wall thickness (mm)
		Path A alloys		
Type 316 SS	900	16 and 7.2	13 and 7.9	0.25
Path A PCA[b]	490	12	13	0.25
USSR Cr-Mn Steel[c]		10.5	2.6	
NONMAGNE 30[d]		18.5	10	
		Path B alloys		
PE-16	140	16 and 7.1	13 and 1.6	0.25
B-1	180			
B-2	180			
B-3	180			
B-4	180			
B-6	180			

Table 8.2.1 (continued)

Alloy	Product form			
	Ingot or bar[a] weight (kg)	Rod diameter (mm)	Sheet thickness (mm)	Thin-wall tubing, wall thickness (mm)
		Path C alloys		
Ti-64			2.5 and 0.76	
Ti-6242S		63	6.3, 3.2, and 0.76	
Ti-5621S			2.5 and 0.76	
Ti-38644			0.76 and 0.25	
Nb—1% Zr		6.3	2.5, 1.5, and 0.76	
Nb—5% Mo—1% Zr		5.3	2.5, 1.5, and 0.76	
V—20% Ti		6.3	2.5, 1.5, and 0.76	
V—15% Cr—5% Ti		6.3	2.5, 1.5, and 0.76	
VANSTAR-7		6.3	2.5, 1.5, and 0.16	
		Path D alloy		
LRO-37[e]			3.3, 1.6, and 0.8	
		Path E alloys		
HT9 (AOD fusion heat)[f]	3400		28.5, 15.8, 9.5, and 3.1	
HT9 (AOD/ESR fusion heat)	7000	25, 50. and 75	28.5, 15.8, 9.5, and 3.1	
HT9			4.5 and 18	
HT9 + 1%Ni			4.5 and 18	
HT9 + 2% Ni			4.5 and 18	
HT9 + 2% Ni + Cr adjusted			4.5 and 18	
T-9 modified[g]			4.5 and 18	
T-9 modified + 2% Ni			4.5 and 18	
T-9 modified + 2% Ni + Cr adjusted			4.5 and 18	
2 1/4 Cr-1 Mo			[h]	

[a]Greater than 25 mm, minimum dimension.

[b]Prime candidate alloy.

[c]Rod and sheet of a USSR stainless steel supplied under the U.S.-USSR Fusion Reactor Materials Exchange Program.

[d]NONMAGNE 30 is an austenitic steel with base composition Fe-14% Mn—2% Ni—2% Cr. It was supplied to the inventory by the Japanese Atomic Energy Research Institute.

[e]LRO-37 is the ordered alloy $(Fe,Ni)_3(V,Ti)$ with composition Fe-39.49. Ni—22.4% V—0.43% Ti.

[f]Alloy 12 Cr-1 MoVW, with composition equivalent to Sandvik alloy HT9.

[g]T-9 modified is the alloy 9 Cr-1 MoVNb.

[h]Material is thick-wall pipe, rerolled as necessary to produce sheet or rod.

Table 8.2.2. Fusion program research materials inventory disbursements October 1, 1983 through March 31, 1984

Alloy	Heat	Product form	Dimension[a] (mm)	Quantity (m)	Quantity (m^2)	Sent to
Path A alloys — austenitic stainless steels						
316 SS ref. heat	X-15893	Sheet	0.25		0.068	Radiation Effects Group, M&C Division, ORNL
Path A PCA[b]	K-280	Rod	6.91	7.72		Radiation Effects Group, M&C Division, ORNL
	K-280	Sheet	0.25		0.082	Radiation Effects Group, M&C Division, ORNL
Path C alloys — reactive and refractory alloys						
V–20% Ti	CAM 832 Top-5	Rod	6.35	1.04		Argonne National Laboratory
	CAM 833-7	Sheet	0.76		0.013	Argonne National Laboratory
V–15% Cr–5% Ti	CAM 835B-2	Rod	6.35	1.05		Argonne National Laboratory
	CAM 835A-6	Sheet	0.76		0.013	Argonne National Laboratory
	CAM 834-3	Sheet	0.76		0.008	Radiation Effects Group, M&C Division, ORNL
Vanstar-7	CAM 836 Top-4	Rod	6.35	0.98		Argonne National Laboratory
	CAM 836 Bot-3	Sheet	0.76		0.014	Argonne National Laboratory
	CAM 031-7	Sheet	0.84		0.012	Radiation Effects Group, M&C Division, ORNL
Path E alloys — ferritic steels						
2 1/4 Cr-1 Mo	38649	Rod	4.57	1.96		Radiation Effects Group, M&C Division. ORNL
	38649	Sheet	0.25		0.04	Radiation Effects Group, M&C Division, ORNL
T-9 modified[c]	ESR-XA-3590-9	Rod	4.57	1.61		Radiation Effects Group, M&C Division, ORNL
T-9 modified + 2% Ni	ESR-XA-3591-9	Rod	4.57	1.54		Radiation Effects Group, M&C Division, ORNL
HT-9	ESR-XAA-3587-4	Rod	4.57	1.70		Radiation Effects Group, M&C Division, ORNL
HT-9 + 2% Ni	ESR-XAA-3589-9	Rod	4.57	1.82		Radiation Effects Group, M&C Division, ORNL
HT-9	AOD-ESR-9607R2	Rod	4.57	3.35		Radiation Effects Group, M&C Division, ORNL
	AOD-ESR-9607R2	Sheet	0.76		0.037	Radiation Effects Group, M&C Division, ORNL
	AOD-ESR-9607R2	Sheet	0.76		0.006	University of California, Santa Barbara
	AOD-ESR-9607R2	Sheet	0.38		0.12	Radiation Effects Groups, M&C Division, ORNL
	AOD-ESR-9607R2	Sheet	0.25		0.037	Radiation Effects Groups, M&C Division, ORNL
	AOD-ESR-9607R2	Sheet	0.25		0.01	University of California, Santa Barbara
T-9	30176	Sheet	0.76		0.006	University of California, Santa Barbara

[a]Characteristic dimension: thickness for plate and sheet, diameter for rod and tubing.

[b]Prime candidate alloy.

[c]T-9 modified is the alloy 9 Cr-1 MoVNb.

9. MATERIALS COMPATIBILITY AND HYDROGEN PERMEATION STUDIES

9.1 CORROSION OF TYPE 316 STAINLESS STEEL, PATH A PCA, AND 12 Cr-1 MoVW STEEL IN THERMALLY CONVECTIVE LITHIUM — P. F. Tortorelli and J. H. DeVan (Oak Ridge National Laboratory)

9.1.1 ADIP Task

ADIP Task I.A.3, Perform Chemical and Metallurgical Compatibility Analyses.

9.1.2 Objective

The purpose of this task is to determine the corrosion resistance of candidate first-wall materials to slowly flowing lithium in the presence of a temperature gradient. Corrosion and deposition rates are measured as functions of time, temperature, additions to the lithium, and flow conditions. These measurements are combined with chemical and metallographic examinations of specimen surfaces to establish the mechanisms and rate-controlling processes for dissolution and deposition reactions.

9.1.3 Summary

Results from lithium thermal convection loops are (1) microstructural variations of prime candidate alloy (PCA) did not strongly influence weight loss behavior, (2) kinetic analysis of data from six runs with type 316 stainless steel showed phase boundary reaction control for dissolution, and (3) the mass transfer of a 12 Cr-1 MoVW steel in lithium changed significantly when the loop temperatures were raised.

9.1.4 Progress and Status

One lithium type 316 stainless steel thermal convection loop with accessible specimens (of a type described previously[1]) has been used to measure weight losses of path A PCA specimens with different thermomechanical treatments. In the first experiment, coupons of path A PCA alloys A1 and A3 were placed at the 600 and 570°C positions in the thermal convection loop, which had previously circulated lithium for greater than 10,000 h The second experiment, which has just been completed, used specimens of PCA alloys A3 and A3A in these loop positions. While A1 (annealed), A3 (cold worked), and A3A (cold worked, nitride stringers) differed microstructurally, they all had the same composition as seen below.

Element	Content (wt %)	Element	Content (wt %)	Element	Content (wt %)
Ni	15.9	Mn	1.9	Al	0.05
Cr	14.0	Si	0.4	C	0.05
Mo	1.9	Ti	0.3	N	<0.01
Fe	65.0				

Because of prior operation with lithium and associated preferential leaching of nickel and chromium, the hot-leg surfaces of the loop were known to have a considerably higher iron concentration than the as-received PCA alloys. However, the cold leg of the loop had been replaced before operation with the PCA specimens.

The initial results from this second PCA loop experiment were reported in the preceding progress report.[2] There was no difference in weight loss behavior of A3 and A3A for up to 5000 h of exposure, and the total weight losses for the A3 specimens in the first and second experiments were similar. Further data now obtained over about 2000 h of additional exposure confirmed these observations. The A3 and A3A specimens at 600°C showed the same weight loss behavior with time over the entire exposure interval of 6631 h [Fig. 9.1.1(*a*)]. Furthermore, the total cumulative weight loss of the A3 specimen exposed 6696 h at 600°C in the first experiment was 148 g/m^2, the same as that of A3 in the second experiment exposed 6691 h. While the agreement is not as exact as the 600°C data, the weight losses for the A3 and A3A specimens exposed at 570°C were also quite similar to each other [see Fig. 9.1.1(*b*)]. It therefore appears that, despite the known influence of nitrogen on the corrosion of ferrous alloys by lithium,[3] the presence of the nitrides in A3A did not lead to accelerated overall dissolution.

When compared with the baseline type 316 stainless steel data, the weight losses and dissolution rates of PCA-A3 are greater (see Table 9.1.1). However, while the cumulative weight losses of A3 and A3A were less than that of A1 at 600°C, the most recent data indicate no difference in the steady-state dissolution rates of the annealed and cold worked versions of the PCA alloy at 600 and 570°C. (There was some previous evidence that the corrosion rate of A1 was greater.*) It therefore appears that microstructural variations of PCA do not strongly influence weight loss behavior in lithium.

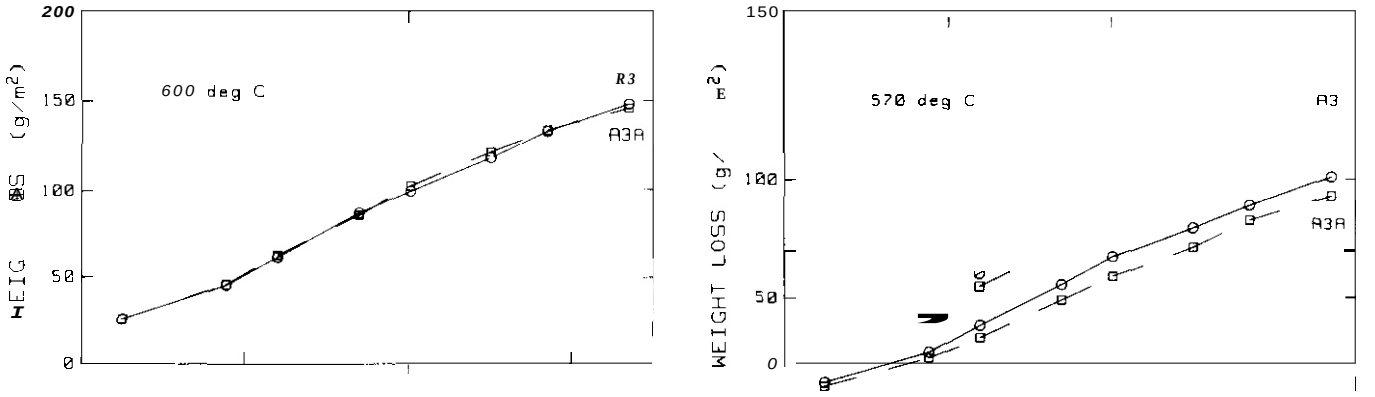

Fig. 9.1.1. Weight loss versus time for cold worked prime candidate alloy in thermally convective lithium. (a) 600°C. (b) 570°C.

Table 9.1.1. Weight losses and steady-state dissolution rates of prime candidate alloy and type 316 stainless steel exoosed to thermallv convective 1ithium

Material	Cumulative weight loss[a] (g/m^2)		Steady-state dissolution rate[b] [$mg/(m^2 \cdot h)$]	
	600°C	570°C	600°C	570°C
Type 316 stainless steel	119	78	13	8
A3[c]	148	97	16	12
A3[d]	148	101	20	14
A3A	145	93	20	13
A1	170	97	21	13

[a]Measured at 7000 ± 10 h.

[b]Obtained from slope of linear portions of weight loss versus time curves.

[c]First experiment

[d]Second experiment

Much of the initial work in the area of liquid metal corrosion involved type 316 stainless steel as a baseline material and model austenitic alloy. Recently, weight change data from a number of thermal convection loop experiments were assessed as a whole for the first time in order to do a more comprehensive kinetic analysis of the mass transfer reactions. Weight loss and gain measurements as a function of time and temperature from six loop runs were considered. Such data are shown in Fig. 9.1.2, and additional results can be found elsewhere.[4] The weight loss data were analyzed by performing a series of curve fits for each specimen in order to arrive at a suitable mathematical form to describe the relationship between the weight losses and time. A power law of the form

$$w_l = at^b, \qquad (1)$$

where w_l is the weight loss, t is time, and a and b are constants derived from the fit, was found to be appropriate when both long- and short-term data were included in each analysis (including w_l = 0 at t = 0). The fitted exponents (b) were found to range between 0.68 and 0.75 for the specimens exposed at 600°C (T_{max}) for various periods of time. However, when only long-term data were included in the analyses (that is, w_l for t > 2100 h), the data correlated equally well with a linear regression (straight line) fit of the form

$$w_l = c + dt \ , \qquad (2)$$

where c and d are constants.

The correlation of the long-term weight losses with a power curve fit was unexpected. A linear time dependence was initially assumed from observation of such weight loss plots such as shown in Fig. 9.1.2 and the prediction of several models (such as that of Brush[5]). Therefore, the assumed attainment of a strict linear time dependence may indeed not be valid for the times involved. However, it should be noted that there is little difference between a linear and $t^{0.7}$ dependence at the exposure times (5000–10,000 h) and system conditions of interest here. Perhaps, in the present experiments, a true steady-state regime was not yet reached because of complex morphological effects influencing the dissolution process. For example, the porosity that develops on austenitic alloys exposed to lithium may inhibit the attainment of steady-state behavior by allowing some preferential leaching to persist. Also, sluggish deposition kinetics may extend the time needed to reach equilibrium dissolution conditions. Finally, while not observed in the present experiments, spallation of parts of the ferrite layer, which has occurred under more aggressive conditions,[6,7] could renew the preferential leaching process and delay true steady-state behavior.

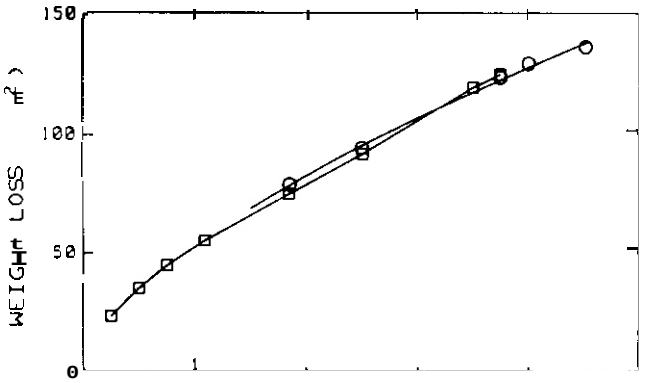

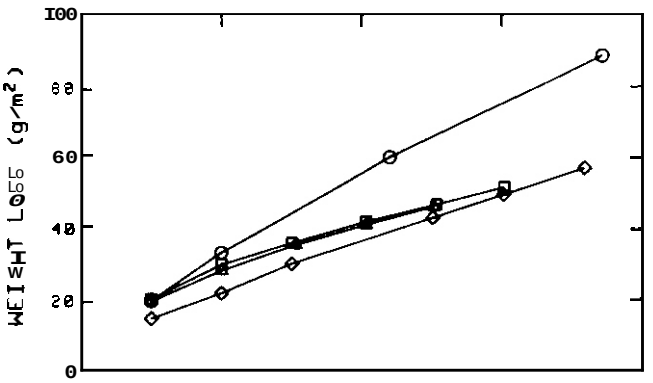

In agreement with the present results, power curve time exponents between 0.5 and 0.7, inclusive, have been observed in other lithium loops[6,8] when entire exposure intervals have been included in the analysis. A 0.7 exponent for a power curve law for the weight loss, as found in this work, can represent a mixed rate control process. A possible example of such would be where the dissolution process consisted of reactions characterized by a $t^{0.5}$ and t (linear) behavior, that is,

$$w_l = ft^{0.5} + gt \quad . \tag{3}$$

If dissolution is then considered as initially dominated by selective leaching and ultimately by steady-state corrosion,[5,9,10] it would be expected that a time dependence of $t^{0.5}$ would dominate at first (as observed by Bauer[8] for t < 500 h), while the linear part would become the principal term at long times. A correlation of Eq. (3) with the relative contributions of preferential leaching and steady-state dissolution would then imply a solid-state diffusion rate-controlling step for the preferential leaching process while rate control for the steady-state or "stoichiometric" dissolution would be elsewhere in the process.

For the sake of simplicity and consistency with other work, a linear time dependence was assumed to hold at longer times in order to calculate steady-state dissolution rates despite the above evidence that, even though a straight line fit is adequate, the present long-term data may not be at equilibrium but just approaching it. When this was done for the long-term loop tests, dissolution rates of type 316 stainless steel at 600°C maximum loop temperature (T_{max}) were found to be 11.2 and 13.3 mg/(m²·h). In a similar manner, the slopes of the lines fitted by linear regression analysis were used to determine the dissolution rates as the maximum temperature of a loop was changed. These rates were then used in an Arrhenius analysis assuming a functional form of

$$dw_l/dt = A \exp(-Q/RT) \quad , \tag{4}$$

where Q is the activation energy for the rate-controlling step of the steady-state dissolution process or the sum of such an activation energy and a heat of solution (as described previously[11]). Such a procedure yielded values of Q that were 196, 188, and 118 kJ/mol (47, 45, and 28 kcal/mol) for the specimens in the three hottest loop positions. Note that the values of Q for the dissolution of the specimens at the two hottest loop positions are essentially the same. If we assume that Q is a combination of an activation energy and a heat of solution (ΔH) and that the relevant ΔH is that for iron in lithium, we can estimate the ΔH to be about 60 kJ/mol (14 kcal/mol) from solubility data.[12] This would then result in a minimum activation energy of about 134 kJ/mol (32 kcal/mol), which is somewhat higher than typical values for liquid phase diffusion (<40 kJ/mol).[13] However, this value is consistent with a phase boundary reaction and with solid-state diffusion as rate-limiting processes. It would therefore appear that, regardless of whether Q is just an activation energy or a sum of two terms, the rate controlling process is a phase boundary reaction since solid-state diffusion can be eliminated by the linear time dependence of steady-state dissolution (see above). The reason for the lower activation energy for the lower temperature specimen is not known, although it may be due to a change in the rate-controlling step in the dissolution process as the temperature is lowered. However, the weight changes at this position were small, particularly when T_{max} was decreased to 500°C (where, over certain intervals, weight gains were measured). The Arrhenius analysis could thus be done only for the two higher temperatures for this specimen and may not be accurate.

While the above analysis may indicate that the rate-controlling step for higher temperature dissolution is a reaction at the solid-liquid interface, the data reported here cannot be used to determine the exact type of such a reaction. However, it is interesting to speculate that just as oxygen affects the steady-state dissolution rate of steel in sodium,[10] nitrogen may play a controlling role in one of the surface reactions in lithium, notwithstanding the relatively low levels of this impurity in the present experiments. Recent work has shown that nitrogen can react with lithium and selected steel components to form stable ternary compounds (Li_9CrN_5) and/or to simply accelerate the dissolution process.[3] Such reactions would also influence the dissolution of ferritic (Fe-Cr-Mo) steels in lithium, and, in this regard, it is interesting that such steels apparently do not show a nonlinear corrosion rate at early times,[6] unlike the nickel-containing steels.

As with the weight loss data, weight gains were found to correlate well with a power law of the form

$$w_g = mt^n \quad , \tag{5}$$

where w_g is the weight gain, t is the exposure time, m is the coefficient obtained from fit, and n is 0.60 to 0.68 depending on the loop run. When only longer term data were considered, both a power curve expression and a linear law were adequate in describing the data. Polley and Skyrme[14] have shown that a linear time dependence can characterize deposition under certain conditions such as laminar boundary layer control. Therefore, again assuming linearity at equilibrium in a similar manner to what was done for dissolution, steady-state deposition rates can be obtained from the slopes of the linear portions of weight gain versus exposure time curves for the long exposure loop runs. These are shown in Table 9.1.2 for specimens at the three coldest loop positions. Note that, in both cases, the maximum steady-state deposition rate is not at the coldest coupon position in the loops. This may be ascribed to the competing influence of parameters that depend on temperature in opposite ways. For example, while the driving force for deposition (that is, the degree of supersaturation of a given element in lithium) increases with decreasing temperature, a thermally activated deposition step would be more sluggish at lower temperature. Such a dependence of deposition on temperature may have significant implications for methods to control deposition in lithium by cold trapping.

Table 9.1.2. Steady-state deposition rates for type 316 stainless steel—lithium thermal convection systems operated at a maximum temperature of 600°C and a temperature differential of 150°C

Specimen set	Deposition rate [mg/(m²·h)]		
	490°C	470°C	450°C
1[a]	3.2	4.3	3.3
2[b]	4.8	5.3	3.7

[a]Exposed for a total of 9034 h

[b]Exposed for a total of 7488 h.

Results from previous reports[2,15] have shown that the corrosion of a 12 Cr-1 MoW steel in thermally convective lithium between 500 and 350°C was not excessive after 10,088 h. The greatest specimen weight loss was at the minimum temperature (T_{min}) position (350°C), corrosion rates were small, and the microstructure was not altered by the corrosion process to any great depth. The reactions were sluggish; most loop specimens did not exhibit much change in weight or surface structure, particularly after the first few thousand hours of exposure. A small amount of mass transfer of chromium and nickel was detected, but, from a consideration of the weight change data, surface analysis, and prior results for austenitic alloys, reactions with carbon and nitrogen were deduced to be the principal corrosion processes. It was therefore thought that at temperatures significantly greater than 500°C, conventional mass transfer may become much more important in nonisothermal 12 Cr-1 MoW steel—lithium systems with a concomitant decrease in the relative contribution of interstitial reactions. Consequently, a loop experiment with a maximum temperature of 600°C and a ΔT of 150°C was started to determine if this is the case. The coupons of this second experiment, which uses the same loop, have recently reached 3605 h of exposure time to lithium and the corresponding weight change results for the specimen at the T_{max} position (600°C) are shown in Fig. 9.1.3, which also contains the data from the T_{max} specimen of the first experiment (500°C). As expected, the 600°C weight loss is greater than

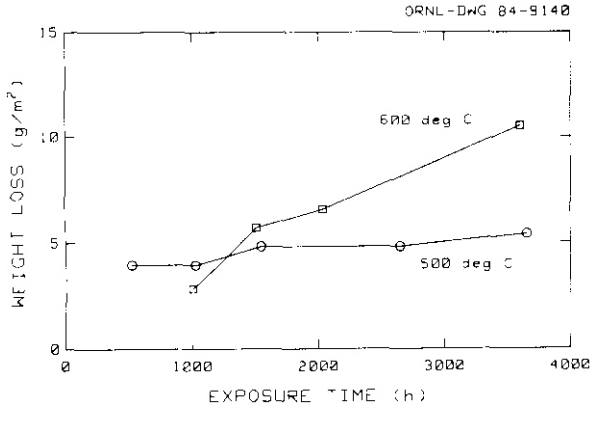

Fig. 9.1.3. Weight loss versus time for 12 Cr-1 MoW steel in thermally convective lithium at maximum loop temperatures of 500 and 600°C.

that measured at a T_{max} of 500°C, and it appears that the dissolution rate (as determined by the slope of the curve) will be greater at the higher temperature. Furthermore, while the coldest (350°C) coupon in the first experiment showed weight losses, the T_{min} specimen in the second experiment (450°C) consistently gained weight (see Fig. 9.1.4) such that a more conventional mass transfer profile was observed by weight change measurements in the T_{max} = 600°C experiment. It is interesting to note, however, that the absolute values of the weight losses at 350°C are greater than the weight gains of the T_{min} specimen of the second experiment and are also greater than the absolute values of the weight losses measured at 600°C (see Fig. 9.1.3). Such observations suggest that the (presumably interstitial) reactions that led to significant corrosion at 350°C are not occurring to the same extent at higher temperatures (>450°C).

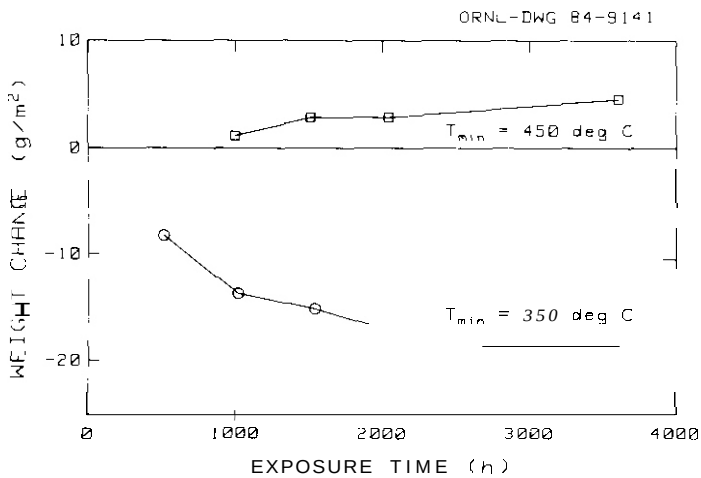

Fig. 9.1.4. Weight change versus time for 12 Cr-1 MoVW steel in thermally convective lithium at minimum loop temperatures of 350 and 450°C (maximum loop temperatures of 500 and 600°C. respectively).

9.1.5 Conclusions

1. Longer-term exposure of cold-worked PCA confirmed that the presence of nitride stringers did not influence the weight loss behavior of this material at 600 and 570°C. Furthermore, very little difference in weight loss behavior was noted between the annealed and cold-worked PCA specimens. The effects of microstructural variations on the dissolution of this alloy in lithium appear minimal.

2. A kinetic analysis of baseline type 316 stainless steel data from six lithium thermal convection loop experiments revealed that dissolution was controlled by a phase boundary reaction. The maximum deposition rate was generally not at the minimum temperature.

3. Initial weight change results from a loop experiment in which 12 Cr-1 MoVW steel is exposed to thermally convective lithium circulating between 600 and 450°C showed substantial changes in the mass transfer profile when compared with data from a lower temperature loop experiment with this alloy. It appeared that raising the system temperature changed the relative contributions of different corrosion reactions such that conventional mass transfer became more important.

9.1.6 References

1. J. H DeVan and J. R. DiStefano, "Thermal-Convection Loop Tests of Type 316 Stainless Steel in Lithium," pp. 200–208 in *ADIP Quart. Prog. Rep. Mar. 31, 1978*, DOE/ET-0058/1, U.S. DOE, Office of Fusion Energy.

2. P. F. Tortorelli and J. H. DeVan, "Corrosion of Path A PCA and 12 Cr-1 MoVW Steel in Thermally Convective Lithium," pp. 197–202 in *ADIP Semiannu. Prog. Rep. Sept. 30, 1583*, DOE/ER-0045/11, U.S. DOE, Office of Fusion Energy.

3. M G Barker et al., "The Interaction of Chromium with Nitrogen Dissolved in Liquid Lithium," *J. Nucl. Mater.* 114, 143–49 (1923).

4. P. F. Tortorelli and J. H. DeVan, "Mass Transfer Kinetics in Lithium-Steel Systems," to be published in *Proc. Third Int. Conf. on Liquid Metal Eng. and Technol. in Energy Production*, British Nuclear Energy Society, April 1984.

5. E. G. Brush, *Sodium Mass Transfer. XVI. The Selective Corrosion Component of Steel Exposed to Flowing Sodium*, GEAP-4232, General Electric, Schenectady, N.Y., March 1965.

6. O. K. Chopra and D. L. Smith, "Environmental Effects on Properties of Structural Alloys," pp. 216–20 in *ADIP Semiannu. Frog. Rep. Sept. 30, 1983*, DOE/ER-0045/11, U.S. DOE, Office of Fusion Energy.

7. P. F. Tortorelli and J. H. DeVan, "Corrosion of an Iron-Base Long-Range-Ordered Alloy in Flowing Lithium," pp. 229–34 in *ADIP Quart. Prog. Rep. Mar. 31, 1981*, DOE/ER-0045/6, U.S. DOE, Office of Fusion Energy.

2. D. G. Bauer, *Kinetics of the Degradation of Type 316 Stainless Steel by Liquid Lithium*, UWFDM-363, University of Wisconsin, Madison, June 1980.

9. J. R. Weeks and ti. S. Isaacs, "Corrosion and Deposition of Steels and Nickel-Base Alloys in Liquid Sodium," *Adu. Corros. Sci. Technol. 3*, 1-66 (1973).

10. B. H. Kolster, "Sodium Corrosion of Asutenitic Stainless Steel," pp. 1524–35 in *Proc. of 7th Int. Conf. on Metallic Corrosion,* Deutche Gesellschaft fur Chemische Apparatewesen e. V., Frankfurt, Federal Republic of Germany, October 1978.

11. P. F. Tortorelli and J. H. DeVan, "Thermal-Gradient Mass Transfer in Lithium-Stainless Steel Systems," *J. Nucl. Mater.* 85&86, 289–93 (1979).

12. H. W. Leavenworth and R. E. Cleary, "The Solubility of Ni, Cr, Fe, Ti, and Mo in Liquid Lithium," *Acta Metall.* 9, 519–20 (1961).

13. L. F. Epstein, "Static and Dynamic Corrosion and Mass Transfer in Liquid Metal Systems," pp. 67–81 in *Liquid Metals Technol., Part I,* Chem. Eng. Prog. Sym. Series, No. 20 vol. 53, American Institute of Chemical Engineers, New York, 1957.

14. M. V. Polley and G. Skyrme, "An Analysis of Radioactive Corrosion Product Transfer in Sodium Loop Systems," *J. Nucl. Mater.* 75, 22637 (1978).

15. P. F. Tortorelli and J. H. DeVan, "Corrosion of Path A PCA, Type 316 Stainless Steel, and 12 Cr-1 MOVW Steel in Flowing Lithium," pp. 186–90 in *ADIP Semiannu. Prog. Rep. Mar. 31, 1983,* DOE/ER-0045/10, U.S. DOE, Office of Fusion Energy.

9.2 ENVIRONMENTAL EFFECTS ON PROPERTIES OF STRUCTURAL ALLOYS IN FLOWING LITHIUM - O. K. Chopra and D. L. Smith (Argonne National Laboratory)

9.2.1 ADIP Task

AOIP Task I.A.3, Perform Chemical and Metallurgical Compatibility Analyses.

9.2.2 Objective

The objective of this program is to investigate the influence of a flowing lithium environment on the corrosion behavior and mechanical properties of structural alloys under conditions of interest for fusion reactors. Corrosion rates are determined by measuring the weight change and depth of internal corrosive penetration as a function of time and temperature. These measurements coupled with metallographic evaluation of the alloy surface are used to establish the mechanism and rate-controlling process for the corrosion reactions. Initial effort on mechanical properties is focused on fatigue and tensile tests in a flowing lithium environment of controlled purity.

9.2.3 Summary

Corrosion data on weight loss and internal penetration are presented for austenitic and ferritic steels exposed for up to 6500 h in flowing lithium at temperatures of 700 and 755 K. A flowing lithium environment has no effect on the tensile properties of the HT-9 alloy at temperatures between 505 and 755 K.

9.2.4 Progress and Status

9.2.4.1 Corrosion Behavior

The effects of a flowing lithium environment on the corrosion behavior of austenitic and ferritic steels are being investigated. Tests are conducted in a forced-circulation lithium loop equipped with a cold-trap purification system. The lithium loop has operated at a maximum temperature of 755 or 700 K (482 or 427°C) and a minimum temperature of 593 K (320°C). The cold-trap temperature is maintained at 498 K (225°C). By hot trapping with Ti or Zr foils (or use of dissolved getters). the nitrogen level in lithium is reduced to <100 wppm, which is considerably below that attainable by cold trapping alone. The concentrations of carbon and hydrogen in lithium are 8 to 12 and -120 wppm, respectively. Flat corrosion coupons -70 x 11 x 0.25-0.4 mm in size, are exposed to flowing lithium and the corrosion behavior is evaluated from measurements of weight loss and depth of internal penetration for specimens exposed for different times.

The corrosion data in flowing lithium at 700 and 755 K indicate that the dissolution rates for austenitic stainless steels reach a steady-state value after an initial period of high rates. The weight losses for austenitic steels may be represented by a power-law relationship with time, whereas weight losses of ferritic steels follow a linear law.[1,2] Variations in the lithium purity, particularly the concentration of nitrogen in lithium, lead to significant variations in weight loss for both austenitic and ferritic steels. For identical exposure conditions. weight losses for the different austenitic steels increase in the following order: annealed Type 304L, annealed Type 316, 20% cold-worked Type 316, and 25% cold-worked PCA. The dissolution rates of the ferritic HT-9 alloy and Fe-9Cr-1Mo steel are an order of magnitude lower than for austenitic steels. The steady-state dissolution rate of Type 316 stainless steel in cold-trapped circulating lithium is an order of magnitude greater than that observed in the thermal convection loop.[3] The austenitic steels develop a porous ferrite scale after exposure to lithium while the ferritic steels show little or no internal corrosion. Limited data indicate that the thickness of ferrite scale on Type 316 stainless steel increases linearly with time.'

During the current reporting period, corrosion tests were continued at 700 and 755 K with several austenitic and ferritic steels to evaluate the long-term corrosion behavior in lithium. Data for weight loss and depth of internal penetration were obtained from specimens exposed to lithium for up to 6500 h. Energy dispersive x-ray analyses (EDAX) were performed to determine the distribution of substitutional elements, e.g., iron, chromium, and nickel, in the lithium-exposed specimens.

The weight losses for Type 316 stainless steel, PCA, and the ferritic HT-9 and Fe-9Cr-1Mo steel exposed at 755 and 700 K in flowing lithium are shown in Figs. 9.2.1-9.2.3. Each symbol type shown in the figures represents weight loss for a single specimen after various exposure times. The ferritic steels, HT-9 and Fe-9Cr-1Mo, were exposed in the normalized and tempered condition. Two different heat treatments were employed for the austenitic steels, viz., solution annealed and solution annealed plus 20% cold work for Type 316 stainless steel and solution annealed plus 25% cold work (treatment A3) and solution annealed plus 8 h at 1073 K plus 25% cold work plus 2 h at 1023 K (treatment B2) for PCA. The results show the following significant features:

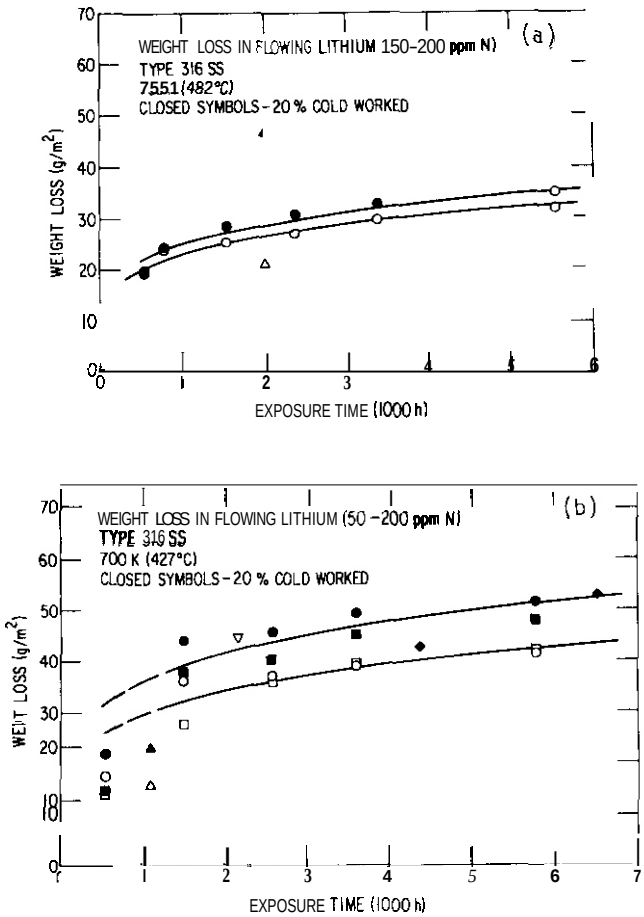

Fig. 9.2.1. Weight loss versus exposure time for annealed and 20% cold-worked Type 316 stainless exposed at (a) 755 K and (b) 700 K to flowing lithium. Each symbol type represents weight loss for a single specimen after various exposure times.

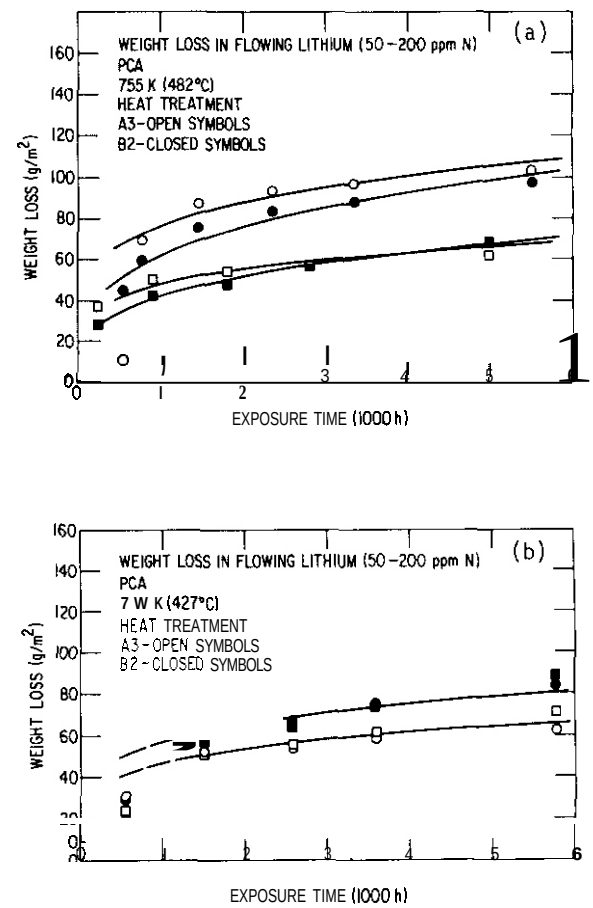

Fig. 9.2.2. Weight loss versus exposure time for PCA (heat treatment A3 and B2) exposed at (a) 755 K and (b) 700 K to flowing lithium. Each symbol type represents weight loss for a single specimen after various exposure times.

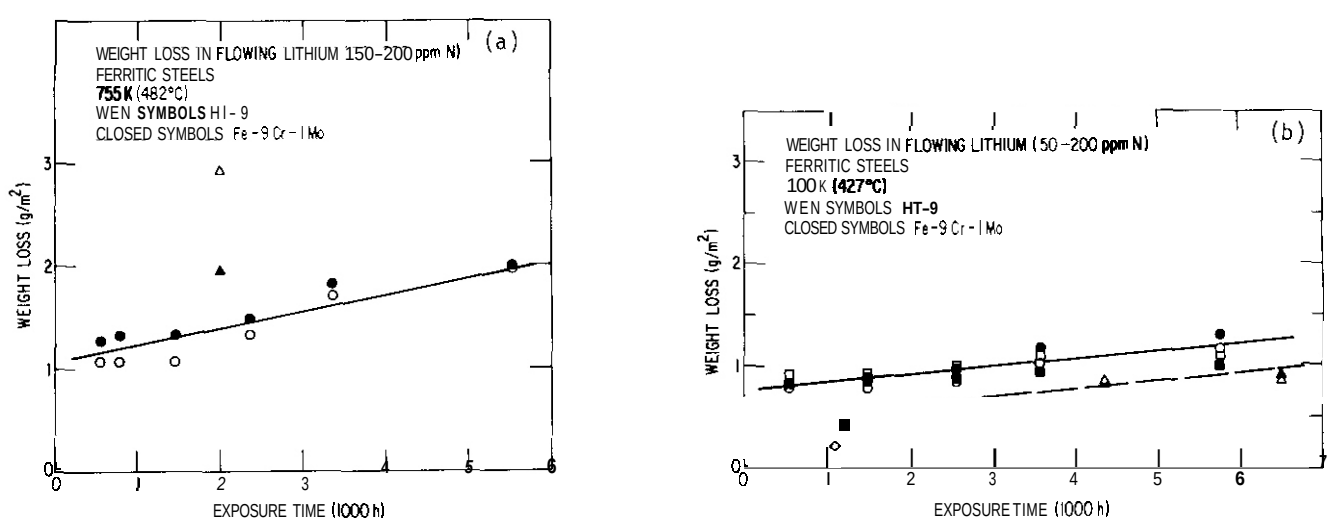

Fig. 9.2.3. Weight loss versus exposure time for HT-9 alloy and Fe-9Cr-1Mo steel exposed to (a) 755 K and (b) 700 K to flowing lithium. Each symbol type represents weight loss for a single specimen after various exposure times.

(a) The dissolution rates for austenitic Type 316 stainless steel and PCA decrease rapidly during the initial period of ~2000 h of exposure to lithium. The rates continue to decrease for longer exposure times but the weight loss data may be represented by a steady-state dissolution rate.

(b) For austenitic stainless steels. the weight loss at 700 K (427°C) is comparable or greater than that at 755 K (482°C).

(c) At both temperatures, the weight loss of austenitic steels increases in the following order: annealed Type 316, 20% cold-worked Type 316, and PCA. The dissolution behavior of PCA in the two different conditions of heat treatment shows inconsistent results, i.e., at 700 K the weight loss of 82 is greater than that for A3 whereas at 755 K. A3 shows greater weight loss than 82.

(d) The weight loss of ferritic HT-9 and Fe-9Cr-1Mo steel is more than an order of magnitude lower than that for Type 316 stainless steel.

(e) The weight loss of ferritic steels increases linearly with exposure time. However, all specimens show significant weight loss after the initial period of ~500 h of exposure to lithium. The weight losses at 700 K are lower than at 755 K.

(f) For both austenitic and ferritic steels, specimens that were exposed at different periods show significant differences in weight loss. For example, the two sets of PCA specimens (heat treatment A3 and B2) exposed to lithium at 755 K show a factor of two difference in weight loss (Fig. 9.2.2.a). The specimens shown by square symbols were exposed ~500 h after the specimens represented by circles. However. duplicate specimens exposed at the same time show comparable values of weight loss, e.g., ferritic steels and PCA exposed to lithium at 700 K (Figs. 9.2.2b and 9.2.3b). The differences in weight loss probably result from variations in the impurity content in lithium, particularly the concentration of nitrogen in lithium.

The weight losses for ferritic steels can be expressed by a linear relationship with time, given by

$$W = A + Rt, \tag{1}$$

where weight loss W is given in g/m^2, R is the steady-state dissolution rate, A is the intercept, and time t is in hours. The data for austenitic stainless steels may be expressed by a power-law relationship between weight loss and time, given by

$$W = Kt^n, \tag{2}$$

where K and n are constants. Least squares analyses of the data yielded values of the time exponent, n, between 0.16 and 0.31 at 755 K and between 0.38 and 0.52 at 700 K. However, excluding the short-term data (i.e., exposure times <1000 h) at 700 K, analyses gave an average n value of 0.2 $\pm$ 0.04 for the data obtained at different temperatures and material conditions. The values of the constants in Eqs. (1) and (2) and the dissolution rates for austenitic and ferritic steels are given in Table 9.2.1. The calculated curves, plotted in Figs. 9.2.1-9.2.3, show good agreement with the experimental data. The dissolution rates for the austenitic stainless steels were obtained from Eq. (2) by calculating the slope of the curve at 5000 h. The results show that the dissolution rates for Type 316 stainless steel in lithium at 700 K are 30 to 40% higher than at 755 K. For PCA, although the weight losses at 700 and 755 K are comparable, the dissolution rate at 700 K is lower than at 755 K.

Specimens exposed to lithium were examined metallographically for measurements of the depth of internal corrosive penetration. The austenitic stainless steels developed a porous ferrite layer, whereas the ferritic steels showed little or no corrosion. Micrographs of the ferrite layers formed on the austenitic steels exposed to flowing lithium at 700 K are shown in Fig. 9.2.4. The distribution of major elements across the ferrite layers on PCA and Type 316 stainless steel is shown in Fig. 9.2.5. Both steels show an ~10-μm-thick surface region depleted in chromium and completely depleted of nickel aver the entire corrosion scale. The concentration of nickel decreases abruptly across the scale/metal interface.

The depth of internal corrosive penetration was determined from the differenge fetween the initial thickness of the specimen and the sound metal remaining (i.e., the unreacted metal) after exposure to lithium. At least 10 measurements were made to obtain an average value for penetration. The weight loss and depth of internal corrosive penetration (i.e., thickness of ferrite layer) for austenitic stainless steels exposed in lithium for various times at 755 or 700 K are given in Table 9.2.2. The results show that the values of depth of penetration follow the weight loss data, i.e., specimens that show large weight loss also develop a thick ferrite scale. For a given amount of weight loss, the thickness of the ferrite scale is smaller at 700 K than at 755 K; also, the scales formed on the various alloys decrease in thickness in the following order: annealed Type 316, 20% cold-worked Type 316, and PCA. For a weight loss of 10 g/m^2, the average thicknesses of the ferrite scale on annealed Type 316, cold-worked Type 316, and PCA are 15.1, 10.4, and 8.2 μm, respectively. at 755 K and 9.4, 8.5, and 6.6 μm, respectively, at 700 K.

Table 9.2.1. Dissolution Rates and Values of the Constants in Eqs. (1) and (2) for Alloys Exposed to Flowing Lithium

Material	Temp. (K)	Constants K ($\times 10^{-3}$)	n	R ($\times 10^{-3}$)	A	Dissolution Rate[a] ($mg/m^2 \cdot h$)
316 SS	755	5.80	0.2	-	-	1.27
	700	7.50	0.2	-	-	1.65
316 CW	755	6.27	0.2	-	-	1.38
	700	9.10	0.2	-	-	2.00
PCA (A3)	755	15.60	0.2	-	-	3.43
	700	11.67	0.2	-	-	2.56
PCA (B2)	755	7.02	0.29	-	-	4.82
	700	14.30	0.2	-	-	3.14
HT-9	755	-	-	0.159	1.067	0.159
	700	-	0.063	0.791	0.063	
9Cr-1Mo	755	-	-	0.159	1.067	0.159
	700	-	0.066	0.784	0.066	

[a]Dissolution rates for austenitic stainless steels calculated at 5000 h.

The internal corrosive penetration for annealed and cold-worked Type 316 stainless steel exposed to lithium at 700 or 755 K is plotted as a function of time in Fig. 9.2.6. The results show that after an initial period of ~1000 h, the increase in the depth of penetration is slow. Most of the data can be represented by a power-law relationship. Least-squares analysis of the data yields a value of 0.34 for the time exponent n.

9.2.4.2 Tensile Properties

Tensile tests are being conducted on austenitic and ferritic steels in a flowing lithium environment to study the possible embrittlement of the material in lithium. Flat specimens, 5.59 x 1.22 mm in cross section and 22.23 mm in gauge length, are used for the tests. Tensile data on 20% cold-worked Type 316 stainless steel indicate that at temperatures between 480 and 755 K (207 and 482°C), a flowing lithium environment has no effect on the tensile strength or total elongation of the steel.[2] Tensile properties at strain rates between 4×10^{-2} and 4×10^{-6} s^{-1} in flowing lithium and in vacuum are comparable.

During the current reporting period, tensile tests were performed on normalized and tempered HT-9 alloy in flowing lithium at temperatures between 505 and 755 K and strain rates of 4×10^{-2}, 4×10^{-4}, and 4×10^{-6} s^{-1}. The tensile strength and total elongation of the material in lithium are shown in Fig. 9.2.7. The curves for ultimate and yield strengths plotted in the figure represent the average values in air. The results show that at all strain rates, a lithium environment has no effect on the tensile properties of the steel.

9.2.5 Conclusions

The corrosion data in flowing lithium at 700 and 755 K indicate that the weight losses of ferritic HT-9 and Fe-9Cr-1Mo steel follow a linear law with time and yield a constant dissolution rate. The dissolution rates at 700 K are a factor of 2 lower than those at 755 K. The dissolution rates of austenitic PCA and Type 316 stainless steel decrease significantly during the initial ~2000-h exposure period. The weight losses and steady-state dissolution rates of Type 316 stainless steel at 700 and 755 K are anomalous; weight loss as well as dissolution rate at 700 K is greater than at 755 K. The data at 700 and 755 K were obtained in two separate vessels of the lithium loop, in which the lithium flow was from the high- to low-temperature vessel. It is possible that differences in lithium purity or downstream effects are responsible for the anomalous results.

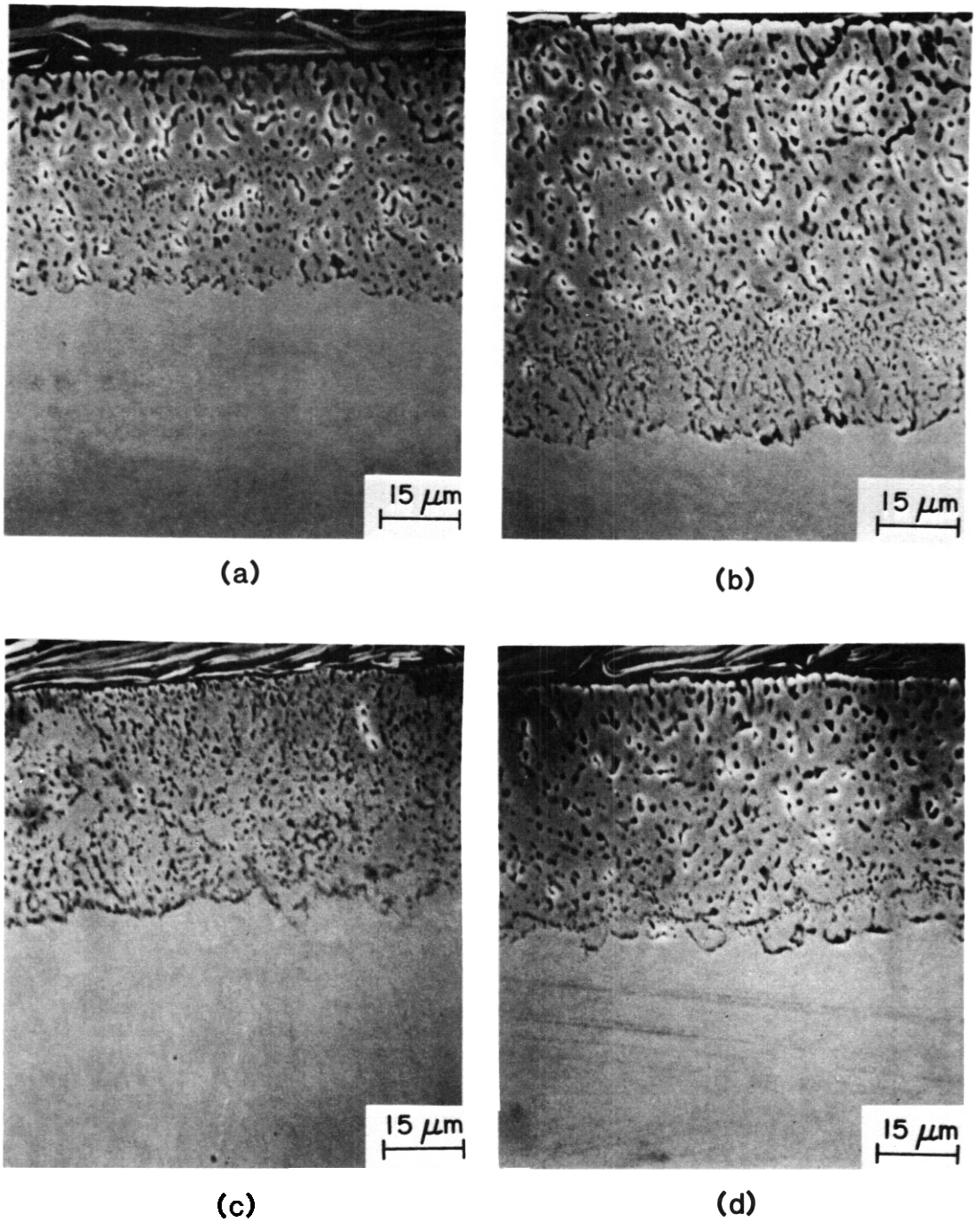

Fig. 9.2.4. Micrographs of the ferrite layers formed on austenitic stainless steels exposed to flowing lithium-at 700 K. **(a) Annealed** Type 316 stainless (2138 **h), (b)** 20% cold-worked Type 316 stainless steel (5739 **h), (c)** PCA **A3** (5521 **h),** and **(d)** PCA B2 (5521 **h).**

Measurements of the depth of internal corrosive penetration for austenitic steels show good correlation with the trends indicated by the weight loss data, **i.e.,** specimens that show large weight loss develop a thick ferrite layer. For a given weight loss, the thickness of the ferrite layer on austenitic steels decreases in the following order: annealed Type 316, cold-worked Type 316, and PCA. Data on weight **loss** and internal penetration follow a power-law relationship with time.

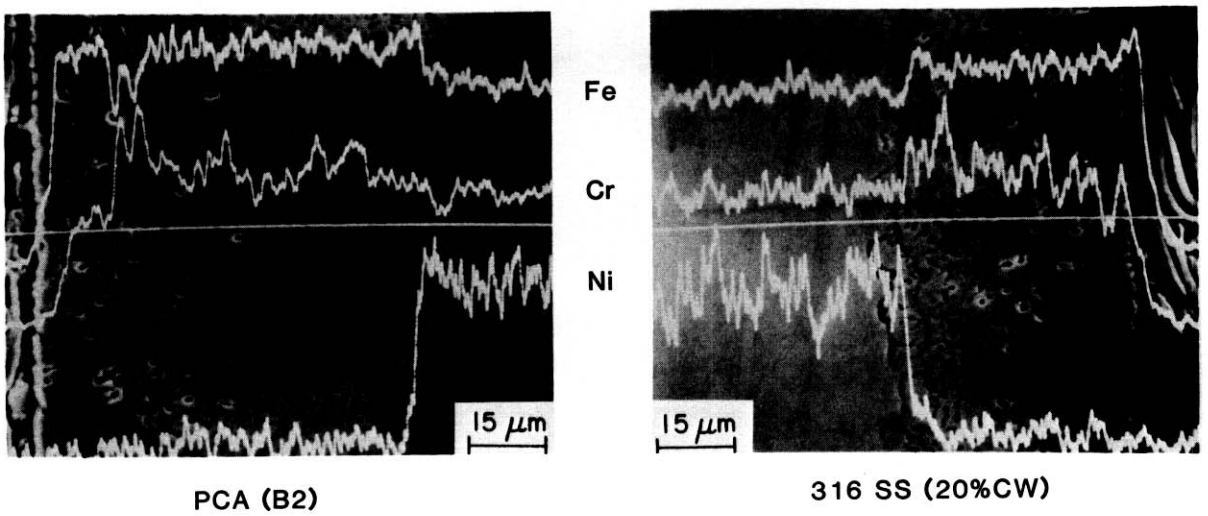

Fig. 9.2.5. Micrographs and concentration profiles for major elements across the ferrite layer of PCA and Type 316 stainless steel exposed to lithium at 700 K.

Table 9.2.2. Weight Loss and Depth of Internal Penetration for Austenitic Stainless Steels Exposed to Flowing Lithium

755 K (482°C)			700 K (427°C)		
Time (h)	Weight Loss (g/m^2)	Penetration (μm)	Time (h)	Weight Loss (g/m^2)	Penetration (μm)
		316 SS Annealed			
1295	6.7	13 ± 2	1100	17.2	21 ± 2
1997	21.0	25 ± 9	2138	44.7	46 ± 8
3000	16.2	34 ± 9	3584	39.5	33 ± 4
3366	29.6	25 ± 7	3584	39.1	30 ± 4
5000	17.0	31 ± 20	5739	42.2	38 ± 2
5521	31.8	37 ± 11	5739	41.5	37 ± 6
		316 SS 20% CW			
1295	23.8	24 ± 3	1100	24.9	25 ± 3
1997	46.5	47 ± 8	3584	45.3	37 ± 5
3366	32.7	31 ± 5	3584	49.4	38 ± 4
5000	60.7	67 ± 6	5739	47.9	42 ± 3
5521	35.0	40 ± 9	5739	51.6	40 ± 2
		650T	52.9	46 ± 9	
		PCA (A3)			
4972	61.9	54 ± 6	5739	62.2	41 ± 5
5521	103.0	76 ± 6	5739	71.1	48 ± 5
		PCA (B2)			
4972	68.9	59 ± 6	5739	83.9	57 ± 4
5521	97.2	80 ± 7	5739	88.8	56 ± 4

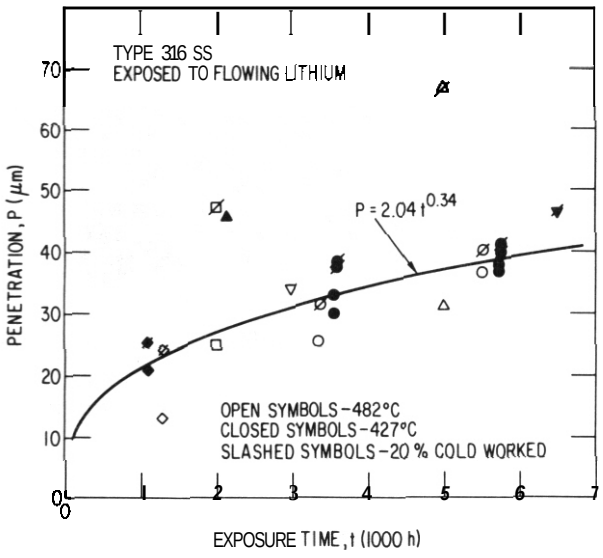

Fig. 9.2.6. Internal penetration versus exposure time for annealed and 20% cold-worked Type 316 stainless steel exposed to lithium at 700 or 755 K. Each symbol type represents penetration for a single specimen after various exposure times.

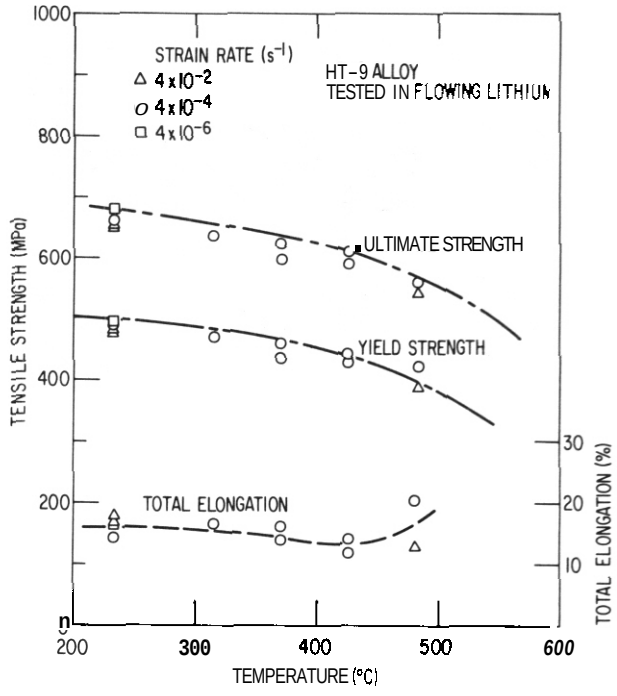

Fig. 9.2.1. Tensile strength and total elongation for normalized and tempered HT-9 alloy tested in flowing lithium. The curves for ultimate and yield strengths represent the average values in air.

Specimens of austenitic and ferritic steels exposed to lithium at different periods show significant variations in weight loss. Such differences in weight loss probably result from variations in the lithium purity during the test. The nitrogen content in lithium varied between 50 and 200 wppm during the test. Corrosion tests at 700 and 644 K (427 and 371°C) are in progress to establish dissolution rates of materials as a function of temperature.

Tensile data for normalized and tempered HT-9 alloy at temperatures between 505 and 755 K and strain rates in the range of 4×10^{-2} to 4×10^{-6} s^{-1} indicate that a flowing lithium environment has no effect on the tensile strength or total elongation of the steel.

9.2.6 References

1. O. K. Chopra and O. L. Smith, "Environmental Effects on Properties of Structural Alloys," pp. 195-200 in Alloy Development for Irradiation Performance: Semiannual Progress Report for Period Ending March 31, 1983, Oak Ridge National Laboratory, DOE/ER-0045/10.

2. O. K. Chopra and D. L. Smith, "Environmental Effects on Properties of Structural Alloys," pp. 216-200 in Alloy Development for Irradiation Performance: Semiannual Progress Report for Period Ending September 30, 1983, Oak Ridge National Laboratory, DOE/ER-0045/11.

3. P. F. Tortorelli and J. H. Devan. "Corrosion of Path A PCA. Type 316 Stainless Steel. and Fe-12Cr-1Mo3VW Steel in Flowing Lithium." pp. 290-300 in Alloy Development for Irradiation Performance: Semiannual Progress Report for Period Ending September 30, 1981, Oak Ridge National Laboratory, DOE/ER-0045/9.

9.3 CORROSION OF STRUCTURAL ALLOYS IN FLOWING Pb-17Li ENVIRONMENT - O. K. Chopra and D. L. Smith (Argonne National Laboratory)

9.3.1 ADIP Task

ADIP Task I.A.3, Perform Chemical and Metallurgical Compatibility Analyses.

9.3.2 Objective

The objective of this program is to investigate the influence of a flowing Pb-17 at. % Li environment on the corrosion behavior and mechanical properties of structural alloys under conditions of interest for fusion reactors. Corrosion behavior is evaluated by measuring the weight change and depth of internal corrosive penetration of alloy specimens exposed to flowing Pb-17Li for various times. The dissolution rates are determined as a function of temperature. Metallographic examination of the alloy surface is used to establish the mechanism and rate-controlling process for the corrosion reactions. Initial effort on mechanical properties is focused on tensile tests in a flowing Pb-17Li environment.

9.3.3 Summary

Corrosion data on weight loss and internal penetration are presented for austenitic PCA and Type 316 stainless steel and ferritic HT-9 and Fe-9Cr-1Mo steel exposed in flowing Pb-17Li up to 3700 h at temperatures of 700 and 127 K. The ferrite scales on austenitic steels show significant depletion of chromium and complete depletion of nickel from the steel.

9.3.4 Progress and Status

The effects of a flowing Pb-17Li environment on the corrosion behavior and mechanical properties of austenitic and ferritic steels are being investigated. Tests are conducted in a forced-circulation Pb-17Li loop operating at temperatures between 727 and 573 K (454 and 300°C). Several analyses of the eutectic alloy show that the alloy composition is Pb-16.3 at. % Li and the concentrations of O, H, and N are 260, 22, and <10 wppm, respectively. The measured level of hydrogen is significantly higher than the predicted values. Thin foils of yttrium and vanadium are being exposed to the Pb-17Li alloy to determine the concentration of hydrogen. Flat corrosion coupons, -13 x 10 x 0.26 mm in size, are exposed to flowing Pb-17Li and the corrosion behavior is evaluated by measurements of weight loss and depth of internal penetration. Weight loss data for Type 316 stainless steel and ferritic HT-9 and Fe-9Cr-1Mo steels in flowing Pb-17Li at 727 and 700 K (454 and 427°C) were presented earlier.[1,2] During the current reporting period, the exposed specimens were examined metallographically to determine the depth of internal corrosive penetration. Energy dispersive x-ray analyses were performed to determine the distribution of major elements in the Corrosion layer on the exposed specimens.

The weight losses of austenitic and ferritic steels in flowing Pb-17Li at 700 and 721 K (427 and 454°C) are plotted as a function of time in Figs. 9.3.1 and 9.3.2, respectively. The results indicate that the weight losses and dissolution rates of both austenitic and ferritic steels in flowing Pb-17Li are an order of magnitude greater than in flowing lithium. However, the overall corrosion behavior of the various alloys in Pb-17Li is similar to that in lithium, i.e., the dissolution rates for Type 316 stainless steel reach a steady-state value (shown by the chain-dashed lines in the figures) after an initial period of high dissolution rates, whereas the weight losses for ferritic steels exhibit a linear increase with time. The weight losses for PCA exposed to Pb-17Li for relatively short times (i.e., -1350 h) show a linear increase with time.

The weight losses for the various alloys can be expressed by a linear relationship with time, given by

$$W = A + Rt, \qquad (1)$$

where weight loss W is given in g/m^2, R is the steady-state dissolution rate, A is the intercept, and time t is in hours. The data for Type 316 stainless steel may also be expressed by a power-law relationship between weight loss and time, given by

$$W = Kt^n, \qquad (2)$$

where K and n are constants. Least-squares analyses of the data for annealed and cold-worked Type 316 stainless steel yield an average value of 0.65 for the time exponent n. Earlier analyses of the data up to -3000 h of exposure indicated that the weight losses for Type 316 stainless steel follow a parabolic law with time [i.e., time exponent of 0.5 in Eq. (2)].[2,3]

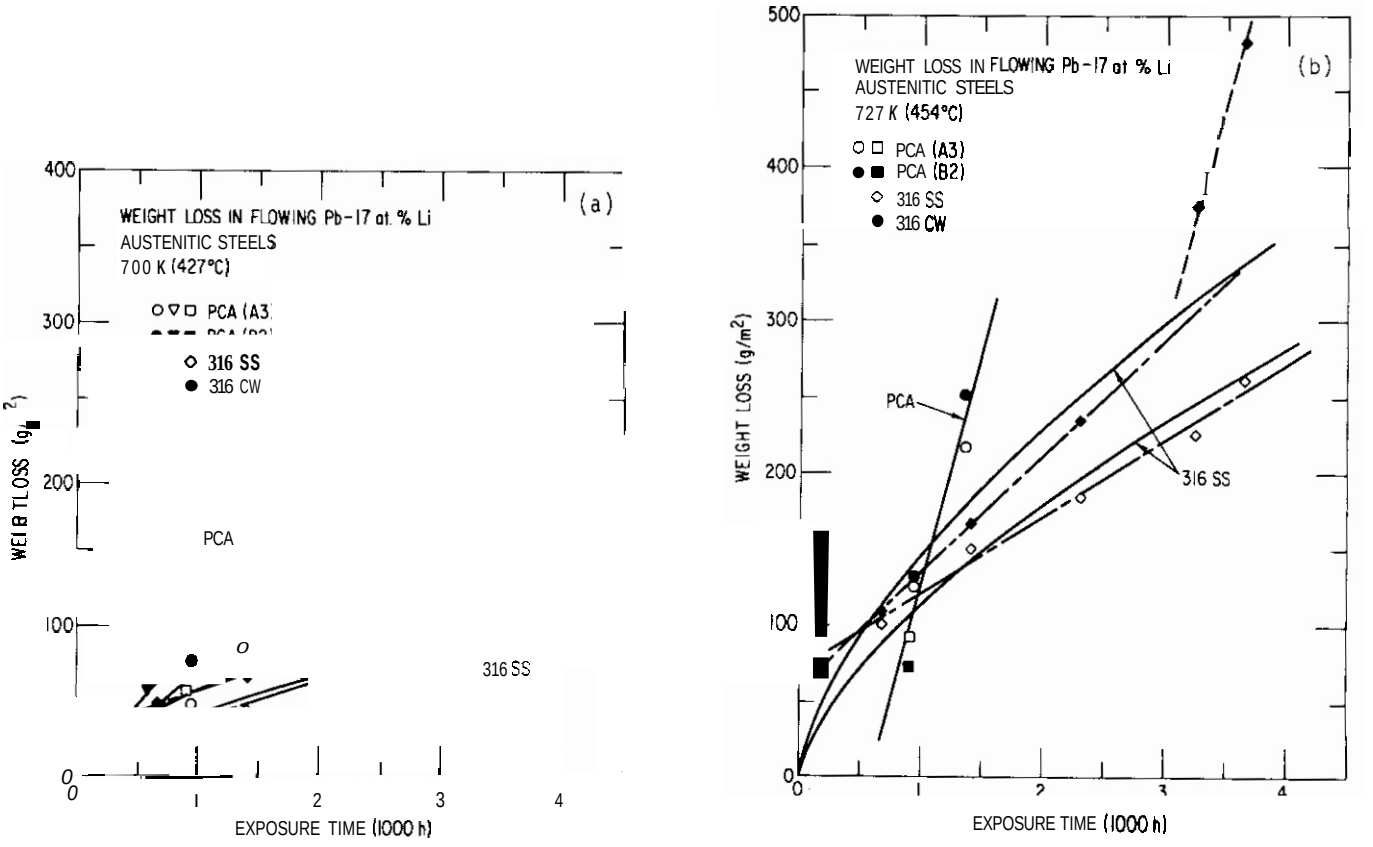

Fig. 9.3.1. Weight loss versus exposure time for PCA and Type 316 stainless steel exposed at (a) 700 K and (b) 727 K to flowing Pb-17Li. Each symbol type represents weight loss for a single specimen after various exposure times.

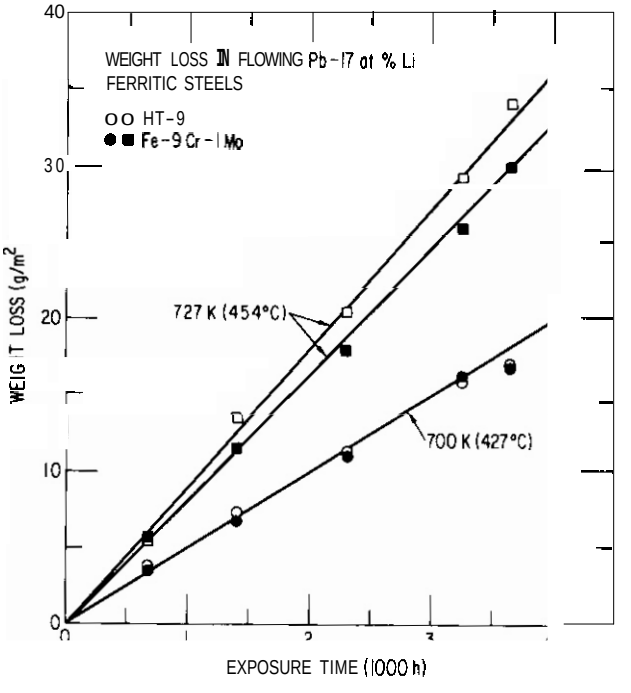

Fig. 9.3.2. Weight loss versus exposure time for HT-9 and Fe-9Cr-1Mo steel exposed at 700 and 727 K to flowing Pb-17Li.

The values of the constants in Eqs. (1) and (2) and the dissolution rates for the various alloys are given in Table 9.3.1. The calculated curves, plotted in Figs. 9.3.1 and 9.3.2, show good agreement with the experimental data. The weight loss for 20% cold-worked Type 316 stainless steel, however, shows a significant increase after a 3000-h exposure at 727 K (454°C). Metallographic evaluation of the exposed specimen indicates that this increase in weight loss is caused by the loss of portions of the degraded ferrite layer on the specimen surface and is not representative of the dissolution of substitutional elements from the steel.

Table 9.3.1. Dissolution Rates and Values of the Constants in Eqs. (1) and (2) for Alloys Exposed to Flowing Pb-17Li

Material	Temp. (K)	Maximum Time (h)	Constants K ($\times 10^{-3}$)	n	R ($\times 10^{-3}$)	A	Dissolution Rate[a] ($mg/m^2 \cdot h$)
316 SS	727	3663	1.28	0.65	50.1	70.9	50.1 (54.0)
	700	3663	0.48	0.65	26.1	13.1	26.1 (20.3)
316 CW	727	3663	1.76	0.65	75.9	59.5	75.9 (73.8)
	700	2310	0.65	0.65	27.4	30.5	27.4 (27.2)
PCA (A3)	727	1353	-	-	309.0	-181.4	309.0
	700	1353	-	-	69.8	0	69.8
PCA (B2)	727	1353			309.3	-181.4	309.0
	700	1356	0	0	94.3	0	94.3
HT-9	727	3663		-	9.0	0	9.0
	700	3663	-	-	5.1	0	5.1
9Cr-1Mo	727	3663	-	-	8.2	0	8.2
	700	3663	-	-	4.9	0	4.9

[a]Dissolution rates for Type 316 stainless steel represent steady-state values, numbers within parentheses are the slope of the power-law curve at 2500 h.

The Arrhenius plots of the dissolution rates for austenitic and ferritic steels in flowing Pb-17Li at 700 and 727 K are shown in Fig. 9.3.3. The dissolution rate for the HT-9 alloy exposed to Pb-17Li at 686 K (413°C) for ~600 h is also plotted in Fig. 9.3.3. Data for Type 316 stainless steel at 773 and 748 K (500 and 473°C) in a Pb-17Li thermal convection loop are included in the figure.[4] The results show that the dissolution rates of the ferritic steels are a factor of ~6 lower than for Type 316 stainless steel. The rates for Type 316 stainless steel are a factor of ~5 lower than for PCA. The data for Type 316 stainless steel and the HT-9 alloy yield an activation energy of ~38 kcal/mole.

The exposed specimens were examined metallographically to determine the depth of internal corrosive penetration. The austenitic stainless steels developed a very porous ferrite layer, whereas the ferritic steels showed little or no corrosion. Micrographs of the ferrite layers formed on PCA and Type 316 stainless steel exposed to flowing Pb-17Li at 727 and 700 K are shown in Figs. 9.3.4 and 9.3.5. The distribution of major elements, i.e., Ni, Cr, and Fe across the ferrite layers on PCA exposed to Pb-17Li at 727 and 700 K is shown in Fig. 9.3.6. The results show a significant depletion of chromium and complete depletion of nickel from the entire corrosion scale. The concentrations of chromium and nickel decrease abruptly across the scale/metal interface. The distribution of Ni, Cr, and Fe across the surface regions of annealed Type 316 stainless steel and ferritic HT-9 is shown in Fig. 9.3.7. The compositional changes across the ferrite scale on Type 316 stainless steel are similar to those for PCA. However, the HT-9 alloy shows no internal corrosion and a slight depletion of chromium from the surface.

The compositional changes in the ferrite scales formed on austenitic steels exposed to flowing Pb-17Li are different from those observed in steels exposed to a flowing lithium environment. Austenitic PCA and Type 316 stainless steel exposed to lithium show slight depletion of chromium near the surface region of the ferrite scale.[5] Specimens exposed to Pb-17Li show significant loss of chromium over the entire ferrite scale. Furthermore, the ferrite scales formed in the Pb-17Li environment are very porous and break off from the specimens either during exposure or the cleaning process.

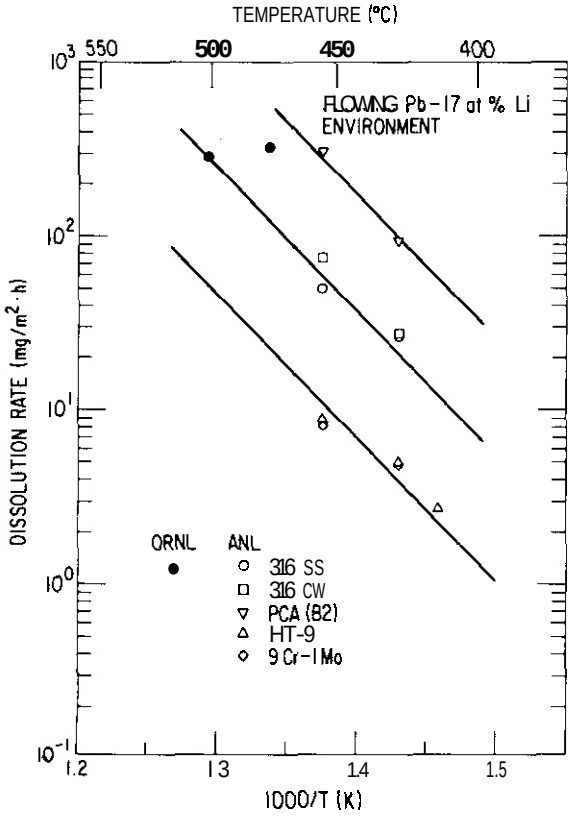

Fig. 9.3.3. Arrhenius plot of dissolution rate data for austenitic and ferritic steels exposed to flowing Pb-17Li.

The depth of iaternal corrosive penetration was determined from the difference between the initial thickness of the specimen and the sound metal remaining (i.e., the unreacted metal) after exposure to Pb-17Li. At least 10 measurements were made to obtain an average value for penetration. The weight loss and depth of internal penetration (i.e., thickness of the ferrite layer) for austenitic steels exposed to Pb-17Li at 700 and 727 K are given in Table 9.3.2. The results show that the values of depth of penetration follow the trends inidicated by height loss data. For a weight loss of 10 g/m^2, the average thickness of the ferritic scale for the various alloys and different exposure temperatures is -2.2 μm. Corrosion data in flowing lithium at 700 K indicate that a 10 g/m^2 loss in weight corresponds to an -7- to 10-urn-thick ferrite scale.[5] These results indicate that the measured weight losses represent dissolution of alloy elements as well as loss of portions of the ferrite scale.

9.3.5 Conclusions

Corrosion data in a flowing Pb-17Li environment indicate that the dissolution rates for both austenitic and ferritic steels are an order of magnitude greater than in flowing lithium. The influence of time, temperature, and alloy composition on the corrosion behavior in Pb-17Li is similar to that in flowing lithium. The weight losses for Type 316 stainless steel follow a power-law relationship with time, while the ferritic steels show a linear increase in weight loss with time. The dissolution rates for the various alloys increase in the following order: Fe-9Cr-1Mo, HT-9. Type 316 SS, and PCA. The limited data in Pb-17Li indicate that the Arrhenius plots of dissolution rates for austenitic and ferritic steels may be represented by an activation energy of 38 kcal/mole, a value identical to that obtained for Type 316 stainless steel in lithium or sodium environments.

After exposure to flowing Pb-17Li, the austenitic steels develop a very porous and weak ferrite scale. Energy dispersive x-ray analyses show significant depletion of chromium and complete depletion of nichel from the ferrite scale. Measurements of the thickness of the ferrite scale indicate that the corrosion data for austenitic stainless steels in Pb-17Li represent loss in weight due to selective dissolution of substitutional elements as well as loss of the degraded ferrite layer from the specimens. The ferritic steels show no internal corrosive penetration and a slight depletion of chromium from the surface.

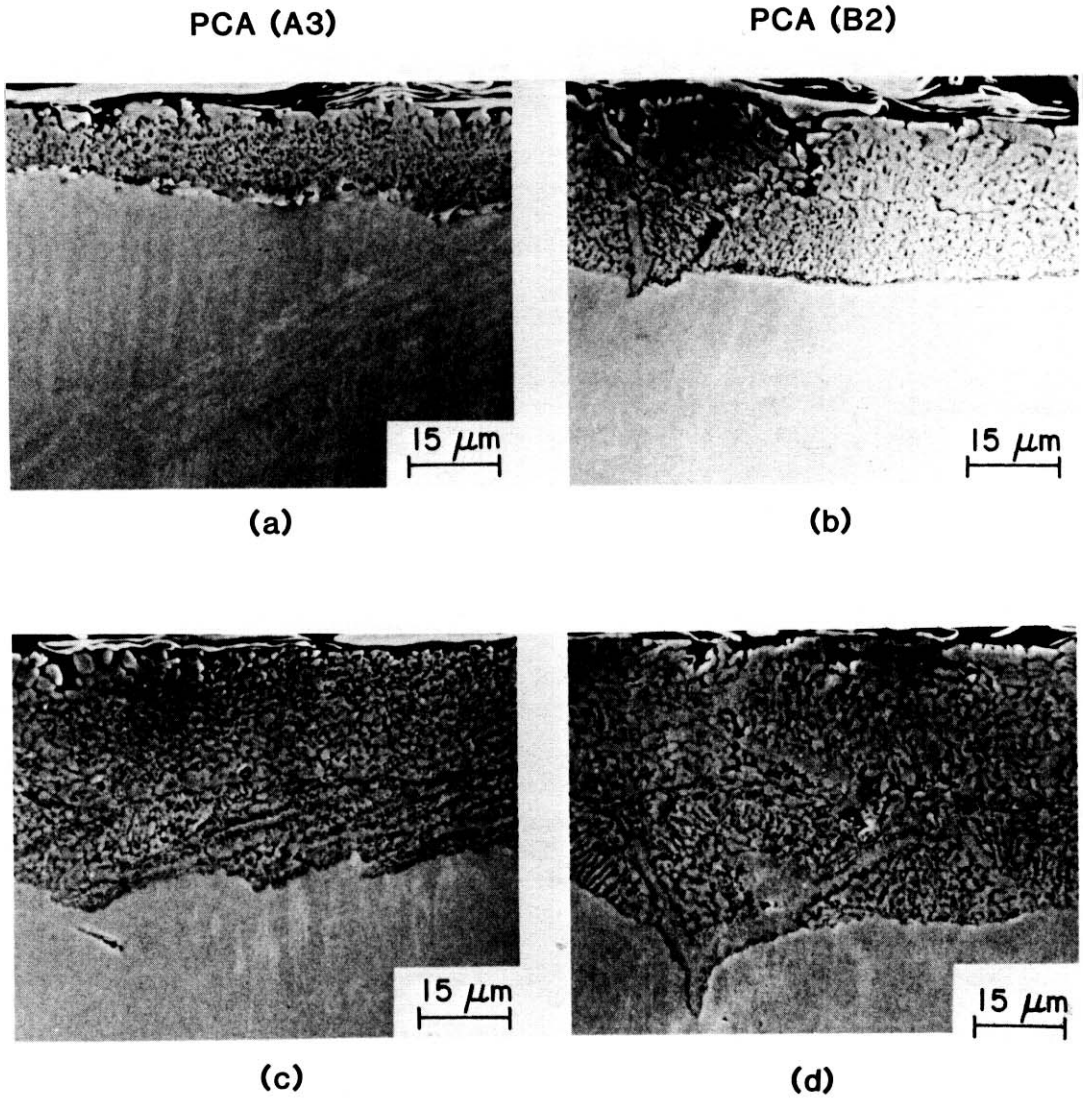

Fig. 9.3.4. Micrographs of the ferrite layers formed on PCA exposed for 1353 h to flowing Pb-17Li at (a) and (b) 700 K and (c) and (d) 727 K.

9.3.6 References

1. O. K. Chopra and D. L. Smith, "Environmental Effects on Properties of Structural Alloys," pp. 195-200 in Alloy Development for Irradiation Performance: Semiannual Progress Report for Period Ending March 31, 1983, Oak Ridge National Laboratory, DOE/ER-0045/10.

2. O. K. Chopra and D. L. Smith, "Environmental Effects on Properties of Structural Alloys," pp. 216-200 in Alloy Development for Irradiation Performance: Semiannual Progress Report for Period Ending September 30, 1983, Oak Ridge National Laboratory, DOE/ER-0045/11.

3. O. K. Chopra and D. L. Smith, "Corrosion of Ferrous Alloys in Eutectic Lead-Lithium Environment," J. Nucl. Mater. 122-123 (1984).

4. P. F. Tortorelli and J. H. Devan, "Corrosion of Type 316 Stainless Steel in Flowing Pb-17 at. % Li," pp. 203-204 in Alloy Development for Irradiation Performance: Semiannual Progress Report for Period Ending September 30, 1983, Oak Ridge National Laboratory, DOE/ER-0045/11.

5. O. K. Chopra and D. L. Smith, "Environmental Effects on Properties of Structural Alloys in Flowing Lithium," this report.

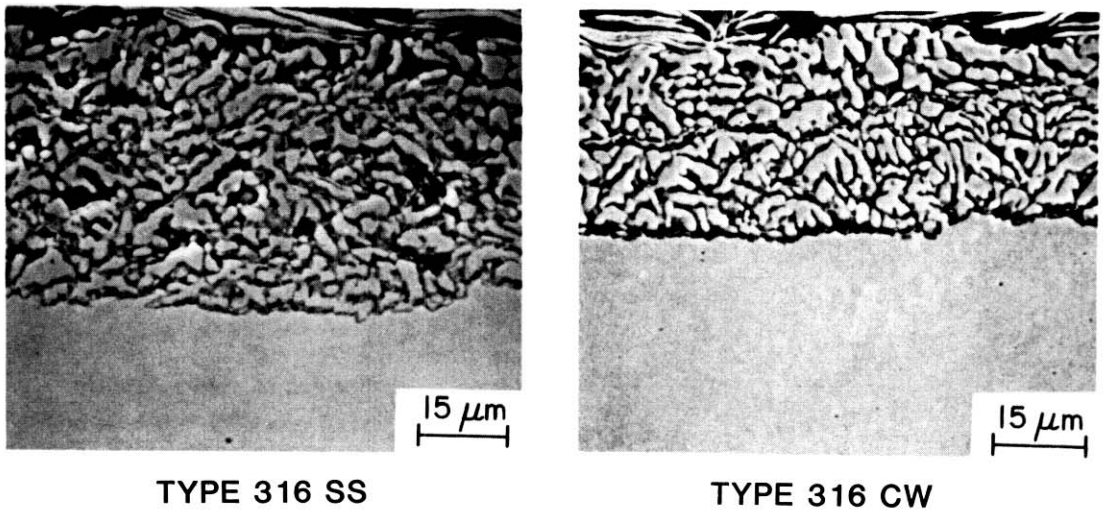

Fig. 9.3.5. Micrographs of the ferrite layers formed on Type 316 stainless steel exposed for 3663 h to flowing Pb-17Li at 727 K.

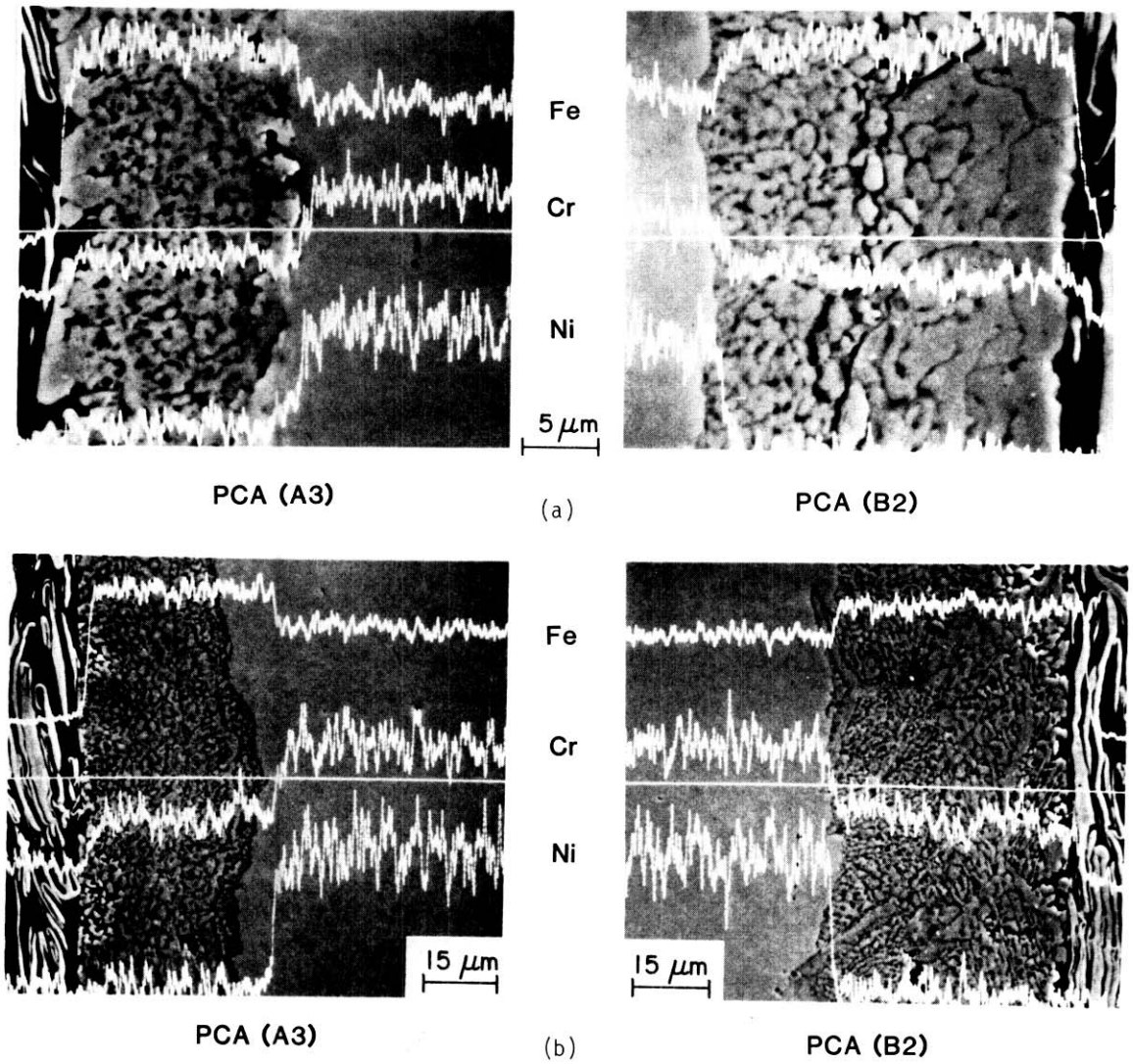

Fig. 9.3.6. Micrographs and concentration profiles for major elements across the ferrite layer of PCA exposed to Pb-17Li for 1353 h at (a) 700 K and (b) 727 K.

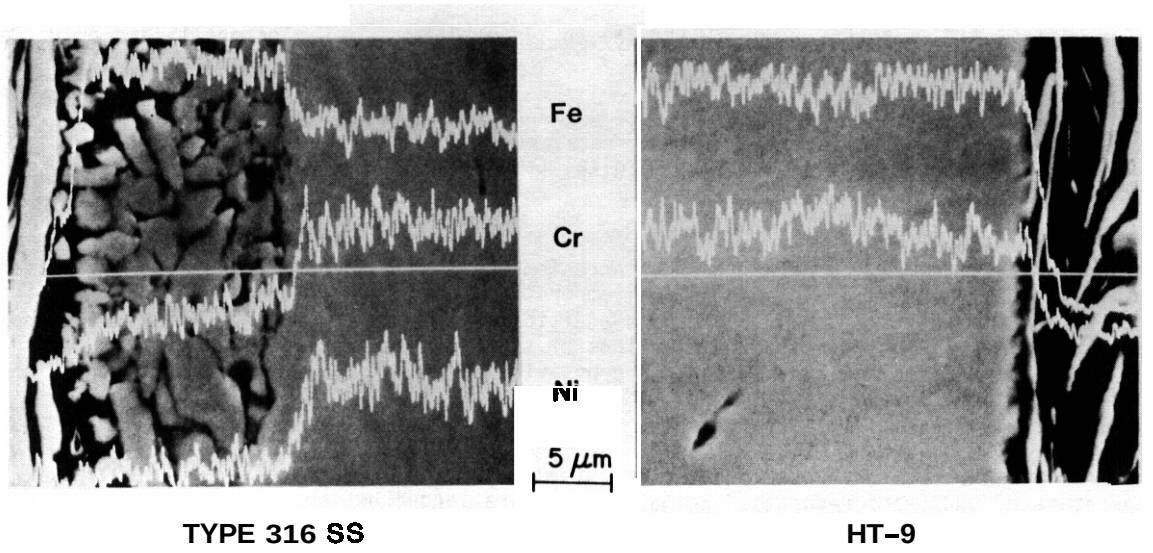

Fig. 9.3.7. Micrographs and concentration profiles for major elements across the ferrite layer of Type 316 stainless steel and the surface region of the HT-9 alloy exposed to Pb-17Li for 3663 h at 727 K.

Table 9.3.2. Weight Loss and Depth of Internal Pentration for Austenitic Stainless Steels Exposed to Flowing Pb-17Li

Alloy	Exposure Time (h)	727 K (454°C) Weight Loss (g/m^2)	727 K (454°C) Penetration (μm)	700 K (427°C) Weight Loss (g/m^2)	700 K (427°C) Penetration (μm)
316 SS	1405	150.3	26 ± 2	45.9	14 ± 3
	3258	224.7	33 ± 6	-	-
	3663	261.7	47 ± 11	110.4	22 ± 6
316 CW	1405	167.2	29 ± 4	66.6	16 ± 2
	3663	482.7	72 ± 16	-	-
PCA (A3)	905	92.3	19 ± 3	58.2	10 ± 2
	1353	217.9	37 ± 4	86.5	21 ± 4
PCA (B2)	905	73.9	28 ± 6	91.1	21 ± 4
	1353	252.0	52 ± 7	123.4	31 ± 8

9.4 CORROSION OF TYPE 316 STAINLESS STEEL IN FLOWING Pb–17 at. % Li — P. F. Tortorelli and J. H. DeVan (Oak Ridge National Laboratory)

9.4.1 ADIP Task

ADIP Task I.A.3, Perform Chemical and Metallurgical Compatibility Analyses.

9.4.2 Objective

The purpose of this task is to determine the corrosion resistance of candidate first-wall materials to slowly flowing Pt–17 at. % Li in the presence of a temperature gradient. Dissolution and deposition rates are measured as functions of time, temperature, and additions to the lead-lithium. These measurements are combined with chemical and metallographic examinations of specimen surfaces to establish the mechanisms and rate-controlling processes for the dissolution and deposition reactions.

9.4.3 Summary

Results from the exposure of type 316 stainless steel to thermally convective Pb–17 at. % Li at a maximum temperature of 500°C are reported. Weight losses were large, but the effects of the postexposure lithium rinse to remove the lead-lithium needed to be taken into account in the data analysis.

9.4.4 Progress and Status

A thermal convection loop (TCL) study of type 316 stainless steel in Pb–17 at. % Li was continued during the current reporting period. The type of loop used in this experiment has been described previously,' and the details of the lead-lithium preparation were given in the preceding progress report.' The loop allowed corrosion coupons to be withdrawn and inserted without interrupting the lead-lithium flow and was one of type 316 stainless steel that had previously circulated lithium for over 10,000 h. The interior surface of its hot leg was therefore depleted in nickel. While the presence of the resultant ferritic surface may affect dissolution of the fresh austenitic loop coupons, this effect has been measured for lithium, was found to be not large, and was taken into account when we compared the present dissolution data with prior results for type 316 stainless steel in lithium by using only data typical of such loop conditions. The maximum loop temperature was 500°C, and initially a temperature difference of 150°C was maintained. However, after a few hundred hours of exposure, sufficient mass transfer had occurred to initiate sane plugging in the cold leg. It was, therefore, necessary to raise the minimum temperature to about 430°C to prevent severe flow restrictions by mass transfer deposits.

In order to acquire weight change data, it was necessary to remove the residual lead-lithium from the coupons by using a lithium soak at about 250°C for about 6 h followed by a rinse in water to remove the lithium. The procedure was then repeated until the weights became constant. In this way, the weight changes of the specimen set were determined for each exposure period. However, it has now been definitely established that such a lithium soak removes much of the corroded surface layer, which is depleted in nickel and chromium and penetrated by lead-lithium.[3,4] Therefore, the lithium soak procedure allows one to determine the total amount of corroded structural metal by subtracting the specimen weight after loop exposure to lead-lithium and subsequent lithium soak(s) from the starting coupon weight. When the same specimen is then reinserted into the loop, a fresh austenitic surface is again exposed to the circulating Pb–17 at. % Li. This is thus somewhat different from many lithium loop experiments, where most of the corrosion layer is not lost during the process of lithium removal prior to weighing. In the case of lithium, reinsertion of the specimens does not expose a fresh austenitic surface. A weight loss versus time curve generated by exposure of the same specimen set is therefore fundamentally different for the lithium and lead-lithium experiments. In the former, the continuous dissolution of an austenitic alloy is approximated by weight changes measured at various times during a loop run. On the other hand, in a Pt–17 at. % Li TCL experiment, such data as a function of time represent a collection of discrete weight losses measured from specimens whose surfaces have been repeatedly stripped of most of their corrosion layers. In the latter case, each exposure interval is essentially independent of the preceding one, and the cumulative exposure time is set back to zero each time. Therefore, in order to generate a proper weight loss (or gain) versus time curve, different specimens need to be exposed to the Pb–17 at. % Li for different lengths of times. This type of data is currently being generated. However, the initial loop run was with specimens that were reinserted several times over a 4125 h period. The data were originally plotted versus time on one curve,[2] but, as described above, this does not give a true kinetic depiction of the dissolution and deposition processes (and, indeed, probably explains the atypical shape of such a curve). Rather, such data should be displayed as in Fig. 9.4.1, where the weight changes over each exposure interval are plotted from the origin. It is interesting to note that these weight losses are still much larger than those for exposure of type 316 stainless steel to pure lithium over similar time intervals.

Examination of polished cross sections of the type 316 stainless steel loop specimens exposed to Pb–17 at. % Li revealed very little evidence of corrosion layers despite the large weight losses (see Fig. 9.4.2). Such observations are consistent with a removal of the corrosion layers during the lithium rinses. Scanning electron microscopy of the corroded specimens showed surface roughening that delineated the various grains (see Fig. 9.4.3). However, energy dispersive x-ray analysis revealed very little preferential leaching of nickel or chromium occurred. The surface compositions were similar to that of the bulk material. This is a further indication that the corrosion layer has been removed prior to examination.

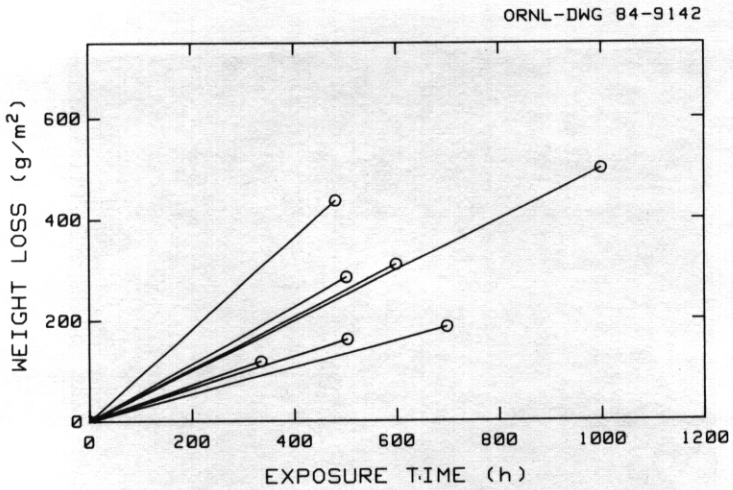

Fig. 9.4.1. Weight loss versus time for type 316 stainless steel exposed to thermally convective Pb–17 at. % Li at 500°C.

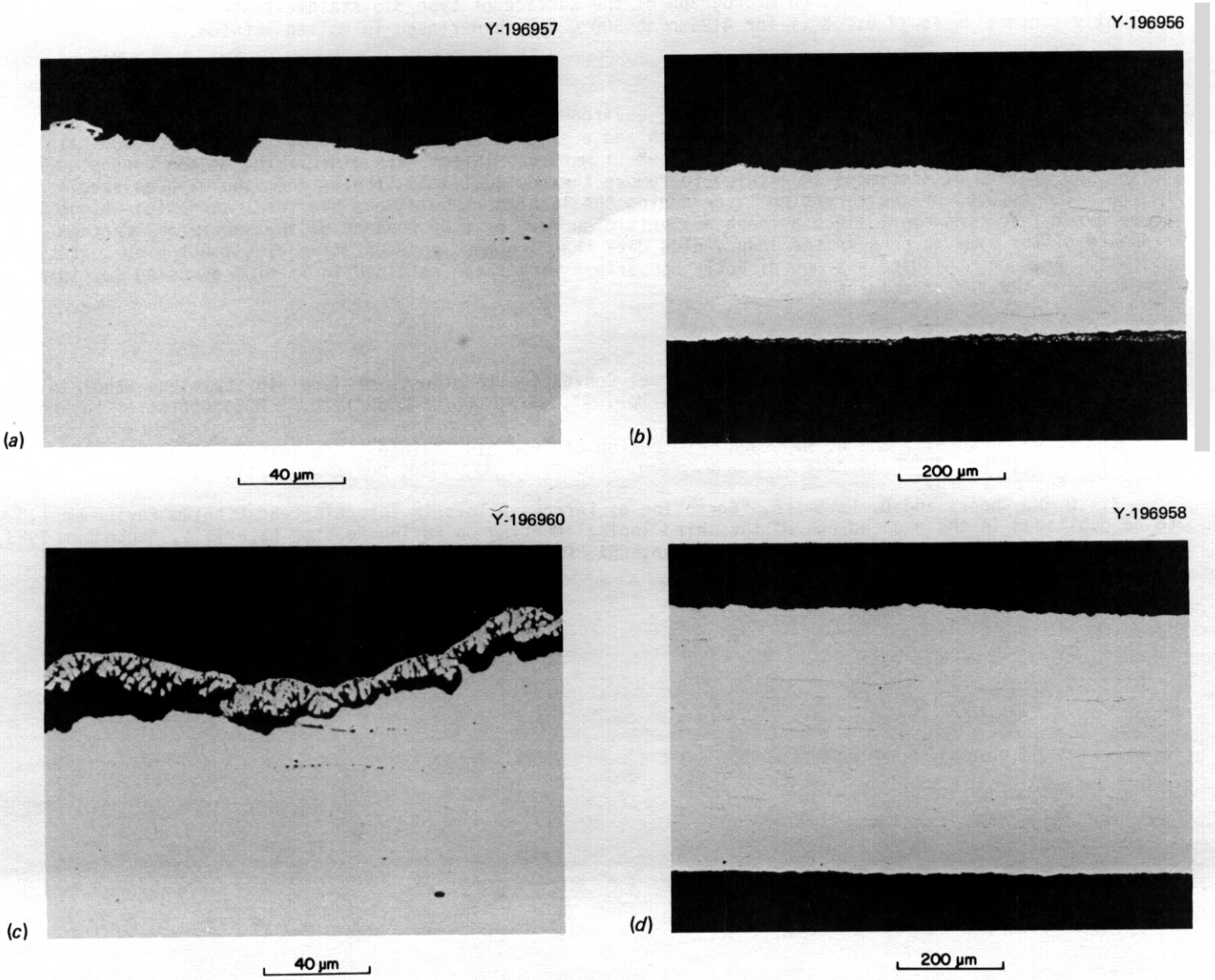

Fig. 9.4.2. Polished cross sections of type 316 stainless steel exposed to thermally convective Pb–17 at. % Li for 4125 h and then rinsed in molten lithium. Exposed at (*a*,*b*) 500°C, (*c*,*d*) 475°C.

M-17043

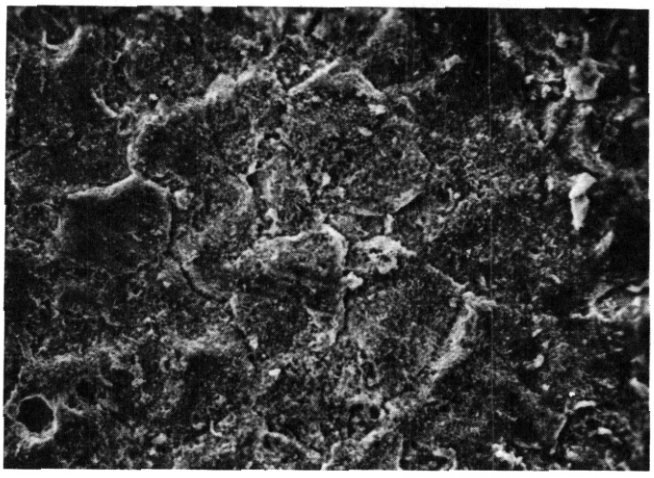

40 μm

Fig. 9.4.3. Scanning electron micrograph of the surface of type 316 stainless steel exposed to thermally convective Pb–17 at. % Li for 4125 h at 500°C and then rinsed in molten lithium.

9.4.5 Conclusions

1. Molten Pt–17 at. % Li is an aggressive environment for austenitic stainless steel.
2. Results from metallographic examination and energy dispersive x-ray analysis of type 316 stainless steel exposed to thermally convective Pt–17 at. % Li were consistent with a stripping of the corrosion layer during the rinsing of specimens in lithium to remove the residual lead-lithium from the exposed specimens.
3. The removal of the corrosion layer during the lithium rinse allows the total corrosion weight loss to be determined. However, since a fresh austenitic surface is then present on the specimens, further exposure of the same coupons in the loop yields data that are not representative of a continuing corrosion process. As such, the data are not directly comparable with those obtained in lithium by using multiple exposures of the same specimens.

9.4.6 References

1. J. H DeVan and J. R DiStefano, "Thermal-Convection Loop Tests of Type 316 Stainless Steel in Lithium." pp. 200–208 in *ADP Quart. Bog. Rep. Mar. 31, 1978,* DOE/ET-0058/1, U.S. DOE, Office of Fusion Energy.
2. P. F. Tortorelli and J. H DeVan, "Corrosion of Type 316 Stainless Steel in Flowing Pb–17 at. % Li," pp. 203–4 in *ADP Semiannu. Bog. Rep. Sept. 30, 1983,* DOE/ER-0045/11, U.S. DOE, Office of Fusion Energy.
3. O. K. Chopra and D. L. Smith, "Corrosion of Ferrous Alloys in Eutectic Lead-Lithium Environment," to be published in the proceedings of the Third Topical Meeting on Fusion Reactor Materials, September 1983.
4. P. Fauvet, G Santarini, and G Sannier, CEA, Fontenay-aux-Roses, France, to be published.

DOE/ER-0045/12
Distribution
Category
uc-20, 20c

DISTRIBUTION

1–6. Argonne National Laboratory, 9700 South Cass Avenue, Argonne, IL 60439

L. Greenwood
V. Maroni
R. F. Mattas
R. E Nygren
D. L. Smith
H. Wiedersich

7–8. Battelle-Pacific Northwest Laboratory, P.O. Box 999, Richland, WA 99352

J. L. Brimhall
D. Dingee

9. Brookhaven National Laboratory, Upton, NY 11973

C. L. Snead, Jr.

10. Carnegie-Mellon University, Pittsburgh, PA 15213

J. C. Williams

11. Colorado School of Mines, Golden, CO 80401

G. R. Edwards

12–195. Department of Energy, Technical Information Center, Office of Information Services, P.O. Box 62, Oak Ridge, TN 37830

For distribution as shown in TID-4500 Distribution Category, UC-20 (Magnetic Fusion Energy), and UC-20c (Reactor Materials)

196–202. Oepartment of Energy, Office of Fusion Energy, Washington, DC 20545

M. M. Cohen
G. M. Haas
T. C. Reuther, Jr. (5 copies)

203. Department of Energy, Oak Ridge Operations Office, P.O. Box E, Oak Ridge, TN 37830

Office of Assistant Manager for Energy Research and Development

204. Energy Technology Engineering Center, P.O. Box 1449, Canoga Park, CA 91304

ETEC Library

205–206. GA Technologies, Inc., P.O. Box 81608, San Diego, CA 92138

T. A Lechtenberg
D. I. Roberts

207–209. Lawrence Livermore National Laboratory, P.O. Box 808, Livermore, CA 94550

E.N.C. Dalder
M. Guinan
C. M. Logan

210. Los Alamos National Laboratory, Mail Stop H809, Los Alamos, NM 87545

M. S. Wechsler

211. Massachusetts Institute of Technology, 138 Albany Street, Cambridge, MA 02139

O. K. Harling

212–213. Massachusetts Institute of Technology, 77 Massachusetts Ave., Cambridge, MA 02139

N. J. Grant
V. B. Vander Sande

214–215. McDonnell Douglas Astronautics Company, East, P.O. Box 516, St. Louis, MO 63166

J. W. Davis
D. A. DeFreece

216. National Materials Advisory Board, 2101 Constitution Ave., Washington, DC 20418

K. M. Zwilsky

217–218. Naval Research Laboratory, Washington, DC 20375

Superintendent, Materials Science and Technology Division
J. A. Sprague

219–258. Oak Ridge National Laboratory, P.O. Box X, Oak Ridge, TN 37831

Central Research Library (2 copies)
Document Reference Section
Laboratory Records Department (2 copies)
Laboratory Records Department, RC
ORNL Patent Section
E. E. Bloom (10 copies)
D. N. Braski
W. R. Corwin
J. H. DeVan
I. T. Dudley
M. L. Grossbeck
R. L. Klueh
R. A. Lillie
C. T. Liu
K. C. Liu
L. K. Mansur
P. J. Maziasz
C. J. McHargue
T. K. Roche
A. F. Rowcliffe
M. J. Saltmarsh
J. L. Scott
P. T. Thornton (3 copies)
P. F. Tortorelli
J. M. Vitek
F. W. Wiffen

259. Princeton University, Plasma Physics Laboratory, P.O. Box 451, Princeton, NJ 08544

P. Bonanos

260–261. Rensselaer Polytechnic Institute, Troy, NY 12181

D. Steiner
N. Stoloff

262–263. Sandia National Laboratories, Livermore Division 8316, Livermore, CA 94550

W. Bauer
J. C. Lippold

264–265. Sandia National Laboratories, P.O. Box 5800, Albuquerque, NM 87185

M. J. Davis
W. B. Gauster

266. Science Applications, Inc., 1200 Prospect, La Jolla, CA 92031

H. Gurol

267–268. University of California, Department of Chemical, Nuclear, and Thermal Engineering, Los Angeles, CA 90024

M. A. Abdou
R. W. Conn
N. M. Ghoniem

269. University of California, Santa Barbara, CA 93106

G. R. Odette

270. University of Missouri, Department of Mechanical and Aerospace Engineering, Columbia, MO 65211

M. Jolles

271. University of Virginia, Department of Materials Science, Charlottesville, VA 22901

W. A. Jesser

272. University of Wisconsin, 1500 Johnson Drive, Madison, WI 53706

W. G. Wolfer

273. Westinghouse Electric Company, Advanced Energy Systems Division, P.O. Box 10864, Pittsburgh, PA 15236

R. Bajaj
W. A. Boltax

274–281. Westinghouse Hanford Company, P.O. Box 1970, Richland, WA 99352

H. R. Brager
D. G. Doran
A. M. Ermi
F. A. Garner
D. S. Gelles
E. C. Opperman
R. W. Powell
J. L. Straalsund

☆U S GOVERNMENT PRINTING OFFICE 1984 746 067/4105